Spring 5-15-2022

Mutual Coupling Reduction Techniques for Multi-band Base Station Antennas

Evan Christopher Wayton
Syracuse University

Abstract

This dissertation proposes antenna design techniques which suppress mutual coupling in densely populated dual-polarized broadband multi-band base station antenna (BSA) arrays for improved radiation characteristics. Array face densification without the proposed techniques leads to undesirable interactions between arrays and radome cover. This research is supported by extensive full-wave electromagnetic simulations, characteristic mode analysis, equivalent circuit models, and array theory. The results are validated through measurements of the radiation patterns and scattering parameters of fabricated prototypes.

Upon excitation of a mid-band (MB) array, an electrically long low-band (LB) parasitic, necessary for broadband matching of the baseline LB dipole, exhibits dipole-like induced currents which degrade the MB radiation patterns. The currents are suppressed through parallel plate series capacitance integrated along the length of the LB dipole arms to lower the dipole self-impedance, enabling broadband matching using an electrically short LB parasitic. The proposed technique improves MB radiation pattern symmetry, cross-polar radiation (CPR), sidelobe level, and gain.

Upon excitation of the proposed LB dipole, the baseline MB dipole balun feed stems exhibit induced common mode currents, which radiate as electrically short monopoles over a conducting ground plane, that degrade the LB radiation characteristics. These currents are suppressed by integrating parallel plate series capacitance along the length of the balanced ports of the MB balun. The proposed balun improves the LB beamwidth stability, CPR, and gain stability.

The proposed serially loaded LB dipole and MB dipole balun feed stem are implemented simultaneously in a six-foot BSA in which the system performance improvements are verified.

Upon excitation of a high-band (HB) array in a tri-band array environment, the dielectric radome behaves as a partially reflecting surface. The reflected waves interfere with the HB excitation, resulting in significant boresight radiation attenuation in the upper part of the HB operating band. A Fabry-Perot cavity antenna (FPCA) operating in the second resonance mode ($N = 1$) is proposed to improve this attenuation through increasing the boresight directivity.

Upon HB excitation of the proposed FPCA, circular-disk MB parasitics, necessary for broadband matching of the neighboring MB array, exhibit dipole-like induced currents. The induced currents radiate as dipoles which reduce the HB half power beamwidth (HPBW) in the lower and middle part of the HB operating band. These currents are suppressed by introducing electrically thin radial slots in the baseline MB parasitic. The radial slots change the characteristic modes and lower their modal significance, which eliminates the secondary radiation sources. The proposed technique increases the HPBW in the lower and middle part of the HB operating band.

These proposed design techniques provide new tools to antenna designers which allow for the densification of BSA arrays for use in next generation cellular networks, while minimizing radiation pattern degradation otherwise present in baseline BSA designs using existing techniques.

Mutual Coupling Reduction Techniques for Multi-Band Base Station Antennas

by

Evan Christopher Wayton

B.S.E.E., University of Toledo 2011
M.S.E.E., Syracuse University 2013

Dissertation

Submitted in partial fulfillment of the requirements for the degree of
Doctor of Philosophy in Electrical and Computer Engineering.

Syracuse University

May 2022

To *Carl W. Gerst*
whose curiosity, unique perspectives,
and thirst for understanding
continue to inspire

and

To *Sam B. Nadler, Jr.*
who would never tell anyone that
an outlet is not worth pursuing and
who found that
asking a continuum of questions
leads to
interesting results

Acknowledgments

I extend sincere gratitude to my advisor Prof. Jay K. Lee, for teaching me electromagnetism throughout my graduate studies. When I thought that I could not go on, he assured me that he believed in me. Out of the kindness of his heart, he agreed to take me on as a graduate student.

I would like to thank Prof. Jun H. Choi, Prof. Sara Eftekharnejad, Prof. Jennifer W. Graham, and Prof. Mustafa C. Gursoy for serving as Committee Members and offering their time to review and provide feedback regarding this dissertation. I am also thankful for Prof. Jeongmin Ahn for serving as Chair of the Oral Examination Committee and representing the Graduate School.

I am grateful for JMA Wireless, for support and commitment to recognizing the importance of their employees' further education. I want to thank Niranjan Sundararajan for his encouragement, support, and flexibility in the pursuit of my doctoral research. Many thanks to Ghanshyam Mishra for the fruitful technical discussions regarding my research which we had the pleasure of sharing.

I owe thanks to many, without whom I would not have completed my doctoral studies. I remember fondly when Michael Enders calmly encouraged me to pursue my goals, despite my self-doubts. I would like to thank Sam Arnold for supporting me through agreeing to climb with me non-stop for a week, cancelling our international trip together to study, always encouraging *J.O.Y. in life*, and reminding me that "you can be anything…". The person I owe the biggest thanks to is my partner in life, Michelle Stantial. Michelle, without your belief in me and your encouragement to pursue my dreams, I did not stand a chance. Thank you for the long list of sacrifices you made which were integral in turning my dreams into reality. We have always shared a common love of understanding, journeys, and puzzles; interestingly, this has been a puzzling

journey in my pursuit for understanding. Thank you for everything, and for being you. Lastly, I want to thank my parents, who in raising me gave me the freedom to forge my own path in life.

Table of Contents

List of Tables

List of Figures

Chapter 1

Introduction

Often times throughout history, innovation occurs without the immediate realization of the revolutionary impacts which are to follow in the wake of the discovery. For example, the invention of the laser was often viewed as a solution without a problem [1]. Reflection on the wide range of technologies which are dependent upon the laser makes readily apparent how previously unforeseen domains of technology can be born through innovation. Although the importance of wireless communication was recognized, the extent to which the world would depend upon it was not realized all at once. The advent of very large scale integrated circuits (VLSI) and lithium batteries acted as the ingredients [2] which would transform cellular mobile communication and wireless technology into integral aspects of the everyday lives of many individuals.

With the advent of wireless communication came an increasing demand for the amount of data which these networks were to transmit and receive. The first commercial mobile communication network was launched in Finland in 1971 and was known as the zero generation (0G) cellular network [2]. Although not commercially successful, this was the spark which influenced the successful first generation (1G) cellular network. Both 0G and 1G networks operated using analog circuitry and thus were fairly large and poorly integrated. The second generation (2G) of cellular networks utilized digital circuitry, allowing for more highly integrated cellular mobile phones as well as increased data rates. 2G networks also offered users of mobile phones the ability to send and receive text messages (short message service or SMS) and download media content such as ring tones [2]. Third generation (3G) networks offered further increases to data rates, with targets of up to 384 kilobits per second (kbps) in outdoor environments and 2 megabits per second (Mbps) indoors [2]. The increased data rates available in 3G networks allowed mobile users to access the

internet and to host video calls. The fourth generation (4G) mobile network further increased the achievable data rates, but more importantly increased the speed at which large amounts of data was accessible to the users. A thorough discussion surrounding the growth of wireless communication usage can be found in [3].

Not only have users begun to utilize exponentially larger amounts of data, but also the number of wireless users has grown exponentially. Part of the reason for the growth in the number of wireless users is that as the technology has matured it has become more affordable and therefore more accessible to the general public. However, this is not the only reason for such a large number of users. As with the development of the laser, the evolution of wireless technology itself has given rise to entirely new areas of use which had not previously existed. With 3G and 4G networks came "smart phones" which put the power of a computer into the palm of the user's hand. Applications were developed for the user to monitor biometric data, bank account activity, and to play low-latency data intensive video games while interacting with other users. Furthermore, it became commonplace to use the video and audio capability of the mobile phone to regularly document and upload live video footage of athletic events, concert experiences, and social gatherings at the level of the individual user. Historically when one wanted to see such footage it had to be provided through a television channel, or a news source which was live on the scene.

When the users' expectations are not met, the wireless communication networks must again transform to meet the demands of the users. At the junction of 4G and 5G there are already additional wireless communication demands which have begun to form and be seriously considered. The target of 5G networks is to support and enable industries of manufacturing, construction, transportation, health, smart cities and communities, education, tourism, agriculture, and finance through low latency, high-quality real-time video transmission, and highly reliable

connectivity [4]. 5G networks have been described as an Internet of Things (IoT) targeting the mobilization and automation of industry processes comprised of tens of billions of "smart devices" which will use their embedded communication capabilities and integrated sensors to act on their local environment based on intelligent logic [5].

As to exactly what new technological domains will be developed with the advent of 5G is yet to be determined. However, with the history of wireless as a guide it is expected that the demand for wireless data throughput will continue to grow in order to support our ever more connected reality here on earth and beyond.

1.1 Background of Base Station Antennas (BSAs)

Base station antennas (BSAs) play an integral role in the infrastructure which upholds the services that the wireless industry depends upon. Much like the wireless industry itself, BSAs have increased in complexity over the years. With each new generation of wireless technology comes a set of increasingly difficult challenges which engineers must overcome. As wireless network providers expand the frequency ranges over which they operate, BSAs have followed suit. Current BSAs utilize polarization and spatial diversity to increase the communication system's throughput over that of single-polarized antenna deployment. In order to support both spatial and polarization diversity within a single BSA at least two spatially diverse arrays offering orthogonal polarizations must be present. In order to further increase utility, BSAs offer these spatially diverse dual-polarized arrays at a variety of frequencies each of which covers a wide bandwidth. This demand for a plurality of wideband frequency-diverse dual-polarized antenna arrays within a single

housing ultimately increases the size of the BSA, as well as the mutual coupling between adjacent arrays.

Throughout this dissertation, the term “mutual coupling” refers to the rescattered component of the mutual coupling, as discussed in [6, pp. 474−476] and [7]. The sources of this component of the mutual coupling are the currents induced on adjacent arrays which reradiate some of the interchanged energy as secondary radiation sources, which thereby changes the far field radiation characteristics. As stated in [7], “the total contribution to the far-field pattern of a particular element in the array depends not only upon the excitation furnished by its own generator (the direct excitation) but upon the total parasitic excitation as well, which depends upon the couplings from and the excitation of the other generators.”

Cellular service providers are licensed to operate wireless networks in designated frequency bands. Some frequency bands are licensed to network providers through auctions, while other frequency bands are considered unlicensed and therefore are open to all network providers for usage. The frequency spectrum used for wireless communication must be shared and therefore frequency bands have been designated for specific uses. It was proposed that the effectiveness of spectrum utilization, one aspect of which is spectrum allocation, in personal communication systems has improved by a factor of about one trillion since 1901, and that it will continue for the foreseeable future [3].

This strategic allocation of spectrum helps ensure minimal radio frequency (RF) interference amongst users while also helping to maximize propagation based on the spectrum usage characteristics. One such use case is that of amateur radio bands in the USA. Knowing that the ionosphere is largely opaque to the spectrum between 3 MHz and 30 MHz, amateur-radio-enthusiast have historically placed their antennas atop tall towers in order to transmit around the

curvature of the earth. As a second use case, which is the focus of this dissertation, the microwave frequencies which pass through most everyday objects with minimal attenuation reside in the range 300 MHz–3.5 GHz [8]. It is precisely these frequencies which the current and next generation of BSAs utilize for mobile communication. It is for this reason that the frequency ranges commonly covered in BSAs are the low-band (LB) spectrum between 617 MHz and 960 MHz, mid-band (MB) spectrum between 1.695 GHz and 2.700 GHz, high-band (HB) spectrum between 3.4 GHz and 4.2 GHz, and the license assisted access (LAA) spectrum between 5.150 GHz and 5.925 GHz.

Periodically, previously unavailable spectrum is licensed to network carriers both in the US and throughout the world via an auction or government designation. For example, through the Federal Communications Commission's (FCC's) "5G FAST Plan," a wide variety of spectrum has been auctioned in order to facilitate America's superiority in 5G technology [9]. For example, in a 2016/2017 auction T-Mobile spent $7.99 billion on licenses granting rights to operate wireless networks utilizing 31 MHz of spectrum between 617 MHz and 698 MHz. This LB spectrum is particularly appealing for rural deployment due to its relatively low free-space path loss [10]. In 2020, the FCC concluded priority access licensing (PAL) auctions of 70 MHz of bandwidth residing between 3.550 GHz and 3.650 GHz, which amounted to over $4.5 billion in proceeds [11]. In December of 2020, the FCC began auctioning off licenses for flexible use of the 280 MHz C-band spectrum between 3.700 GHz and 3.980 GHz for use in upcoming 5G networks, raising a record-breaking $81.1 billion in proceeds [12]. The spectrum allocation growth does not stop at the sub-6 GHz spectrum, as the FCC recently auctioned licenses in the millimeter-wavelength (mm-wave) spectrum in the 24 GHz and 28 GHz bands [13] as well as the 37 GHz, 39 GHz, and 47 GHz bands [14]. A summary of the spending at FCC auctions for wireless usage is compiled

and shown in Figure 1-1, where the amount of bandwidth auctioned is shown in bold for each auction [15].

Although spectrum allocation has allowed for expansion of wireless networks, the primary means supporting the increase in the demand for wireless data since the 1950s has been through the densification of BSA deployments atop tall towers and buildings [3]. By placing BSAs closer together, and in turn reducing the service area of each BSA, frequencies are able to be reused between adjacent cells without significant inter-cell interference. Given that mm-waves suffer from a relatively high free-space path loss, further reduction in cell size in support of ultra-dense networks would greatly improve the deployment of mm-wave wireless networks.

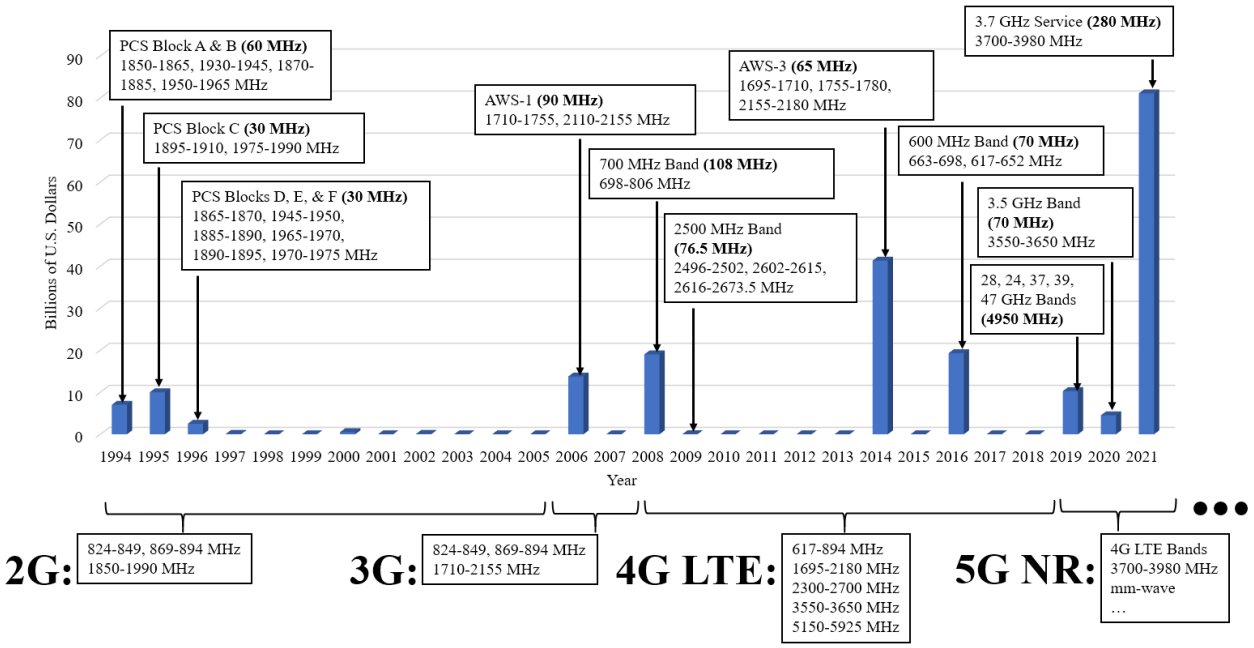

Figure 1-1: Spending at FCC auctions for the licensing of electromagnetic spectrum for wireless usage as a function of calendar year. Data compiled from [15].

1.2 Motivation

The reduction of mutual coupling in the design of antennas is important not only to BSAs but also to the design of user equipment (UE) such as smartphones [8]. The challenge of the so-called compact shared aperture antennas which house multiple frequency bands has also arisen in work focusing on unmanned aeronautical vehicles (UAVs), applications in which size and power are severely limited [16]. Careful placement of each antenna within the packaging proves to be an integral aspect of the design process. In fact, in both of the cases mentioned above the designers have suggested that the optimization of each element alone will not suffice, and therefore they prefer to optimize the antennas in the environment in which they will be present in the final application. This forces an iterative approach to the design cycle.

Provided the integral role that BSAs play in wireless communication, it is important that BSA design techniques found in the literature are able to accommodate the demands of increasing bandwidths, array density, and additional frequency bands co-located within a single BSA housing. The importance of minimizing inter-array mutual coupling and interference in BSAs is paramount when increasing the number of frequency and polarization diverse antenna arrays present within a fixed volume. How dense the antenna array face can be made, without significantly sacrificing the antenna performance, will play an important role in the future, as additional frequency bands become available for use in 5G wireless systems and beyond. Currently, BSA engineers are being challenged to accommodate new frequency bands into existing BSAs without increasing the volume or compromising the performance of the system. Through the discovery and understanding of new design techniques, which reduce the inter-array mutual coupling present in BSAs, engineers will succeed in meeting the demands of the wireless industry.

1.3 Current Mutual Coupling Reduction Techniques for Use in BSAs

There is a growing wealth of knowledge within the domain of BSA design and inter-array mutual coupling reduction techniques for dense wideband dual-polarized multi-band arrays. An extensive history of BSAs and design techniques available prior to 2009 are captured in Chen and Luk's work [2]. A more concise publication of similar topics was published by C. Beckman [17].

BSA realization, for sub-6 GHz applications, relies on the design of dual-polarized antenna elements covering all or part of the LB, MB, HB, and LAA frequency bands. The radiating elements are most often situated over a conducting ground plane, often referred to as a reflector. Linear ±45° polarization is commonplace for BSA arrays. While horizontal and vertical (HV) polarizations are found in older BSAs, undesirable radiation pattern asymmetries result between the two polarizations due to the aspect ratio of the reflector. In particular, reflectors are typically much longer in the vertical plane (V-plane), i.e., xz-plane, than they are wide in the horizontal plane (H-plane), i.e., yz-plane, which leads to differing effects in a linear array of horizontally polarized dipoles as compared to vertically polarized dipoles. Circularly polarized (CP) BSAs can also be found; however, they typically result in increased design complexity due to the need for hybrid couplers or complex feed networks for intrinsically CP antenna elements. Due to the symmetry of the reflector, the design of ±45° polarized arrays improves the pattern tracking between polarizations while also offering ease of manufacturing [2].

A wide variety of radiating elements have been proposed for use in dual-polarized BSAs for sub-6 GHz frequencies including crossed [18]–[21], bent [22]–[24], and looped [25]–[27] electric dipoles, full-wavelength dipoles [28]–[31], patch/suspended plate antennas (SPAs) [32]–[34], magneto-electric dipoles [35], [36], Vivaldi [37], [38], and slot antennas [39]. Each of these antenna types have their benefits as well as their drawbacks. For example, the crossed electric

dipole offers simplicity, high isolation, and has been shown to be tunable over a wide bandwidth. However, in order to achieve a unidirectional radiation pattern, the dipole is deployed approximately one-quarter of a wavelength above a metallic reflector. While this requirement may not add a significant amount of depth to the overall BSA for MB and HB frequencies, the depth required to accommodate LB dipoles may be unacceptable. The multilayer SPA offers a lower profile design; however, it suffers from an inherently narrower bandwidth, and often has complex feed mechanisms for enhancing bandwidth and radiation performance.

A variety of bandwidth enhancing techniques exist for dipole antennas. Bandwidth enhancing techniques typically focus on lowering the self-resistance of the dipole, introducing electrical resonances, and using wideband baluns to match the stabilized dipole impedance. Dipole antennas have utilized combinations of parasitic elements [40] such as rods [41], [42], patches [43], [44], rings [45], and crosses [19], [46] above and adjacent to [47]–[49] the radiators in order to lower the dipole resistance and capacitively load the antennas for the introduction of an electrical resonance. Slots in the dipole arms have also been used to increase dipole bandwidths. The slots shorten the current path lengths, and hence lower the self-resistance of the dipole [43], [50]. This technique exploits the fact that the radiation resistance of a dipole is proportional to the square of the dipole electrical length [51]. Although not in the context of BSAs, one bandwidth enhancing technique which has been recently proposed for use in dipole and loop antennas is the use of series capacitance in the radiating dipole arms or conducting loop [52]–[55]. This technique is of particular significance to this work and is discussed in more detail in Chapter 2 and Chapter 3.

Two common balun feed mechanisms for dipole antennas are the open stub Marchand balun [56], later re-discovered by Roberts in 1957 [57], and the shorted stub Pawsey balun [58]. The open stub Marchand balun, as shown in Figure 1-2, is most often found as the balun of choice in

BSAs due to its ability to be implemented using via-less microstrip transmission lines. The shorted stub Pawsey balun, as shown in Figure 1-3, requires a short circuit from the single ended transmission line to one of differential outputs.

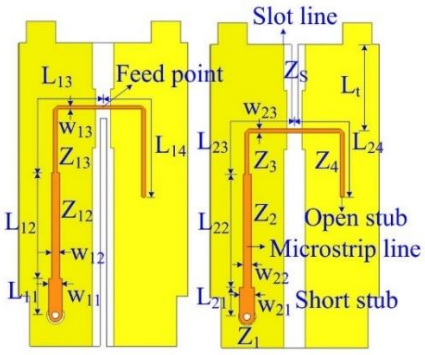

Figure 1-2: Example of two open stub Marchand baluns realized using microstrip transmission lines. Figure reproduced from [44]. Copyright © 2020, IEEE

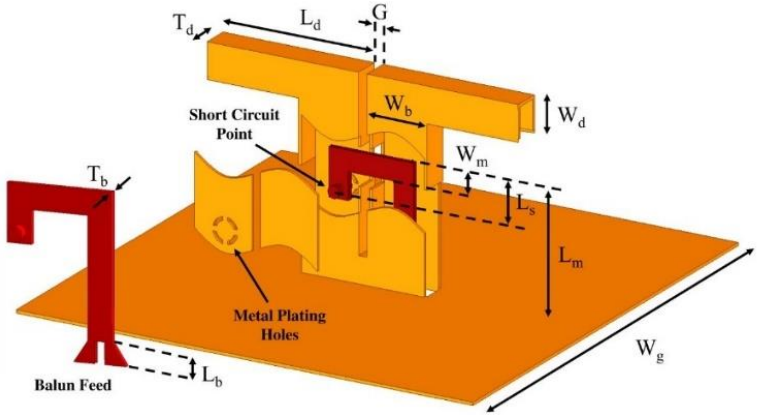

Figure 1-3: Example of a shorted stub Pawsey balun realized using an air stripline transmission line. Figure reproduced from [58]. Copyright © 2020, IEEE

Broadband patch/SPA design techniques have been covered extensively in [59]. The methods for increasing the bandwidth of patch antennas involve lowering the quality factor (Q) of the antenna, introducing additional resonances, and introducing impedance matching networks. The Q of the antenna can be lowered through reducing the substrate permittivity, increasing the height

of the patch antenna above the ground plane, or through the introduction of losses. Impedance matching techniques include external matching circuits and feed point optimization of the patch. The introduction of additional resonances has been realized through the use of secondary patches either above, or co-planar with the directly excited patch antenna [59].

Optimization of the antenna bandwidth alone does not suffice if the resulting radiation pattern and efficiency are not satisfactory. Thus, techniques have been proposed for enhancing certain radiation pattern attributes of BSAs. The telecommunication industry has developed guidelines for defining BSA radiation pattern characteristics in order to ensure commonality throughout the industry [60], [61]. One of the most fundamental techniques for controlling the radiation pattern is through the use of multiple radiating elements connected together to form an array. The relative excitation phases and element spacings determine the beamwidth, sidelobe levels, and radiation direction through a combination of the element patterns and the array factor [62]. While the array factor most often is introduced in the context of the element patterns and the spacing of the driven elements present within an array, currents induced on adjacent arrays and parasitic elements also play a significant role in determining the overall radiation characteristics of an array. The implications of electromagnetic coupling between adjacent arrays are of particular importance to the telecommunication industry due to the density of the multi-band arrays and the plurality of frequency bands present in BSAs.

While the optimization of the antenna element alone may reveal fundamental insights into particular benefits and limitations of the element design, it does not reveal the full story of how the element will perform in the presence of other radiating elements. The excitation of neighboring elements within the array will further alter the antenna impedance. It is for this reason that the active voltage standing wave ratio (VSWR) [63], or perhaps more appropriately called the scan

impedance [64], of the antenna elements should be the determining factor of the achievable bandwidth of an antenna within an array environment. This active impedance is defined as the ratio of the voltage across the terminals of an array element to the current flowing at those terminals when all array elements are in place and excited [65]. Similarly, radiation characteristics should also be evaluated within the array environment under active condition. This change in dipole impedance and radiation characteristics, caused by adjacent elements and neighboring arrays, is known as mutual coupling [66]. It is important to note that although mutual coupling is a near field phenomenon, the far field pattern acts as an indicator of the amount of mutual coupling present within the array [67].

Although the radiation characteristics in all of space are important, at this time BSA patterns are predominantly characterized by their radiation patterns in the H-plane and V-plane, which throughout this dissertation correspond to radiation cuts in the yz-plane and xz-plane, respectively. The H-plane beamwidth, or horizontal beamwidth (HBW), of a BSA is largely defined through the width of the reflector and the design of the radiating elements. Without a wide enough reflector, area on the reflector will not be available to control the HBW through the use of an array factor in the H-plane. The half power, –3 dB, beamwidth (HPBW) and the –10 dB HBW are commonly used metrics to describe the angular sectors beyond which the magnitude of the radiation pattern falls to half, or one-tenth, of the peak power radiated in a given direction. The desired HPBW for sector antennas is often 60° but can range between 40° to 80°. The optimal HBW is a function of the environment, and thus the path loss exponent, as well as the frequency re-use plan selected for the planned network [2], [17]. Although the –10 dB HBW is always wider than the HPBW, it is typically advantageous to make this as narrow as possible to minimize inter-cell interference.

The reflector length is typically determined by the targeted HPBW in the V-plane, or vertical beamwidth (VBW), as well as any local zoning restrictions regarding the maximum BSA size. Antenna elements within an array typically extend through all or a portion of the reflector length. Although additional factors such as overall antenna weight, wind loading, and vibration play an important role in determining feasible BSA dimensions, they are beyond the scope of this work.

While the overall size of the reflector is often limited due to design specifications of the BSA, techniques have been proposed which partially overcome these limitations through manipulation of the internal reflector shape. For example, reflector flanges [68], [69], corrugations [70], metallic cavities over both traditional reflectors [71]–[73], and reflectors made of artificial magnetic conductors (AMCs) [74], have been proposed to reduce frequency dependence of the HBW caused by limited reflector sizes. The use of partially reflecting surfaces (PRSs) above radiating elements [75], such as dielectric slabs or metamaterial structures has also been proposed for increasing the directivity of antennas and antenna arrays [76]–[79]. The phenomenon exploited in this technique is that of a resonant Fabry-Perot cavity, and the antennas are known as Fabry-Perot cavity antennas (FPCAs). Recently, researchers have overcome the bandwidth limitations typically present in the use of PRSs through using multiple layers of thin dielectric slabs [80]. The design of an FPCA for directivity enhancement is discussed in more detail in Chapter 5.

Another factor which limits the BSA size is the depth of the antenna. The maximum radome dimensions are often provided as a design specification. The radome is most often realized as a dielectric protective covering, which is part of the BSA, that shields the circuitry from direct exposure to rain, snow, wind, and solar radiation. Much effort has gone into proposing methods for depth reduction of BSAs. For example, the use of AMC reflectors allows electric dipoles to be deployed $<< \lambda/4$ above the reflector, where λ is the free-space wavelength at the frequency under

consideration. While the reduction in BSA depth achieved through the use of AMC reflectors is most pronounced at LB frequencies [81], it has also been demonstrated for MB [74], [82], [83], HB [84], and LAA [85] frequencies. While dual-band [86] and tri-band [87], [88] AMCs have been realized, their bandwidths are currently too narrow to fully accommodate the demands of sub-6 GHz BSAs. Novel usage of frequency selective surfaces (FSSs) and parasitic loading have been demonstrated to greatly reduce the height of LB dipoles when placed above the radiating element [89], [90].

Given the limited spatial volume available in BSAs, much consideration must go into determining the optimal configuration of the arrays for a given design specification. There are three common architectures currently found in dense multi-band BSAs, namely interleaved, embedded, and stacked architectures.

Interleaved architectures are most commonly found in industry due to their relatively low-cost and ease of manufacturing. This architecture, as shown in Figure 1-4, intersperses two or more arrays operating in different frequency bands along the width and length of the reflector. Due to closely guarded intellectual property, the exact architectures used by companies which design BSAs are rarely made public unless first in the form of a patent application. Numerous examples of interleaved architectures are found in the literature [31], [91]–[95].

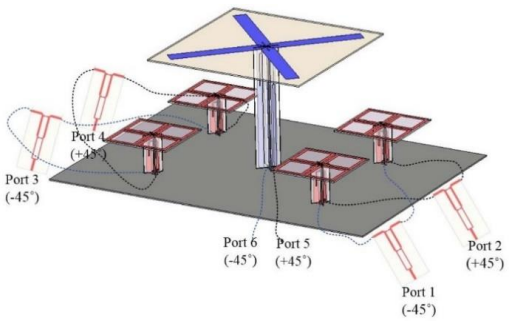

Figure 1-4: Example of an interleaved array architecture. Figure reproduced from [94]. Copyright © 2019, IEEE

Embedded architectures, as shown in Figure 1-5, are based on the ability to nest a higher frequency band element within the footprint of a lower frequency band element. For arrays using embedded architectures the co-design of radiating elements is paramount. The application of the embedded architecture is typically limited to the cases in which the first array operates at approximately twice the frequency as the second array, thus allowing both arrays to have approximately half-wavelength spacing. Numerous examples of embedded architectures are found in the literature [73], [96]–[98].

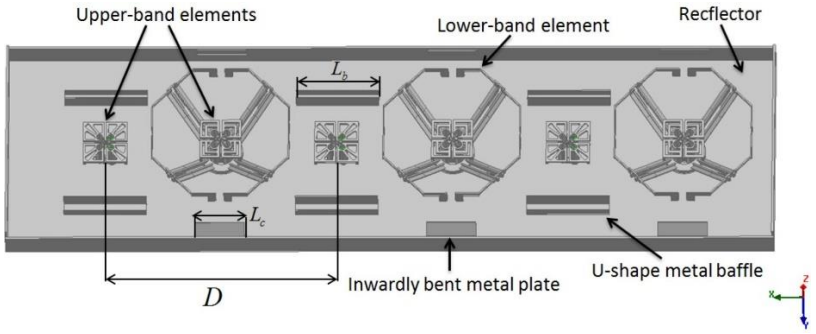

Figure 1-5: Example of an embedded array architecture. Figure reproduced from [99]. Copyright © 2017, IEEE

Stacked architectures, as shown in Figure 1-6, place antennas which operate at a relatively high frequency band on top of those which operate at a lower frequency band. Stacked architectures have been proposed in which the LB radiators act as the ground plane of the MB radiators [100]. While this technique increases the density of the array face, it leads to complicated feed networks and can increase the overall BSA depth. The increase in depth often exhibited by the stacked architecture has been overcome by loading the LB dipole with an FSS which allows for a reduction in the LB dipole height [89]. The FSS acts as a low-pass filter which reflects HB frequencies. A further simplification to the realization of a stacked architecture was proposed by replacing the FSS with four parasitic metallic plates [90].

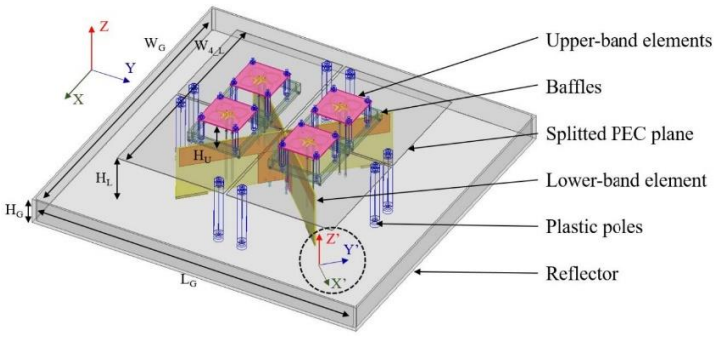

Figure 1-6: Example of a stacked array architecture. Figure reproduced from [90]. Copyright © 2019, IEEE

Depending upon the design specifications, any of these three architectures may be suitable candidates for the design of a BSA. However, the selection of these architectures cannot be made in isolation from the design specifications. The selection of the type of radiating elements used in the array and array architecture itself are intimately connected, together with the design specifications. For example, consider a design specification which demands two dual-polarized MB arrays and one dual-polarized LB array. Furthermore, the design requires minimizing the reflector and radome width for a given LB array factor in the H-plane (yz-plane). One attempt at realizing the design specifications, referred to as Option A, may be to utilize dual-polarized crossed dipoles for both LB and MB radiating elements with the H-plane array factor set by the distance, LB_y, as shown in Figure 1-7. Another method for achieving the design specifications, call it Option B, may be to utilize dual-polarized crossed dipoles for MB elements while using single-polarized bent LB dipoles with the same H-plane spacing, namely LB_y, as shown in Figure 1-8. Here the array consists of two unit cells (UCs), UC 1 and UC 1', repeated along the length of the reflector. The width spanned by the LB dipoles in the H-plane is denoted as X_1 and X_2 for Option A and Option B, respectively. For a given H-plane spacing, LB_y, it is observed that $X_2 < X_1$. Therefore, it is expected that Option B can utilize a narrower reflector and radome for a given H-plane array

factor, and hence is the suitable candidate provided the design specifications. Such is the case for the BSA design specifications which drove the selection of the dipoles and architecture of the UCs of Chapter 2 and Chapter 3, and the BSA array discussed in Chapter 4. Depending upon the design of the radiating elements, Option B may exhibit a reduction in the inter-array mutual coupling in comparison to Option A.

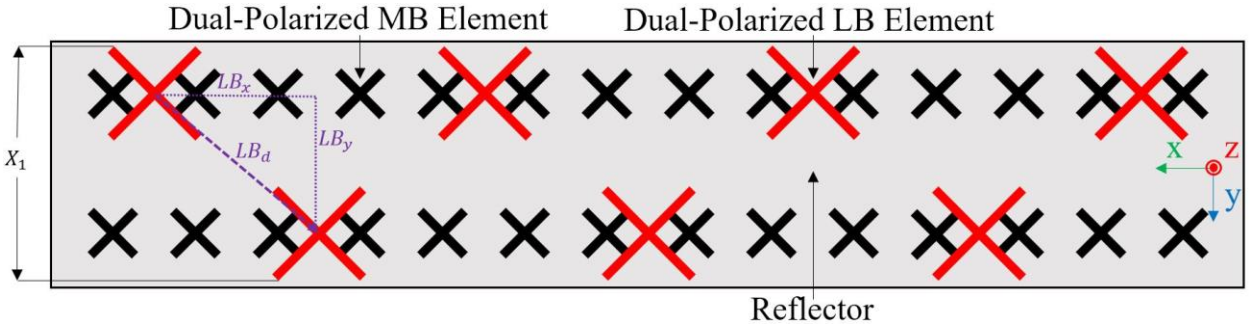

Figure 1-7: Example of Option A, a dual-band array using dual-polarized crossed MB and LB dipoles with an array factor in both H-plane and V-plane.

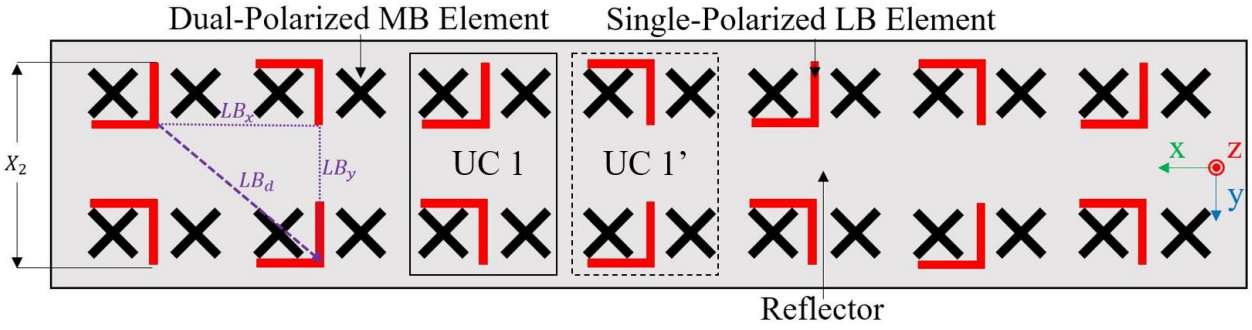

Figure 1-8: Example of Option B, a dual-band array using dual-polarized crossed MB dipoles and single-polarized bent LB dipoles with an array factor in both H-plane and V-plane.

Much work has gone into proposing methods which reduce the mutual coupling in arrays utilizing interleaved architectures. For example, resonant inductor-capacitor (LC) networks have been integrated into dipole arms [94], [101]–[103], and balun feed stems [104] for the suppression of in-band resonances which corrupt radiation patterns of adjacent arrays. In [94], the LC network

acts as a low-pass filter with the inductor behaving as an RF choke at MB frequencies. Unfortunately, the LC network limits the achievable LB bandwidth of [94] to 19.7% (0.840–1.000 GHz) whereas typical LB operating bands for BSAs range from 24.6% (698–894 MHz) to 43.5% (617–960 MHz). The main limitations associated with designs utilizing inductive RF filtering is the losses associated with the inductance. Other proposed methods for suppression of mutual coupling between adjacent arrays are mantle cloaking [105], [106] and filtering antennas [95], [107].

One common cause of performance degradation due to mutual coupling in multi-band arrays is the presence of induced common-mode (CM) currents in radiating elements adjacent to the excited array. The current on a pair of conductors can be expressed as a superposition of CM and differential-mode (DM) currents. The CM currents on the two conductors have identical amplitude and phase, while the DM currents have equal amplitude and opposite phase. If the separation of the conductors is small with respect to the wavelength, then, in the far field, the superposition of the electric fields radiated by the CM currents have a tendency to be constructive over a large portion of space. On the other hand, the radiated fields generated by the DM currents have a tendency to be destructive in much of space. It is for this reason that although the magnitude of the DM current present in a circuit is often much larger than that of the CM currents, the radiated emissions are most often dominated by the fields generated by the CM currents [108]. The topic of CM filtering in the context of electromagnetic compatibility (EMC) is well studied [109]. Suppression of mutual coupling, caused by induced CM currents, is of particular importance to this work and is discussed in detail in Chapter 3.

Several proposed solutions for the suppression of disruptive CM currents are available in the literature. For example, Cavallo et al. recognized that changing the balun feed length or dipole

length can push the CM resonance out of the band of interest [110]. However, they proposed an alternative approach based on an aperture-coupled transformer which acts as a CM rejection circuit. Other researchers later carried out what Cavallo et al. had recognized and changed the length of the balun feeds [111], [112] and dipole arms [104] to achieve CM rejection. Other proposed techniques include dipole feed networks which utilize CM rejecting microstrip-slotline transitions [113] and power dividers [26], as well as capacitor-inductor-capacitor (CLC) filtering circuits which push the resonance out of band [114].

1.4 Research Objectives

The objective of the dissertation is to propose design techniques not currently found in the literature for the reduction of mutual coupling in wideband dual-polarized multi-band BSAs. In particular the following techniques are explored.

1. An electrically long parasitic, necessary for tuning a bent LB dipole over a wide bandwidth, is shown to lead to unwanted resonances upon excitation of adjacent MB dipoles. These resonances corrupt the MB radiation characteristics. A low-loss technique for transforming the self-impedance of the LB dipole through integrating series capacitance into the LB dipole arms is proposed, which allows for wideband matching of the LB radiator with an electrically short parasitic.

2. Upon the excitation of an LB radiating element, the effective electrical path length of the balun feed stems are shown to support induced CM currents in the adjacent MB subassembly. These induced CM currents, present within the MB subassemblies, corrupt the LB radiation characteristics. Reduction of the magnitude of radiation due to the CM

currents induced on the conducting vertical MB dipole feed stems is proposed through the integration of series capacitance into the ground of the MB microstrip balun feed stem.

3. The proposed mutual coupling techniques of Chapter 2 and Chapter 3 are implemented together in a fully functional BSA to verify the BSA system improvements.

4. The presence of an MB parasitic necessary for the wideband operation of an MB dipole is shown to lead to undesirable resonances upon the excitation of adjacent HB dipoles. These resonances, present within the MB parasitics, corrupt the HB radiation characteristics. The presence of the radome is also shown to lead to additional HB radiation pattern distortion. A composite technique is proposed which introduces slots into the MB parasitics to remove the undesired resonance from the HB frequency band of interest, while introducing an HB Fabry-Perot cavity antenna (FPCA) to increase the directivity of the HB array.

This research was conducted over a six-year period primarily in the spirit of Michael Faraday, namely first through empirical means after which the theoretical explanations were investigated. The design techniques were developed as solutions to complex problems which occurred throughout the design cycle of real BSA systems. Although conducting research for enhancing industrial BSA applications proved to be challenging, the reward of contributing not only to the literature and understanding of BSA design techniques but also directly to the critical BSA infrastructure on which so much of our society relies, proved to be a fruitful undertaking.

1.5 Chapter Overview

The structure of the dissertation is as follows. Chapter 2 introduces a dual-band UC, in which the mutual coupling between the LB and MB arrays leads to degradation in the MB radiation

pattern. The root cause of the MB radiation pattern degradation is investigated. After the source of the mutual coupling is identified as the electrically long LB parasitic, an innovative series-capacitance based mutual coupling reduction technique is proposed to allow the LB dipole to be matched using an electrically short LB parasitic. The proposed solution is verified through full-wave finite element simulations as well as through prototype measurements.

Chapter 3 considers two different dual-band UCs in which the mutual coupling between the MB and LB arrays leads to degradation of the LB radiation patterns. The first UC considered, UC 1, is the proposed UC of Chapter 2. The second UC considered is a distinctly different UC in which both the LB and MB arrays operate over broader bandwidths. The root cause of the LB radiation pattern degradation is investigated for both UCs. After the source of the mutual coupling is identified as the conducting vertical MB balun feed stems, an innovative series-capacitance based mutual coupling reduction technique is proposed to reduce the CM currents in the MB vertical dipole feed stems, and hence the mutual coupling. The proposed solution is verified through full-wave finite element simulations as well as through prototype measurements of both UCs.

Chapter 4 evaluates the performance of a dual-band BSA, with an architecture as shown in Figure 1-8. The performance of the BSA is evaluated though full-wave finite element simulations as well as through prototype measurements, with and without the use of the mutual coupling reduction techniques proposed in Chapter 2 and Chapter 3.

Chapter 5 considers a tri-band array environment in which the mutual coupling of the HB array to the LB and MB arrays, and dielectric radome, leads to degradation of the HB radiation patterns. The root causes of the HB radiation pattern degradation are investigated analytically as well as through the use of characteristic mode (CRM) analysis. After the mutual coupling sources are identified as the dielectric radome and baseline MB parasitics, two mutual coupling reduction

techniques are proposed for elimination of the two sources of mutual coupling. The proposed solution includes the design of an HB FPCA and modifications to the baseline MB parasitics. The proposed solution requires the use of both proposed mutual coupling reduction techniques and is verified through full-wave finite element simulations as well as through prototype measurements.

Chapter 6 provides a summary of the dissertation while highlighting the key contributions. In addition, extensions to the conducted research as well as areas of future research are detailed and discussed.

Chapter 2

A Serially Loaded Capacitive Dipole for Mutual Coupling Reduction

This chapter focuses on the mid-band (MB) performance of a small section of the array architecture proposed in Figure 1-8. This section of the array is referred to as a unit cell (UC). The base station antenna (BSA) shown in the figure is composed of two UCs, UC 1 and UC 1', one of which will be the focus of this chapter. A method for mutual coupling reduction is proposed which improves the MB performance in the presence of the low-band (LB) dipoles. The electrically long metallic LB parasitic, necessary for broadband matching of the baseline LB dipole, is identified as the main source of the MB performance degradation. The proposed technique integrates series capacitance throughout the length of the LB dipole arms in order to reduce the self-impedance of the LB dipole. With the lower self-impedance, an electrically short metallic LB parasitic becomes a viable option for broadband LB matching. The proposed solution leads to significant MB performance improvements in comparison to the baseline UC.

The baseline and proposed solutions are investigated through the use of three dimensional (3−D) Full-wave Electromagnetic analysis using Ansys HFSS [115] after which a prototype is built and measured. The S-parameter measurements are carried out using a Keysight E5071C ENA Series Network Analyzer. The radiation patterns are measured in an anechoic spherical near field chamber built by NSI-MI. The near field data is measured and then a near field to far field transformation is carried out using NSI's software package, NSI2000 [116]. Patents which utilize the proposed method in a dual-band BSA array have been granted [117]–[121].

2.1 Design of Dual-Band Baseline Unit Cell (UC) 1

The UC considered in this chapter consists of two MB sub-arrays, and two LB sub-arrays as shown in Figure 2-1. The word "sub-array" is reserved in this text for use when describing arrays within a UC, it acts as a reminder to the fact that the UC is only a portion of a larger array; one such array is discussed in Chapter 4. The LB and MB operating bands are 698–894 MHz and 1.695–2.180 GHz, respectively. All LB and MB printed circuit boards (PCBs) are designed to use a 0.030" thick dielectric material with relative permittivity $\varepsilon_r = 3.4$ and dielectric loss-tangent $\delta_t = 0.0027$.

Both the left and right MB sub-arrays are composed of two dual-polarized crossed dipoles separated by a distance $S_{MB2} = 4.800"$, corresponding to approximately $0.787\lambda_{f_c}$ where λ_{f_c} represents the free-space wavelength at the center of the MB operating band. The input port of each polarization is connected to an equal-split two-way microstrip T-junction power divider. The two outputs of each power divider feed the two elements comprising the sub-array and polarization to which it is connected. Therefore, there are four power dividers, two feeding the ±45° elements in the left sub-array, and two feeding the ±45° elements in the right sub-array. The inter-array spacing, S_{MB1}, between the left and right MB sub-arrays is chosen to provide sufficient spatial diversity and array-to-array isolation while having minimal overlap with the LB dipoles. Each LB sub-array is a single-polarized bent LB dipole. The shape and locations of the LB dipoles are selected to minimize the reflector width when the UC is used as part of a larger array. Such an array was proposed in Figure 1-8 to minimize the reflector width for a given LB horizontal plane (H-plane) array factor and will be the focus of Chapter 4. The relative positions of the LB and MB dipoles on the reflector, as labeled in Figure 2-1, are tabulated in Table 2-1.

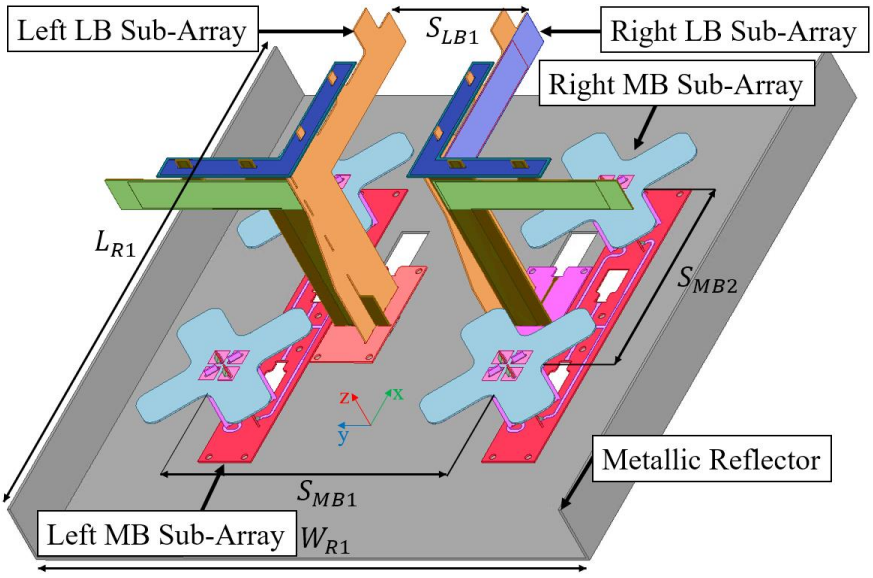

Figure 2-1: Dual-band baseline UC with left and right dual-polarized MB sub-arrays and left and right single-polarized LB sub-arrays.

Table 2-1: Dimensions controlling layout of dual-band UC. All units are in inches.

L_{R1}	W_{R1}	S_{LB1}	S_{MB1}	S_{MB2}
12.650	13.000	3.234	6.727	4.800

A dual-polarized half-wave dipole, fed by open stub Marchand balun feed stems, is designed to operate in the MB frequency range of 1.695–2.180 GHz. The geometry pertinent to the dipole performance is labeled in Figure 2-2 and tabulated in Table 2-2. The MB dipole tops, ±45° polarization balun feed stem PCBs, and the MB feed board comprise the MB dipole subassembly. The assembled MB dipole sub-array is shown in Figure 2-3.

All three PCBs comprising the MB dipole have a top metallization layer, L1, bottom metallization layer, L2, as well as top and bottom solder mask layers. There are reliefs in the solder mask to expose the solder pads of the metallization layers in areas which require direct electrical connectivity between PCBs. The +45° and –45° PCB feed stems have upward/downward slots, respectively, which allow them to interlock orthogonally to each other during assembly. The dipole

top is mounted perpendicular to the two feed stems. The balanced ports, provided by the balun feed stems, are soldered to the square metallic pads, of width w_{11}, on the L1 layer of the dipole top PCB. These square metallic pads capacitively feed the radiating dipole arms which are located beneath the square pads on the L2 layer. The unbalanced port of each balun solders to the output of the two-way splitter located on the feed PCB. The L2 layer of the balun feed stems are grounded via solder to the L2 layer of the feed board. The feed board is mounted to the reflector.

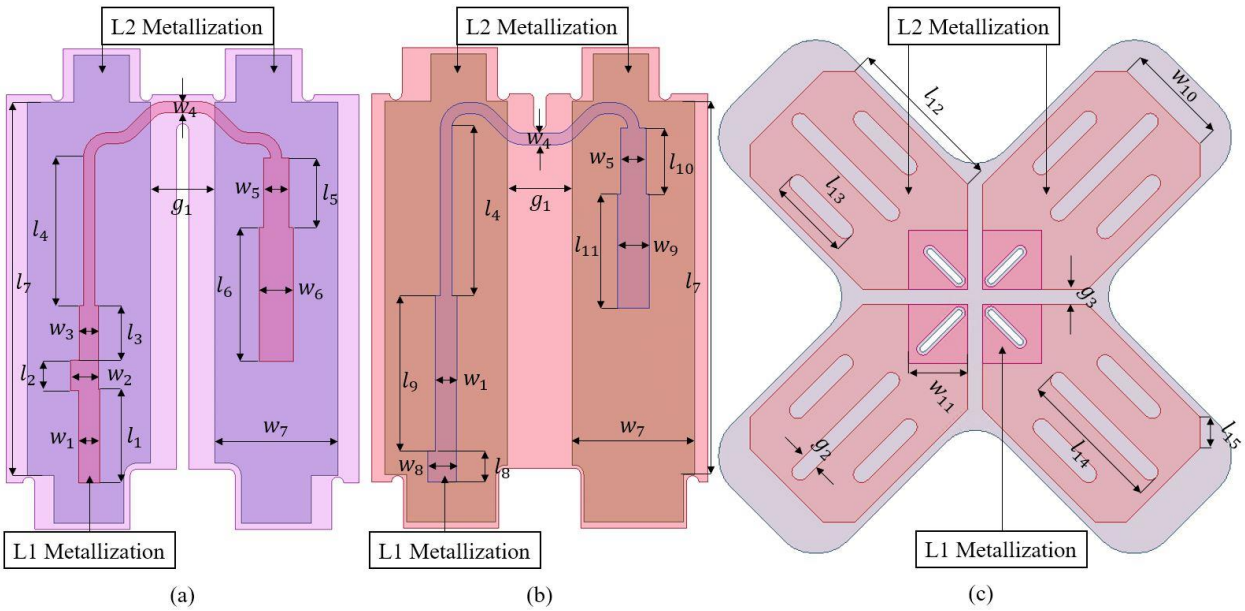

Figure 2-2: Baseline MB PCBs for (a) +45° balun feed stem, (b) –45° balun feed stem, and (c) dipole top.

Table 2-2: Dimensions of baseline MB dipole subassembly. All units are in inches.

w_1	w_2	w_3	w_4	w_5	w_6	w_7	w_8	w_9	w_{10}	w_{11}	l_1	l_2	l_3	l_4
0.069	0.091	0.061	0.037	0.083	0.111	0.400	0.094	0.104	0.631	0.359	0.301	0.099	0.176	0.480
l_5	l_6	l_7	l_8	l_9	l_{10}	l_{11}	l_{12}	l_{13}	l_{14}	l_{15}	g_1	g_2	g_3	
0.227	0.434	1.213	0.100	0.505	0.215	0.371	0.972	0.508	0.887	0.192	0.210	0.100	0.092	

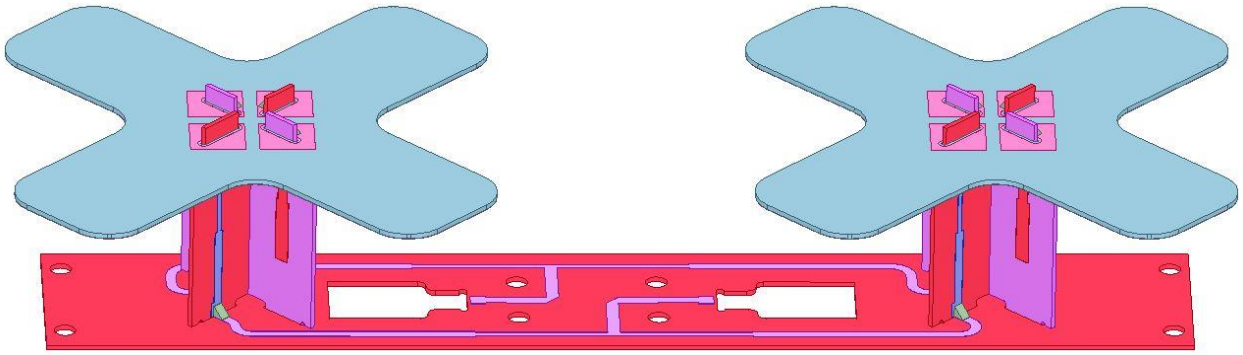

Figure 2-3: Simulation model of assembled baseline MB sub-array.

The LB dipole is a single-polarized directly fed half-wave bent dipole designed to operate in the LB frequency range of 698–894 MHz. The geometry that is pertinent to the baseline LB performance is labeled in Figure 2-4 and tabulated in Table 2-3. The PCBs corresponding to the −45° LB dipole are mirror images of those used for the +45° LB dipole. Each LB dipole assembly is comprised of a feed board mounted to the reflector, two vertically mounted PCBs comprising the LB dipole and vertical feed, and an L-shaped PCB which acts as a parasitic element, as shown in Figure 2-5. The vertically mounted PCBs have slots and corresponding tabs which allow them to interlock perpendicular to each other while also mounting to slots in the microstrip feed board. The microstrip transmission line on the horizontal feed board is soldered to the vertical microstrip transmission line on layer L1 of the LB dipole feed stem of PCB 1. The L2 layer of PCB 1 and the L2 layer of the LB feed board are soldered together where the LB stem passes through the feed board. The L2 layer of PCB 1 acts both as the microstrip ground as well as one of the dipole arms. The microstrip transmission line on PCB 1 travels vertically upward and is soldered to the L1 layer of PCB 2, at the orthogonal interconnection between the two PCBs. The L1 layer of PCB 2 is the second arm of the LB dipole. The baseline LB parasitic also has mounting slots which connect to the vertical PCBs, PCB 1 and PCB 2, upon installation. The LB parasitic is mounted at a height

g_4 above the LB dipole arms. The LB parasitic is capacitively coupled to the conductors which comprise the dipole.

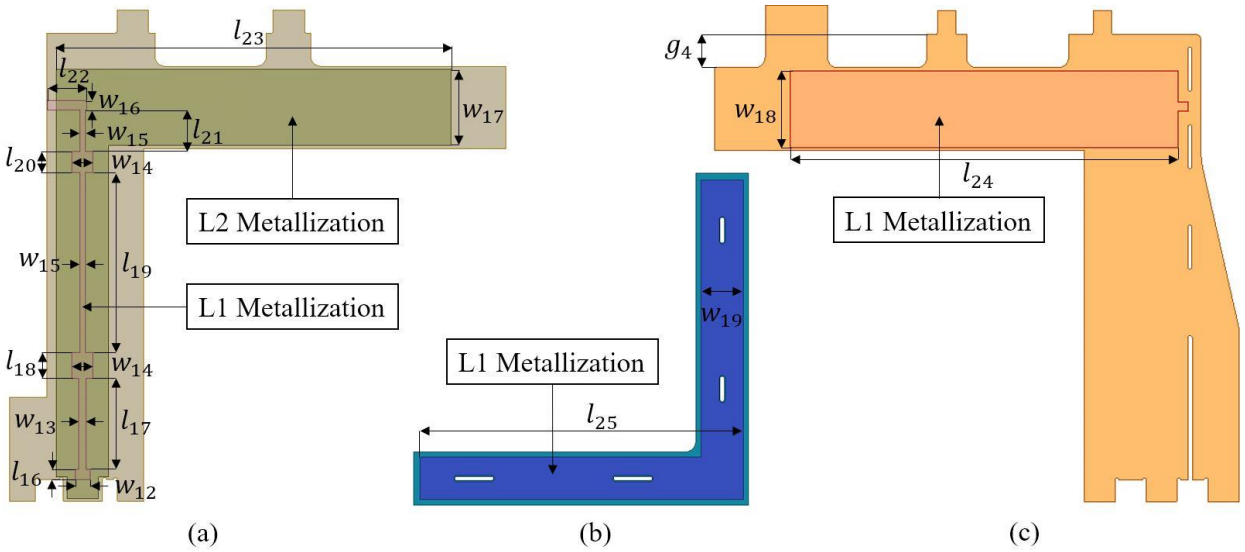

Figure 2-4: Baseline +45° LB dipole (a) PCB 1, (b) LB parasitic, and (c) PCB 2.

Table 2-3: Dimensions of the baseline LB dipole subassembly. All units are in inches.

w_{12}	w_{13}	w_{14}	w_{15}	w_{16}	w_{17}	w_{18}	w_{19}	l_{16}	l_{17}	l_{18}
0.140	0.069	0.200	0.050	0.088	0.730	0.734	0.400	0.010	0.872	0.250
l_{19}	l_{20}	l_{21}	l_{22}	l_{23}	l_{24}	l_{25}	g_4			
1.725	0.200	0.400	0.374	3.799	3.742	3.057	0.320			

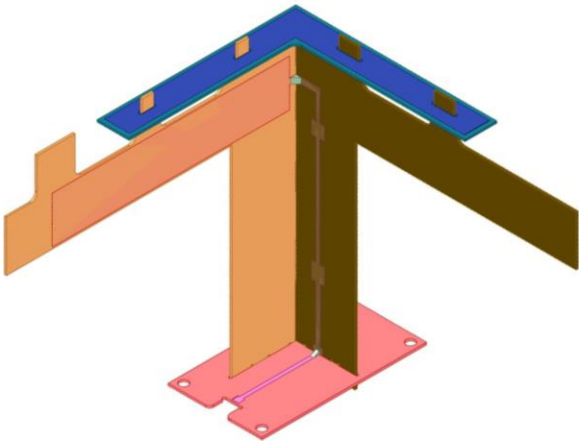

Figure 2-5: Simulation model of assembled baseline LB sub-array.

2.1.1 Parametric Analysis of LB Parasitic

In order to understand the role of the LB parasitic on determining the achievable LB dipole self-impedance, and therefore realizable LB bandwidth, parametric analyses of the parasitic length, l_{25}, height above the LB dipole, g_4, and orientation are carried out. The length of the parasitic is varied from 1" to 3" in 1" increments for three different heights above the LB dipole. The parasitic height above the LB dipole is varied from 0.085" to 0.585", in 0.25" increments.

A parametric study of the LB dipole reflection coefficient and self-impedance as a function of the parasitic length, l_{25}, is conducted in order to understand the length necessary for broadband matching from 698 MHz to 894 MHz. For the parametric study of the LB reflection coefficient, the UC is simulated at LB frequencies with the LB feed boards having lumped ports at the inputs of the 50 Ω microstrip lines, while the MB feed boards are terminated in 50 Ω loads. The results of the LB reflection coefficient for the different parasitic lengths are shown in Figure 2-6. Without the presence of the parasitic, the reflection coefficient varies widely across the band, as shown in Figure 2-6(b). Even if a broadband matching network were used to feed the LB dipole, the large variation in the dipole's reflection coefficient limits the realizable bandwidth of the LB dipole without an LB parasitic. As the length of the parasitic increases, the reflection coefficient reduces across the band. As is apparent from the results of the parametric analysis, a parasitic length close to 3" is required for broadband matching of the LB dipole. The necessity of the electrically long LB parasitic for broadband matching is further explored in analyzing the self-impedance of the LB dipole with varying LB parasitic lengths.

For the simulation of the LB self-impedance, the LB vertical microstrip feed line and corresponding ground plane are removed from the HFSS model, as is shown in Figure 2-7. In their place, lumped ports are placed between the two arms of each of the half-wave bent LB dipoles. In

this way the Z-parameters of the LB dipoles are used to understand the impact of the LB parasitic length, height, and orientation on the self-impedance, and therefore achievable bandwidth, of the baseline LB dipole. The parametric analyses are carried out for a parasitic oriented both co-planar with and perpendicular to the reflector, as is shown in Figure 2-7(a) and Figure 2-7(b), respectively.

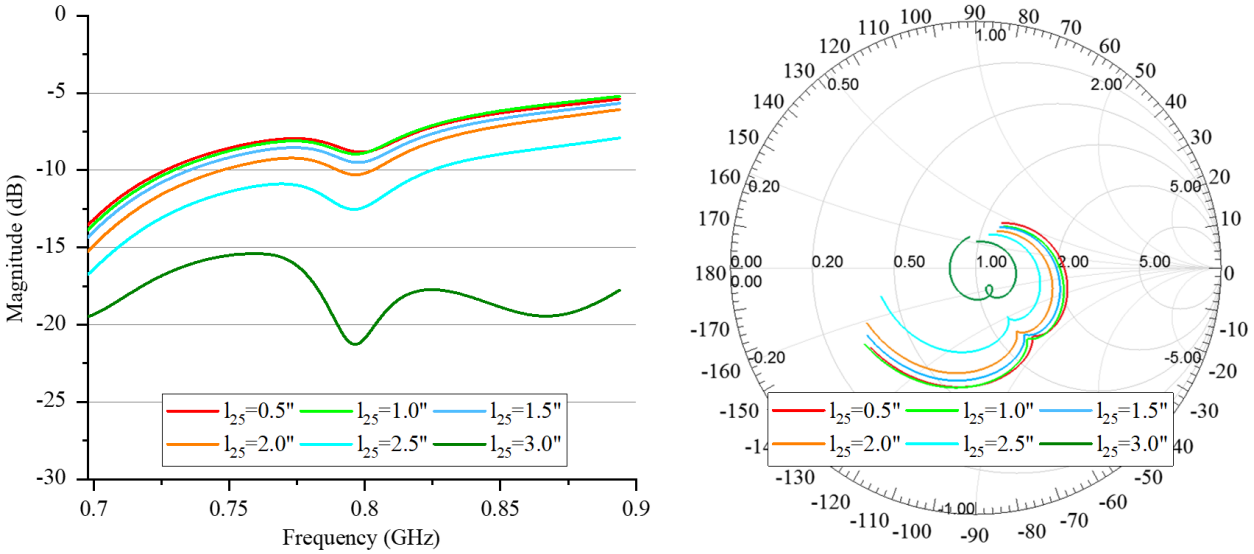

(a) (b)

Figure 2-6: The input reflection coefficient of the left +45° LB sub-array as a function of the parasitic length, l_{25}, as a (a) Cartesian plot and (b) Smith chart.

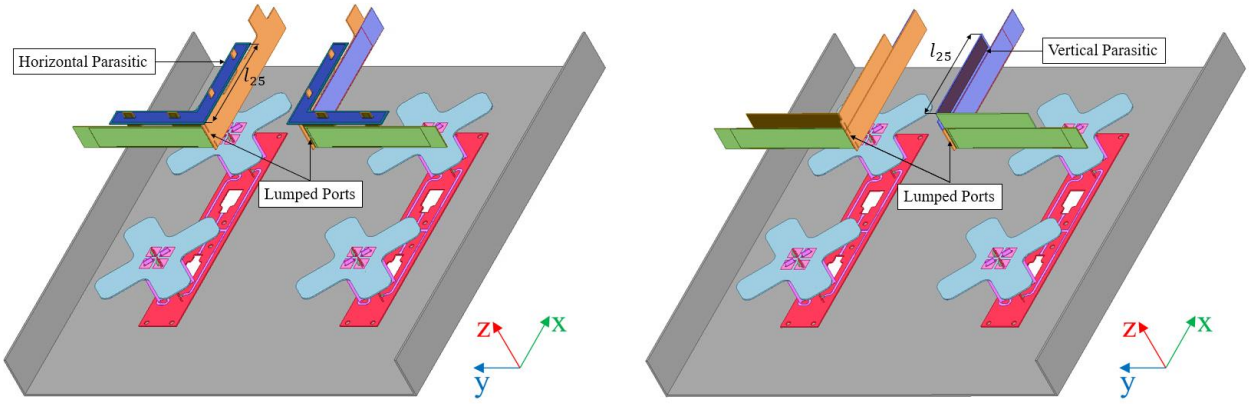

(a) (b)

Figure 2-7: UC model for simulating the LB dipole self-impedance as a function of the LB parasitic length and height above the dipole for (a) horizontally and (b) vertically oriented parasitic PCBs.

As the length of the horizontally oriented LB parasitic increases from 1” to 3” for parasitic heights g_4= 0.585”, 0.335”, and 0.085”, the peak self-resistance of the LB dipole reduces from 236 Ω to 103 Ω for l_{25} = 1”, 239 Ω to 90 Ω for l_{25} = 2”, and 240 Ω to 56 Ω for l_{25} = 3” respectively, over the operating band. This variation in self-impedance for the different cases is shown in Figure 2-8. Therefore, both increasing the length of the parasitic and reducing the parasitic height above the LB dipole lowers the peak self-resistance of the LB dipole, thereby increasing the tunable bandwidth. For each case, the peak self-resistance within the operating band has been marked using a colored circle with a solid black outline. A self-impedance which is approximately 50 Ω across the entirety of the LB bandwidth will yield the broadest tunable bandwidth.

Similarly, the inductive reactance of the LB dipole decreases in the upper part of the frequency band when either the parasitic length is increased, or the parasitic height above the LB dipole is decreased. The dependence of the self-reactance on the parasitic length and height above the LB dipole is shown in Figure 2-8. This control over the inductive reactance allows the electrical resonance, for which the reactance becomes zero, to be moved in-band allowing for broadband matching. In the figure, electrical resonances have been denoted using colored circles with dashed outlines. For example, for the parasitic height of g_4= 0.585” all electrical resonances reside outside of the LB operating band as is shown in Figure 2-8(a). However, with a parasitic height of g_4= 0.085”, the higher frequency resonance can be shifted down in frequency into the operating band of the LB dipole, as is shown in Figure 2-8(c). In fact, for a 3” horizontally oriented parasitic situated 0.085” above the LB dipole arm two resonances occur within the operating band. These two resonances, along with the LB dipoles low self-resistance, give rise to the broadband matching which is observed in the reflection coefficient parametric study shown in Figure 2-6. This

demonstrates the necessity of the electrically long LB parasitic for broadband matching of the baseline LB dipole.

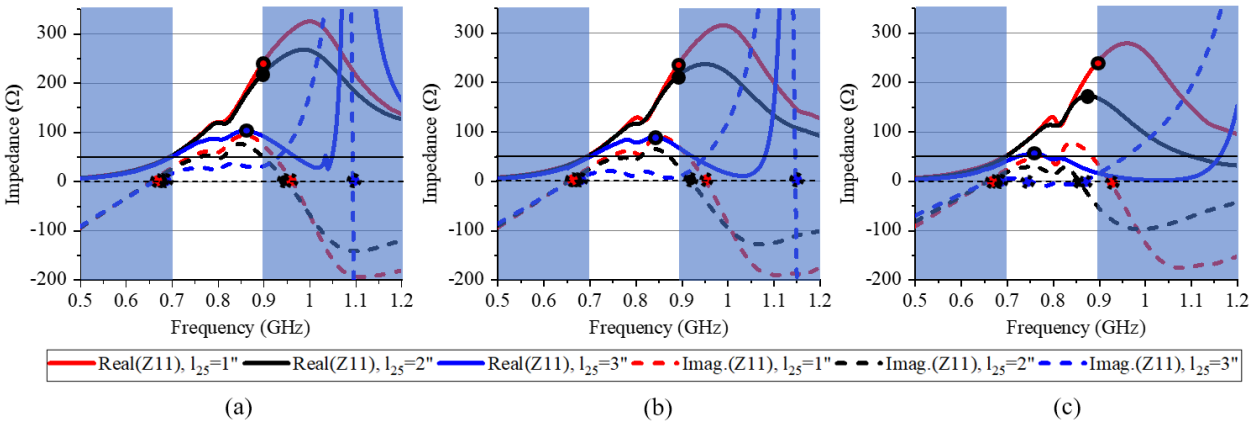

Figure 2-8: Parametric analysis of the LB dipole self-impedance as a function of parasitic length for a horizontally oriented parasitic of height (a) g_4= 0.585”, (b) g_4= 0.335”, and (c) g_4= 0.085”.

The same parametrization is carried out for the vertically oriented parasitic. As is shown in Figure 2-9, the relations which are observed with the horizontally oriented parasitic hold true for the vertically oriented parasitic. When comparing the results of the two parasitic orientations for a fixed parasitic height and length, the vertically oriented parasitic offers slightly lower peak self-resistance, and a higher frequency electrical resonance. For the purpose of the baseline LB dipole the horizontally oriented parasitic is selected.

The results of the simulations show that the baseline LB dipole requires an electrically long 3” parasitic for broadband operation. Furthermore, the results show that the orientation of the parasitic is of minor importance in comparison to the length and height above the LB dipole.

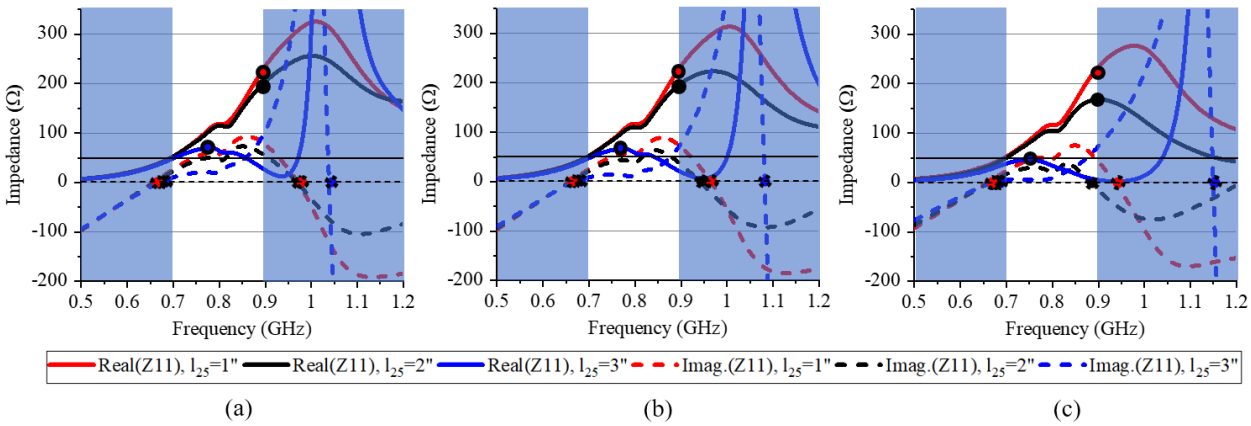

Figure 2-9: Parametric analysis of the LB dipole self-impedance as a function of parasitic length for a vertically oriented parasitic of height (a) g_4= 0.585", (b) g_4= 0.335", and (c) g_4= 0.085".

2.2 Impact of Inter-Array Mutual Coupling on MB Radiation

The problem that needs to be overcome when designing a multi-band shared aperture array is exemplified in this section through the comparison of the performance of one of the dual-polarized MB sub-arrays with and without the presence of the LB sub-arrays. Furthermore, one of the main contributors to the inter-array mutual coupling is identified as the electrically long LB parasitic through a pair of simulations with and without the LB parasitics present.

The performance comparison of a single MB sub-array is sufficient for characterization of this UC. Due to the symmetry of the UC, the $\pm$45° ports of the left sub-array exhibit nearly identical performance to the $\mp$45° ports of the right sub-array. For the purpose of comparing simulated system gain with measured system gain later in this chapter, a 24" input cable with a loss of 0.015 dB/in at 2.0 GHz is assumed in simulation.

2.2.1 Simulation of Baseline UC with and without LB Presence

This sub-section compares the results of the MB sub-array for four different environments in order to help uncover the root cause of the inter-array mutual coupling. First, the MB sub-arrays are simulated alone on the reflector, as is shown in Figure 2-10(a). Next, the MB sub-arrays are

simulated in the baseline UC configuration, as proposed in Figure 2-1. Then, the MB performance is evaluated through simulation in the presence of the LB dipoles without LB parasitics, as shown in Figure 2-10(b). Finally, the MB is simulated in the presence of the LB parasitics alone, as shown in Figure 2-10(c). When the LB dipoles are present in the model, the feed boards to which they are connected are terminated in 50 Ω loads.

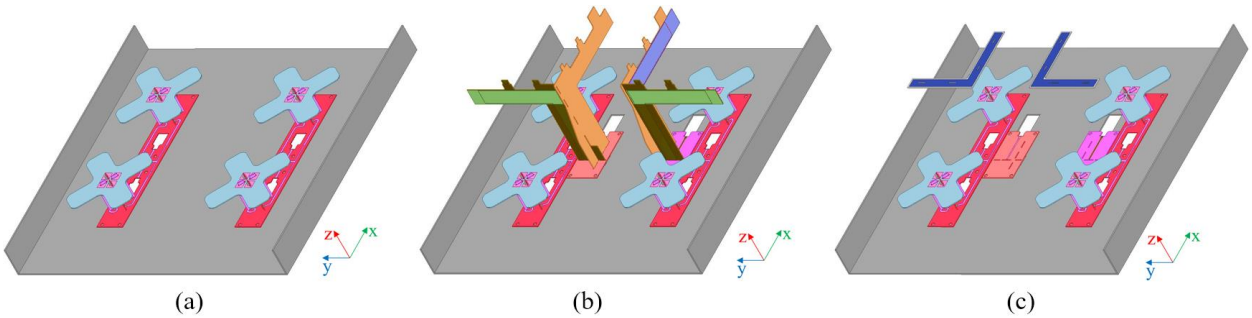

Figure 2-10: UCs with MB sub-arrays (a) alone, (b) with LB sub-arrays without parasitics, and (c) with LB parasitic without LB dipoles.

2.2.1.A H-Plane Radiation Characteristics

The +45° H-plane (yz-plane) radiation patterns of the left MB sub-array in the absence and presence of the baseline LB sub-arrays are shown in Figure 2-11(a) and Figure 2-11(b), respectively. Upon the introduction of the LB radiators, the half power beamwidth (HPBW) and −10 dB horizontal beamwidth (HBW) of the +45° polarization increase slightly over the operating band. Furthermore, upon the introduction of the LB sub-arrays the peak cross-polar radiation (CPR) increases slightly at 1.70 GHz from –14.8 dB to –13.1 dB. There is also a slight increase in the amount of co-polar radiation occurring in the sector opposite boresight, i.e., a decrease in the front-to-back ratio [122].

When the LB parasitic is removed from the simulation, the CPR shows improvement over that of the baseline UC. This improvement is apparent in comparing the CPR levels of the baseline UC

with parasitics, shown in Figure 2-11(b), to the results without parasitics, shown in Figure 2-11(c). Furthermore, when the MB performance is simulated in the presence of the LB parasitics alone, the peak CPR and deviation in the co-polar pattern is more severe than when the parasitics are not present, as is seen in comparing Figure 2-11(d) and Figure 2-11(c), respectively.

The change in H-plane radiation patterns observed upon the introduction of the baseline LB sub-arrays is much more severe for the –45° left MB sub-array [Figure 2-12] than for the +45° left MB sub-array [Figure 2-11], the reasons of which are presented in Section 2.3. Severe asymmetries in the –45° H-plane co-polar patterns occur upon the introduction of the baseline LB sub-arrays. Both the peak and average CPR increase across the band. For example, upon the introduction of the LB sub-arrays the peak MB CPR at 1.80 GHz increases from –15.6 dB to –9.5 dB, as shown in Figure 2-12(a) and Figure 2-12(b). The HPBW and –10 dB HBW vary widely across the band when in the presence of the LB dipoles. For example, the –10 dB HBW at 1.90 GHz increases from 113° to 143° upon the introduction of the baseline LB sub-arrays. Furthermore, the front-to-back ratio decreases upon the introduction of the baseline LB radiators with parasitics.

When the LB parasitics are removed from the LB dipoles, the MB performance improves relative to when the parasitics are present. The MB performance in the presence of the LB dipoles without parasitics for the –45° H-plane pattern is shown in Figure 2-12(c). While the LB dipoles themselves do still cause MB pattern performance degradation, the ripple in the co-polar pattern is less severe without the parasitics, as is the peak CPR level. When the LB dipoles are removed completely from the UC, leaving just the MB sub-arrays and LB parasitics, the co-polar pattern exhibits severe ripples and high peak CPR values, as shown in Figure 2-12(d). Furthermore, the effects of the mutual coupling are larger in the presence of the parasitics alone, than when the LB

dipoles are present without parasitics, as is apparent in comparing Figure 2-12(d) and Figure 2-12(c), respectively.

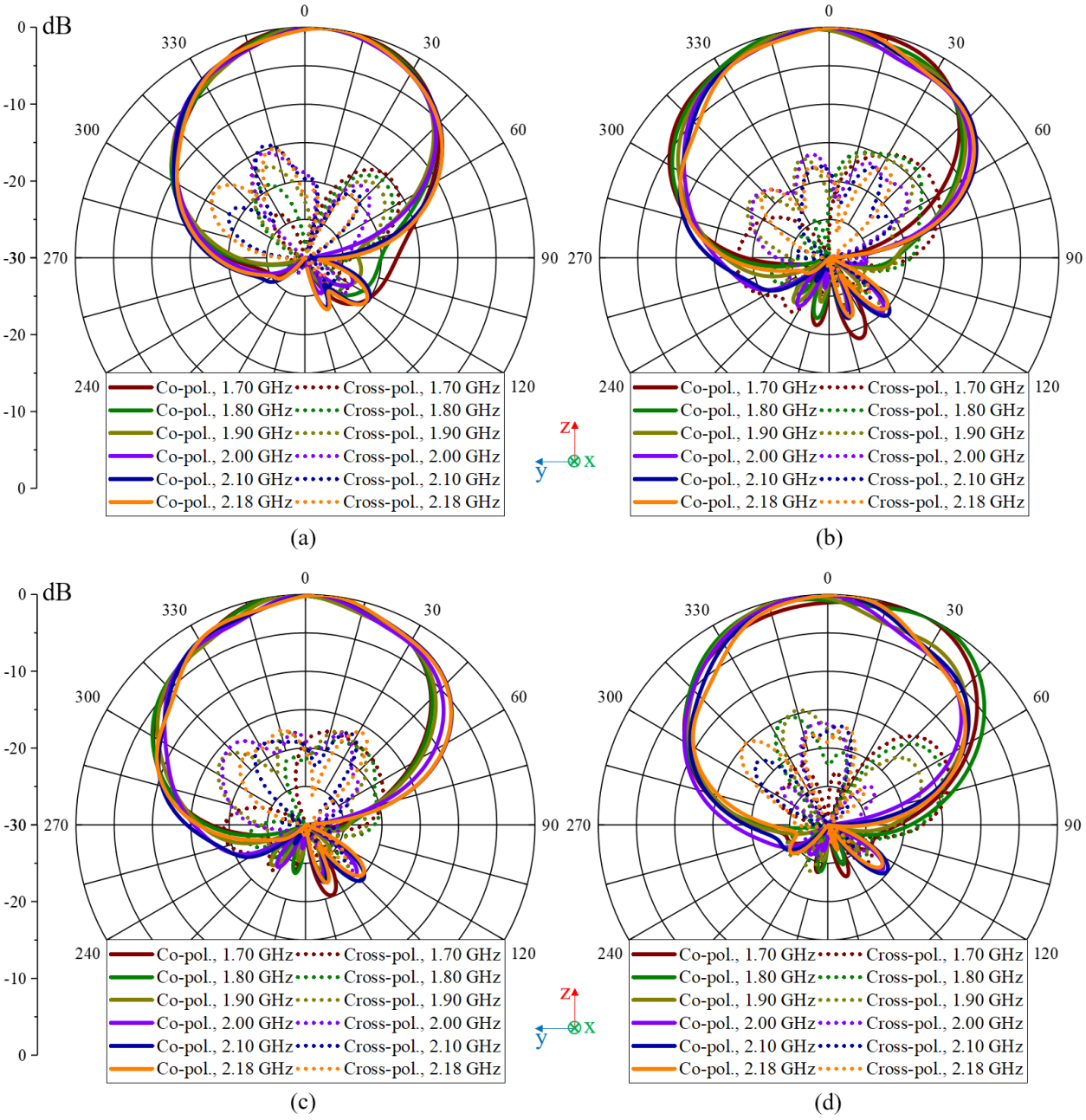

Figure 2-11: Simulated +45° left MB sub-array H-plane patterns with (a) only MB, (b) both MB and baseline LB dipoles with LB parasitics, (c) both MB and baseline LB dipoles without LB parasitics, and (d) LB parasitics without LB dipoles present on the reflector.

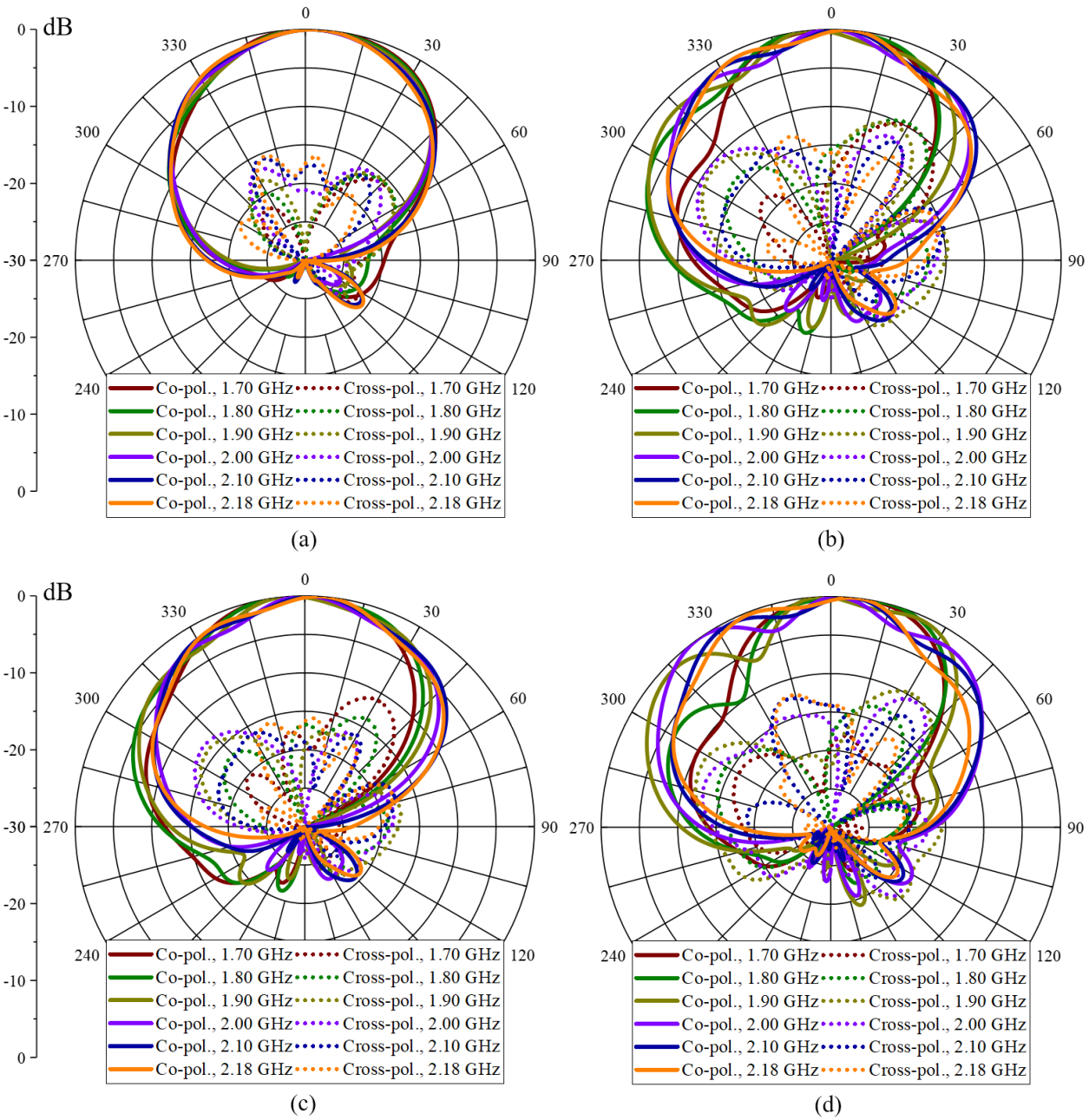

Figure 2-12: Simulated –45° left MB sub-array H-plane patterns with (a) only MB, (b) both MB and baseline LB dipoles with LB parasitics, (c) both MB and baseline LB dipoles without LB parasitics, and (d) LB parasitics without LB dipoles present on the reflector.

2.2.1.B V-Plane Radiation Characteristics

The +45° V-plane (xz-plane) radiation patterns of the left MB sub-array in the absence and presence of the baseline LB sub-arrays are shown in Figure 2-13(a) and Figure 2-13(b),

respectively. After the LB sub-arrays are added, the lower sidelobes merge with the main beam for frequencies 1.70–1.90 GHz. The distinction between the upper sidelobes and the main beam also becomes less apparent due to the increase in null fill upon the addition of the LB radiators. Both when the LB parasitics are removed from the LB dipoles, as well as when only the parasitics are present with the MB sub-arrays, similar V-plane degradation is observed for the +45° polarization, as shown in Figure 2-13(c) and Figure 2-13(d), respectively.

Similar to the H-plane radiation patterns, the V-plane radiation characteristics are more severely degraded for the –45° left MB sub-array than the +45° left MB sub-array. The –45° V-plane radiation patterns of the left MB sub-array in the absence and presence of the baseline LB sub-arrays with baseline parasitics are shown in Figure 2-14(a) and Figure 2-14(b), respectively. The peak sidelobe levels (SLLs) increase across the band upon the introduction of the baseline LB radiators. For example, at 2.18 GHz the peak upper sidelobe level (PUSLL) increases from –10.2 dB to –6.8 dB after the addition of the LB sub-arrays. There is also a decrease in the front-to-back ratio.

Upon the removal of the LB parasitics the PUSLLs reduce, as shown in Figure 2-14(c), as compared to the baseline UC. When the LB dipoles are removed from the model, leaving just the MB sub-arrays and the LB parasitics, the PUSLLs increase, as shown in Figure 2-14(d). The upper SLLs in the presence of the LB parasitics alone approach those of the baseline UC, as is apparent in comparing Figure 2-14(d) and Figure 2-14(b), respectively. Furthermore, both the upper and lower SLLs are higher in the presence of the LB parasitics alone than with the LB dipoles present without parasitics.

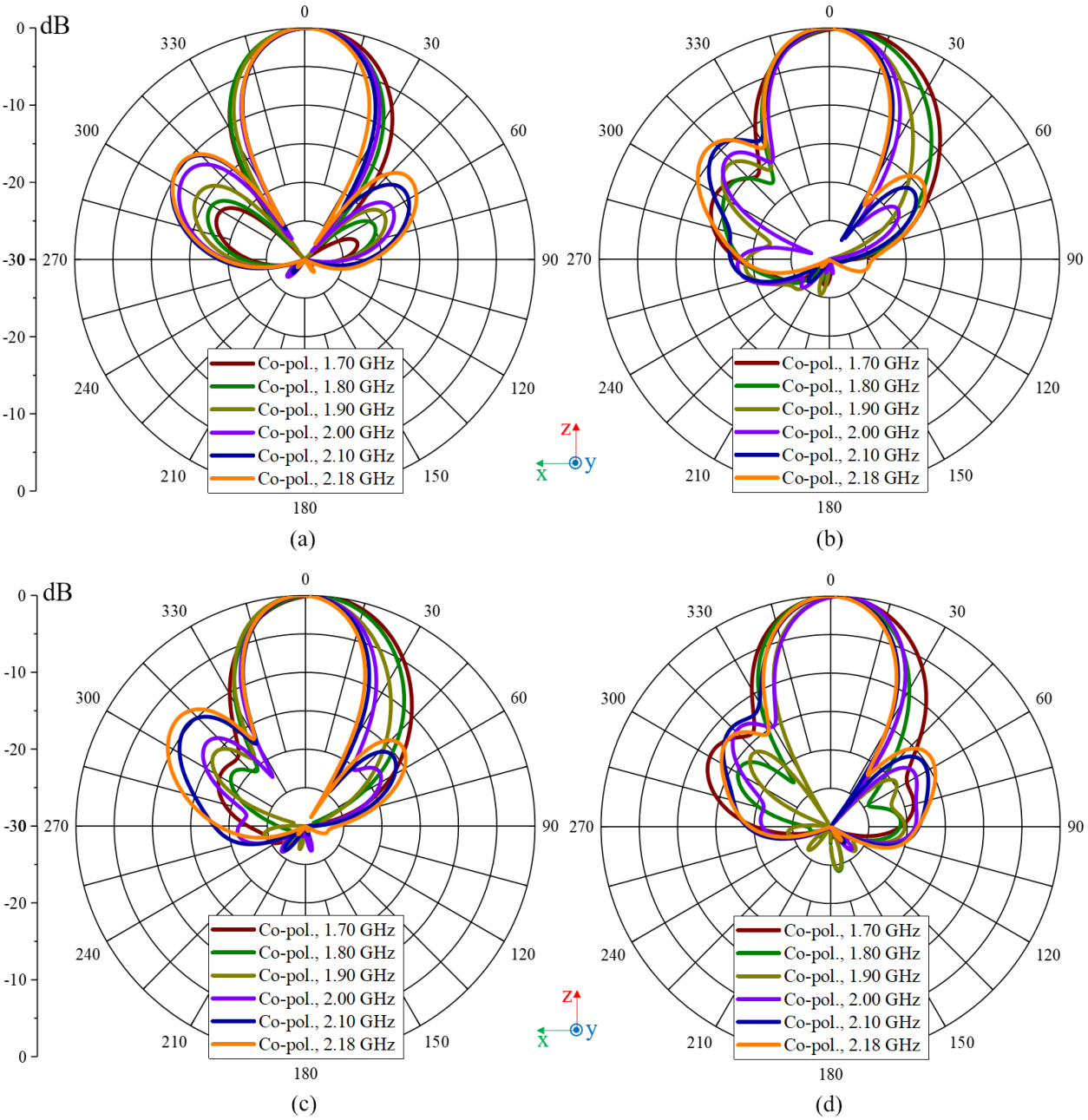

Figure 2-13: Simulated +45° left MB sub-array V-plane patterns with (a) only MB, (b) both MB and baseline LB dipoles with LB parasitics, (c) both MB and baseline LB dipoles without LB parasitics, and (d) LB parasitics without LB dipoles present on the reflector.

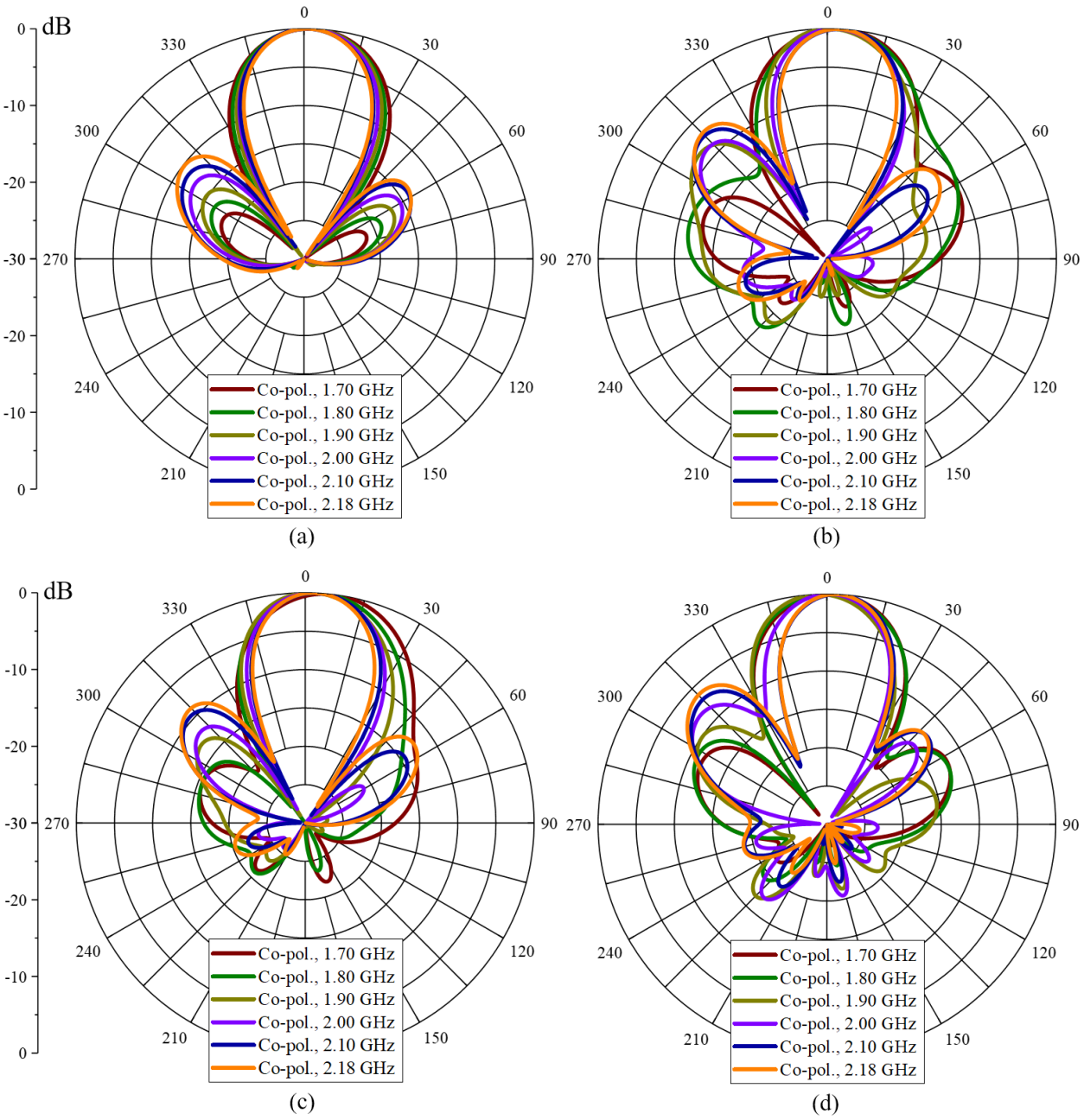

Figure 2-14: Simulated –45° left MB sub-array V-plane patterns with (a) only MB, (b) both MB and baseline LB dipoles with LB parasitics, (c) both MB and baseline LB dipoles without LB parasitics, and (d) LB parasitics without LB dipoles present on the reflector.

The redirection of radiation away from boresight, which occurs in both the H and V-planes upon the addition of the baseline LB sub-arrays, reduces the directivity and thus the peak system gain of the left MB sub-array. At 1.700 GHz the gain of the +45° polarization reduces from 11.36

dBi with MB only to 9.28 dBi in the presence of the baseline LB sub-arrays, more than a 2.08 dB reduction in gain, as shown in Figure 2-15(a). However, the reduction in system gain is even more severe for the –45° polarization. For example, at 1.900 GHz the gain reduces from 11.82 dBi to 8.94 dBi, nearly a 2.90 dB degradation, after the introduction of the baseline LB sub-arrays, as shown in Figure 2-15(b).

When the LB parasitics are removed from the LB dipoles the gain improves as compared to the baseline UC for both the +45° and –45° polarizations, as shown in blue in Figure 2-15(a) and Figure 2-15(b), respectively. The improvement in the system gain upon removal of the LB parasitics is much higher for the –45° polarization. Due to the severe pattern distortion observable when the LB parasitics alone are present, the gain varies widely across the band. For example, the reduction of the H-plane HPBW for +45°/–45° polarizations at 2.18/1.70 GHz, respectively, result in an increase in directivity when only the LB parasitics are present. This increase in directivity leads to an increase in the gain at those frequencies, as shown Figure 2-15(a) and Figure 2-15(b). However, when the H-plane HPBW increases with LB parasitic only present, such as at 1.80/1.90 GHz for the +45° polarization, the directivity and hence gain decrease. Although the distorted patterns lead to an increase in gain, the HPBW and PUSLLs are not maintained.

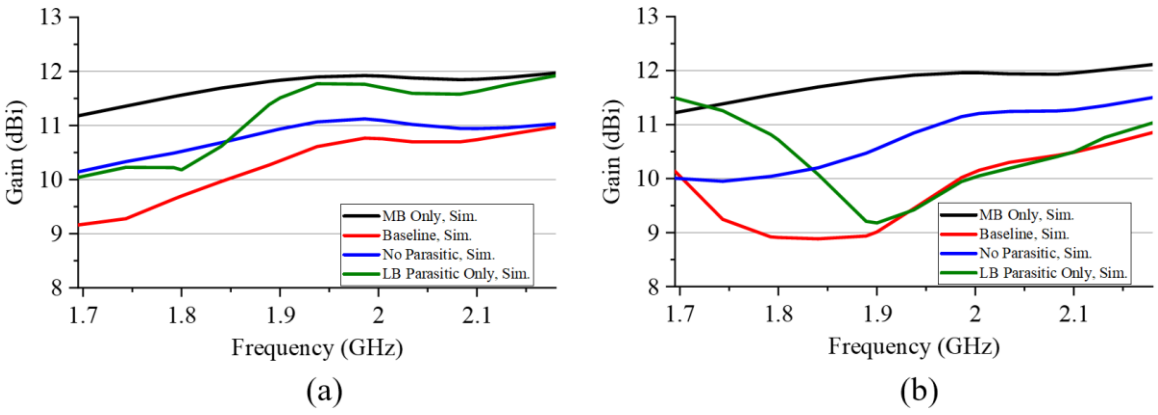

Figure 2-15: Simulated system gains of left MB sub-array for (a) +45° and (b) –45° polarizations for four different array environments.

2.2.2 Discussion of Baseline UC Performance

The degree to which to the mutual coupling between the LB and MB sub-arrays degrades the MB performance has been demonstrated through full-wave simulation. Furthermore, the mutual coupling has been shown to be stronger with the presence of the LB parasitic than without it. A discussion of the implications of the performance degradation to applications within a BSA system follows.

If the baseline dual-band UC were to be used as part of a BSA, the asymmetries in the MB co-polar H-plane radiation patterns would lead to differences in cellular coverage amongst users at a fixed distance on the left as compared to the right side of the service cell. Furthermore, the targeted HPBW of a BSA is specified at the outset of the design to ensure optimal coverage over the sector which it will service. The increase in HPBW observed in the baseline dual-band UC would spread the power over a broader angular sector. This would lead to a reduction in signal strength within the sector. For a fixed receiver sensitivity, this reduction in power density would effectively shrink the service cell radius and could lead to a drop in coverage between adjacent service cells. The −10 dB HBW of a BSA is specified to ensure that the signal strength drops off sufficiently fast outside the sector of interest in order to prevent inter-cell interference. The increase in –10 dB HBW observed in the baseline dual-band UC simulation could lead to undesirable inter-cell interference due to a reduction in the signal-to-noise ratio (SNR) at the cell edge. The degradation of the SNR could force the communication system to use a lower-order modulation scheme, which would ultimately reduce the information throughput of the wireless communication link over that which could be realized using a system with a higher SNR.

Given that BSAs are typically deployed atop tall towers, the intended direction of radiation in the V-plane is typically at or slightly below the horizon. Therefore, any radiation which occurs in

the direction of the upper sidelobes is energy which will not make it to the users below the BSA. It is for this reason that the increase in the upper SLL observed in the simulated UC in the presence of the LB dipoles is of such concern to the design of BSAs, in comparison to the lower SLLs.

On the downlink, in which the BSA transmits to the user, the gain of the BSA determines the power available to a cellular user within a given service area for a given input. The gain is an important aspect used in wireless network planning when computing the link budget of the communication system. If the efficiency of the system is low, or the directivity of the BSA is not what was intended, the signal strength available to the user will decrease. An increase in HPBW, peak and average upper SLLs, as well as reduction in the front-to-back ratio of the MB radiation pattern in the presence of the LB dipoles imply reduction of the realized system gain of the UC.

The addition of the baseline LB dipoles, in particular, with the electrically long baseline LB parasitics, would result in unacceptable MB performance were the UC to be used as part of a larger array in a BSA system. In order to better understand the predominant source of the mutual coupling, a root cause analysis is carried out and presented in the following section.

2.3 Identification of the Root Cause of Inter-Array Mutual Coupling

The purpose of this section is to identify the source of the strong mutual coupling which occurs between the MB and LB sub-arrays through simulation. The results of Section 2.2 demonstrate that the presence of the baseline LB parasitic is a significant contributor to the inter-array mutual coupling in the baseline UC. This section demonstrates that the root cause of a significant amount of the mutual coupling is traceable to currents induced on the electrically long LB parasitic upon excitation of the MB sub-array.

2.3.1 Evaluation of Current Induced on LB Parasitics

The far field effects observed upon the introduction of the LB elements to the array face should be identifiable from their sources in the near field. Sources include direct sources, such as the MB sub-arrays, as well as any secondary sources such as currents induced on the LB radiators and/or LB parasitics. In order to understand these sources, the surface current density induced on the baseline LB parasitic, upon excitation of the MB array, is overlaid on the baseline LB parasitic geometry as a function of frequency in Figure 2-16. It is seen from the figure that the magnitude of the surface current density induced on the baseline LB parasitic decreases with increasing frequency. The most severe degradation in radiation characteristics occurs near the lower part of the MB frequency range, where the magnitude of the induced surface current density is the greatest.

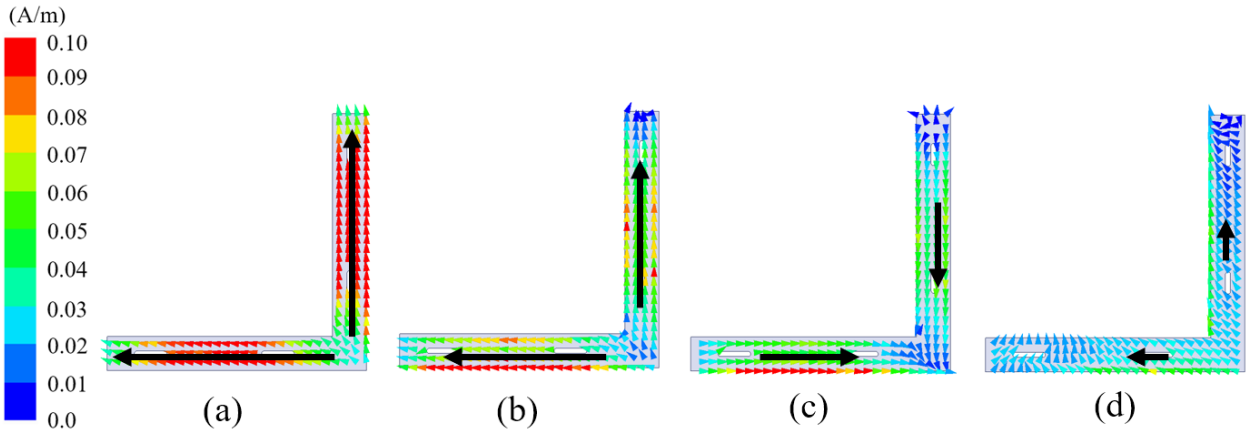

Figure 2-16: The induced vector surface current density vector, on the baseline +45° LB parasitic of the baseline UC upon the excitation of the –45° left MB sub-array at (a) 1.700 GHz, (b) 1.900 GHz, (c) 2.000 GHz, and (d) 2.180 GHz.

The induced surface current density vector, occurring at 1.700 GHz, is overlaid on the baseline UC geometry upon the excitation of the left MB sub-array for both +45° and –45° polarizations, as shown in Figure 2-17 and Figure 2-18, respectively. The MB input excitation phase is varied from 0° to 270° in 90° increments in order to capture how the currents oscillate with excitation

phase. There are currents induced on the vertical LB feed stem, LB dipole arms, and LB parasitics. The magnitude of the induced surface current density present on the LB stem and parasitic, as represented in the figures as the color of the vector fields, are much stronger for the –45° polarization excitation of Figure 2-18 as compared to the +45° polarization excitation of Figure 2-17. This result is consistent with the results of Section 2.2, in which the pattern distortion upon the introduction of the baseline LB sub-arrays is seen to be much more severe for the –45° polarization of the left MB sub-array than the +45° polarization. The currents induced on the LB stem at 1.700 GHz are similar to those of an electrically long monopole antenna operating over a ground plane, which in this case is the metallic reflector. The currents induced on the L-shaped LB parasitic are similar to two dipoles which reside in the H and V-planes, co-planar with the plane of the metallic reflector.

While it is important to consider the vector of the induced surface current density in order to understand the orientation of the resulting electric and magnetic fields in the far field, additional information can be obtained upon examining the magnitude of the surface current density. For this reason, the surface current density is plotted as a function of the location along one side of the symmetric L-shaped LB parasitic for different excitation phases at 1.700 GHz, as shown in Figure 2-19. In comparing Figure 2-19(a) and Figure 2-19(b) the peak magnitude of the surface current density for +45° is 59.1 mA/m and 133.5 mA/m for –45°. Therefore, the peak induced surface current density at 1.700 GHz along the length of the LB parasitic is approximately 2.25 times larger for the –45° polarization than the +45° polarization. Furthermore, the oscillatory nature of the current distribution is apparent through the magnitude repeating with every 180° of excitation phase. After the excitation phase changes by 180° the direction of the current also changes by 180° while the magnitude repeats the same values as the first half of the cycle.

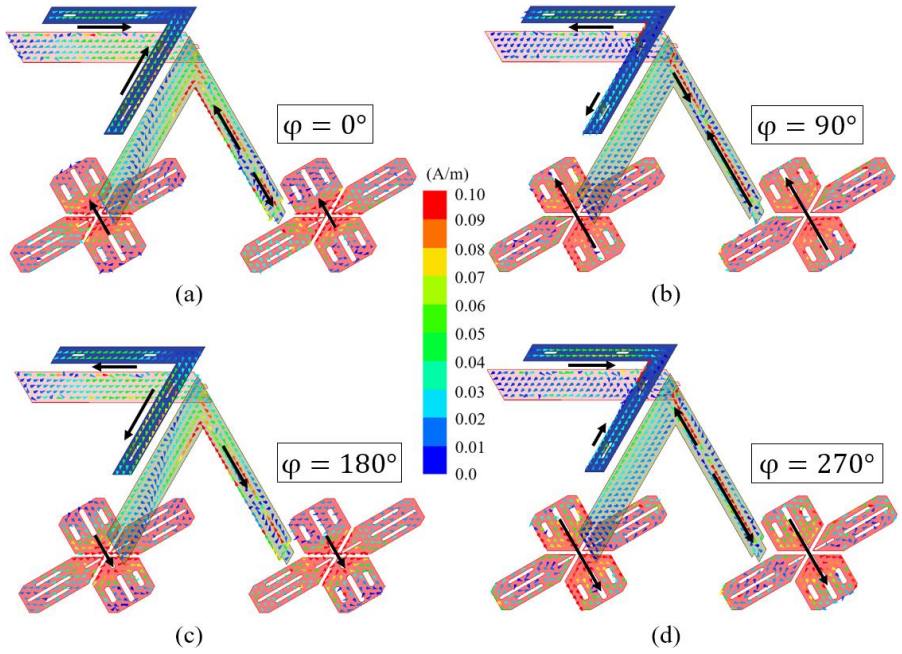

Figure 2-17: Surface current density vector, at 1.700 GHz overlaid on the conductors of the +45° LB sub-array of the baseline UC upon the excitation of the +45° left MB sub-array with excitation phase (a) φ = 0°, (b) φ = 90°, (c) φ = 180°, and (d) φ = 270°.

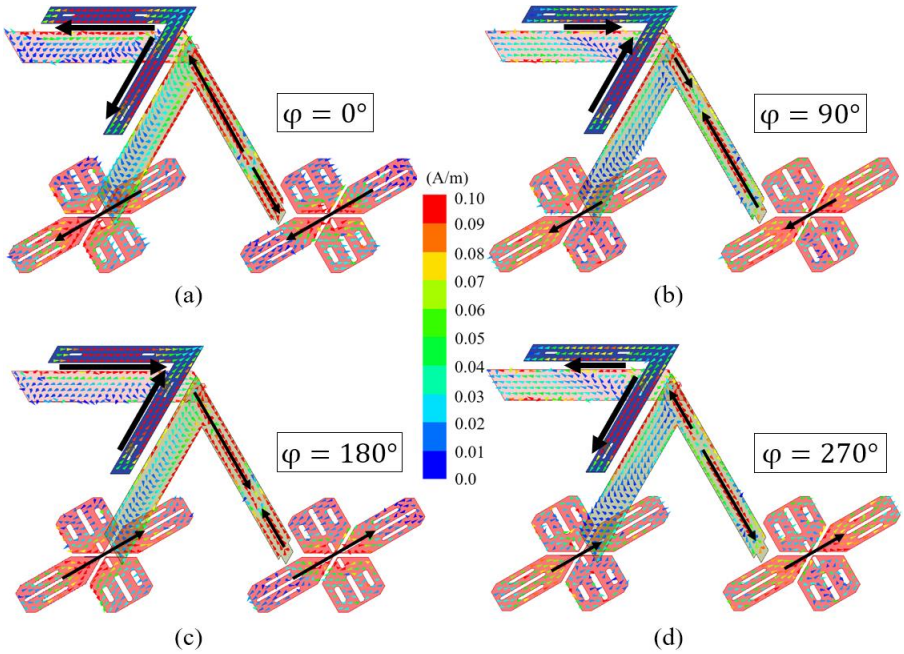

Figure 2-18: Surface current density vector, at 1.700 GHz overlaid on the conductors of the +45° LB sub-array of the baseline UC upon the excitation of the –45° left MB sub-array with excitation phase (a) φ = 0°, (b) φ = 90°, (c) φ = 180°, and (d) φ = 270°.

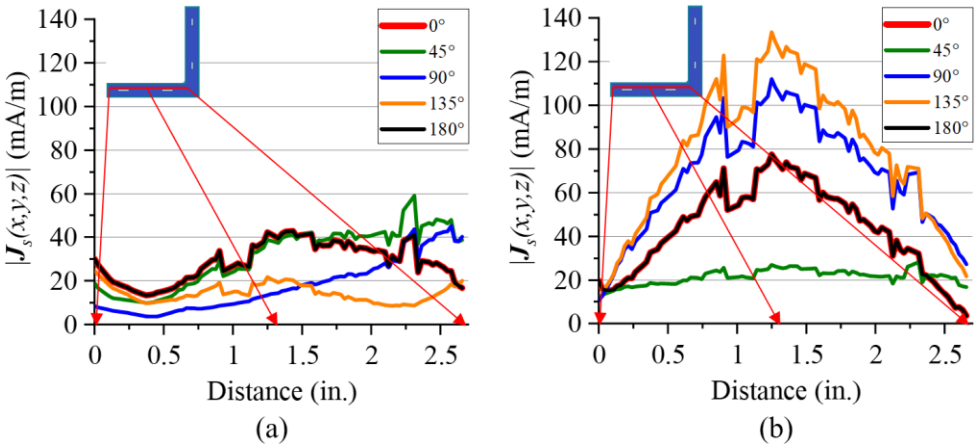

Figure 2-19: Parametric analysis of excitation phase for the magnitude of induced surface current density, at 1.700 GHz as a function of position on the +45° LB parasitic of the baseline UC upon excitation of left MB sub-array (a) +45° and (b) –45° polarizations.

Next, the peak induced surface current density at each location along one half of the symmetric L-shaped LB parasitic is plotted across the MB operating frequency for both +45° and –45° polarization excitations, as shown in Figure 2-20(a) and Figure 2-20(b), respectively. As expected, the peak magnitudes of the surface current densities across the length of the parasitic for each frequency are larger for –45° than for +45° polarizations. Across all frequencies, the largest induced surface current density upon excitation of the left MB sub-array for the +45° polarization occurs at 1.800 GHz, whereas for the –45° polarization it occurs at 1.700 GHz with lower magnitudes being induced with increasing frequency. This result is also in agreement with the observations made in Section 2.2, in that the most severe degradation in the radiation characteristics occurs in the lower part of the MB frequency band, with the effects of the mutual coupling decreasing with increasing frequency.

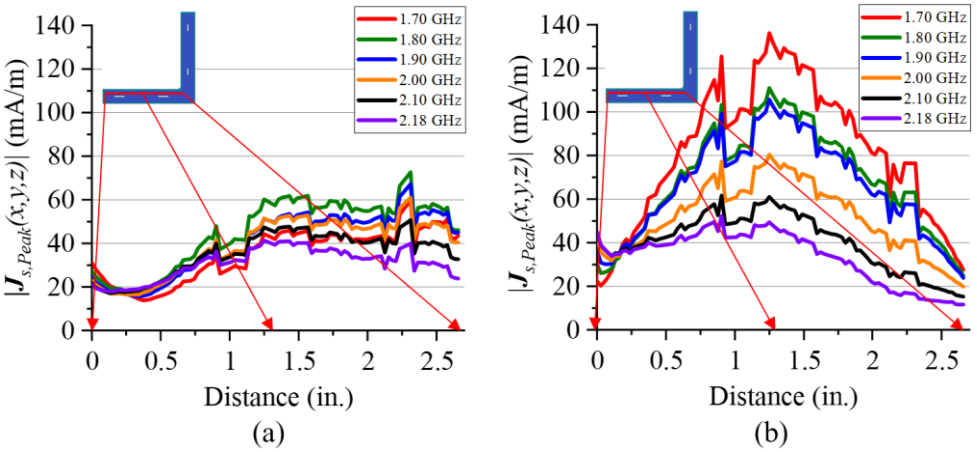

Figure 2-20: Parametric analysis of excitation frequency for the peak magnitude of induced surface current density, as a function of position on the +45° LB parasitic of the baseline UC upon excitation of left MB sub-array (a) +45° and (b) –45° polarizations.

2.3.2 Discussion of Root Cause Analysis Results

The finite element electromagnetic solutions of the baseline UC allow visualization, and ultimately confirmation, of the induced surface current density present on the LB parasitic upon the excitation of the MB sub-array. The results numerically validate the hypothesis that the LB parasitics are significant contributors to the inter-array mutual coupling, which in turn gave rise to degraded MB performance. The LB feed stems also have a substantial amount of induced current, and the minimization of these currents warrants its own future work.

Due to the complex nature of the UC, the current distributions and far fields cannot be calculated analytically. However, a thought experiment which uses the concept of an array factor calculation proves beneficial for understanding how the induced currents contribute to the far field. The MB only UC can be thought of in terms of a simplified array factor calculation in which the element pattern of each MB dipole is multiplied by the array factor in order to approximate the MB only pattern performance. The induced currents, and their resulting effects in the far field, can be considered in a similar manner. The currents induced on each arm of the L-shaped LB parasitic

can be thought of as parasitic dipole radiators positioned at a height above the reflector which is much larger than a quarter of a wavelength at MB frequencies. Each of the two parasitic dipole radiators have both co-polar and cross-polar components, with respect to the MB excitation under consideration, due to their orientations being in the H and V-planes as opposed to the ±45° polarization planes. Since the height of the parasitic dipole radiators above the ground plane is much larger than one-quarter wavelength at MB frequencies, neither their resulting images present in the ground plane nor the radiation from the MB radiators will constructively interfere with the fields induced by these currents at boresight. It can in this way be understood why the currents induced on the LB parasitics result in both co-polar and cross-polar distortion in the MB radiation patterns which vary with angle. Furthermore, the vertical current induced on the vertical LB feed stem also acts as a parasitic radiator and can be thought of as a third radiation source which has an element pattern similar to that of an electrically long monopole fed against a ground plane.

While there are also currents which are induced on the LB dipole arms, the radiating arms of the LB dipole cannot be removed. Therefore, the question becomes whether there is a technique which can be used in order to allow a reduction in the length of the LB parasitic for minimization of the inter-array mutual coupling, while still maintaining broadband LB matching. A method of achieving one such dipole is proposed in Section 2.4.

2.4 Proposition for Reduction of Inter-Array Mutual Coupling

The purpose of this section is to propose a design technique through which the mutual coupling between the LB and MB sub-arrays can be greatly reduced, thereby leading to significant improvements in the MB radiation characteristics while in the presence of the LB dipoles. The

design technique is then used to propose a new LB dipole. The results of Section 2.1.1 show that an electrically long metallic LB parasitic is required for broadband matching of the baseline LB dipole. However, the results of Section 2.2 identify the LB parasitic as the main contributor to the MB performance degradation. In Section 2.3, one of the main sources of the MB radiation pattern degradation is identified as current induced on the LB parasitic upon the excitation of the MB sub-array. The proposed technique must provide broadband matching of the LB dipoles while also improving the MB performance over that of the dual-band baseline UC.

After describing the proposed mutual coupling reduction technique, the results of several parametric analyses are presented, followed by a discussion. The purposes of the parametric analyses are to understand how the LB dipole impedance changes as a function of several key parameters of the proposed LB dipole. After developing an understanding of the role that these key parameters play, dimensions of each parameter are selected for implementation of the proposed technique. After discussing the results of the parametric analyses, a new LB dipole design is proposed based on the findings of the parametric analyses.

2.4.1 The Proposed Mutual Coupling Reduction Technique

The proposed mutual coupling reduction technique uses series capacitance distributed along the length of the LB dipole arms to reduce the peak self-resistance, as well as to cancel the inductive reactance of the baseline LB dipole at the center of the band. Capacitively loading the centers of dipole arms was first proposed in 1968 [123] for one, two, and three equally spaced capacitive sections. In that paper, Maclean derives the analytic expression of the currents in each section of the dipole for the single capacitively loaded case, as well as the self-impedance of the resulting dipole. The calculations for multiple capacitive sections were carried out experimentally by Maclean due to the complexity which was involved in solving the simplest case of the single

capacitive section. Maclean's results show that increasing the number of capacitive sections along the dipole arm greatly reduces the dipole self-resistance, while also shifting the first resonance up in frequency and resulting in lower inductive reactance. Maclean studied the impact of varying the value of the capacitance on the dipole self-impedance. The results of the parametric study show that decreasing the capacitance increases the frequency at which the first resonance occurs.

A simulation based parametric analysis, in which the capacitance value was varied, was more recently carried out in 2020 by Li and Li [55] for the single capacitively loaded case using interdigital capacitors with findings similar to those of Maclean. Furthermore, they studied the impact of the location of the capacitors along the length of the dipole arms on the dipole self-impedance. The result of shifting the capacitance away from the center of the half-wave dipole is that the first resonance moves down in frequency, and the second excited resonance moves up in frequency which results in spreading of the resonance mode separation and a reduction in bandwidth. It is for this reason that they moved the capacitive sections towards the center of the half-way dipole, so that the first and third resonant modes are compressed, resulting in a wider bandwidth. Others have also investigated multiple capacitive sections through simulation and measurement outside of BSA applications, as found in [52]–[54].

In this dissertation, although the cancellation of the inductive reactance at the center of the band would increase the bandwidth, it is not sufficient for realizing an operating band of 698–894 MHz. An electrically short parasitic is proposed for shifting the third resonance mode of the dipole down in frequency into the upper part of the LB frequency range. This research shows that the combination of distributed capacitive loading of the LB dipole arms along their length, with the use of an electrically short LB parasitic, provides sufficient LB bandwidth while greatly improving

the MB radiation characteristics when in the presence of the proposed LB radiators over that of the baseline UC.

The method of realizing the addition of capacitance along the length of the LB dipole arms chosen for this research is through the implementation of tightly coupled parallel plate capacitors separated by a thin dielectric layer. This capacitive coupling can be realized through multilayer PCB bonding techniques using prepreg materials for bonding two dielectric cores together, each of which houses one plate of the parallel plate capacitor, and in which the prepreg acts as the thin dielectric between the parallel plates. While the multilayer PCB technique offers the advantage of precision PCB manufacturing process common to PCB manufacturers, the costs associated with this may not be suitable for the target cost of the BSA in which it will be used. It is for this reason that instead of using two PCBs which are bonded using prepreg, this research uses two dielectric cores which are bonded together using pressure sensitive adhesive which can be activated by hand using a press or rolling pin over the surface of the subassembly.

An example of the chosen method for integrating capacitive sections into an electrical conductor is shown in Figure 2-21. The primary substrate, denoted as “Primary Substrate”, is the dielectric on which the first metallization layer, denoted as “Primary Metallization Layer”, resides. The metallization layer is segmented in four locations to create five conductive sections. A solder mask, denoted as “Primary Mask Layer”, is applied over this metallization layer. On a second dielectric substrate, denoted as “Secondary Substrate”, four rectangular metallic plates are etched. The spacing between the centers of the rectangular metallic plates is the same as the spacing between consecutive segmentation locations on the Primary Metallization Layer. A 0.0056” thick pressure sensitive adhesive denoted “Adhesive Layer,” is applied to the Secondary Metallization Layer on the Secondary Substrate. The Secondary Substrate assembly is then aligned such that the

centers of the rectangular metallic plates coincide with the center of the gaps between the five metallic segments on the Primary Metallization Layer. Once aligned, the pressure sensitive adhesive is activated with a press or a hand-held rolling device. This bonded PCB assembly is the method chosen for this research in how the series capacitance is introduced along the length of the proposed LB dipole arms.

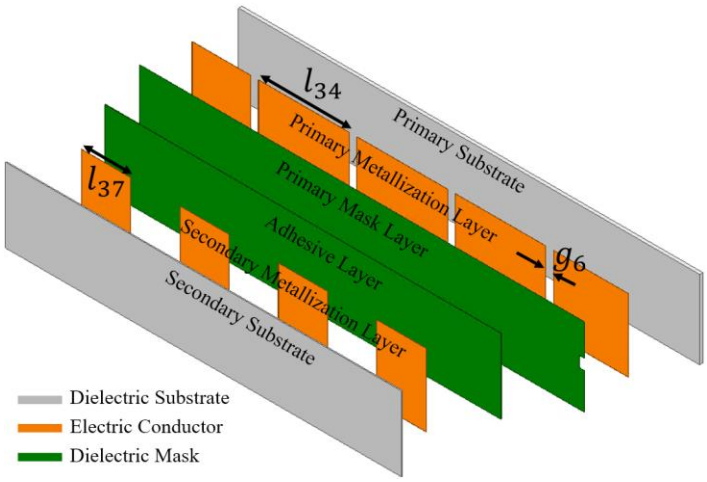

Figure 2-21: Proposed realization of series capacitance using a multilayer PCB assembly.

This method of introducing series capacitance along a conductor introduces several parameters which are not present in the baseline conductor. For example, the number of capacitive sections, the distance between each capacitive section, the location of the capacitive section along the length of the conductor, as well as the gap formed by the segmentation of the Primary Metallization Layer play a role in the electrical characteristics of the proposed serially loaded conductor. In order to understand the role which some of these parameters play in determining the LB dipole impedance, when implemented on the arms of the LB dipole, several parametric analyses are carried out.

First, the number of equally spaced capacitive sections present on the LB dipole arms, in the absence of an LB parasitic, is varied from one to four. In this parametric study the equally spaced

segments are centered on the LB dipole arms, as well as shifted towards and away from the center of the LB dipole by $+\delta = +0.5$" and $-\delta = -0.5$", respectively. The results of this study provide the designer with an understanding of how many sections are required to lower the self-resistance of the LB dipole and cancel the inductive reactance at the center of the band. Furthermore, it provides insight into the sensitivity of the self-impedance to the location of the capacitance along the length of the dipole. These results also determine whether an LB parasitic is necessary at all.

In the second parametric study, a vertical LB parasitic is introduced above the LB dipole and the length of the parasitic is varied from 1" to 3" in 1" increments. The parasitic length variations are carried out for up to four equally spaced capacitive sections centered on the LB dipole arms. The results of this study provide the designer with an understanding of the necessity of the LB parasitic and its corresponding length. It also provides insight regarding the required number of capacitive sections necessary to achieve the desired operating band if centered along the length of the LB dipole arms.

2.4.2 Parametric Analysis of the Number of Capacitive Sections and Their Locations

In order to understand how the LB dipole self-impedance changes upon the introduction of the capacitive sections, the vertical feed stem is eliminated from the simulation model and the LB dipole is excited directly at the center of the element using a lumped port, similar to what is done in Section 2.1.1 with the baseline LB dipole. The corresponding LB dipole top is shown in Figure 2-22. The parameter δ, shown in Figure 2-22, sets the distance the capacitive sections are offset together from their centered locations on each LB dipole arm. For a value of $+\delta = +0.5$" all of the segments are shifted by 0.5" towards the center of the LB dipole feed point. For a value of $-\delta = -0.5$" all of the segments are shifted by 0.5" away from the center of the LB dipole feed point.

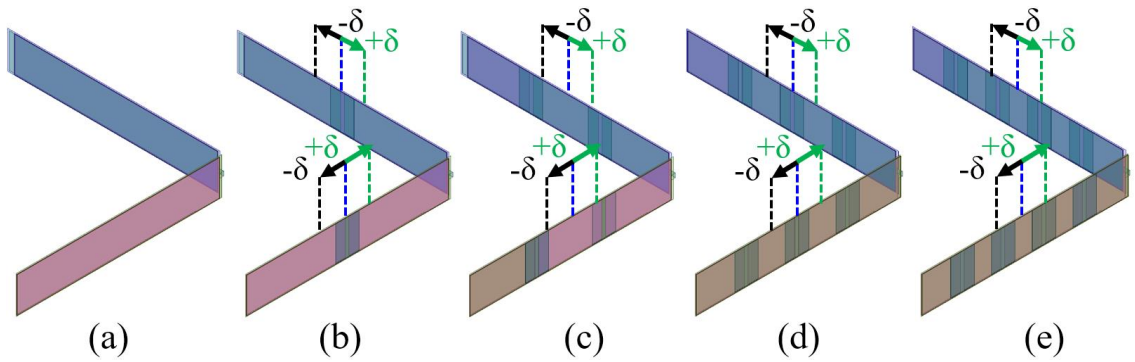

Figure 2-22: Example of the LB dipole without LB parasitic with (a) 0, (b) 1, (c) 2, (d) 3, and (e) 4 capacitive sections equally spaced and centered along the length of the dipole. Labels show how the capacitive segments are parametrically shifted along the length of the dipole.

The results of the parametric study investigating the LB dipole self-impedance as a function of frequency for a varying number of capacitive sections and locations of those capacitive sections are shown in Figure 2-23. As the number of capacitive sections increases, the electrical length of the dipole reduces and the peak self-resistance of the dipole decreases, as observed by comparing the solid lines in Figure 2-23(a)–(d). For example, for a single capacitive section with $\delta = 0$" the self-resistance varies from 77 Ω to 329 Ω, whereas with four capacitive sections the self-resistance varies from 37 Ω to 149 Ω across the band.

Furthermore, with each additional capacitive section the inductive reactance reduces, and the lower frequency electrical resonance is shifted higher in frequency towards the operating band, as shown by the dashed lines in Figure 2-23. For example, for a single capacitive section with $\delta = 0$", the reactance varies from j0 Ω to +j82 Ω, whereas for four capacitive sections the reactance varies from −j35 Ω to +j22 Ω. When only one capacitive section is used the two electrical resonances reside at 621 MHz and 893 MHz, the lower frequency resonance falling outside of the operating band. However, with four capacitive sections the electrical resonances are at 810 MHz

and 940 MHz. Therefore, by adding four capacitive sections the lower frequency electrical resonance is shifted into the center of the band.

The location of the capacitive sections on the LB dipole arms cause a second order perturbation in the effects mentioned above. For example, when the capacitive sections are shifted away from the dipole center feed point, corresponding to $-\delta = -0.5$", both the self-resistance and inductive reactance are slightly higher than when $\delta = 0$" for a given number of capacitive sections, as can be seen in comparing the black and blue lines in Figure 2-23, respectively. Conversely, when $+\delta = +0.5$" the self-resistance and inductive reactance are slightly lower than when $\delta = 0$", as observed in comparing the green and blue lines of Figure 2-23, respectively.

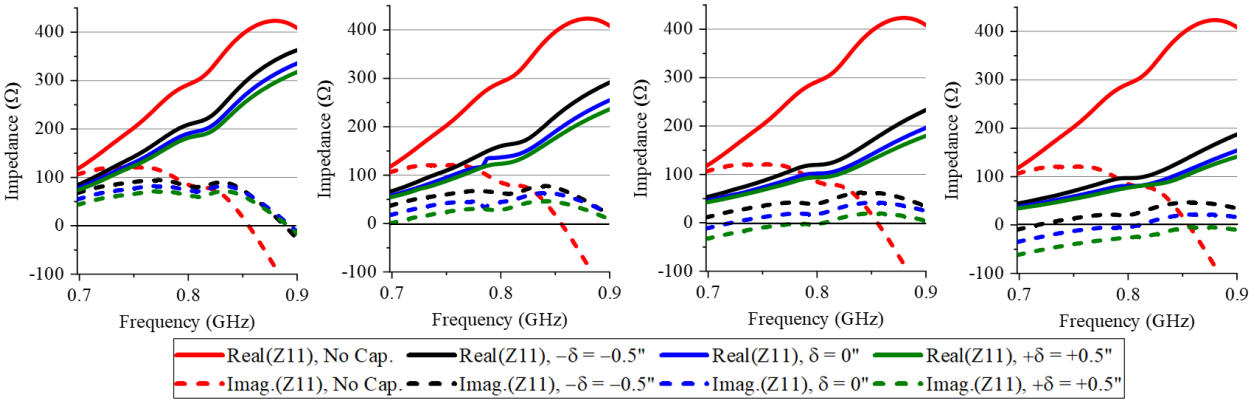

Figure 2-23: Parametric analysis of the serially loaded LB dipole self-impedance for different capacitance locations with (a) 1, (b) 2, (c) 3, and (d) 4 equally spaced capacitive segments.

Although the self-resistance is lowered drastically through the introduction of multiple capacitive sections, and the reactance is canceled at the center of the band, the results will not support the full operating band without a parasitic. Therefore, the next parametric study examines how a combination of capacitive sections integrated along the length of the LB dipole arms, along with an electrically short parasitic allows for sufficient bandwidth.

2.4.3 Parametric Analysis of the Number of Capacitive Sections and the Parasitic Length

A parametric analysis of the serially loaded LB dipole self-impedance versus frequency for different parasitic lengths is carried out, in a manner similar to Section 2.1.1. However, this parametric analysis of the parasitic length is carried out for one to four capacitive sections integrated equidistance and centered along the length of the LB dipole arms. Although it is known from the results of Section 2.2 that a 3" long parasitic will introduce too much mutual coupling at MB frequencies, the simulation is considered such that the dipole impedance of the baseline LB dipole, which has a 3" parasitic, can be compared to the capacitive LB dipole with the same length parasitic. The results of Section 2.1.1 show that whether the LB parasitic is oriented horizontally or vertically is of minor importance to the LB dipole impedance, therefore for this study a vertically oriented LB parasitic identical to that which was shown in Figure 2-7(b) is implemented.

The results of the LB dipole self-impedances for 1", 2", and 3" long parasitics with up to four equally spaced capacitive sections centered on each LB dipole are shown in Figure 2-24. As expected from the previous parametric analysis, the capacitive sections transform the self-resistance to a lower peak value across the band, while partially cancelling the inductive reactance. For a given parasitic length, the reduction in the self-resistance and inductive reactance, as compared to the baseline LB dipole, is much greater. For example, for a vertical parasitic length of 1" the self-resistance of the baseline LB dipole varies from 51 Ω to 227 Ω, as shown in Figure 2-9(c); however, the self-resistance varies from 35 Ω to 137 Ω when four capacitive sections are used with the same length parasitic, as shown in Figure 2-24(d). Even when only three capacitive sections are used, the variation in self-resistance is much less than the baseline LB dipole with an equivalent 1" vertical parasitic, varying from 43 Ω to 175 Ω, as shown in red in Figure 2-24(c).

When a 1” parasitic is used with the baseline LB dipole there are no electrical resonances excited within the band. In fact, for an identically located vertically oriented 1” LB parasitic the baseline LB dipole reactance varies from +j22 Ω to +j75 Ω, with no electrical resonances in the operating band. Whereas, for three and four capacitive sections, used with the same parasitic, the reactance varies from –j15 Ω to +j23 Ω, and –j37 Ω to +j7 Ω, respectively. Unlike the baseline LB dipole, this serially loaded dipole shows that with a parasitic length of just 1”, two electrical resonances reside within the design bandwidth if three or four capacitive sections are used, as represented by the dashed red lines in Figure 2-24(c) and Figure 2-24(d), respectively. The two resonances which are shifted in-band with three capacitive sections occur at 733 MHz and 894 MHz, and four capacitive sections at 823 MHz and 889 MHz.

This result paves the way for a broadband capacitively loaded bent LB dipole which uses an electrically short parasitic. The use of an electrically short parasitic shows promise for greatly reducing the inter-array mutual coupling, as the electrically long parasitic is shown in Sections 2.2 and 2.3 to be a significant contributor to the degradation of the MB radiation performance.

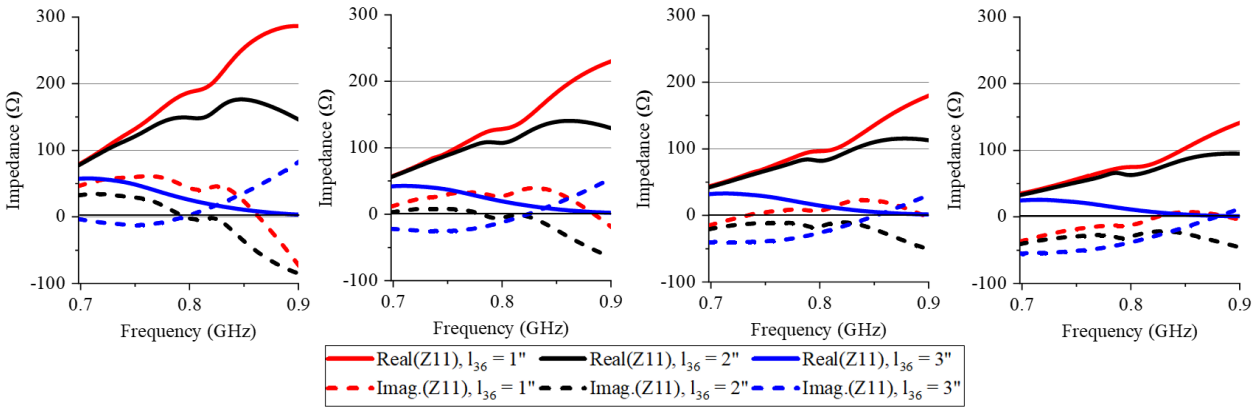

Figure 2-24: Parametric analysis of the serially loaded LB dipole self-impedance for different parasitic lengths with (a) 1, (b) 2, (c) 3, and (d) 4 equally spaced and centered capacitive segments.

2.4.4 Discussion of Results

The simulation results of the LB dipole self-impedance in the absence of a parasitic, for multiple capacitive sections along the dipole arms, are in agreement with the relations found by Maclean in 1968 [123]. In particular, as the number of capacitive sections increase the peak self-resistance and inductive reactance reduces greatly across the band of interest, which results in the shifting of the first electrical resonance mode up in frequency. When only one capacitive section is present, such as the results of Figure 2-23(a), the resonance occurs at 621 MHz, outside the operating band of 698–894 MHz. When four capacitive sections are added, this resonance shifts to the center of the band at 809 MHz, as shown in Figure 2-23(d).

Furthermore, the results of shifting the capacitive segments away from the center of the LB dipole are in agreement with the findings of Li and Li [55]. In particular, as the capacitive segments are shifted toward the LB dipole center by $+\delta = +0.5$" the first resonant frequency mode shifts up in frequency, this results in a compression of the resonance modes. Although the introduction of the capacitive segments helps to reduce the impedance of the LB dipole across the band, the LB dipole resistance and inductive reactance is still too high to match the antenna across a broadband without a parasitic. However, the reduced impedance provides a better starting point for the introduction of a parasitic for realizing a broadband LB dipole with an electrically short parasitic.

Upon the introduction of the LB parasitic, the LB dipole self-resistance and inductive reactance further reduce. The LB parasitic controls the second excited resonance, shifting it lower in frequency into the upper portion of the LB frequency band. For example, prior to the introduction of the parasitic with four equally spaced capacitive sections this resonance occurs outside of the band of interest at 933 MHz. With the introduction of a 1" parasitic this resonance shifts in-band to 894 MHz. This introduction of a second resonance within the operating band, in addition to the

first resonance which has been moved in-band in the lower part of the bandwidth using the capacitive sections, allows for broadband tuning of the new capacitively loaded LB dipole with just a 1” long parasitic, as compared to the 3” long parasitic required in the baseline LB design.

The integration of series capacitance along the length of the LB dipole arms allows for the transformation of the LB dipole self-impedance to significantly lower values than that of the baseline dipole in the absence of a parasitic. The proper selection of the capacitive segment parameters allows the first resonance mode to be shifted into the lower part of the operating band. Upon reducing the LB dipole impedance across the band, an electrically short parasitic is introduced to shift a second resonance into the upper part of the operating band. Through a combination of these two techniques, a path for realizing a broadband LB dipole with reduced inter-array mutual coupling for improved MB performance has been realized.

2.4.5 Proposed Broadband LB Dipole for Reduction of Inter-Array Mutual Coupling

Using the results of the parametric studies, a modified LB dipole is designed which is used for the simulation and measurement of the proposed UC. In order to reduce the number of PCBs, a vertically oriented LB parasitic is selected. It has been investigated that the plane in which the parasitic resides does not play a significant role in determining the amount of mutual coupling present between the arrays.

The dimensions of the proposed LB dipole pertinent to its operation are noted in Figure 2-25 and tabulated in Table 2-4. The LB dipole PCBs are designed such that all features which interface with the LB feed board on the reflector are identical to the baseline LB dipoles discussed in Section 2.1. The assembled +45° LB sub-array is shown in Figure 2-26. As is explained in Section 2.4.1, PCB 3B/4B will be aligned and adhered to PCB 3/4, respectively, using pressure sensitive adhesive. The gap $g_5 = 0.115$”, places the bottom edge of the metallic parasitic at the same location

as the bottom edge of the metallic parasitic in Section 2.1.1 in which $g_4 = 0.085$". The difference in these two values, namely 0.030", is due to the fact that g_4 is the distance from just above the top edge of the L1 copper layer to the bottom of the 0.030" thick FR-4 substrate, above which the horizontal parasitic resides, whereas g_5 is the copper-to-copper spacing.

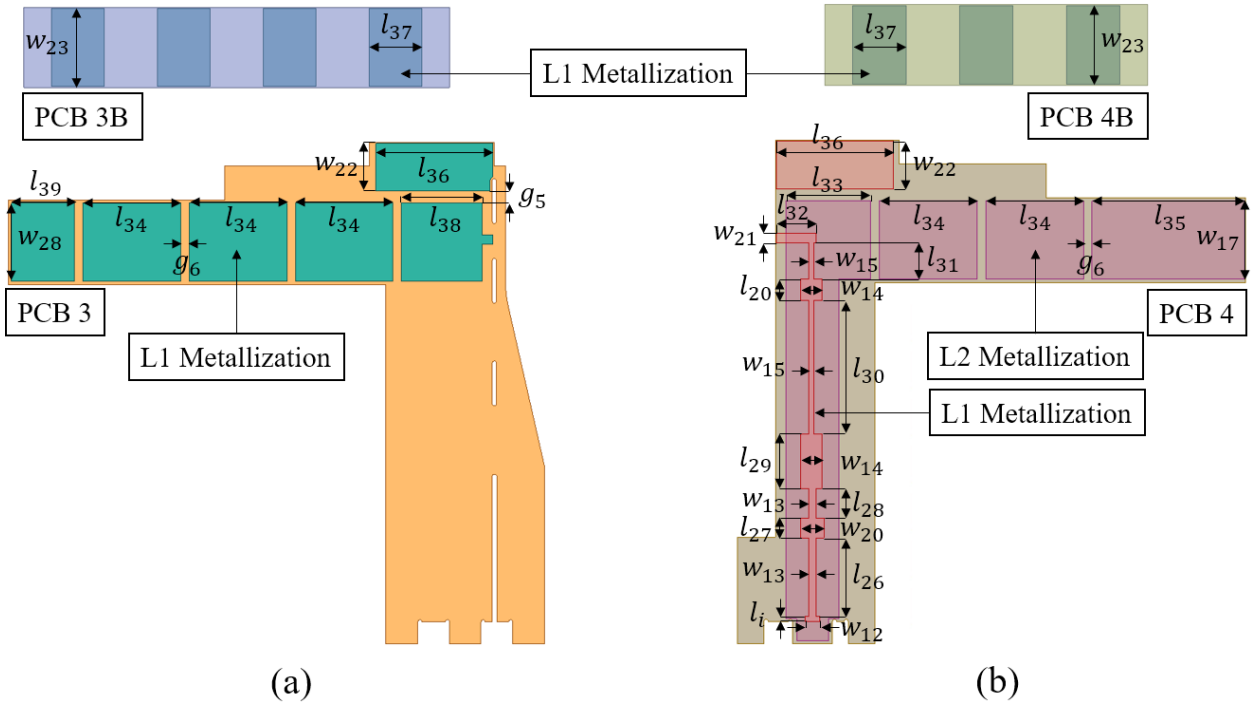

Figure 2-25: Proposed +45° LB dipole for improved MB radiation pattern performance. (a) PCB 3 and PCB 3B, and (b) PCB 4 and PCB 4B.

Table 2-4: Dimensions of the proposed LB dipole.

w_{20}	w_{21}	w_{22}	w_{23}	l_i	l_{26}	l_{27}	l_{28}	l_{29}	l_{30}	l_{31}
0.219	0.088	0.445	0.734	0.050	0.732	0.185	0.280	0.510	1.248	0.342
l_{32}	l_{33}	l_{34}	l_{35}	l_{36}	l_{37}	l_{38}	l_{39}	g_5	g_6	
0.374	0.800	0.920	1.431	1.100	0.500	0.760	0.593	0.115	0.080	

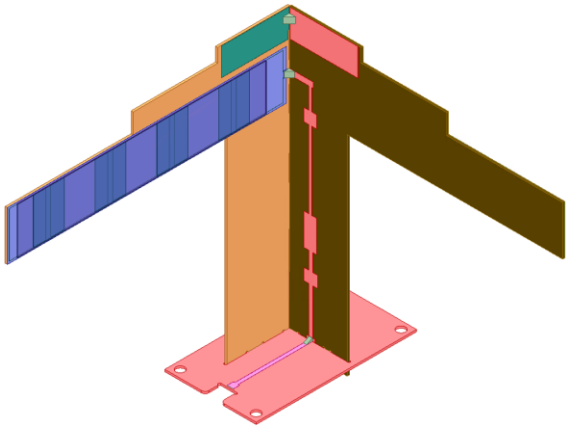

Figure 2-26: Simulation model of the assembled proposed LB sub-array.

2.5 Evaluation of the Proposed Mutual Coupling Reduction Technique

The purpose of this section is to present the simulated and measured results of the MB sub-array with the proposed LB dipole designed using the technique proposed in Section 2.4. The UC is simulated using HFSS in the exact configuration of that which is presented in Figure 2-1. The prototype PCBs are bonded together using pressure sensitive adhesive. The PCBs before and after bonding are shown in Figure 2-27. The proposed simulated and measured UCs are shown in Figure 2-28(a) and Figure 2-28(b), respectively.

An L-shaped FR-4 PCB is used as an LB dipole structural support in the prototyped UC. The structural PCB is the yellow PCB present on top of the LB dipoles shown in Figure 2-28(b). The only metal features present on the structural FR-4 PCB are several small solder pads which secure it to the PCBs which comprise the dipole. The structural support helps to prevent the LB dipoles from twisting or vibrating during the near field measurement. The proposed prototype UC is shown in the spherical near field chamber, in Figure 2-28(c), just prior to carrying out measurements.

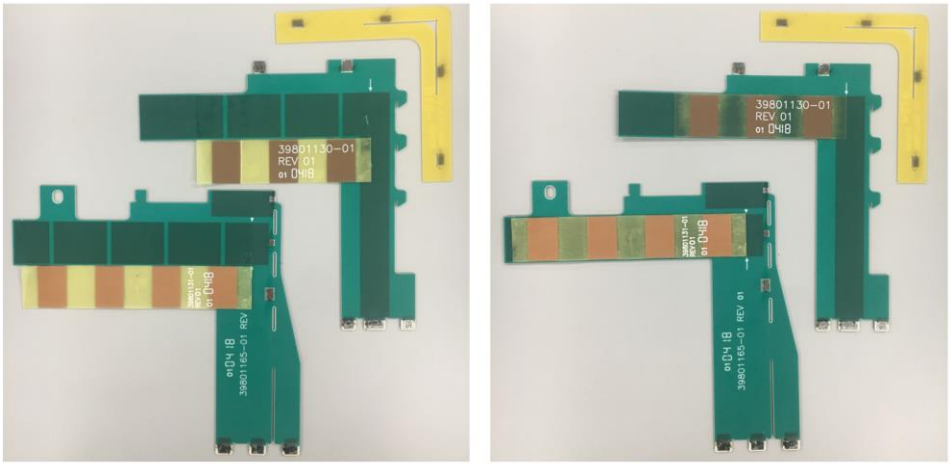

(a) (b)

Figure 2-27: The proposed LB dipole PCBs (a) before and (b) after bonding capacitive PCBs.

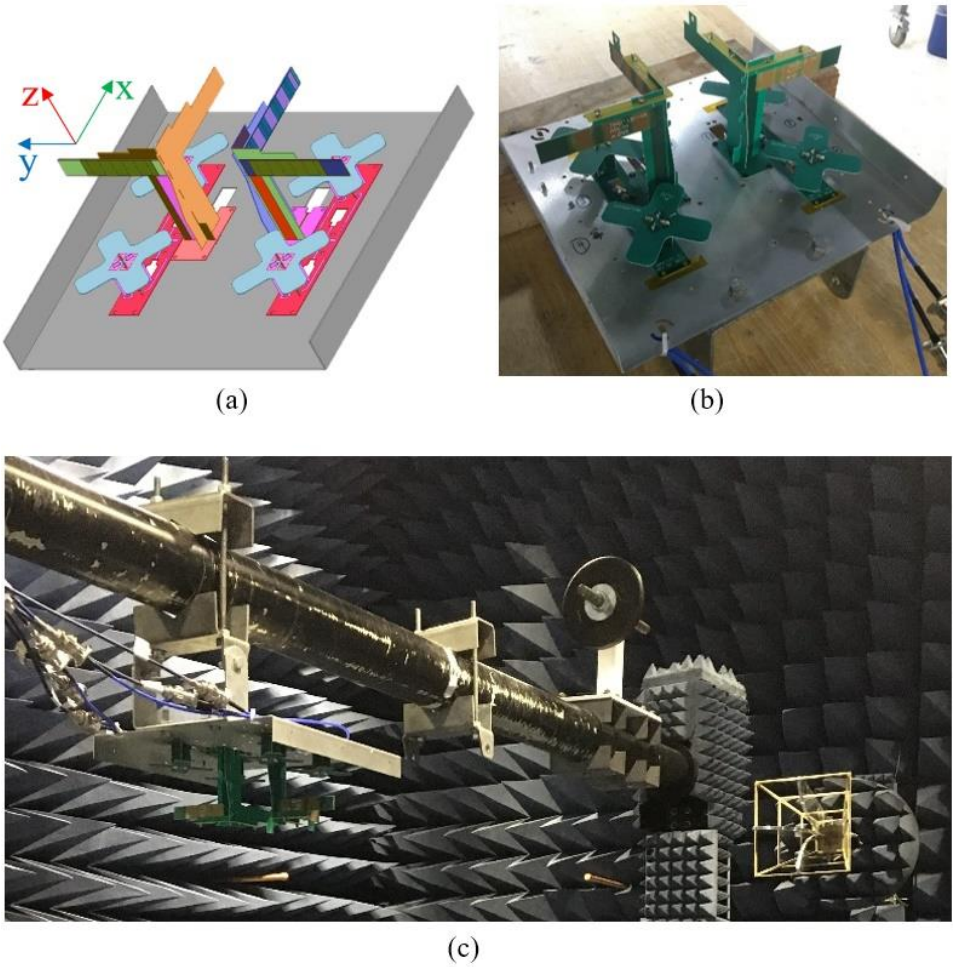

(a) (b)

(c)

Figure 2-28: UC 1 using proposed LB capacitive loading technique (a) simulation model and (b) prototype in (c) spherical near field chamber.

Although the goal of the proposed design is to improve the MB radiation characteristics over those of the baseline design, it is important to maintain similar or better S-parameters in moving to the proposed design. Both the baseline and proposed MB return losses are better than 10 dB across the band, as shown in Figure 2-29(a). Furthermore, the simulated and measured S-parameters agree closely with each other. The worst-case measured MB return loss is 11.5 dB in the presence of both the baseline and proposed LB dipoles. The proposed simulated and measured peak MB intra-array cross-polar isolations show slight improvement over the baseline UC between 1.750 GHz and 1.850 GHz, as shown in Figure 2-29(b). The measured peak isolation improves from −15.0 dB to –17.1 dB from the baseline UC to the proposed UC. Therefore, no significant degradation in S-parameters is observed in moving from the baseline to the proposed design.

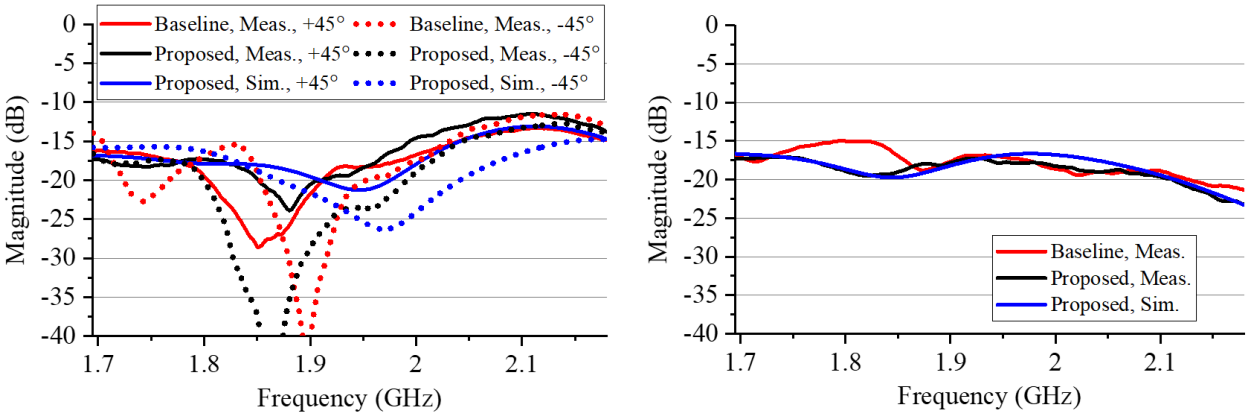

Figure 2-29: Left MB sub-array simulated and measured (a) reflection coefficient for ±45° polarizations and (b) intra-array cross-polar isolation of the baseline and proposed UC.

Although the radiation patterns were measured at 39 different frequency points across the band, for the sake of brevity only the radiation pattern characteristics at 1.700 GHz, 1.800 GHz, 1.900 GHz, 2.000 GHz, 2.100 GHz, and 2.180 GHz are presented. These six frequencies are representative of the radiation performance across the band.

The simulated and measured H-plane radiation patterns are shown in Figure 2-30 and Figure 2-31 for +45° and –45° polarizations, respectively. The +45° polarization shows little to no improvement with the proposed technique. However, both the peak and average cross-polar radiation (CPR) for the –45° polarization of the left MB sub-array improves in the presence of the proposed LB dipole in simulation and in measurement. The improvement in peak CPR is tabulated in Table 2-5. The –10 dB HBW also shows improvement across the band. For example, at 2.000 GHz the –10 dB HBW reduces from 141° to 129° (8.5%), as is observable from Figure 2-31(d).

The V-plane radiation patterns are shown in Figure 2-32 and Figure 2-33 for the +45° and −45° polarizations, respectively. The simulated and measured V-plane radiation patterns show no improvement for the +45° polarization. In fact, from 2.000 GHz to 2.180 GHz the peak upper side-lobe levels (PUSSLs) become worse. However, the V-plane radiation patterns in both simulation and measurement show improvement in side-lobe level (SLL) across the band for the –45° polarization of the left MB sub-array, as shown in Figure 2-33. The improvement in PUSLL is tabulated in Table 2-5.

The simulated and measured gain of the UCs are shown for ±45° polarizations in Figure 2-34. The average measured gain of the +45° polarization of the left MB sub-array before and after implementing the proposed technique are approximately the same across the band, namely 10.1 dBi and 9.9 dBi, respectively. Both the simulated and measured gains of the –45° polarization of the left MB sub-array show significant improvements across most of the band. For example, the average gains for the –45° polarization of the baseline and proposed UCs are 9.6 dBi and 10.6 dBi, respectively. The peak improvement across the band occurs at 1.900 GHz, for which the proposed UC measures 10.5 dBi whereas the baseline UC measures only 9.0 dBi, a 1.5 dB improvement after implementing the proposed LB dipole in place of the baseline LB dipole.

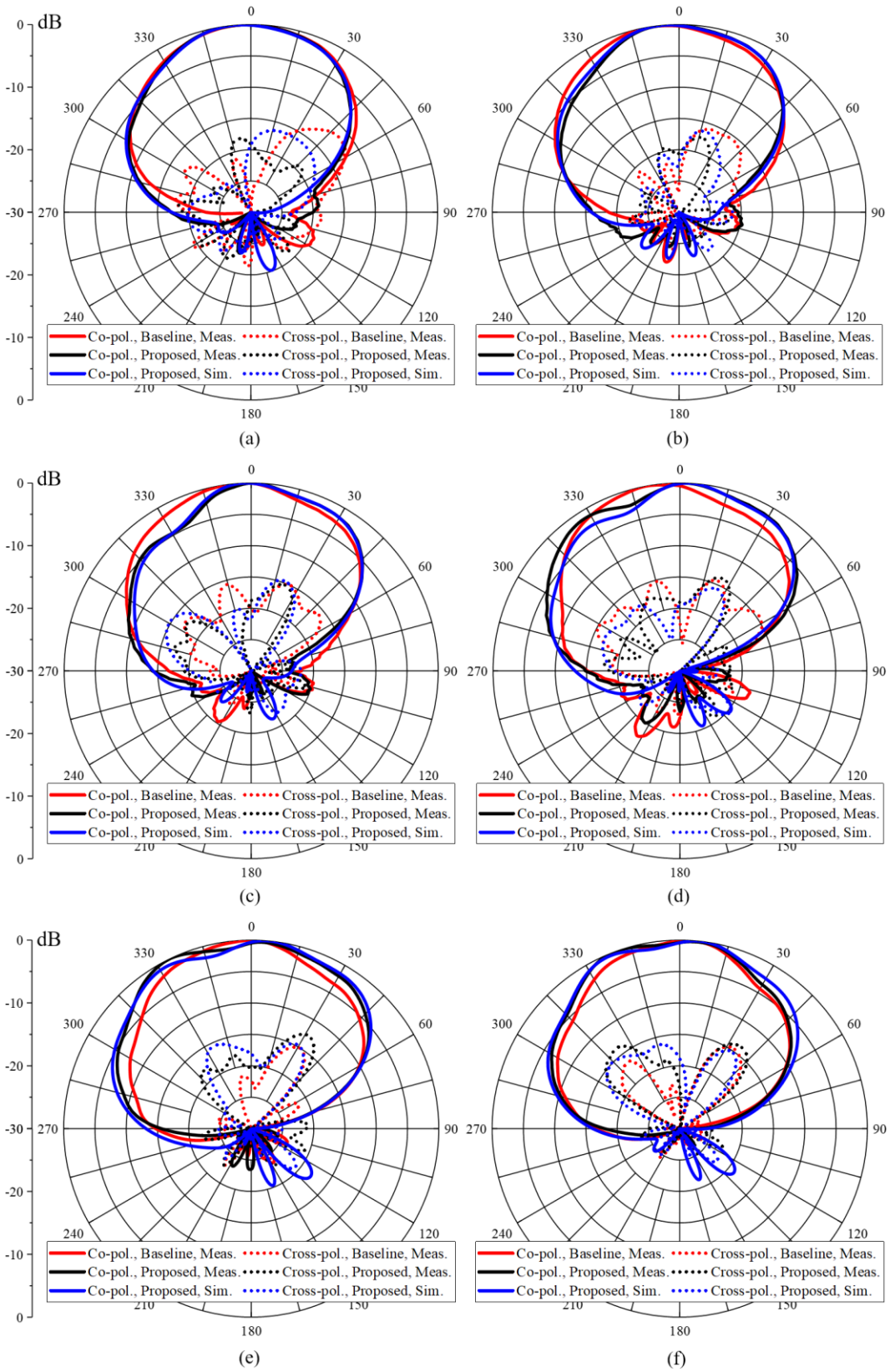

Figure 2-30: Simulated and measured H-plane radiation patterns of +45° left MB sub-array at (a) 1.700 GHz, (b) 1.800 GHz, (c) 1.900 GHz, (d) 2.000 GHz, (e) 2.100 GHz, and (f) 2.180 GHz.

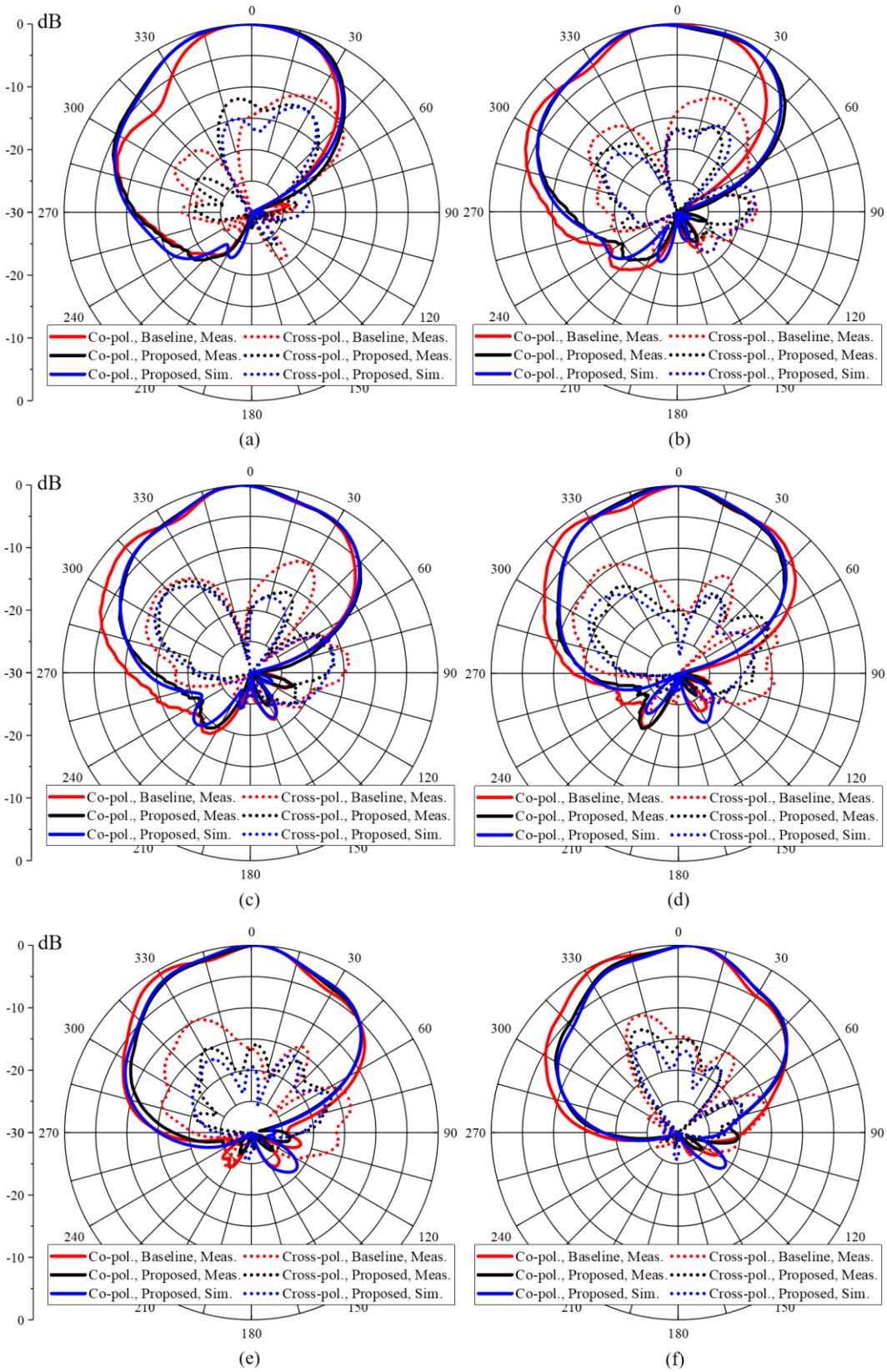

Figure 2-31: Simulated and measured H-plane radiation patterns of –45° left MB sub-array at (a) 1.700 GHz, (b) 1.800 GHz, (c) 1.900 GHz, (d) 2.000 GHz, (e) 2.100 GHz, and (f) 2.180 GHz.

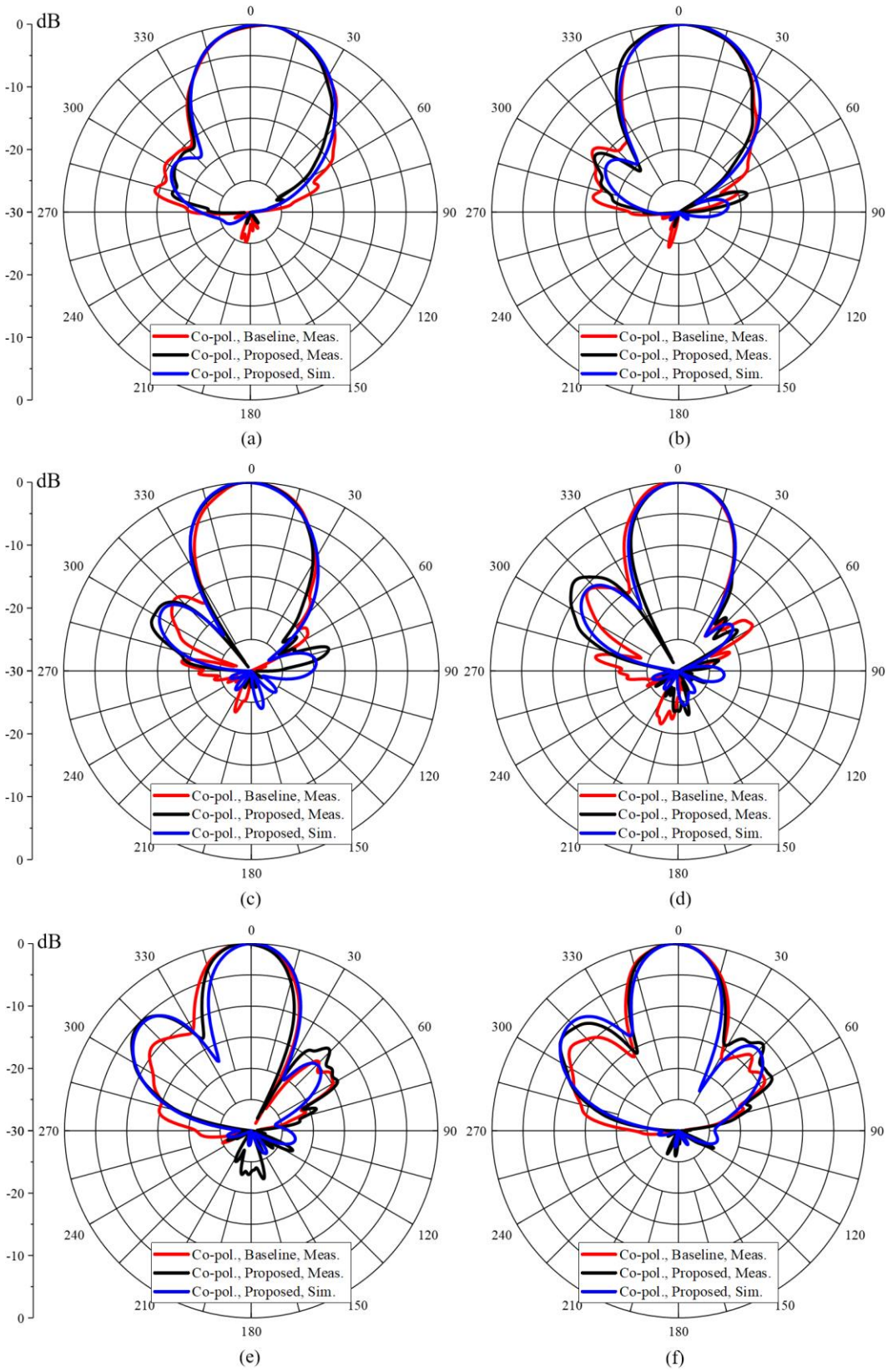

Figure 2-32: Simulated and measured V-plane radiation patterns of +45° left MB sub-array at (a) 1.700 GHz, (b) 1.800 GHz, (c) 1.900 GHz, (d) 2.000 GHz, (e) 2.100 GHz, and (f) 2.180 GHz.

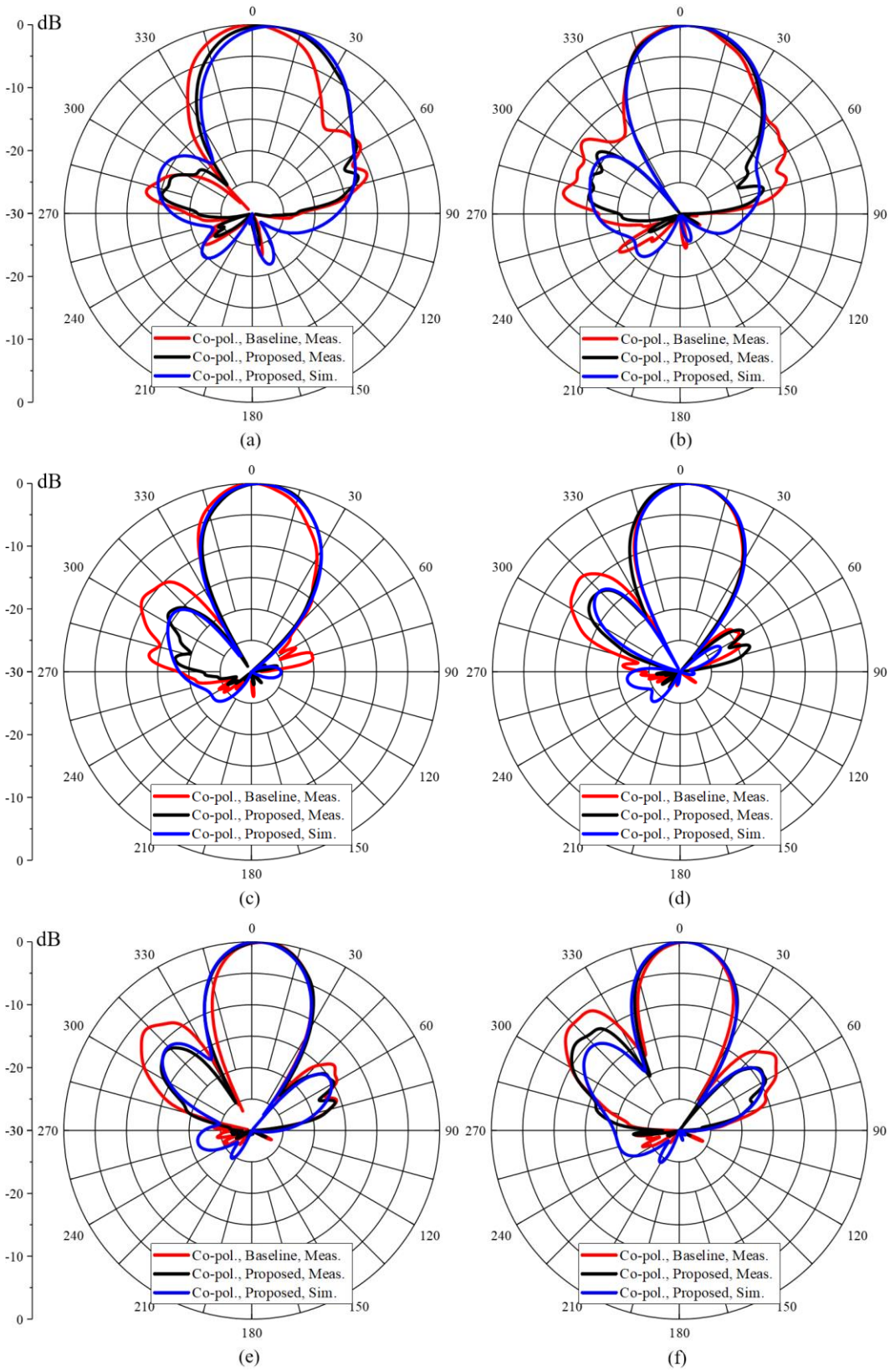

Figure 2-33: Simulated and measured V-plane radiation patterns of –45° left MB sub-array at (a) 1.700 GHz, (b) 1.800 GHz, (c) 1.900 GHz, (d) 2.000 GHz, (e) 2.100 GHz, and (f) 2.180 GHz.

Table 2-5: Comparison of simulated and measured key performance parameters for UC 1.

Frequency (GHz)	Peak CPR (dB): Baseline/Proposed	PUSLL (dB) Baseline/Proposed
1.700	–8.9/–11.5	–12.8/–15.3
1.800	–10.6/–15.4	–9.0/–13.8
1.900	–10.3/–11.3	–10.6/–13.6
2.000	–9.2/–13.0	–8.1/–11.7
2.100	–9.8/–14.7	–6.7/–11.4
2.180	–10.2/–12.3	–6.0/–8.5

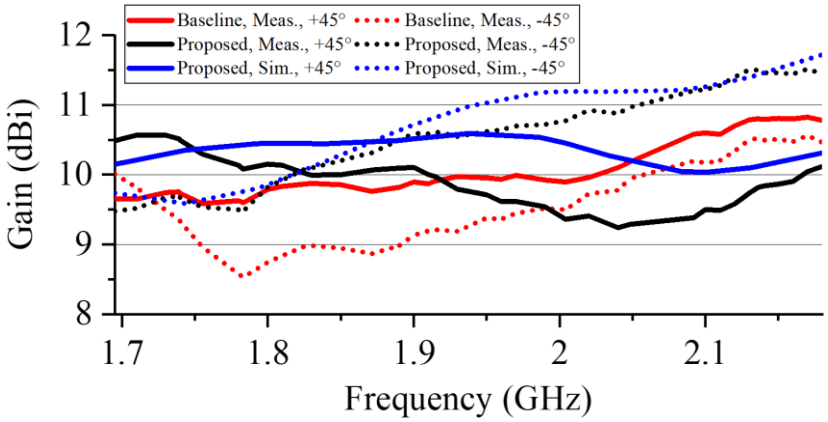

Figure 2-34: Simulated and measured peak system gain of the left MB sub-array.

2.5.1 Discussion of the Proposed UC 1 Performance

One aspect of the proposed UC which deserves attention is that despite the –45° polarization showing significant improvements, the +45° radiation characteristics do not show such improvements. In fact, in some respects the +45° polarization of the left MB sub-array shows degradation over that of the baseline UC. It is shown in Section 2.3 that the parasitic of the left +45° LB dipole predominantly degrades the –45° polarization of the left MB sub-array, leaving the +45° polarization performance largely unaffected. Therefore, it is expected that the solution proposed to reduce the LB parasitic impact will only improve the –45° polarization performance. One may then expect that the proposed technique will only improve one polarization when in a

BSA array, such as that which is proposed in Figure 1-8; however, this is not the case and is verified in Chapter 4.

The BSA array architecture of Figure 1-8 is made up of two distinct UCs, UC 1 and UC 1'. In UC 1, the UC considered in this chapter, the +45° LB dipole is on the left, and the –45° LB dipole is on the right. Whereas, in UC 1' the –45° LB dipole is on the left, and the +45° LB dipole is on the right. In UC 1, the baseline patterns for the –45° dipoles of the left MB sub-array are poor due to the presence of the parasitic on the left +45° LB dipole. It can be shown that, in UC 1', the baseline patterns of the +45° dipoles of the left MB sub-array are poor due to the presence of the parasitic on the –45° LB dipole which is also located on the left side. Therefore, it is expected that for a fixed MB polarization the proposed technique will improve the performance of every other UC along the length of the array. This will lead to an overall performance improvement in all MB polarizations present within a BSA using this technique, as is verified in Chapter 4.

The improvements observed in the CPR of the H-plane pattern would improve the polarization purity of a BSA if the proposed UC were to be used as part of a larger array. This improved polarization purity would improve the impact of the polarization diversity on the system performance. The reduction in the –10 dB HBW over that of the baseline UC would help to reduce inter-cell interference if used as part of a larger BSA array. An improvement in H-plane symmetry has been observed over most of the band. This improved symmetry would help to ensure that users on the left side of the BSA receive similar signal strength to those on the right side of the BSA. Although some asymmetries still exist in the H-plane, for example at 1.800 GHz, improvements have been realized across the band.

The improved V-plane SLLs would reduce the amount of energy radiated above the horizon, thereby increasing the signal strength received by the user on the downlink from BSA to user. The

average and peak gain improvements which are observed for the –45° left MB sub-array are due to the increase in directivity achieved in the proposed UC through narrowing the –10 dB HBW and through reduction of the V-plane SLLs. If this UC were to be used as part of a BSA, the resulting increase in gain would correspond to an increase in power density within the service area of the BSA, thereby extending the cell radius and SNR present at the receiver in the downlink.

2.6 Summary

In this chapter a technique for reducing the mutual coupling between LB and MB sub-arrays in a UC for improved MB performance is proposed. One of the main sources of mutual coupling is identified as the electrically long LB parasitic which is required for broadband matching of the baseline LB dipoles. It is shown that by integrating series capacitance into the arms of the LB dipoles, the self-resistance of the dipole can be reduced, and the inductive reactance can be canceled at the center of the operating band. The resulting dipole impedance can be matched over the band through the use of an electrically short parasitic, which introduces a second resonance in the LB dipole self-impedance. The electrically short LB parasitic causes significantly less inter-array mutual coupling as compared to the original electrically long LB parasitic.

Although the proposed technique does not completely eliminate the inter-array mutual coupling, significant improvements across several key performance parameters are observed. Improvements observed in the HBW, CPR, pattern symmetry, upper SLL and gain of the –45° left MB sub-array are expected to lead to pattern performance improvements if the UC were used as part of a larger BSA array, such as that shown in Figure 1-8. The overall simulated and measured improvements in the UC's MB performance after the introduction of the proposed LB dipole show promise for application in a BSA array, as is verified in Chapter 4.

Chapter 3

A Serially Loaded Capacitive Dipole Balun for Mutual Coupling Reduction

This chapter focuses on identifying and reducing a source of mutual coupling which leads to low-band (LB) performance degradation in a multi-array environment. Just as the mid-band (MB) performance is impacted in the presence of the baseline LB sub-arrays, due to the inter-array mutual coupling, so too is the LB radiation pattern degraded in the presence of the baseline MB sub-arrays. The first unit cell (UC), UC 1, under consideration is the serially loaded LB UC proposed in Chapter 2. The LB dipole in UC 1 operates from 698 MHz to 894 MHz. In addition to this, a second UC, UC 2, is considered in which a crossed LB dipole is tuned from 698 MHz to 960 MHz. For UC 2 the baseline MB dipoles operate from 1.695 GHz to 2.700 GHz instead of from 1.695 GHz to 2.180 GHz. The purpose of presenting both UC 1 and UC 2 is two-fold. First, it exemplifies that the inter-array mutual coupling is a phenomenon which is not limited to the UC 1 architecture and bandwidth originally proposed. Secondly the versatility and achievable bandwidth of the proposed mutual coupling reduction technique are demonstrated through consideration of UC 2.

A method for mutual coupling reduction is proposed which improves the LB performance in the presence of the MB sub-arrays for both UC 1 and UC 2. The MB dipole feed stems are identified as the main source of the LB performance degradation. It is demonstrated that upon the excitation of an LB dipole, the baseline MB dipole top and the MB dipole feed stems support induced currents which radiate similar to an electrically short monopole above a conducting ground plane. The proposed technique integrates series capacitance along the length of the MB balun feed stems to reduce the common mode (CM) currents induced on the conducting stems. The proposed solution leads to significant LB performance improvements in both of the UCs.

Both UCs were prototyped in their baseline and proposed configurations. The prototype measurements are compared with simulated results to demonstrate the accuracy of the methods used for investigating the mutual coupling phenomenon.

3.1 Design of Baseline Broadband UC 2

One of the UCs presented in this chapter, UC 2, consists of two MB sub-arrays, and one dual-polarized LB dipole as shown in Figure 3-1. The LB and MB operating bands are 698–960 MHz and 1.695–2.700 GHz, respectively. The fractional bandwidth of these LB and MB sub-arrays are 31.6% and 45.7%, as opposed to the 24.6% and 25.0% bandwidths considered in UC 1. The LB printed circuit boards (PCBs) are designed to use a 0.030" thick dielectric material with relative permittivity $\varepsilon_r = 2.94$ and dielectric loss-tangent $\delta_t = 0.0025$. The baseline MB PCBs are identical to those which are considered in UC 1 of Chapter 2.

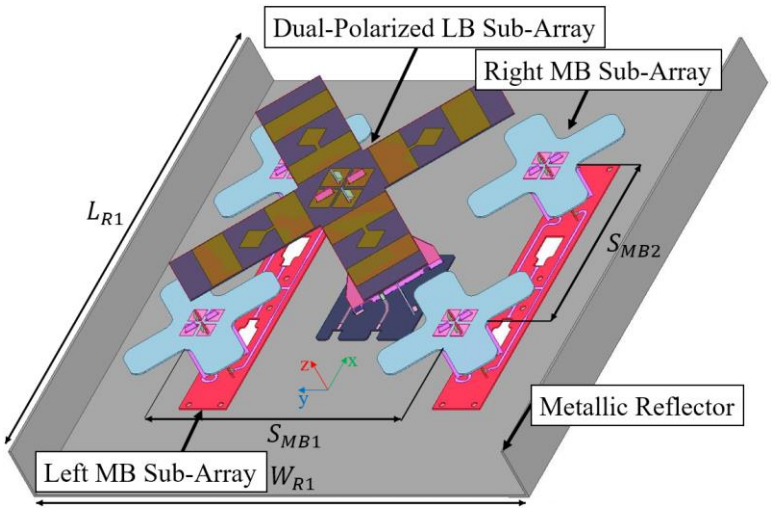

Figure 3-1: UC 2 is a broadband dual-band UC with a dual-polarized LB sub-array and left and right dual-polarized MB sub-arrays.

The LB radiator is a crossed LB dipole which is approximately $0.5\lambda_{f_c}$ where λ_{f_c} represents the free-space wavelength at 829 MHz. Although the LB dipole itself is not the focus of this work, some description is appropriate, as it is not a conventional crossed dipole. The crossed dipole is realized using alternating copper layers, L1 and L2, which capacitively couple to each other through the dielectric PCB substrate. Between the capacitive sections a short narrow high impedance section is present. This design, along with the capacitive feed allows for broadband operation. Furthermore, as opposed to the LB dipole in UC 1, which is considered in Chapter 2, this crossed LB dipole is fed using an open stub Marchand balun. Therefore, the feed mechanism utilized in the LB dipole of UC 2 is similar to the MB vertical feed stems which feed the MB dipole tops. The vertical LB feed stems interlock with an LB feed board which has both ±45° 50 Ω microstrip feed lines present. The feed board is designed to allow coaxial cables to be soldered to the microstrip transmission lines for excitation of the LB dipole. The LB PCBs and corresponding dimensions pertinent to the broadband operation are shown in Figure 3-2 and Table 3-1.

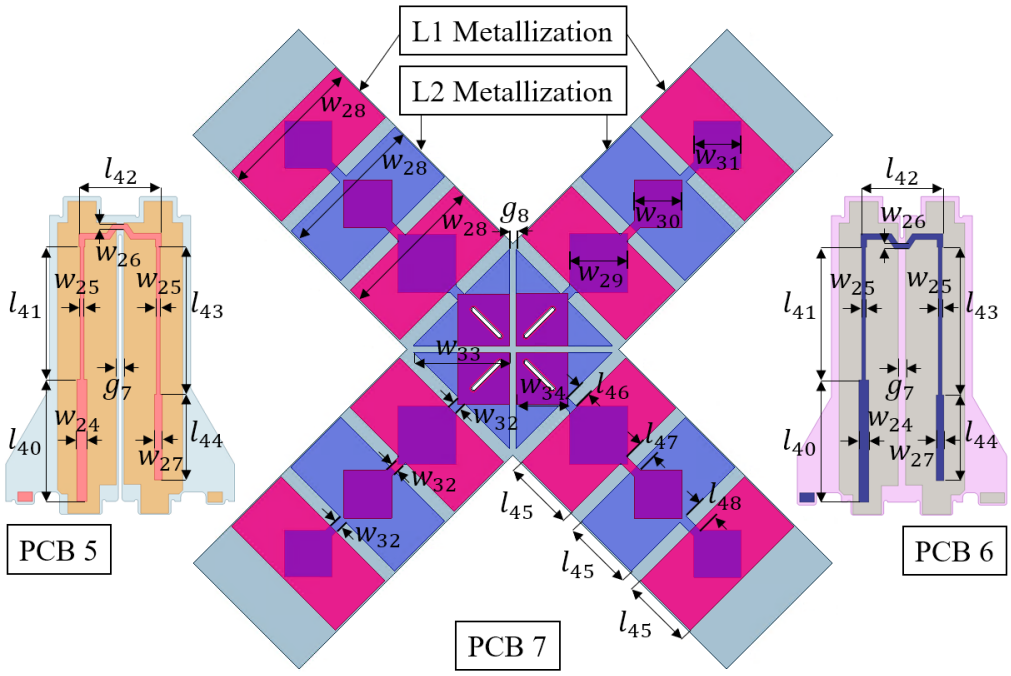

Figure 3-2: LB dipole PCBs for UC 2.

Table 3-1: Dimensions of LB dipole for UC 2.

w_{24}	w_{25}	w_{26}	w_{27}	w_{28}	w_{29}	w_{30}	w_{31}	w_{32}	w_{33}	w_{34}
0.105	0.040	0.061	0.0802	1.577	0.629	0.513	0.507	0.096	0.981	0.557
l_{40}	l_{41}	l_{42}	l_{43}	l_{44}	l_{45}	l_{46}	l_{47}	l_{48}	g_7	g_8
1.281	1.392	0.861	1.548	0.900	0.755	0.126	0.208	0.212	0.079	0.072

3.2 Impact of Inter-Array Mutual Coupling on LB Radiation

The impact of the presence of the baseline MB sub-arrays on the LB radiation characteristics is investigated for UC 1 and UC 2. Due to the symmetry of the dual-polarized UCs, the performance of the +45° LB sub-arrays suffice in characterizing the LB performances in the presence and absence of the MB sub-arrays. The input cable lengths and losses used in simulation are 24" and 0.010 dB/in at 894 MHz, respectively.

3.2.1 Simulation of Baseline UCs with and without MB Presence

This sub-section presents the results of the LB sub-array of UC 1 from 698 MHz to 894 MHz, as proposed in Chapter 2, as well as the LB sub-array of UC 2 from 698 MHz to 960 MHz, in the absence and presence of the baseline MB sub-arrays. First, the LB sub-arrays of UC 1 and UC 2 are simulated alone on the reflector, as shown in Figure 3-3(a) and Figure 3-3(b), respectively. Next, the LB sub-arrays are simulated in the presence of the baseline MB sub-arrays, as shown in Figure 2-28(a) and Figure 3-1 for UC 1 and UC 2, respectively. When the MB dipoles are present in the models, the feed boards to which they are connected are terminated in 50 Ω loads.

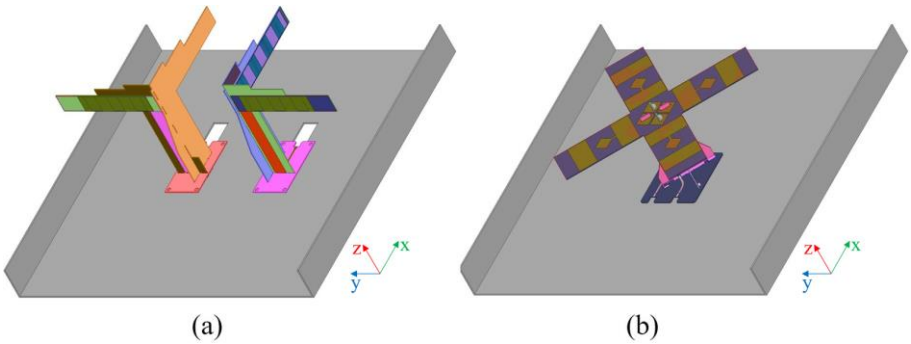

Figure 3-3: LB only models for (a) UC 1 and (b) UC 2 configurations.

The +45° H-plane (yz-plane) radiation patterns of the LB sub-array in the absence and presence of the baseline MB sub-arrays are shown for UC 1 in Figure 3-4(a) and Figure 3-4(b), respectively. For UC 1, the introduction of the baseline MB sub-arrays lead to broadening of the half power beamwidth (HPBW) and –10 dB H-plane beamwidth (HBW). For example, the HPBW at 737 MHz increases from 65° to 74° (13.8%) upon the addition of the baseline MB sub-arrays. Similarly, the –10 dB HBW at 796 MHz increases from 133° to 159° (19.5%). The frequency dependence of the HBW also increases upon the introduction of the baseline MB sub-arrays. Furthermore, the peak cross-polar radiation (CPR) increases upon the introduction of the MB sub-arrays. For example, the worst-case CPR across the band increases from –14.9 dB (without MB) to –10.1 dB (with MB) after introducing the MB sub-arrays. The front-to-back ratio also decreases upon the introduction of the baseline MB sub-arrays. This decrease in the front-to-back ratio over a ±30° sector is most apparent at 796 MHz for which it decreases from 20.4 dB to 13.5 dB.

The impact of the MB presence on the LB H-plane radiation pattern for UC 2 is even more severe than that which occurs in UC 1. The H-plane patterns in the absence and presence of the baseline MB dipoles are shown in Figure 3-5(a) and Figure 3-5(b), respectively. Both the HPBW and –10 dB HBW increase drastically upon the introduction of the baseline MB sub-arrays. For example, at 777 MHz the HPBW and –10 dB HBW increase from 67° to 148° (120.9%) and from

124° to 258° (108.1%), respectively, upon the introduction of the MB sub-arrays. The peak and average CPR also increase drastically with the addition of the MB radiators. For example, the peak magnitude of the CPR at 829 MHz increases from –17.9 dB to –9.0 dB upon the introduction of the MB sub-arrays.

Similar to the H-plane radiation patterns for UC 1, the V-plane (xz-plane) radiation patterns also exhibit broadening of the HPBW and –10 dB V-plane beamwidths (VBWs) upon the introduction of the MB radiators, as is seen in comparing the VBWs of Figure 3-6(a) and Figure 3-6(b) for each frequency. For example, for UC 1 the V-plane HPBW at 737 MHz increases from 77° to 89° (15.6%) after introducing the MB sub-arrays. Furthermore, the front-to-back ratio decreases upon the introduction of the MB sub-arrays, as is prominently observed at 796 MHz for which the magnitude of the co-polar radiation increases from –23.9 dB to –11.3 dB at 225° from boresight.

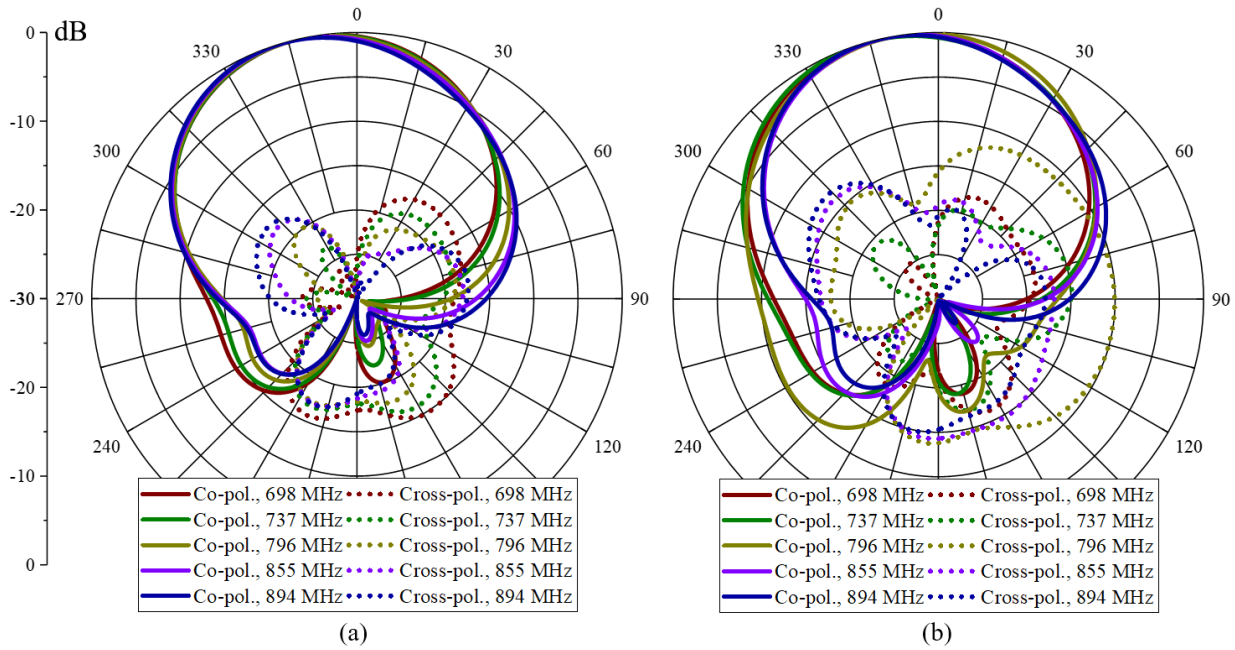

Figure 3-4: Simulated +45° LB H-plane radiation patterns with (a) only LB, (b) both LB and baseline MB sub-arrays for UC 1.

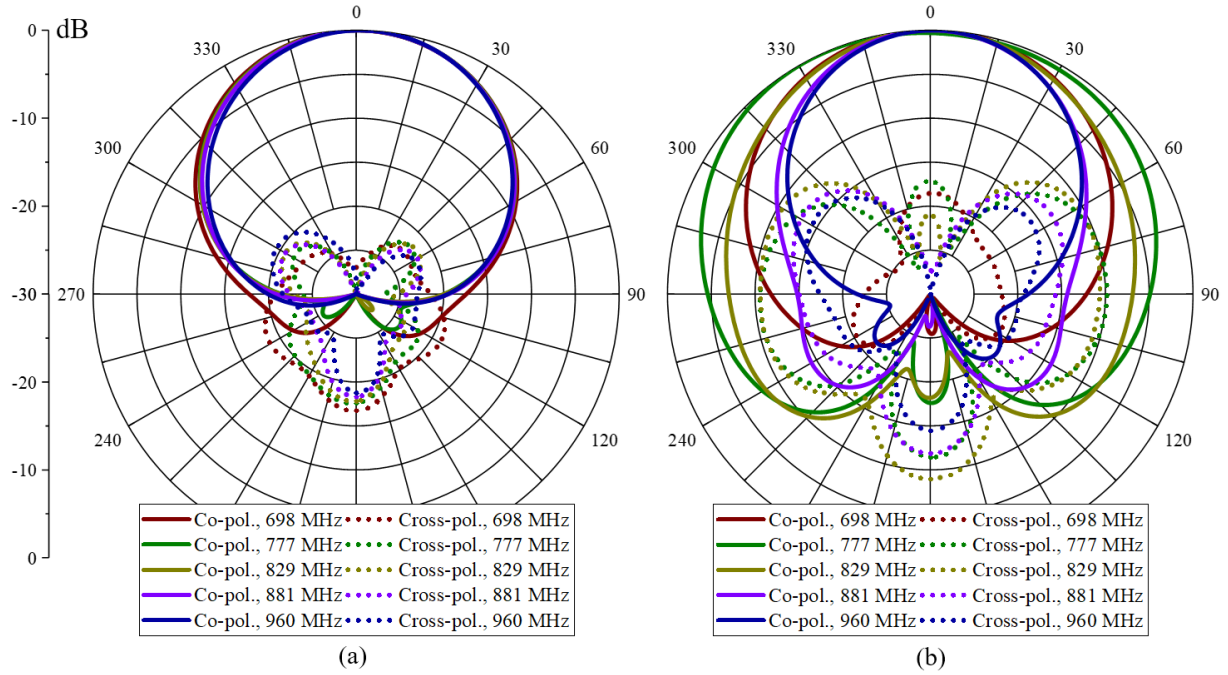

Figure 3-5: Simulated +45° LB H-plane radiation patterns with (a) only LB, (b) both LB and baseline MB sub-arrays for UC 2.

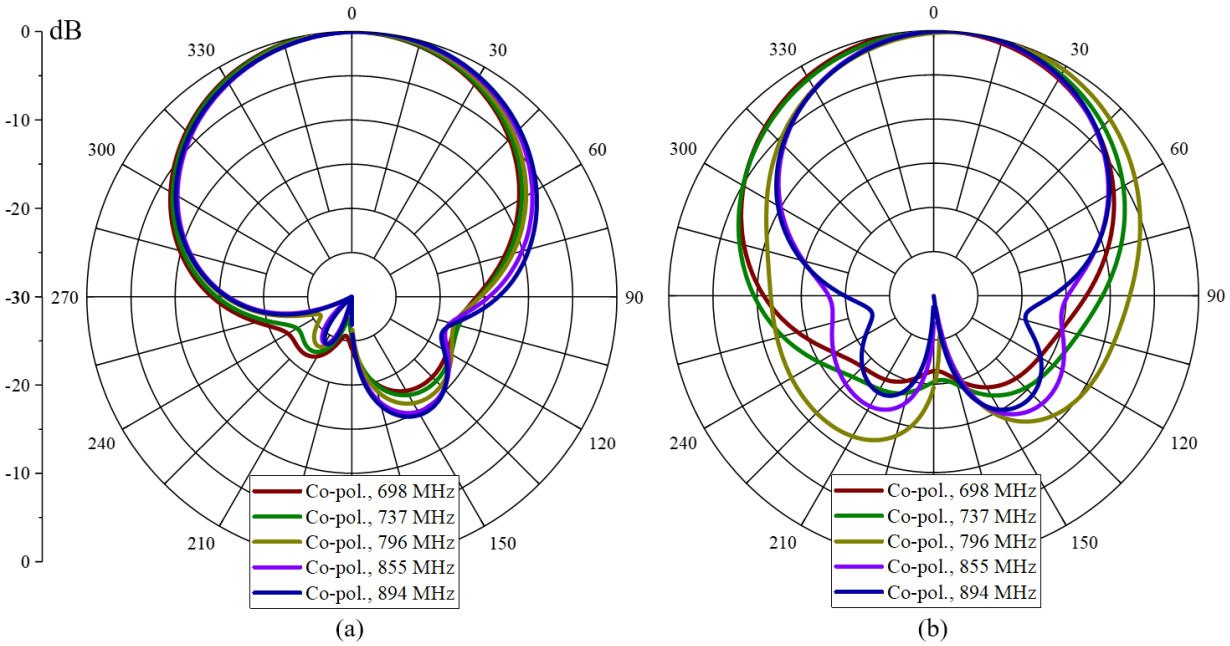

Figure 3-6: Simulated +45° LB V-plane patterns with (a) only LB, (b) both LB and baseline MB sub-arrays for UC 1.

The +45° LB V-plane radiation patterns in the absence and presence of MB radiators for UC 2 are shown in Figure 3-7(a) and Figure 3-7(b), respectively. Similar trends in the V-plane radiation patterns for UC 2 are observed upon the introduction of the MB dipoles. For example, the HPBW and –10 dB VBW at 777 MHz increase from 73° to 143° (95.9%) and from 134° to 244° (82.0%), respectively. The frequency dependence of the VBW also increases with the introduction of the MB radiators. A much larger portion of the total radiated power resides in the 180° sectors opposite of boresight when the MB dipoles are present as compared to when the LB dipoles are alone on the reflector.

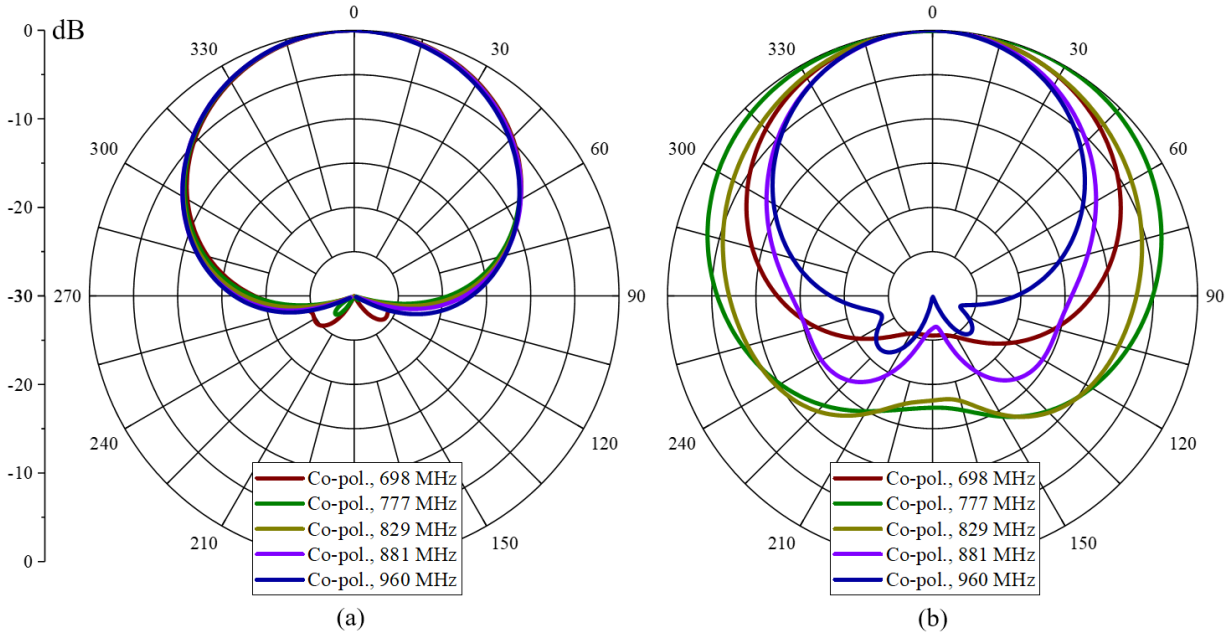

Figure 3-7: Simulated +45° LB V-plane patterns with (a) only LB, (b) both LB and baseline MB sub-arrays for UC 2.

The broadening of both the H-plane and V-plane beamwidths, the decrease in front-to-back ratio, and increase in CPR all result in a reduction in both the peak and average directivity and thus peak and average system gain of the LB sub-array across the operating bands. The system gains for UC 1 and UC 2 are shown in Figure 3-8(a) and Figure 3-8(b), respectively. The largest

degradation in gain for UC 1 occurs at 796 MHz for which gain reduces from 7.59 dBi to 6.11 dBi, a 1.48 dB reduction in gain. For UC 2, an even more drastic reduction in gain is observed across the operating band of 698–960 MHz. The largest degradation in gain for UC 2 occurs at 803 MHz for which the gain reduces from 7.96 dBi to 3.94 dBi, a 4.02 dB reduction in gain. Comparisons of the simulated key performance parameters of UC 1 and UC 2 before and after the introduction of the MB sub-arrays are found in Table 3-2 and Table 3-3, respectively.

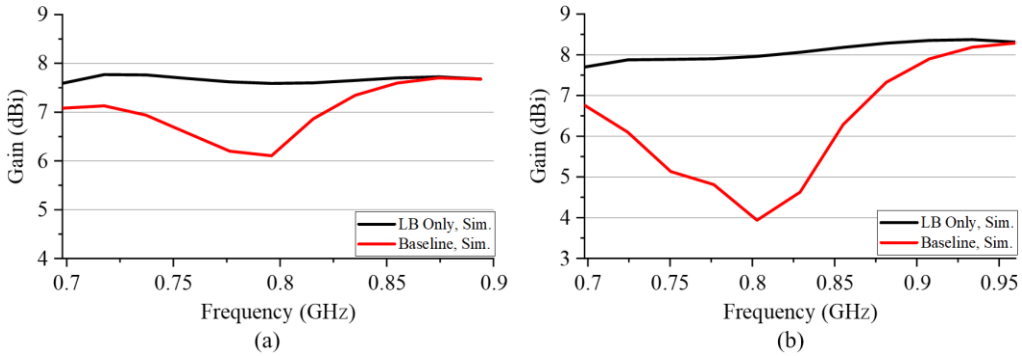

Figure 3-8: Simulated system gain of +45° LB sub-array for (a) UC 1, and (b) UC 2 with and without the presence of the MB sub-arrays.

Table 3-2: Comparison of simulated key performance parameters for UC 1.

	H-Plane			V-Plane		Front-to-Back Ratio ±30° Sector (dB) LB/LB+MB	Peak System Gain (dBi) LB/LB+MB
Frequency (MHz)	Peak CPR (dB) LB/LB+MB	HPBW (deg.) LB/LB+MB	–10 dB HBW (deg.) LB/LB+MB	HPBW (deg.) LB/LB+MB	–10 dB VBW (deg.) LB/LB+MB		
698	–14.9/–16.3	66/72	128/142	77/85	143/163	18.7/19.2	7.59/7.08
737	–16.1/–15.1	65/74	129/149	77/89	161/177	19.3/19.3	7.76/6.94
796	–17.1/–10.1	65/75	133/159	77/86	171/198	20.4/13.5	7.59/6.11
855	–17.1/–14.2	64/64	128/133	79/70	172/131	21.7/17.5	7.70/7.60
894	–17.1/–12.9	63/64	140/140	82/71	179/133	21.7/18.9	7.68/7.68

Table 3-3: Comparison of simulated key performance parameters for UC 2.

	H-Plane			V-Plane		Front-to-Back Ratio ±30° Sector (dB) LB/LB+MB	Peak System Gain (dBi) LB/LB+MB
Frequency (MHz)	Peak CPR (dB) LB/LB+MB	HPBW (deg.) LB/LB+MB	–10 dB HBW (deg.) LB/LB+MB	HPBW (deg.) LB/LB+MB	–10 dB VBW (deg.) LB/LB+MB		
698	–16.8/–18.5	68/83	128/161	77/87	132/162	27.9/25.5	7.70/6.76
777	–17.9/–9.9	67/148	124/258	73/143	134/244	29.6/14.5	7.90/4.81
829	–17.9/–9.0	65/83	124/267	74/99	135/248	31.1/14.6	8.06/4.63
881	–18.4/–11.9	64/61	122/124	77/67	137/134	33.1/19.7	8.29/7.32
960	–18.8/–14.3	62/59	108/113	77/63	135/122	33/23.2	8.29/8.29

3.2.2 Discussion of Performance of the Baseline UCs

The degree to which the mutual coupling between the proposed LB and baseline MB sub-arrays degrades the LB performance has been demonstrated for UC 1 and UC 2 through full-wave simulations. The implications of the increase in HBW, VBW, CPR, and reduction in the front-to-back ratio and gain on base station antenna (BSA) system performance are discussed below.

If the baseline dual-band UC 1 or UC 2 were to be used as part of a BSA, the increase in CPR observed in Figure 3-4(b) and Figure 3-5(b) would decrease the effectiveness of the polarization diversity of the dual-polarized LB array. Significant degradation in CPR can lead to the need for lower order modulation schemes, which reduces the overall throughput of the wireless network over its higher order equivalent. The increase in CPR occurs in all directions, which leads to a degradation in the directivity of the LB pattern.

The increase in the H-plane and V-plane HPBWs, upon the introduction of the baseline MB dipoles, increases the solid angle over which half of the power is radiated. This increase in beamwidth reduces the power density in the service sector, which lowers the power available for a receiver at a fixed distance from the BSA. Therefore, for a given receiver sensitivity the

maximum serviceable radius from the BSA, known as the service cell radius, reduces upon the introduction of the baseline MB dipoles.

The increase in the –10 dB HBW not only reduces the directivity but would also lead to an increase in interference between adjacent service cells. A sharp angular rejection between the HPBW and –10 dB HBW is desirable to maximize the energy directed to the users within the sector, while suppressing the energy in the directions serviced by adjacent BSAs. In this way, inter-cell interference between adjacent cells can be minimized.

In a similar manner, radiation directed opposite boresight results in a reduction in the directivity while also leading to inter-cell interference with the cell which services the sector opposite boresight of the BSA under consideration. For example, if a BSA has a poor front-to-back ratio this means that a user standing behind this BSA would receive relatively strong signals from it. However, this angular region is ideally being serviced by a different BSA, potentially at the same frequency of operation. This means that for a receiver located in this region, which is communicating with the BSA meant for servicing this angular region, the signal-to-noise ratio will decrease. This decrease in signal-to-noise ratio will result in degradation of the communication link and reduction in the throughput of the communication channel.

The broadening of the VBWs present in both UC 1 and UC 2 result in an increase in the amount of radiation which is directed above the horizon. For BSAs it is desirable to direct the radiation at or below the horizon, where the cellular users are typically located. Any radiation directed above the horizon reduces the received signal strength of cellular users present below the horizon.

The increase in CPR, HBW, VBW, and the reduction in front-to-back ratios of UC 1 and UC 2 lead to an overall degradation in the directivity and gain upon the introduction of the MB

radiators to the UCs. In order to utilize either of these architectures in a BSA array, significant improvement to the LB performance in the presence of the MB radiators must take place.

The impact of the mutual coupling is most pronounced in the lower part of the frequency bands, with peak degradation occurring near 796 MHz. Unlike the MB radiation patterns in the presence of the baseline LB dipoles, the LB patterns maintain a great degree of symmetry despite the strong effects of the mutual coupling. The envelope of the increase in both the co-polar and CPR levels in the H-plane resemble the radiation pattern of a monopole antenna oriented perpendicular to the reflector. It is this characteristic attribute of the mutual coupling which alludes to the possibility that the MB dipole stems, and dipole tops could in fact be acting as electrically short parasitic L-shaped monopole antennas. This proposition is investigated through simulation, and the results of the root cause analysis are presented in the following section.

3.3 Identification of the Root Cause of Inter-Array Mutual Coupling

This section confirms the hypothesis that the conductive MB dipole feed stems behave as electrically short monopoles fed over a conducting ground plane at LB frequencies. In particular, upon the excitation of the LB dipoles, common mode (CM) currents are induced on the MB subassemblies. Although differential mode (DM) currents are also induced on the vertical conducting feed stems, the radiation from electrically close DM currents is significantly less than that due to CM currents, due to phase cancellation in the far field. Since the currents induced on the MB subassemblies, upon the excitation of the LB dipole, have both CM and DM components, examination of the total currents induced on the MB stems does not provide much insight into the underlying phenomenon. However, exciting the MB subassembly in the two different modes,

namely CM and DM, and observing the resulting radiation provides a much clearer picture of the underlying phenomenon leading to the LB radiation pattern distortion.

First, a discussion regarding CM and DM currents in the context of the MB dipole subassembly is presented. Then, a baseline MB dipole is directly excited at LB frequencies using lumped ports to excite CM and ±45° DMs. Upon the excitation of the CM and DMs, the magnitude of radiation and the simulated radiation pattern characteristics are presented. A discussion regarding the results of the root cause analysis, as well as a proposed solution, follows.

3.3.1 Hypothesis of Induced CM Currents

The theory of CM and DM currents and their respective contributions to radiated emissions relies on the principle of superposition. This theory is discussed in Section 1.3 and has been covered at length in the literature [108], [124], [125]. The currents present on two conductors can be expressed as the superposition of CM and DM currents, as shown in Figure 3-9.

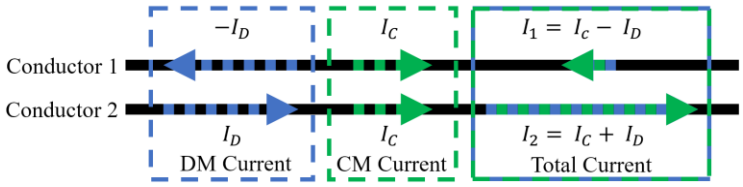

Figure 3-9: The total current present on two conductors is expressible as the superposition of CM and DM currents.

In the context of the baseline MB subassembly, the CM currents on the four conductors comprising the vertical balun feed stems, which are soldered together at their bases, have the same magnitude and phase as each other. Due to the symmetry of the structure, and the fact that the balanced ports of the vertical balun feed stems are soldered to the MB dipole top, the phase and amplitude of the CM current induced on the MB dipole top is expected to be radially symmetric as shown in Figure 3-10(a), where the green arrows represent the CM current induced upon

excitation of the CM lumped port (location shown in green). For a given polarization, the ±45° polarization DM currents on the MB stems are expected to be equal in magnitude and opposite in phase. The resulting DM currents are expected to be similar to an electrically short, crossed dipole being differentially excited, as shown in Figure 3-10(b), where the yellow arrows represent the current induced upon excitation of the −45° lumped port (location shown in yellow) and the blue arrows represent the current induced upon excitation of the +45° lumped port (location shown in blue). This method of analyzing a radiating element in terms of CM and DM currents has been previously carried out for multi-mode radiators, and can be found in the literature [126], [127].

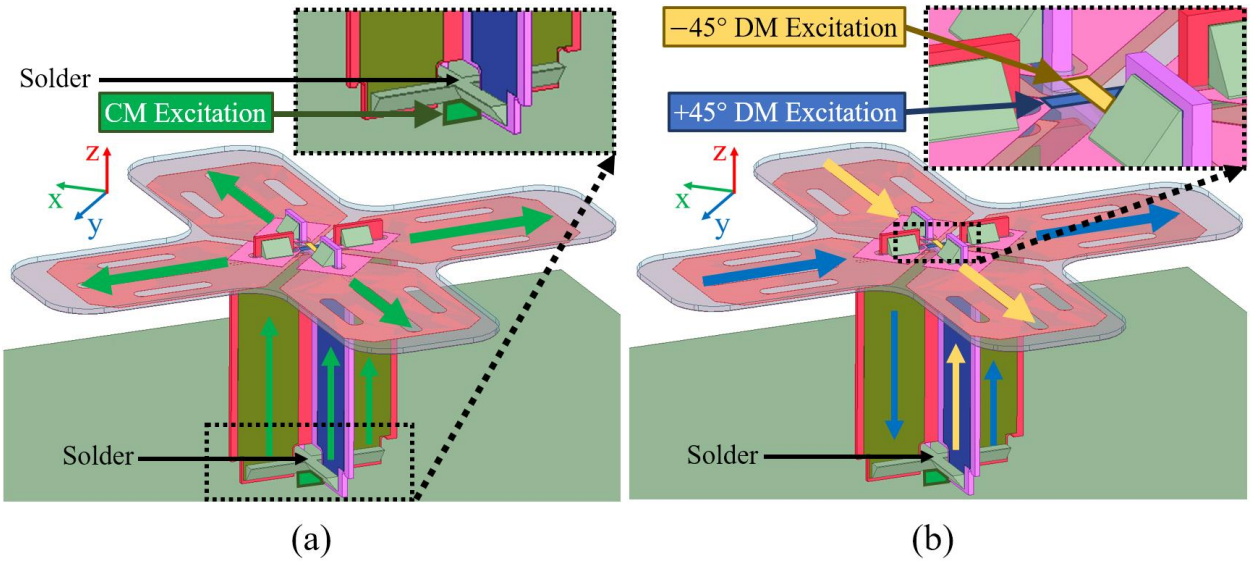

Figure 3-10: The MB dipole and expected current distributions for the (a) CM and (b) DM excitations.

Each MB dipole subassembly consists of two orthogonally polarized dipoles which are fed using two orthogonally oriented vertical balun feed stems situated perpendicular to the reflector. The unbalanced microstrip transmission line present on a vertical balun feed stem has two vertical ground planes which are both the ground planes for the transmission line as well as the balanced ports of the balun. As is described in Section 2.1, the bottom of all four of the vertically oriented

microstrip ground planes are soldered to the ground plane of the feed PCB. The feed PCB is then tightly coupled to the metallic reflector, separated only by a thin dielectric mask present on the ground of the feed board.

The distance between the adjacent vertical conductors varies from approximately 0.014λ to 0.068λ, where λ is the wavelength at 800 MHz, depending on which location is taken as reference along the width of the vertical conducting MB feed stems. Given that the CM currents are in phase with each other and the separation between these currents is electrically small, it is expected that the far field contributions due to the CM currents on the vertical stems will be constructive. However, due to the fact that the DM currents are 180° out of phase with each other and the separation between them is electrically small, it is expected that the far field contributions of the DM currents will largely cancel out.

Therefore, it is expected that the radiated emissions due to the CM currents will dominate over that of the DM currents. Furthermore, it is expected that the radiated fields caused by the CM currents will be approximately omni-directional in the plane of the reflector, similar to a monopole antenna or bent L-shaped/capped monopole antenna as is discussed in the literature [128], [129].

3.3.2 Evaluation of CM and DM Currents on the Baseline MB Dipoles

A single baseline MB crossed dipole element is situated above a small metallic reflector as shown in Figure 3-11. Three excitations, one CM and two DMs (±45° polarizations), are present in the HFSS model using lumped ports in the same location as shown in Figure 3-10(a) and Figure 3-10(b), respectively. Next, the resulting current distributions, magnetic field orientations, and radiation characteristics are presented.

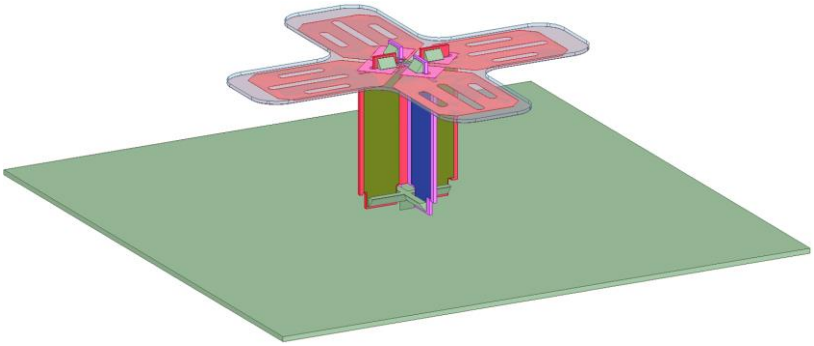

Figure 3-11: Baseline MB dipole situated above a small metallic reflector for CM and DM excitations using three lumped ports in HFSS.

The simulated vector surface current density at 960 MHz is overlaid with the MB dipole geometry in Figure 3-12, for both the CM and +45° DM excitations. The resulting currents match the expected distributions illustrated in Figure 3-10. The induced currents result in magnetic fields in the vicinity of the MB dipole stem and MB dipole top. The CM currents present on the MB stems induce magnetic fields which are in the same direction as each other. The DM current on the left stem, being 180° out of phase with respect to the current on the right stem, induces magnetic fields circulating around the stem which oppose those induced by the current on the right stem. Due to the close spacing of the left and right stems the DM magnetic fields will largely cancel, just as the far field contributions are expected to.

From the current distribution on the MB dipole, it is expected that the radiation pattern of the CM excitation of the MB dipole at LB frequencies will resemble that of an electrically short monopole antenna over a conducting ground plane, and the radiated fields due to the DM currents will be negligible. In order to evaluate this, the radiation patterns are plotted at 698 MHz, 805 MHz, and 960 MHz for both CM and +45° DM excitations. From the symmetry of the model, the resulting far field patterns under the –45° DM excitation mode are nearly identical to the fields which result upon the +45° DM excitation.

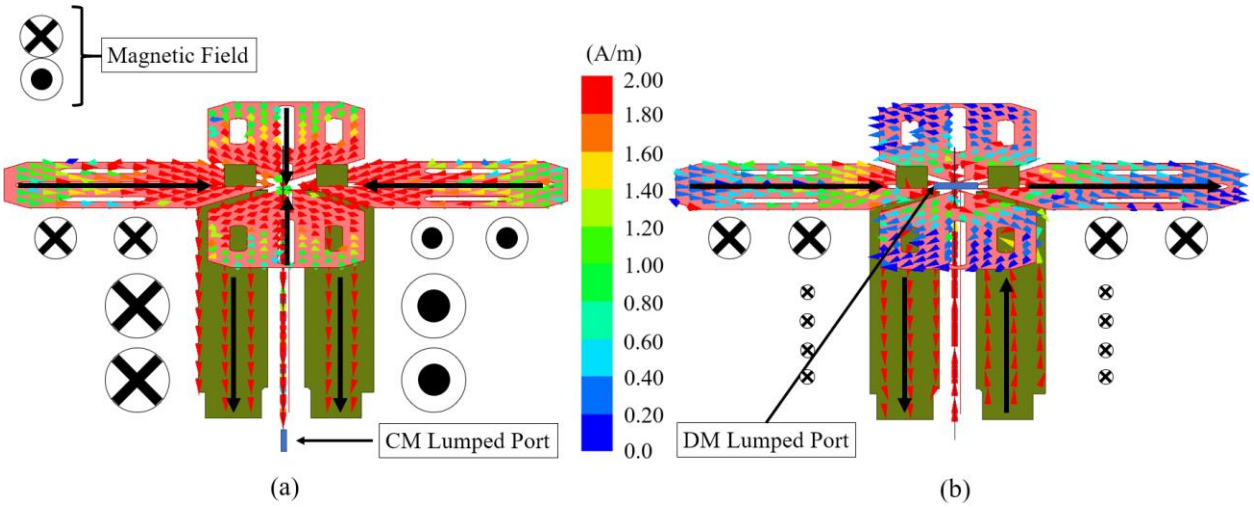

Figure 3-12: Simulated vector surface current density on the baseline MB dipole above a small metallic reflector in (a) CM and (b) +45° DM excitation modes at 960 MHz.

As expected, the CM excitation results in a radiation pattern which closely resembles that of a monopole antenna over a small conducting ground plane. The total radiated electric field is shown in Figure 3-13 at three LB frequencies for the CM excitation. The magnitude of the radiated emissions increases with frequency. The DM excitation mode results in minimal radiated emissions, as shown in Figure 3-14. These two results clearly demonstrate the dominance of CM currents in their contributions to radiated emissions.

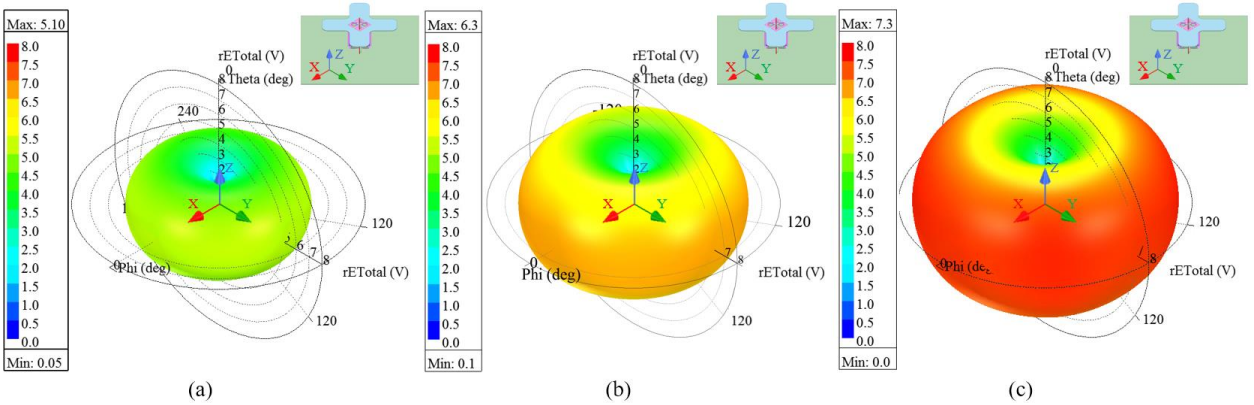

Figure 3-13: Total radiated electric field due to the CM excitation at (a) 698 MHz, (b) 805 MHz, and (c) 960 MHz for the baseline MB dipole.

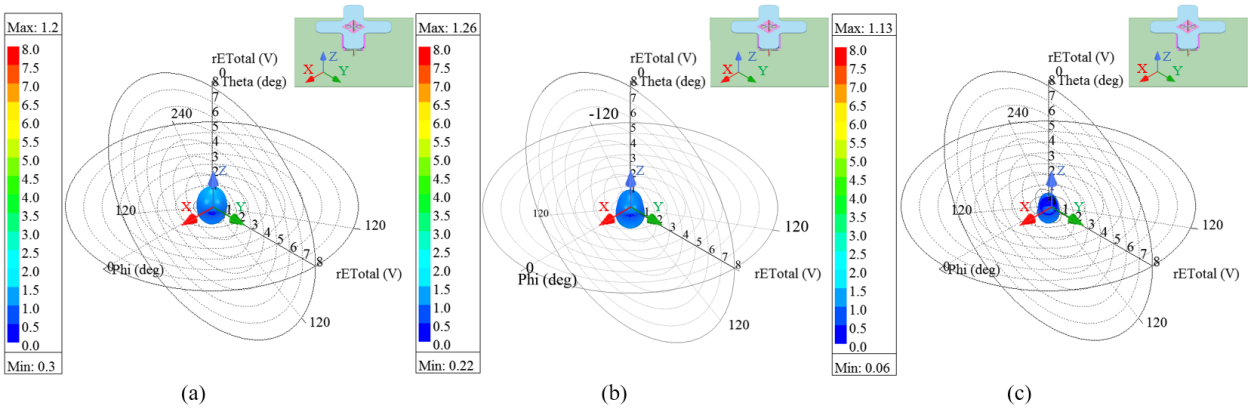

Figure 3-14: Total radiated electric field due to the +45° DM excitation at (a) 698 MHz, (b) 805 MHz, and (c) 960 MHz for the baseline MB dipole.

3.3.3 Discussion of Results of the Root Cause Analysis

It is shown through simulation that the baseline MB dipole supports CM and DM currents in the LB operating band of 698–960 MHz. The CM currents are shown to be the dominant contributor to far field radiation, as compared to the DM current contributions. Since the distance between the vertical conductors on the MB dipole feed stems is electrically small at LB frequencies the dominance of the CM radiated emissions was expected.

The CM currents are shown to be present on both the dipole arms themselves, as well as the vertical MB dipole feed stems. From the shape of the radiation pattern, the dominant source of the radiated emissions corresponds to the vertical conducting MB stems. This is apparent through observing the shape of the CM radiation pattern, which resembles that of a monopole over a small conducting ground plane. Although CM currents are also present on the baseline MB dipole tops, these currents are found not to be dominant.

The connection of the vertical conducting MB dipole feed stems to the MB dipole top forms a monopole which is loaded with a cross-shaped conductor. A similar, but simpler, single-polarization case of an L-shaped wire monopole antenna has been previously considered in the

literature [128]. The impact of the aspect ratio of the stem length to the top horizontal conductor length on the radiation pattern for various current distributions has been discussed [128]. The radiation pattern result they obtain for a triangular current distribution, which they mention as being more realistic than a uniform current distribution, is in agreement with the monopole shaped radiation pattern found in this section. For the dimensions of the baseline MB dipole, the ratio of the stem height to the dipole arm length is 0.829 at 800 MHz, and the total length of the MB dipole stem and dipole arm, combined, and normalized with respect to the wavelength at 800 MHz is 0.200. Observing Figure 4 of [128] reveals that the radiation for such ratios for a simple L-shaped wire antenna with a triangular current distribution is expected to be dominated by monopole-like radiation, as opposed to patch-like radiation which would occur if the horizontal dipole arm radiation were dominant.

3.4 Proposition for the Reduction of Inter-Array Mutual Coupling

This section proposes a method for reducing the CM currents induced on the MB dipole feed stems upon the excitation of the LB dipoles. The method is based on serially loading the MB feed stems with capacitance, in order to create a high-pass filter response on the MB dipole feed stems. Although this capacitance can be realized in a number of different ways, such as discrete capacitors or interdigital capacitors, the method chosen for this research is through the use of parallel plate capacitors, similar to how the series capacitance of Chapter 2 is realized. With this implementation, the L2 metallization layer of the MB feed stem is segmented into several sections with adjacent segments captively coupled to each other using 0.002” thick pressure sensitive adhesive. While multi-layer PCB fabrication techniques can be utilized for realizing the capacitors with improved precision, in lieu of the adhesive, it would increase the cost of circuit boards.

Care is taken to ensure that the resulting MB feed stems remain operable over the broad MB frequency range. If too many capacitive sections are utilized, or if the capacitance at each junction is too low, the resulting MB balun feed stems will reject both LB and MB frequencies. If the capacitance value is too high, then the LB currents are not rejected and thus the mutual coupling and radiated emissions persist.

3.4.1 Proposed MB Dipole for the Reduction of Inter-Array Mutual Coupling

The optimal capacitive coupling is found through iterative modeling in HFSS, in which first one, then up to four capacitive sections are introduced in the L2 metallization layer of the MB feed stems. In each configuration both the feasibility of matching the MB dipole over the broadband as well as the degree to which the configuration suppresses the inter-array mutual coupling are evaluated. Acceptable performance is achieved for the case in which three segments are present on the L2 metallization which acts as the microstrip ground for the open stub side of the MB balun, and one segment is present on the L2 metallization of the unbalanced side of the balun. If three segments were to be present on both sides of the L2 metallization layer comprising the MB baluns, the mutual coupling suppression would be superb; however, the return loss of the MB dipole would be worse than 3 dB in the lower part of the band due to the cutoff of the high-pass filter shifting up in frequency.

The pertinent dimensions of the proposed MB dipoles are noted in Figure 3-15 for UC 1, Figure 3-16 for UC 2 and tabulated in Table 3-4. The MB baluns for both UC 1 and UC 2 utilize the same capacitive coupling PCBs. PCB L adheres to the left side of PCB 5/7 and PCB 6/8, and PCB R adheres to the right side of PCB 5/7 and PCB 6/8, as oriented in Figure 3-15 and Figure 3-16. Due to the difference in mutual coupling between UC 1 and UC 2, and therefore the impedances of the MB dipoles, the L1 metallization layers for both ±45° MB baluns are tuned differently for the two

different UCs. Only the marked dimensions of Figure 3-16 differ from those of Figure 3-15. The MB dipole PCBs are designed such that all features which interface with the MB feed board on the reflector are identical to the baseline MB dipoles discussed in Section 2.1. The assembled ±45° MB sub-array is shown in Figure 3-17. PCB R and PCB L are aligned and adhered to PCBs 5–8 using pressure sensitive adhesive.

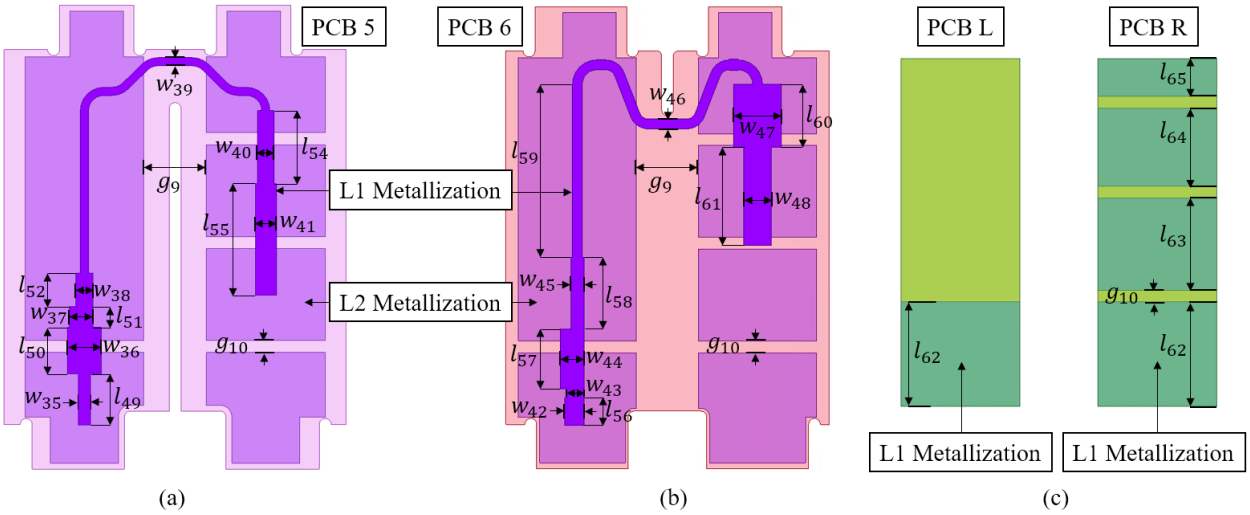

Figure 3-15: Proposed (a) +45° and (b) –45° MB balun PCBs and (c) left and right capacitive coupling PCBs for UC 1.

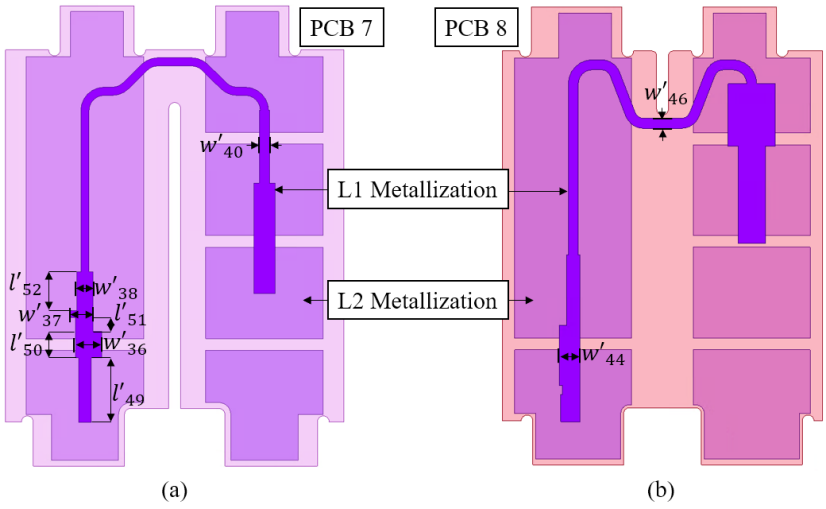

Figure 3-16: Proposed (a) +45° and (b) –45° MB balun PCBs for UC 2.

Table 3-4: Dimensions of the proposed MB dipole subassembly. All units are in inches.

w_{35}	w_{36} w'_{36}	w_{37} w'_{37}	w_{38} w'_{38}	w_{39}	w_{40} w'_{40}	w_{41}	w_{42}	w_{43}	w_{44} w'_{44}	w_{45}
0.043	0.113 0.088	0.079 0.078	0.057 0.055	0.028	0.055 0.035	0.071	0.066	0.059	0.082 0.070	0.046
w_{46} w'_{46}	w_{47}	w_{48}	l_{49} l'_{49}	l_{50} l'_{50}	l_{51} l'_{51}	l_{52} l'_{52}	l_{53}	l_{54}	l_{55}	l_{56}
0.033 0.034	0.161	0.092	0.172 0.219	0.157 0.090	0.071 0.046	0.111 0.132	0.547	0.246	0.375	0.093
l_{57}	l_{58}	l_{59}	l_{60}	l_{61}	l_{62}	l_{63}	l_{64}	g_9	g_{10}	
0.202	0.244	0.584	0.213	0.331	0.352	0.310	0.263	0.210	0.040	

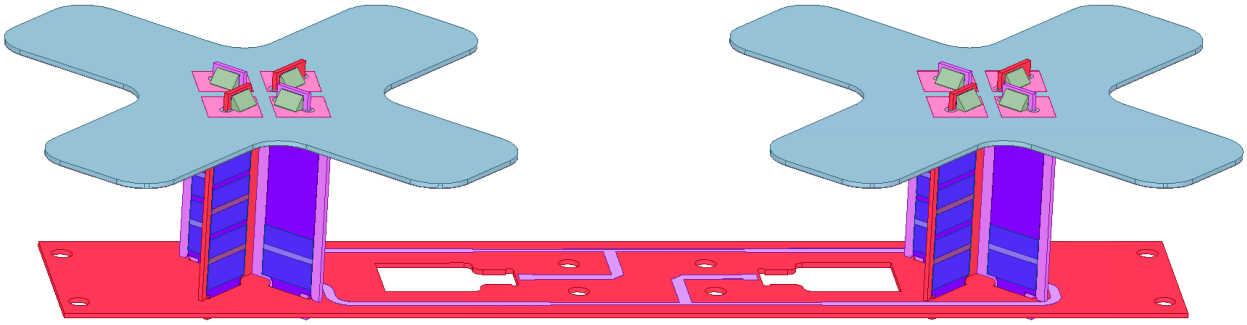

Figure 3-17: Simulation model of the assembled proposed MB sub-array.

3.4.2 Evaluation of CM and DM Currents of the Proposed MB Dipole

In a manner similar to Section 3.3, the effects of the CM and DM currents supported by the proposed MB dipole are evaluated through simulation. First, the proposed MB dipole is excited in CM and DMs and the radiation patterns are evaluated under the same operating conditions as the baseline dipole of Figure 3-11. Next, both the baseline and proposed MB dipoles are simulated in the presence of a magnetic field probe to detect the magnitude of the magnetic flux linking the probe due to the CM and DM currents as a function of frequency. The resulting insertion loss induced from the excited ports to the magnetic field probe is then compared with the baseline MB dipole. Finally, a discussion compares the baseline MB dipole radiated emissions to those of the proposed MB dipole.

The CM radiation patterns of the proposed MB dipole at three frequencies, shown in Figure 3-18, exhibit a similar shape to that of the baseline dipole, namely a monopole. For ease of comparison, the same scales are used for Figure 3-13 and Figure 3-18. A direct comparison of Figure 3-13 and Figure 3-18 shows that the magnitudes of the CM radiated emissions from the proposed MB dipole are significantly reduced over those of the baseline MB dipole.

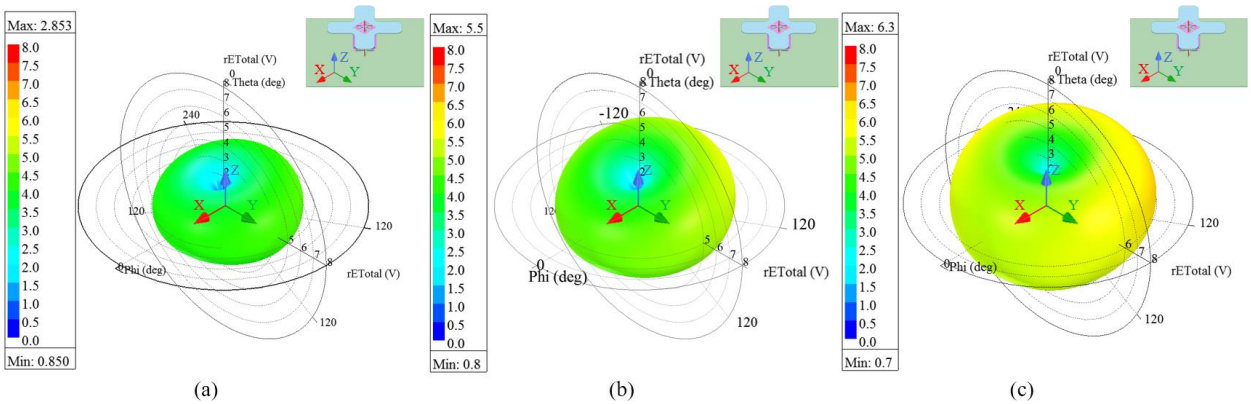

Figure 3-18: Total radiated electric field due to the CM excitation at (a) 698 MHz, (b) 805 MHz, and (c) 960 MHz for the proposed MB dipole.

The DM radiation patterns, shown in Figure 3-19, also exhibit a similar shape to that of the baseline MB dipole upon excitation of the DM modes. The magnitude of the resulting DM radiated emissions have increased for the proposed MB dipole over that of the baseline MB dipole. In order to better understand the level of CM suppression which has been achieved, and the relative magnitude to which the DM currents have increased, a magnetic field probe is designed and placed near both MB dipoles, as shown in Figure 3-20. The magnitude of the resulting insertion loss induced by the magnetic flux linkage is evaluated as a function of frequency.

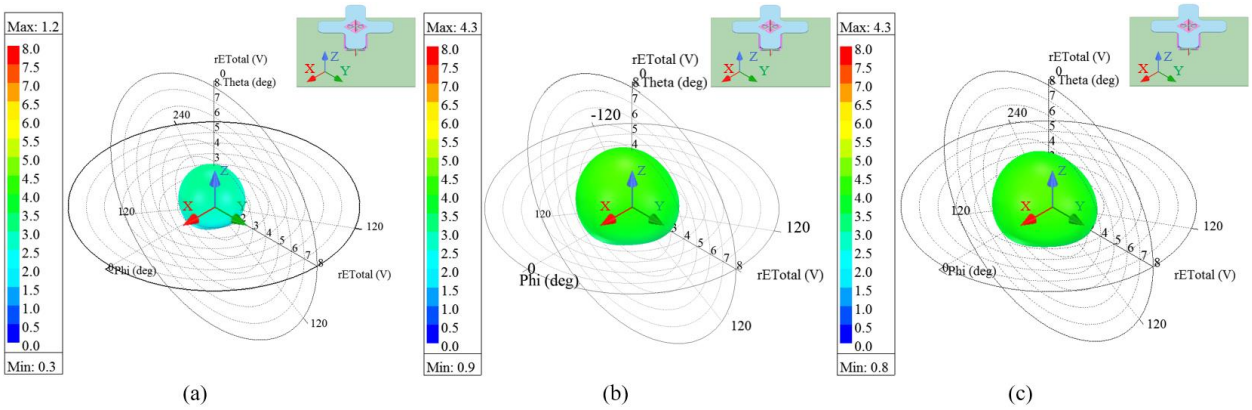

Figure 3-19: Total radiated electric field due to +45° DM excitation at (a) 698 MHz, (b) 805 MHz, and (c) 960 MHz for the proposed MB dipole.

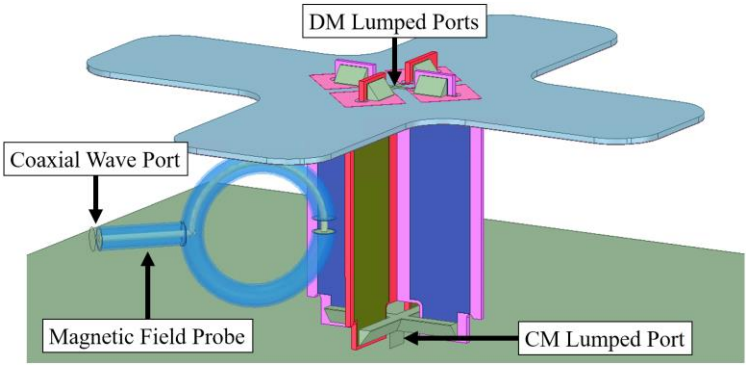

Figure 3-20: Magnetic field probe positioned below the baseline MB dipole.

The magnetic field probe is designed assuming it is made out of the same 50 Ω 0.141" diameter coaxial cable used in the fabrication of the UCs. A wave port is placed on the face of the coaxial cable to act as a receiving port for any signal which is induced in the probe due to magnetic flux linkage through the cross section of the probe. The induced signal strength in the magnetic field probe for the CM and DMs of excitation are then evaluated to characterize their relative magnitudes as a function of frequency.

Upon the excitation of the CM lumped port and the ±45° DM lumped ports, the signal strength induced into the magnetic field probe is evaluated both for the baseline and proposed MB dipole,

as shown in Figure 3-21. The CM insertion loss of the proposed MB dipole is less than the baseline MB dipole for all frequencies across the band. The peak difference between the CM insertion loss of the proposed and baseline MB dipoles occurs at 800 MHz, with a suppression difference of more than 3.45 dB, nearly a 55% reduction in magnitude. The DM insertion losses of the proposed MB dipole increase over that of the baseline MB dipole. From the increase in DM radiated emissions observed in Figure 3-19, this result is expected. The results of this simulation validate the expectation that the magnetic field induced by the DM currents will mostly cancel, with the effects of the CM currents remaining dominant and constructively interfering. The results of the radiation patterns and insertion losses in the presence of a magnetic field probe are in support of the proposed design.

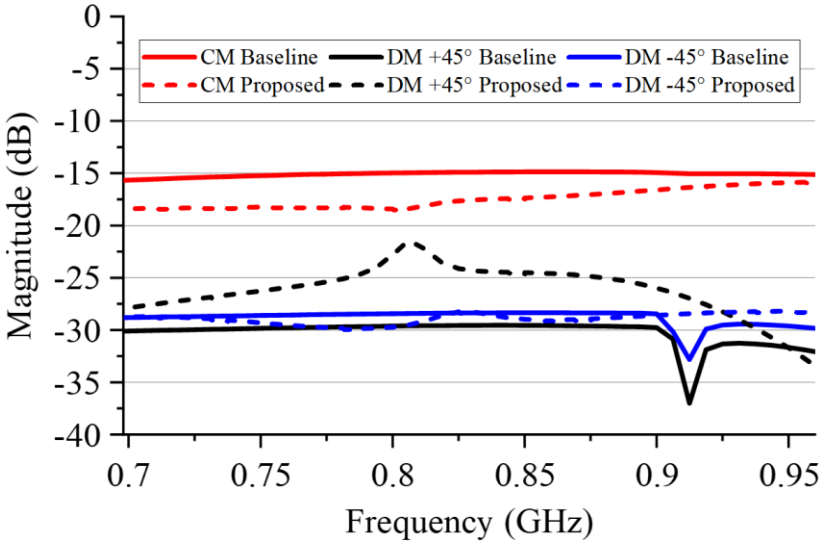

Figure 3-21: Insertion loss from CM and DM lumped ports to wave port of the magnetic field probe.

3.4.3 Discussion of Results

The simulation results demonstrate, via two different simulation techniques, that the radiated emissions resulting from the CM excitation of the proposed MB dipole are reduced relative to those of the baseline MB dipole. First, the radiation patterns of the proposed MB dipole were

presented, which exhibit a reduction in CM radiation over that of the baseline dipole. Then, a magnetic field probe was modeled to quantify the magnitude of the induced CM and DM currents as a function of frequency for both the baseline and proposed MB dipole. The use of a magnetic field probe eliminates the need to save the field values for each frequency, since the magnetic field probe transforms the magnetic flux linkage to an induced voltage in the probe. Both simulations demonstrate a reduction in CM effects from 698 MHz to 960 MHz. The peak improvement in CM suppression is seen to be near 800 MHz.

The segmentation of the MB balun feed stem, and subsequent capacitive coupling acts as a high-pass filter. It is for this reason that the effectiveness of this technique degrades with increasing frequency. The CM suppression has maximum improvement from 698 MHz to 800 MHz, corresponding to the frequency range which has the most severe degradation in radiation characteristics upon the introduction of the baseline MB radiator in Section 3.2.1.

Although the proposed MB dipole results in an increase in DM radiation, the relative magnitude of radiated emissions is significantly less than that of the dominant CM radiation. For example, the DM insertion loss increases from –29.6 dB to –21.4 dB, an 8.2 dB increase. In terms of magnitude, this is merely an increase from 0.001 to 0.007. As a comparison, the CM insertion loss of the baseline and proposed MB dipoles are –15.0 dB and –18.4 dB, respectively. This 3.4 dB improvement in CM suppression is a reduction in magnitude from 0.032 to 0.014. Therefore, it is expected that the benefit that the proposed technique provides, in CM rejection, will outweigh the degradation due to the increase in DM radiation when used in a UC environment.

3.5 Evaluation of the Proposed Mutual Coupling Reduction Technique

The purpose of this section is to present the simulated and measured results of the LB sub-arrays in the presence of the baseline and proposed MB dipole assemblies. Due to symmetry, only the LB radiation patterns of the +45° polarization are presented. To demonstrate the broadband and versatile nature of the proposed technique, the results of both UC 1 and UC 2 are presented.

UC 1 and UC 2 are simulated in the same array configurations as shown in Figure 2-1 and Figure 3-1, respectively. Alignment arrows are present on a silkscreen layer on the proposed vertical MB feed stems to aid in the alignment of PCBs L/R to PCBs 5–8, as shown for PCBs 5/6 in Figure 3-22. The simulation model and prototype of UC 2 are shown in Figure 3-23.

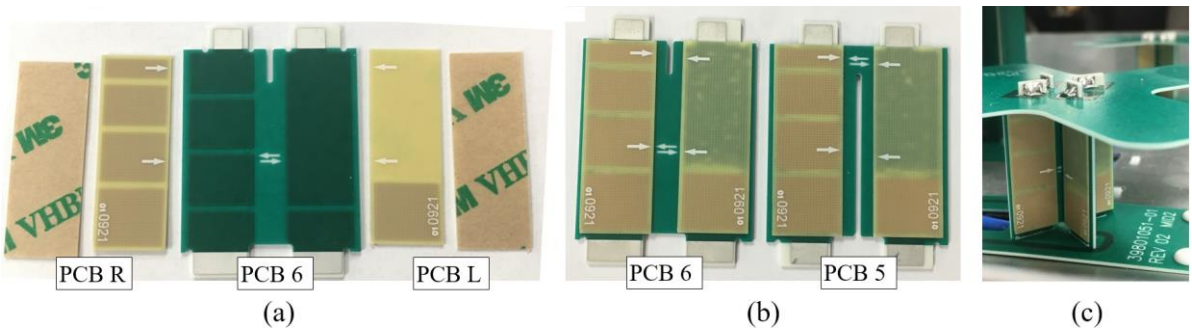

Figure 3-22: Proposed MB dipole feed stems (a) unbonded, (b) bonded, and (c) assembled.

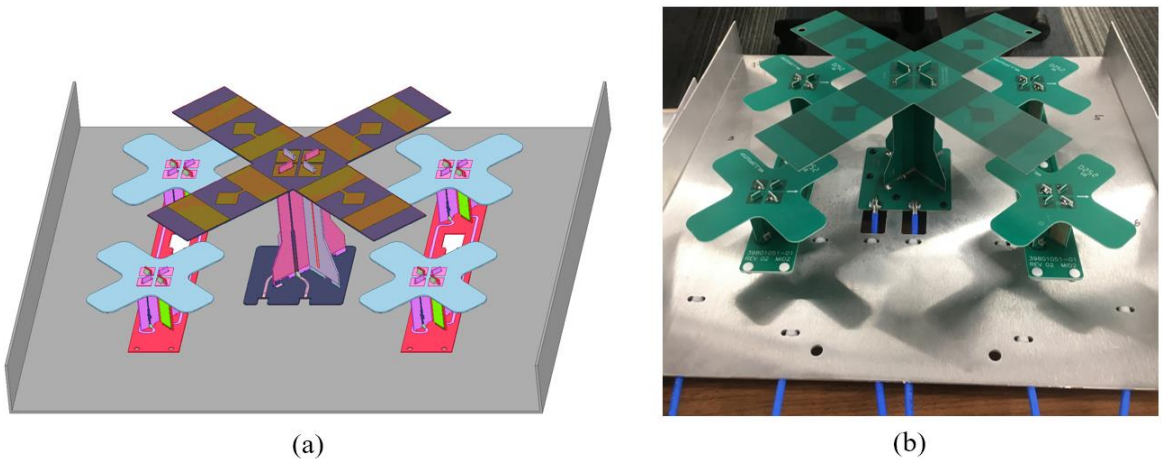

Figure 3-23: Proposed UC 2 (a) simulation model and (b) prototype.

3.5.1 UC 1 Results

Although the goal of the proposed design is to improve the LB radiation characteristics over those of the baseline design, it is important to maintain acceptable S-parameters in moving to the proposed design. Both the baseline and proposed return losses are better than 10 dB across the band, as shown in Figure 3-24(a). The simulated and measured S-parameters agree closely with each other. The worst-case measured LB return loss in the presence of the baseline/proposed MB dipole is 13.9/13.2 dB, as shown in Figure 3-24(a). The proposed LB intra-array cross-polar isolation improves from 698 MHz to 783 MHz, however it degrades slightly from 784 MHz to 887 MHz, as shown in Figure 3-24(b). The measured peak intra-array cross-polar isolation degrades slightly from –17.7 dB to –17.1 dB from the baseline UC to the proposed UC. Therefore, the proposed UC 1 maintains acceptable LB S-parameters in comparison to the baseline UC 1.

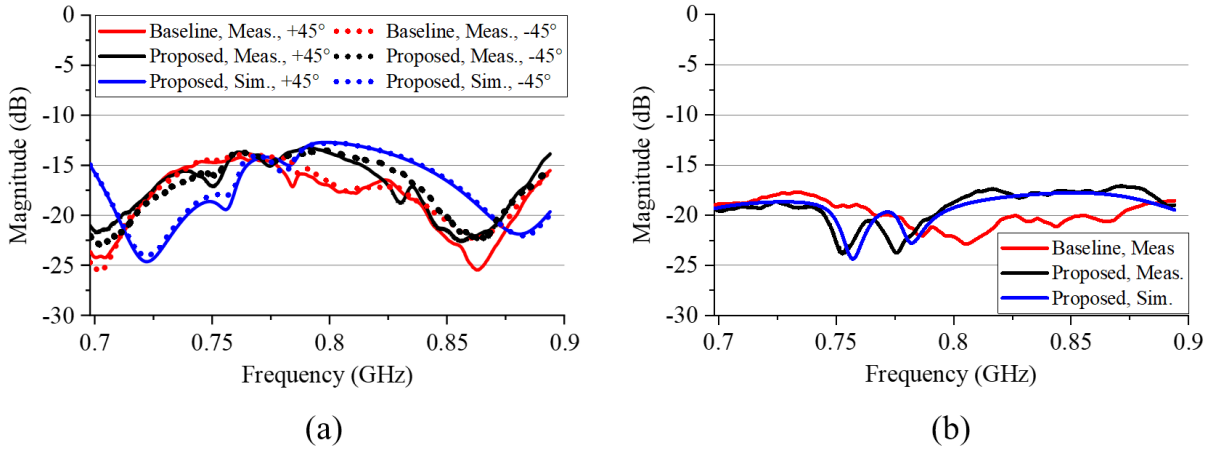

Figure 3-24: Simulated and measured (a) reflection coefficient for ±45° polarizations and (b) intra-array cross-polar isolation of the baseline and proposed LB dipole of UC 1.

The measured peak and average H-plane CPR, HPBW, and −10 HBW improve over most of the band in moving to the proposed UC, as shown in Table 3-5. The simulated and measured LB H-plane radiation patterns are shown for the +45° polarization in Figure 3-25. The peak/average CPR at 796 MHz improves from –8.6/−4.5 dB to –15.4/−9.9 dB in moving to the proposed UC, as

shown in Figure 3-25(c). The −10 dB HBW improves at 816 MHz, decreasing from 167° to 141° (15.6%) in moving from the baseline to the proposed UC, as shown in Figure 3-25(d).

The LB V-plane radiation patterns are shown for the +45° polarization in Figure 3-26. The VBW of the proposed UC deviates slightly from simulation to measurement; the measured results show better performance than the simulation. The proposed UC shows improvements in the −10 dB VBW at 796 MHz, for which it decrease from 165° to 142° (13.9%), as shown in Figure 3-26(c). The measured key performance parameters are tabulated for the V-plane in Table 3-5.

Although the −45° polarization radiation patterns are not shown, due to the mirror symmetry of the LB dipoles about the xz-plane in UC 1, the corresponding H-plane radiation patterns closely resemble the +45° H-plane patterns mirrored about the xz-plane. The V-plane radiation patterns of the −45° polarization of UC 1 match closely with those observed in the +45° polarization. This similarity in the +45° polarization and −45° polarization radiation patterns, while expected from symmetry, is also apparent in comparison of their similar gain characteristics.

Table 3-5: Comparison of measured key performance parameters for UC 1.

	H-Plane				V-Plane		Front-to-Back Ratio ±60° Sector (dB) Baseline/ Proposed
Frequency (MHz)	Peak CPR (dB) Baseline/ Proposed	Average CPR (dB) Baseline/ Proposed	HPBW (deg.) Baseline/ Proposed	–10 dB HBW (deg.) Baseline/ Proposed	HPBW (deg.) Baseline/ Proposed	–10 dB VBW (deg.) Baseline/ Proposed	
698	−15.5/−17.1	−21.4/−20.8	67/64	136/139	72/89	145/146	15.9/14.7
740	−16.1/−13.4	−19.1/−19.6	70/68	143/137	84/101	158/157	17.7/15.7
796	−8.6/−15.4	−14.5/−19.9	85/71	156/142	87/83	165/142	14.4/16.3
816	−10.4/−15.0	−14.5/−19.3	71/71	167/141	83/75	143/146	12.0/15.7
858	−11.7/−13.4	−15.9/−18.3	74/72	143/143	69/73	132/149	15.2/16.8
894	−11.3/−12.7	−16.4/−16.9	66/70	148/145	69/83	133/153	16.4/15.2
Worst-Case	−8.6/−12.7	−14.5/−16.9	85/72	167/145	87/101	165/157	12.0/14.7

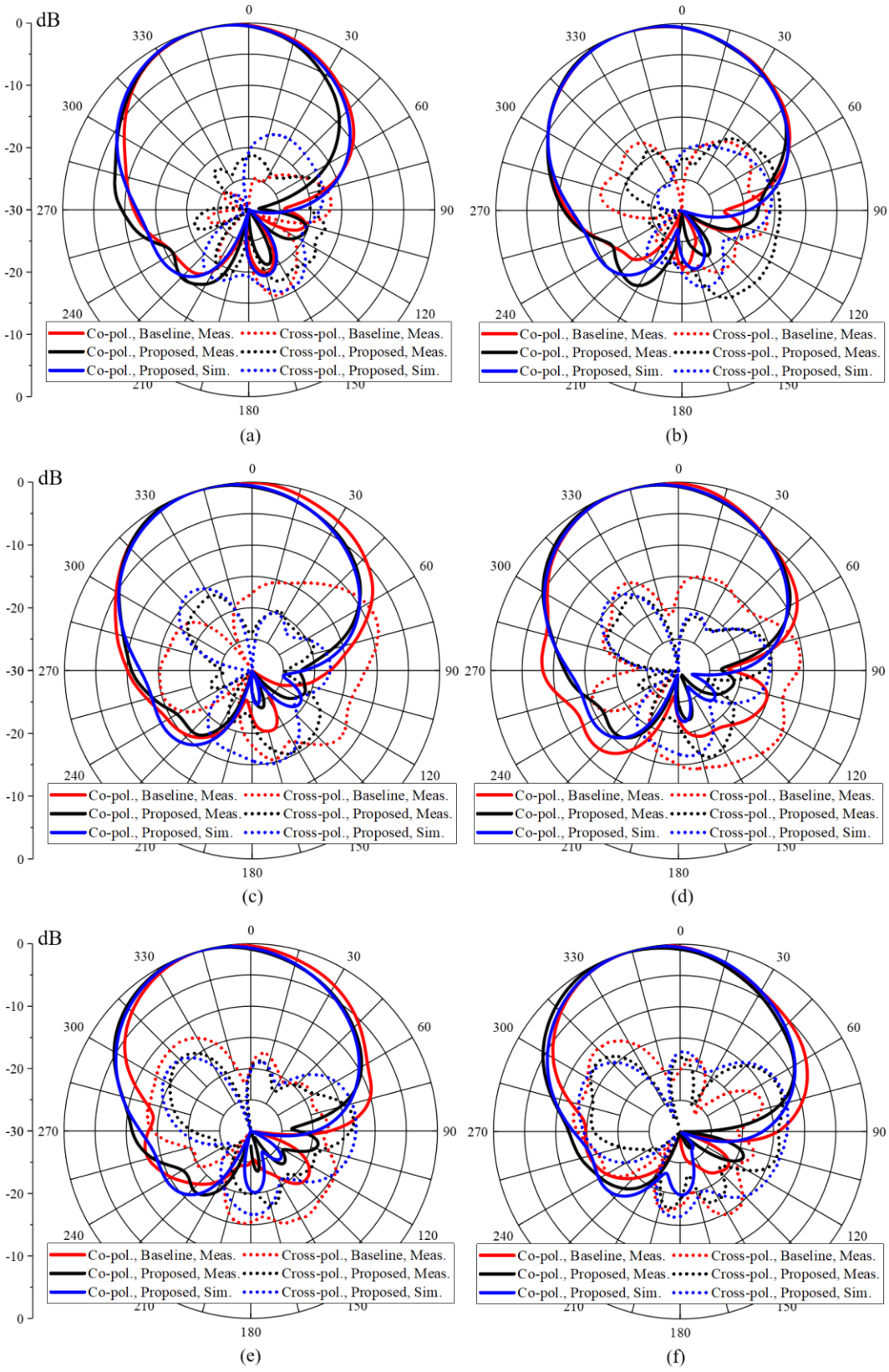

Figure 3-25: Simulated and measured +45° H-plane radiation patterns of UC 1 LB sub-array at (a) 698 MHz, (b) 740 MHz, (c) 796 MHz, (d) 816 MHz, (e) 858 MHz, and (f) 894 MHz.

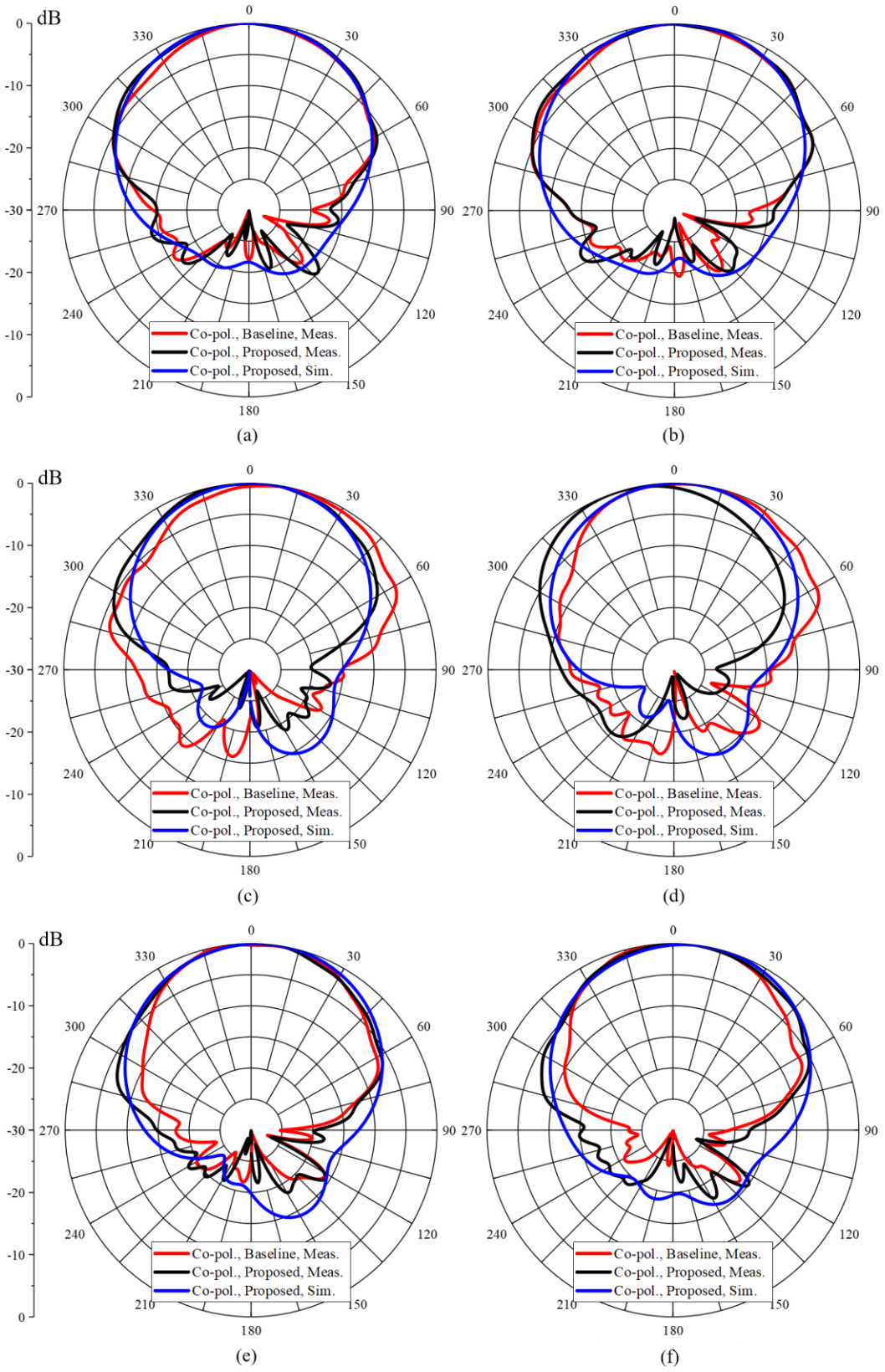

Figure 3-26: Simulated and measured +45° V-plane radiation patterns of UC 1 LB sub-array at (a) 698 MHz, (b) 740 MHz, (c) 796 MHz, (d) 816 MHz, (e) 858 MHz, and (f) 894 MHz.

The simulated and measured gains of the baseline and proposed UC 1 are shown in Figure 3-27 for both ±45° polarizations. The average measured gains of the baseline and proposed UCs are 6.85 dBi and 7.05 dBi, respectively, for +45° and 6.74 dBi and 7.02 dBi for –45° polarizations. Given that BSA designers often seek even 0.1 dB average gain improvements, these results are a welcome and meaningful improvement to the UC. The peak improvement occurs at 803 MHz for the –45° polarization, for which the proposed UC measures 7.20 dBi whereas the baseline UC measures only 5.74 dBi, a 1.46 dB improvement in moving to the proposed UC 1.

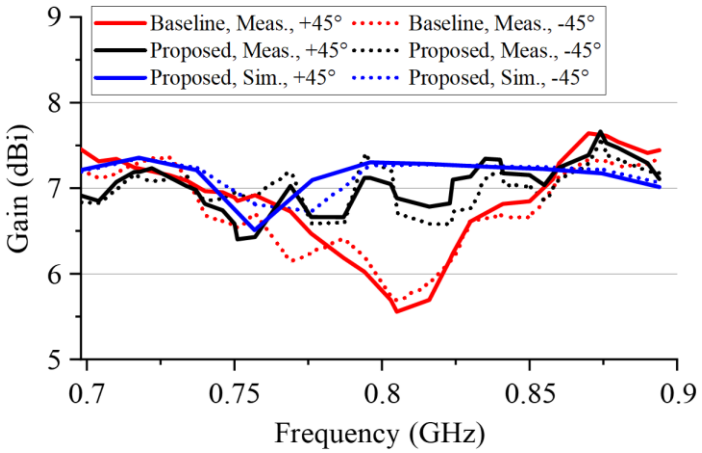

Figure 3-27: Simulated and measured peak LB system gain of UC 1.

3.5.2 UC 2 Results

The performance of the baseline and proposed S-parameters is shown in Figure 3-28(a). The baseline and proposed return losses are better than 10 dB across the band. The worst-case measured LB return loss in the presence of the baseline/proposed MB dipole is 13.3/14.3 dB. The proposed intra-array cross-polar isolation degrades, with the peak isolation degrading from –25.5 dB to −17.3 dB in moving to the proposed UC. Despite the degradation in isolation, the proposed UC 2 has acceptable LB S-parameters for consideration of the LB radiation patterns.

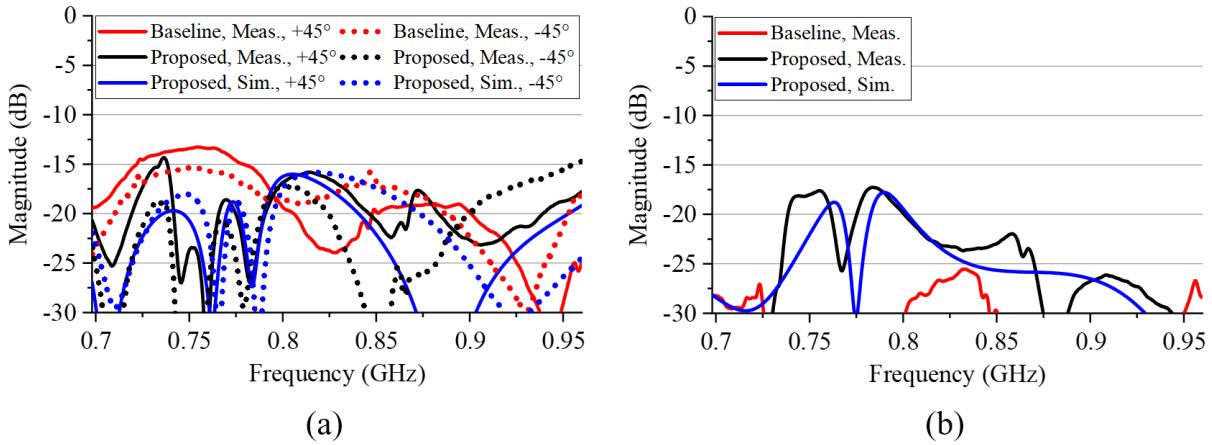

Figure 3-28: Simulated and measured (a) reflection coefficient for ±45° polarizations and (b) intra-array cross-polar isolation of the baseline and proposed LB dipole of UC 2.

The undesirable variation in the H-plane HPBW and –10 dB HBW present in the baseline UC are drastically reduced in moving to the proposed UC, as shown for the HPBW in Figure 3-29 and is summarized across the operating band in Table 3-6. The measured HPBW varies from 59° to 146° across the band in the baseline UC and from 65° to 93° using the proposed MB assemblies. The corresponding simulated and measured LB H-plane radiation patterns are shown for the +45° polarization in Figure 3-30. There are also drastic improvements in peak and average CPR in the presence of the proposed MB assemblies across most of the operating band. For example, the peak CPR at 698 MHz improves from –15.4 dB to –21.3 dB, as shown in Figure 3-30(a). At 777 MHz the peak CPR improves from –10.7 dB to –16.1 dB, whereas at 805 MHz and 829 MHz the improvement is from –7.7 dB to –13.9 dB and from –6.7 dB to −15.9 dB, respectively. The –10 dB HBW also shows significant improvements in magnitude and stability across the band. For example, at 805 MHz and 829 MHz the –10 dB HBW reduces from 242° to 155° (36.0%) and from 225° to 164° (27.1%), respectively, as is observable from Figure 3-30(c) and Figure 3-30(d), respectively. Furthermore, the average front-to-back ratio improves greatly across the band in

moving to the proposed MB assemblies. The improvements are summarized across the band in Table 3-6.

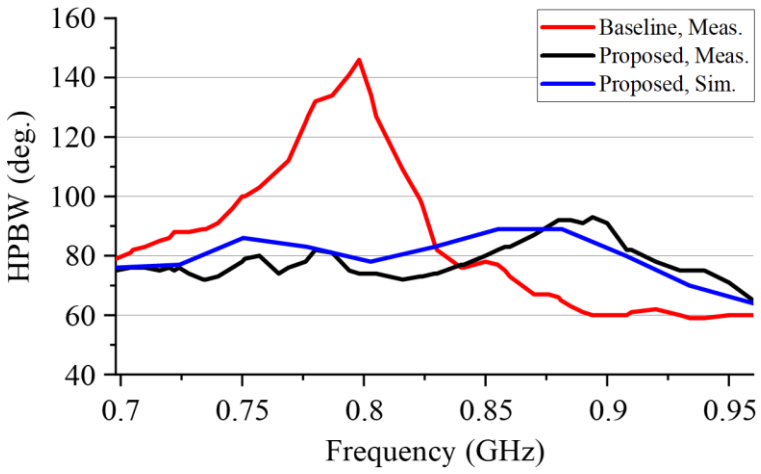

Figure 3-29: Simulated and measured +45° H-plane HPBW.

Table 3-6: Comparison of measured key performance parameters for UC 2.

	H-Plane				V-Plane		Front-to-Back Ratio ±60° Sector (dB) Baseline/ Proposed
Frequency (MHz)	Peak CPR (dB) Baseline/ Proposed	Average CPR (dB) Baseline/ Proposed	HPBW (deg.) Baseline/ Proposed	–10 dB HBW (deg.) Baseline/ Proposed	HPBW (deg.) Baseline/ Proposed	–10 dB VBW (deg.) Baseline/ Proposed	
698	−15.4/−21.3	−20.7/−26.8	88/76	161/149	87/78	146/139	18.0/20.9
777	−10.7/−16.1	−14.9/−18.9	118/79	221/159	128/98	169/150	10.1/14.2
805	−7.7/−13.9	−10.7/−21.5	174/77	242/155	128/67	181/131	11.1/16.9
829	−6.7/−15.9	−11.4/−23.9	86/75	225/164	106/73	182/141	10.9/17.9
881	−12.6/−16.5	−15.8/−19.8	72/98	132/172	63/90	133/154	16.0/14
960	−15.5/−15.0	−18.9/−17.2	59/68	114/144	60/73	126/148	20.0/17.1
Worst-Case	−6.7/−13.9	−10.7/−17.2	174/98	242/172	128/98	182/154	10.1/14.0

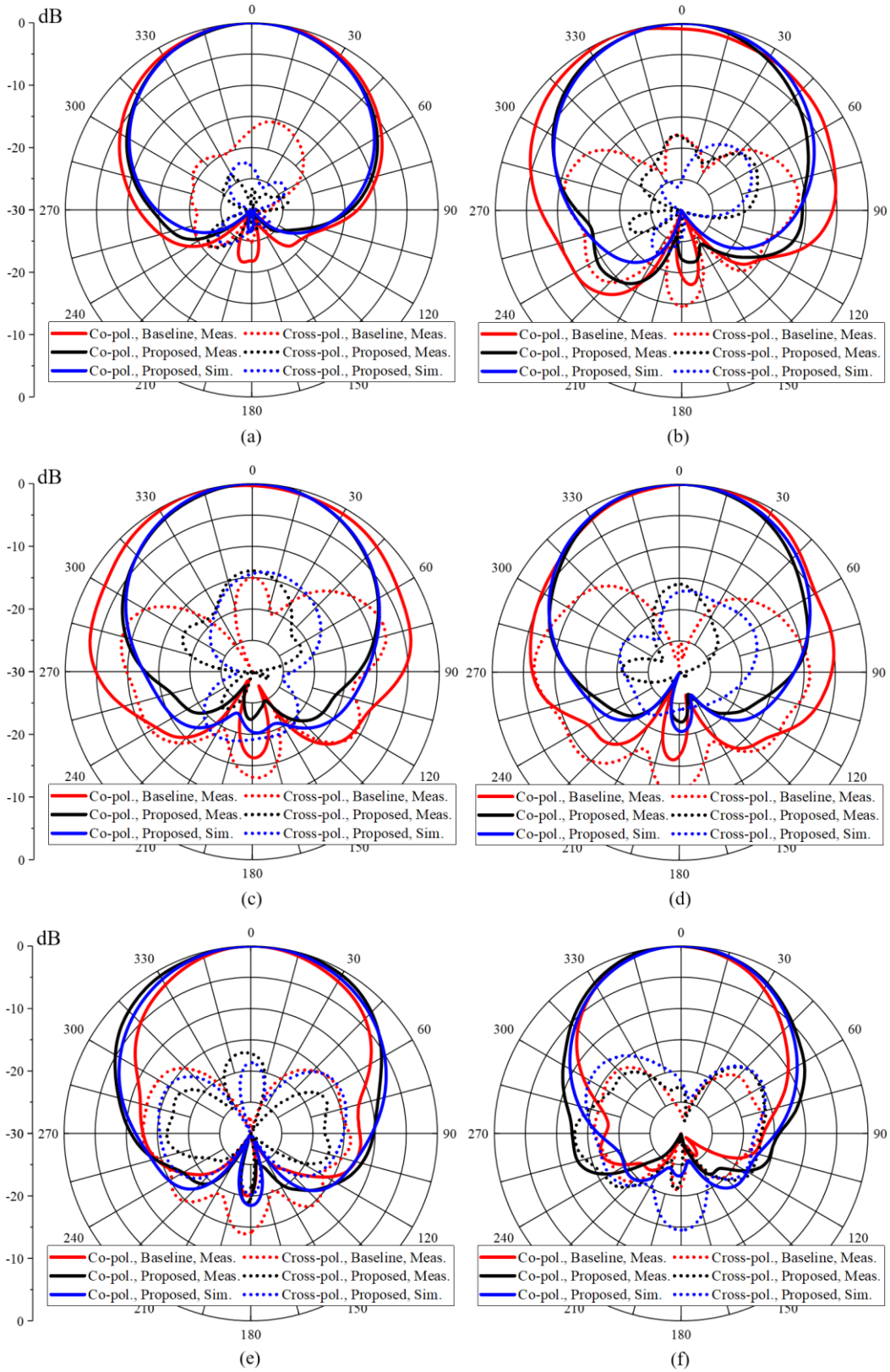

Figure 3-30: Simulated and measured +45° H-plane radiation patterns of UC 2 LB sub-array at (a) 698 MHz, (b) 777 MHz, (c) 805 MHz, (d) 829 MHz, (e) 881 MHz, and (f) 960 MHz.

The LB V-plane radiation patterns are shown for the +45° polarization in Figure 3-31. The V-plane radiation patterns in both simulation and measurement show improvement in HPBW and −10 dB VBW stability over frequency as compared to the baseline UC, as is summarized for the measured UC in Table 3-6. The peak –10 dB VBW at 805 MHz improves, decreasing from 181° to 131° (27.6%), as shown in Figure 3-31(c). The V-plane HPBW spanned 69° from 59° to 128° in the baseline UC, spanning 25° from 73° to 98° in the proposed UC. Therefore, the stabilization of the V-plane HPBW is similar to the stability improvement observed in the H-plane HPBW.

The simulated and measured gains of the baseline and proposed UC 2 are shown in Figure 3-32 for both ±45° polarizations. Both the simulated and measured LB gains of the proposed UC 2 agree well and exhibit stabilized gain across the band. The average measured gains of the baseline/proposed UCs are 6.22 dBi/6.57 dBi for the +45° polarizations and 6.36 dBi/6.61 dBi for –45° polarizations. These results are a meaningful improvement to the UC for use as part of a larger BSA. The peak improvement occurs at 805 MHz for the +45° polarization, for which the proposed UC measures 6.92 dBi, with the baseline UC measuring only 4.33 dBi, a 2.59 dB peak gain improvement upon implementation of the proposed MB dipole assembly in place of baseline MB dipole assembly. Although the gain of the baseline UC exceeds that of the proposed UC for frequencies above 858 MHz, it is at the expense of the H-plane and V-plane HBW stability.

The narrowing of the HBW in the baseline UC for frequencies above 858 MHz, as shown for the H-plane HPBW in Figure 3-29, increases the baseline directivity, and thus the peak system gain. However, this variation in the HBW will lead to angular coverage which varies drastically with frequency, were the baseline UC to be used as part of a BSA. Whereas the proposed design realizes a stable HBW, and thus gain across the band, which will provide more uniform angular coverage across the band if the proposed UC were used as part of a BSA.

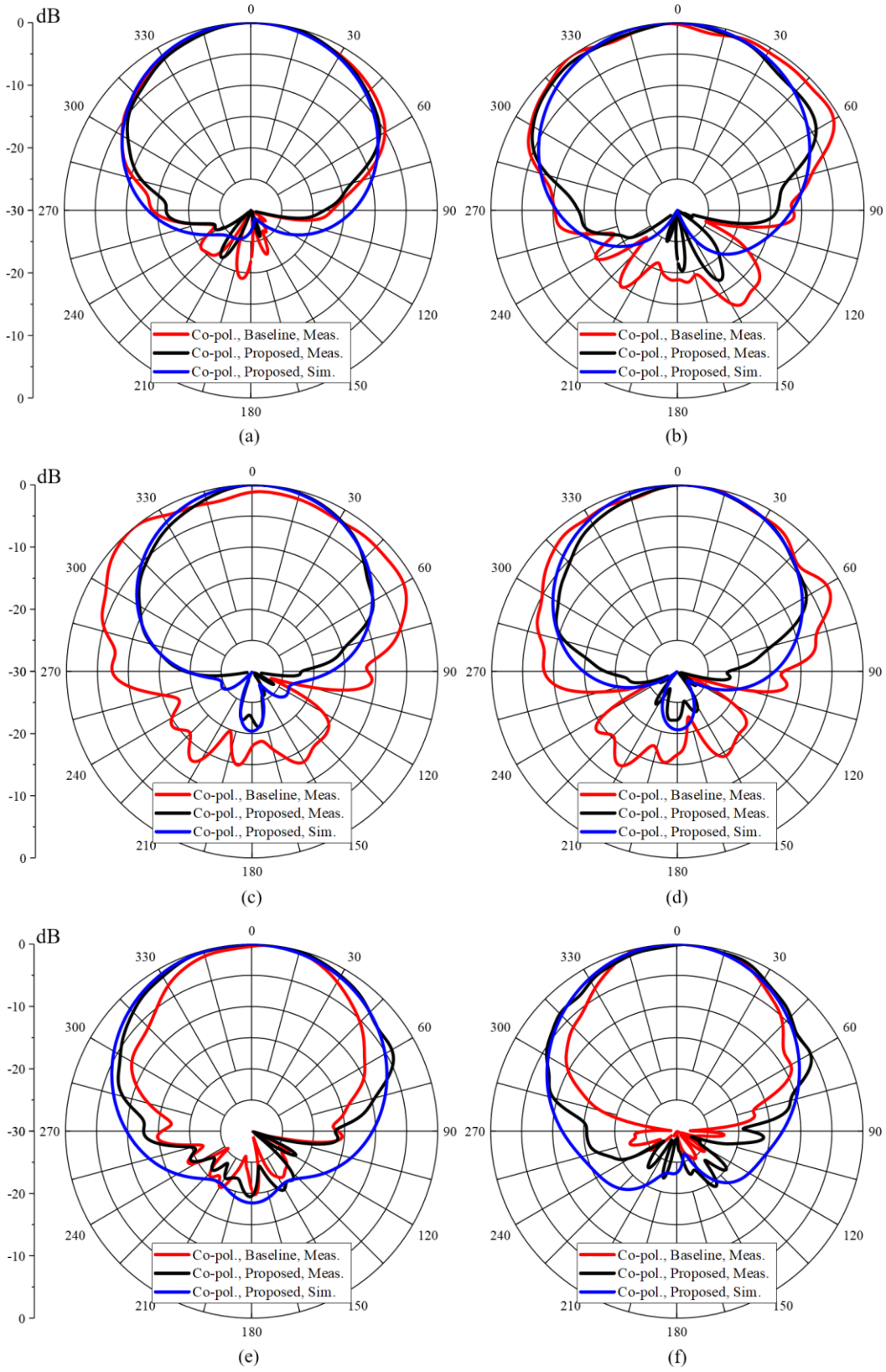

Figure 3-31: Simulated and measured +45° V-plane radiation patterns of UC 2 LB sub-array at (a) 698 MHz, (b) 777 MHz, (c) 805 MHz, (d) 829 MHz, (e) 881 MHz, and (f) 960 MHz.

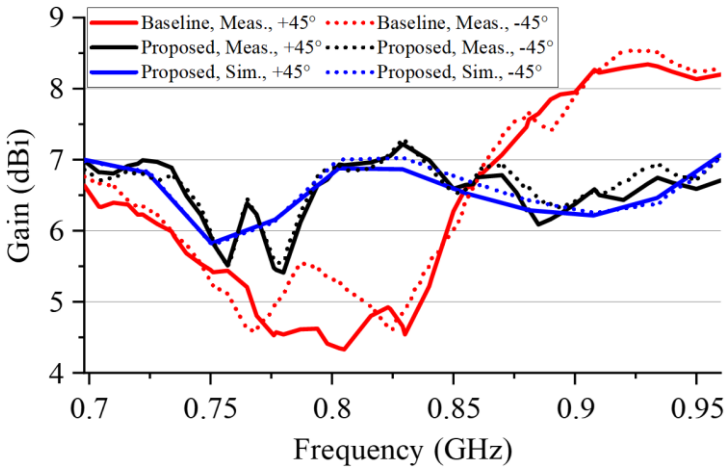

Figure 3-32: Simulated and measured peak system gain of the LB dipole of UC 2.

3.5.3 Discussion of the Performances of the Proposed UCs

Both UC 1 and UC 2 demonstrate significant improvements in the LB radiation characteristics upon the implementation of the proposed CM suppression technique. The peak radiation pattern improvements were predicted in Section 3.4 to be expected near 800 MHz, which is precisely where the proposed UCs exhibit the most significant radiation pattern improvements.

It is expected that the improvements present in the CPR, of the proposed H-plane radiation patterns, will improve the polarization diversity of a BSA if either of the proposed UCs are used as part of a larger BSA array. The reduction in the proposed H-plane HPBW and –10 dB HBW over those of the baseline UC will help to reduce inter-cell interference if used as part of a larger BSA array. The reduction in HBW directs the radiated energy into the desired angular region along the horizon, greatly reducing the radiated emissions which would otherwise occur outside of this angular region. Furthermore, the stabilization of the HBW across frequency would result in a more uniform cellular coverage area across the band, if the proposed UC were to be used in a BSA. The reduction in the VBW reduces the amount of radiation which is otherwise inaccessible to the user due to the radiation being directed above the horizon. The suppression of radiation in the sector

opposite of boresight in the proposed UC 2 is particularly drastic and would prevent the array from causing undesirable inter-cell interference to sectors serviced by neighboring BSAs. This improvement in the front-to-back ratio also increases the overall directivity of the antenna, which thereby increases the realizable cell radius for a fixed receiver sensitivity by increasing the signal strength available to a receiver at a fixed distance from the BSA.

These improvements lead to an increase in the average system gain across the band for both UCs. As was mentioned at the end of Section 3.5.2, the reason that the gain of the proposed UC 2 is lower than the baseline UC 2 for frequencies above 858 MHz is due to the narrow HBWs and VBWs of the baseline UC at those frequencies. Although gain is an important parameter, the gain cannot be maximized at the expense of other key performance parameters, such as HBW and VBW stability. The proposed UCs help to stabilize the HBW and VBW, thereby stabilizing the directivity and gain. Stable HBWs and VBWs ensure uniform spatial cellular coverage across the band.

The most significant improvements are observed near the center of the band. This finding is consistent with the results of Section 3.4.2. For example, from Figure 3-21 it is expected that the proposed technique offers the most suppression of CM currents at 800 MHz, which is where both proposed UCs exhibit the greatest improvements in radiation characteristics.

The biggest downfall of the proposed technique is the impact on the intra-array cross-polar isolation of the LB dipoles in UC 2. However, there are a number of existing techniques which have been discussed in Chapter 1 which can be used to improve isolation. Therefore, if either of these UCs is used as part of a larger BSA it may be desirable to include parasitic fences and/or parasitic dipole elements to improve the intra-array cross-polar isolation of the LB array.

3.6 Summary

In this chapter a versatile technique for reducing the mutual coupling between the LB and MB sub-arrays is proposed and verified through simulation and prototype measurements of two distinct UCs. The main contributor to the mutual coupling is identified as the baseline vertical MB dipole feed stems. Upon the excitation of the LB dipoles, strong CM currents are induced on the baseline vertical MB dipole feed stems. These CM currents radiate as electrically short monopoles over a conducting ground plane. It is shown that by introducing series capacitance into the vertical MB dipole feed stems, the CM currents can be reduced significantly. This reduction in CM current is shown though simulation to suppress the magnitude of undesirable CM radiated emissions.

Although the proposed technique does not completely eliminate the inter-array mutual coupling, significant improvements across several key performance parameters are realized in both UC 1 and UC 2. The H-plane and V-plane key performance parameters for the baseline and proposed UC 1, shown in Table 3-5, show the proposed UC exhibits improvements in peak CPR, average CPR, HPBW, and −10 dB HBW over most of the operating band. The improvements in the V-plane HPBW, −10 dB VBW, and front-to-back ratio are confined to the center of the LB operating band. The H-plane and V-plane key performance parameters for the baseline and proposed UC 2, shown in Table 3-6, show the proposed UC exhibits improvements in peak CPR, average CPR, HPBW, −10 dB HBW, V-plane HPBW, −10 dB VBW, and front-to-back ratio over most of the operating band. These improvements along with the gain improvements of the proposed LB sub-arrays are expected to lead to overall pattern performance improvements if the UCs are used as part of a larger BSA array, such as those shown in Figure 1-7 and Figure 1-8. The improvements in the LB radiation characteristics upon introduction of the proposed MB dipoles show promise for use of the proposed technique in a BSA array, as is verified in Chapter 4.

Chapter 4

A Dual-Band Base Station Antenna Array with Mutual Coupling Reduction

This chapter focuses on an application of the mutual coupling reduction techniques developed in Chapter 2 and Chapter 3 to a 6-foot-long base station antenna (BSA). This chapter validates that when the two design techniques are used simultaneously in a BSA the improvements predicted in Chapter 2 and Chapter 3 are significant enough to lead to system level improvements in the BSA. The array architecture chosen for the application of the proposed techniques is that of Figure 1-8 of Chapter 1. From the results of Chapter 2 and Chapter 3, it is expected that the serially loaded capacitive low-band (LB) dipole and capacitively loaded mid-band (MB) dipole feed stems will improve the MB and LB radiation characteristics, respectively, over those of the baseline BSA. The peak magnitudes of the S-parameters are expected to be similar in moving from the baseline to the proposed BSA. However, validation is necessary due to the fact that Chapter 2 and Chapter 3 only consider one of the two unit cells (UCs) which comprise the chosen BSA architecture of Figure 1-8. Furthermore, although Chapter 3 presents the improvement of the proposed LB dipole of Chapter 2 in the presence of the proposed MB sub-arrays, the performance of the serially loaded proposed MB sub-arrays has not yet been presented. New observations in the array environment beyond those predicted in previous chapters are discussed, along with implications of the results to the BSA system performance.

The 3-D models used to simulate the arrays are shown for the baseline and proposed BSAs in Figure 4-1(a) and Figure 4-1(b), respectively. The element-to-element spacing and reflector dimensions, as labeled in Figure 4-1, are tabulated in Table 4-1. The spacing and reflector dimensions are the same for both the baseline and prototype designs. The measured baseline BSA prototype is shown in Figure 4-2. The eight white plastic arches shown in Figure 4-2 are radome

supports as well as LB dipole arm stabilizers. If the radome supports are removed prior to measurement, the movement of the antenna within the anechoic chamber during test may lead to vibrations in the LB dipoles which could affect the measurement results. The radome supports have been included in the measurements to prevent these vibrations. Although the radome supports are not included in the simulations, it is expected that due to the low dielectric constant of the radome support material, their presence will have a negligible impact on the measurements as compared to the simulations.

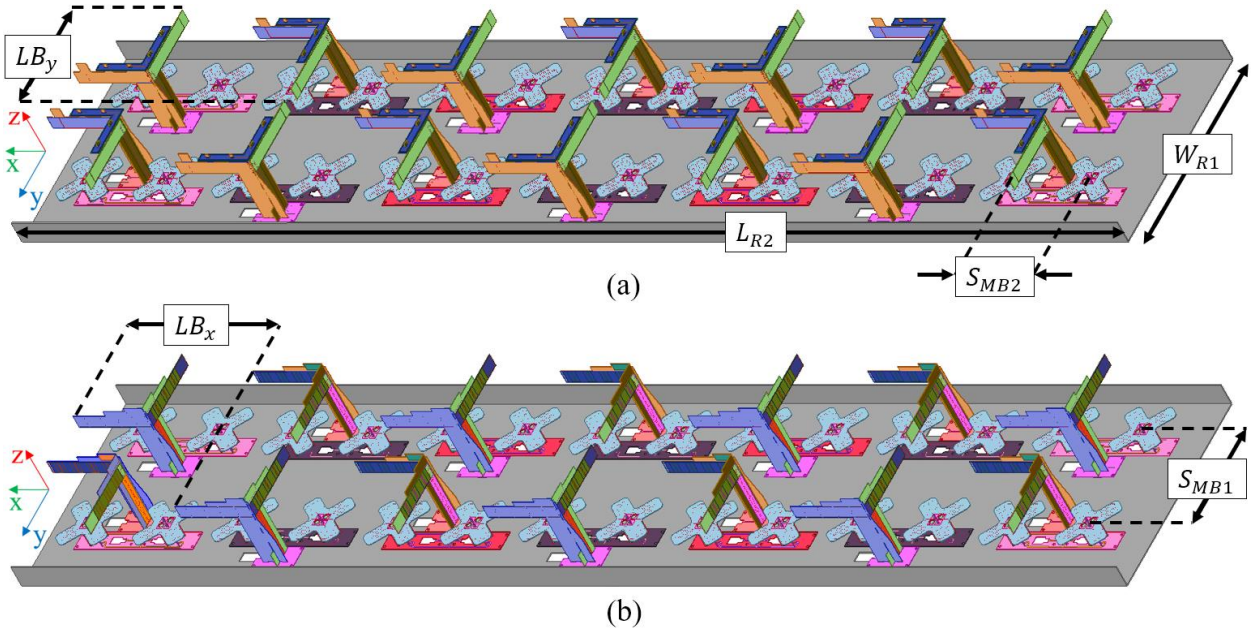

Figure 4-1: 3-D ANSYS HFSS models designed for full-wave electromagnetic simulation of the (a) baseline and (b) proposed BSAs.

Table 4-1: Dimensions of the BSA array layout. All units are in inches.

W_{R1}	LB_x	LB_y	L_{R2}	S_{MB1}	S_{MB2}
13.000	9.600	6.499	69.000	6.727	4.800

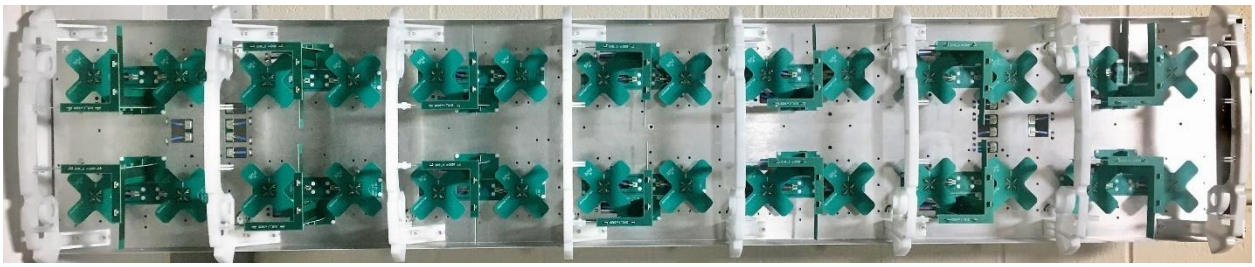

Figure 4-2: Prototype of the baseline BSA.

The baseline HFSS models are solved on a compute node consisting of 768 GB of physical memory (RAM) and two Intel Xeon Gold 6234 CPUs operating at 3.30 GHz, with a total of 16 logical processor cores. The proposed HFSS models are solved on a compute node consisting of 512 GB of RAM and two Intel Xeon E7-4890 v2 CPUs operating at 2.80 GHz, with a total of 30 logical processor cores. Due to the tight coupling and multilayer conductor approach in the proposed MB dipole feed stems and proposed LB dipoles, the initial LB mesh of the proposed BSA model takes nearly 45.9 hours, the adaptive mesh 9.1 hours, the discrete frequency sweep 24.7 hours, and the interpolated frequency sweep 10.8 hours, totaling 90.5 hours of simulation for this single model over a single operating band. The convergence criteria for the adaptive mesh is set to have a maximum change in S-parameters of 2% between consecutive meshes. This results in 6,834,060 unknowns to be solved for the proposed LB BSA simulation. Stricter convergence criteria would further increase solve time and RAM usage.

In order to reduce the cost of prototype materials and to ensure that the same losses are present in both the baseline and proposed measurements, a single prototype was built. Since the baseline and proposed dipoles have the same locations, the corresponding baseline/proposed printed circuit boards (PCBs) were swapped out/in prior to testing. Due to the symmetry of the BSAs it is sufficient to measure one LB polarization and one MB column. The LB and MB antenna arrays are fed using a combination of PCB phase shifters, power dividers, coaxial cables, and 4.3-10 input

connectors to set the amplitude and phase taper across each array. The details of the feed network are omitted from this work, as they are not an integral aspect of the proposed design techniques and are kept common throughout the simulations and measurements.

4.1 Evaluation of the LB Performance

First, the LB S-parameters of the BSAs are measured to ensure that the inclusion of the phase shifters, power dividers, and coaxial cables necessary for feeding the array do not significantly degrade the active scan impedance of the array. The simulated and measured S-parameters agree well with each other. Given the number of components in the BSA system and a convergence criterion of 2% (as compared to the more common industry standard of 0.2%), some differences are expected between simulation and measurement. The measured worst-case LB return loss degrades slightly from the baseline to the proposed BSA, decreasing from 13.4 dB to 12.9 dB, respectively, as shown in Figure 4-3(a). However, both return losses exceed the 10 dB bandwidth targeted in simulation. The improvement in measurement over simulation for the proposed design is likely due to losses present in the prototype which are not fully captured in simulation. Overall, the system return losses of both the baseline and proposed BSAs are acceptable for validation of the radiation pattern improvements expected in moving to the proposed BSA design.

The measured LB cross-polar isolation improves significantly across most of the band in moving to the proposed design, as shown in Figure 4-3(b). Both the simulated and measured baseline cross-polar isolation exhibit a sharp discontinuity just before 800 MHz. The measured worst-case LB cross-polar isolation for the baseline/proposed BSA is −16.3 dB/−26.0 dB. The maximum improvement in the measured LB cross-polar isolation occurs at 792 MHz for which

the baseline and proposed isolations are −16.3 dB and −37.4 dB, respectively. This improvement in cross-polar isolation is not predictable from the results of UC 1 in Section 3.5.1 but is predicted in the baseline array simulation. These results are discussed in detail in Section 4.3.

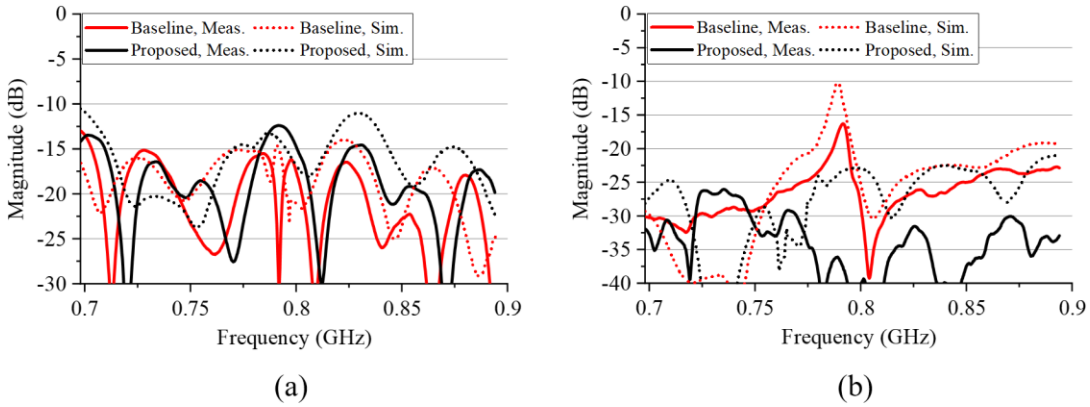

Figure 4-3: Simulated and measured LB (a) reflection coefficient and (b) cross-polar isolation of the baseline and proposed BSAs for the +45° polarization.

The LB H-plane (yz-plane) radiation patterns are shown for the +45° polarization in Figure 4-4. Although the measured cross-polar radiation (CPR) becomes slightly higher at 698 MHz for the proposed design, the CPR improves from 796 MHz to 894 MHz. For example, the measured peak CPR for the +45° polarization at 796 MHz and 894 MHz improves from −16.3 dB to −19.3 dB and from −12.7 dB to −18.0 dB, respectively, upon implementation of the proposed techniques. The relatively higher CPR in the baseline design is predictable from the UC 1 results of Section 3.5.1 due to the strong CM currents present in the baseline MB dipole feed stems at these frequencies. Furthermore, the front-to-back ratio over a ±60° sector increases significantly at 796 MHz in the proposed design. For example, the measured front-to-back ratio over a ±60° sector improves at 796 MHz from 18.1 dB to 23.7 dB for the +45° polarization, as shown in Figure 4-4(f). This improvement in the front-to-back ratio is predicted through simulation, as shown in Figure 4-4(e).

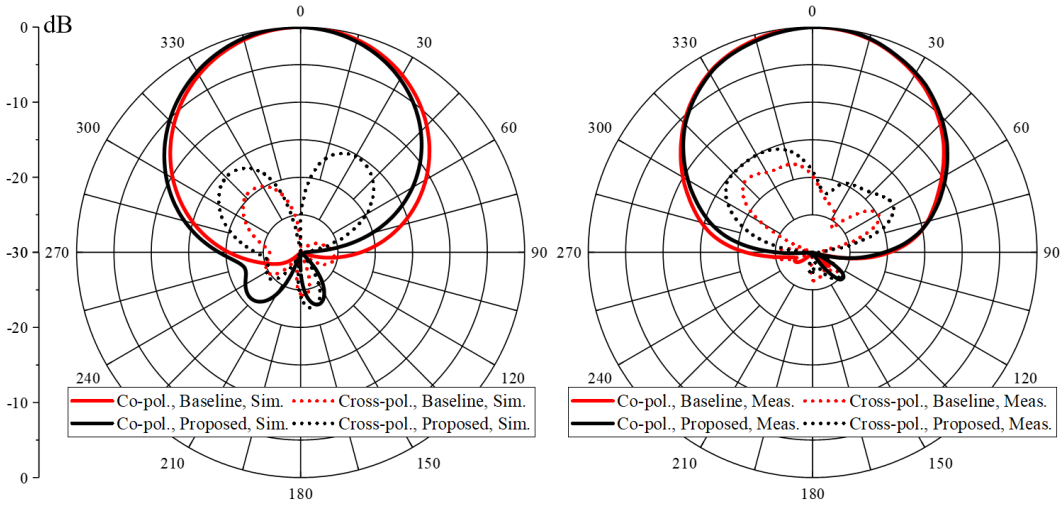
dB
0
-10
-20
-30
-20
-10
0
30
60
90
120
150
180
210
240
270
300
330
Co-pol., Baseline, Sim.
Cross-pol., Baseline, Sim.
Co-pol., Proposed, Sim.
Cross-pol., Proposed, Sim.

(a)

0
30
60
90
120
150
180
210
240
270
300
330
Co-pol., Baseline, Meas.
Cross-pol., Baseline, Meas.
Co-pol., Proposed, Meas.
Cross-pol., Proposed, Meas.

(b)

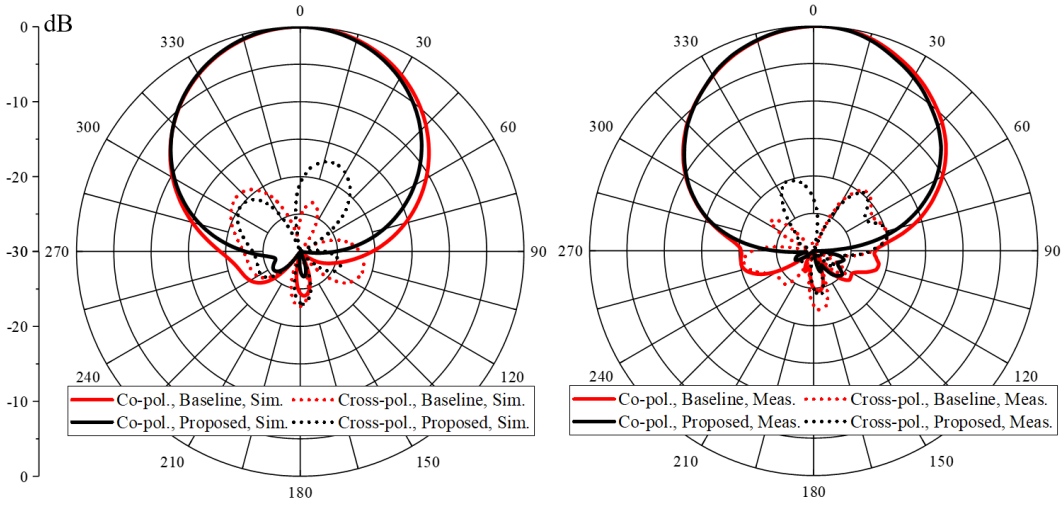
dB
0
-10
-20
-30
-20
-10
0
30
60
90
120
150
180
210
240
270
300
330
Co-pol., Baseline, Sim.
Cross-pol., Baseline, Sim.
Co-pol., Proposed, Sim.
Cross-pol., Proposed, Sim.

(c)

0
30
60
90
120
150
180
210
240
270
300
330
Co-pol., Baseline, Meas.
Cross-pol., Baseline, Meas.
Co-pol., Proposed, Meas.
Cross-pol., Proposed, Meas.

(d)

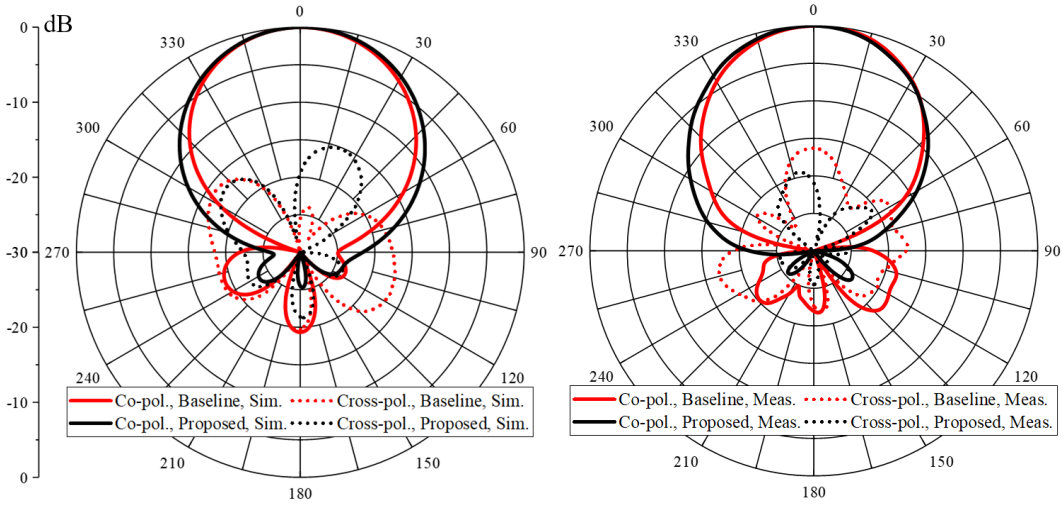
dB
0
-10
-20
-30
-20
-10
0
30
60
90
120
150
180
210
240
270
300
330
Co-pol., Baseline, Sim.
Cross-pol., Baseline, Sim.
Co-pol., Proposed, Sim.
Cross-pol., Proposed, Sim.

(e)

0
30
60
90
120
150
180
210
240
270
300
330
Co-pol., Baseline, Meas.
Cross-pol., Baseline, Meas.
Co-pol., Proposed, Meas.
Cross-pol., Proposed, Meas.

(f)

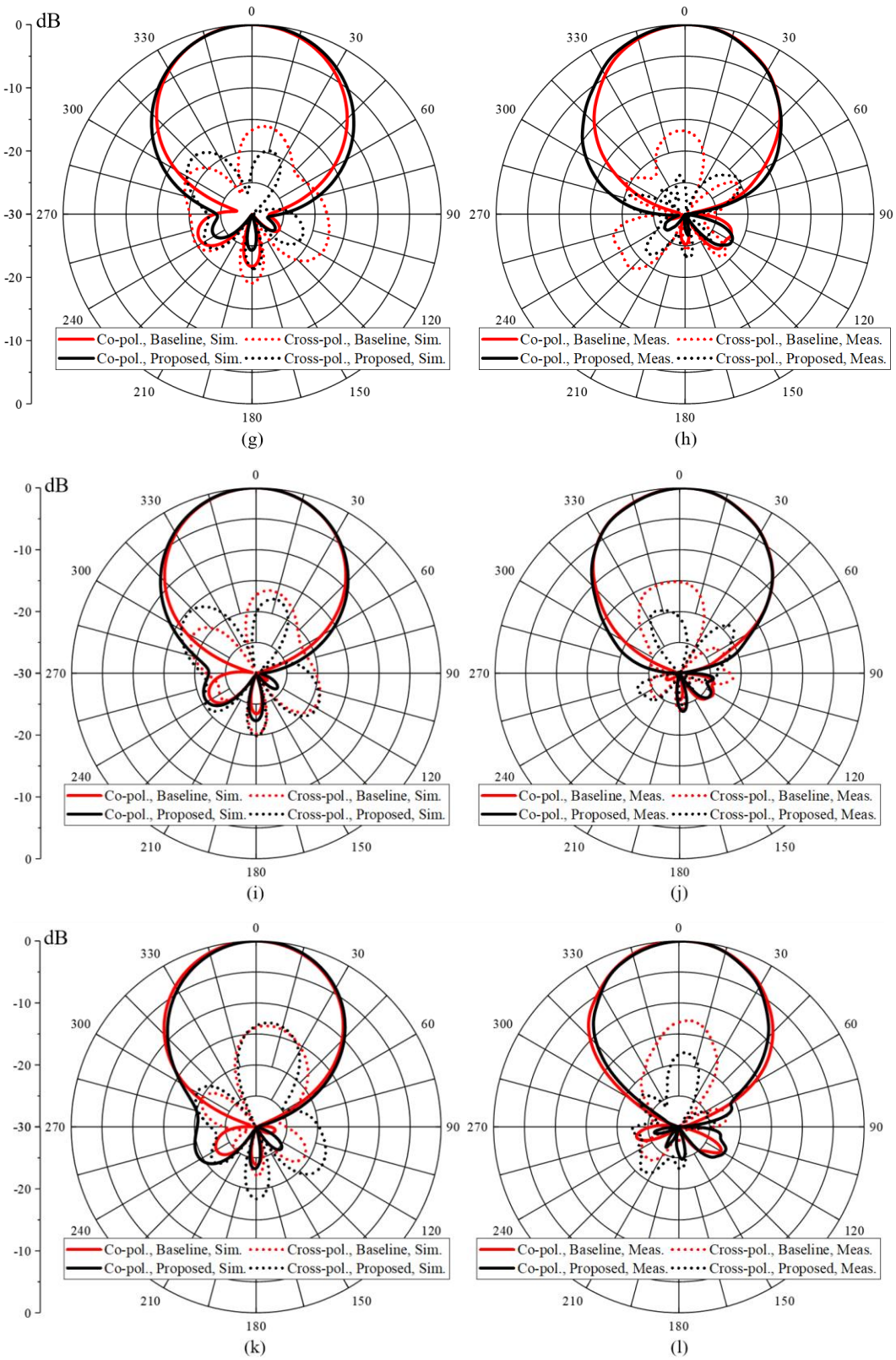

Figure 4-4: Simulated/measured +45° H-plane radiation patterns of the LB array at (a)/(b) 698 MHz, (c)/(d) 740 MHz, (e)/(f) 796 MHz, (g)/(h) 816 MHz, (i)/(j) 858 MHz, and (k)/(l) 894 MHz.

The LB V-plane (xz-plane) radiation patterns are shown for the +45° polarization in Figure 4-5. While the V-plane radiation characteristics are similar across most of the LB frequency range for the baseline and proposed BSAs, the performance of the proposed BSA improves at 796 MHz in both simulation and measurement, as shown in Figure 4-5(e) and Figure 4-5(f), respectively. This is the same frequency at which the baseline cross-polar isolation exhibits a sharp discontinuity, and at which the H-plane radiation pattern exhibits the most degradation in the baseline design. For the +45° polarization, the measured peak upper side lobe level (PUSLL) at 796 MHz improves from −12.8 dB to −18.3 dB in moving from the baseline to the proposed BSA. This improvement is predictable from the UC 1 results of Section 3.5.1 due to the strong CM currents present in the baseline UC at this frequency, which are suppressed in the proposed design.

The simulated and measured LB gains of the baseline and proposed BSAs are shown in Figure 4-6(a) for the +45° polarization. The severe reduction in the baseline gain which occurs at 796 MHz is eliminated in the proposed BSA. For example, the measured peak LB gain at 796 MHz for the +45° polarization improves from 12.0 dBi to 13.2 dBi in moving to the proposed BSA design, a 1.2 dB improvement. This improvement is predictable from the UC 1 results of Section 3.5.1 due to the strong CM currents present in the baseline UC at this frequency, which are suppressed in the proposed design; however, the improvement is even more drastic in the array environment. The shape of the simulated and measured gain curves are similar; however, the simulated gains are slightly higher than the measured gains. These differences are likely a combination of the inexact simulated losses in the components which make up the LB array feed network, manufacturing tolerances, and measurement accuracy.

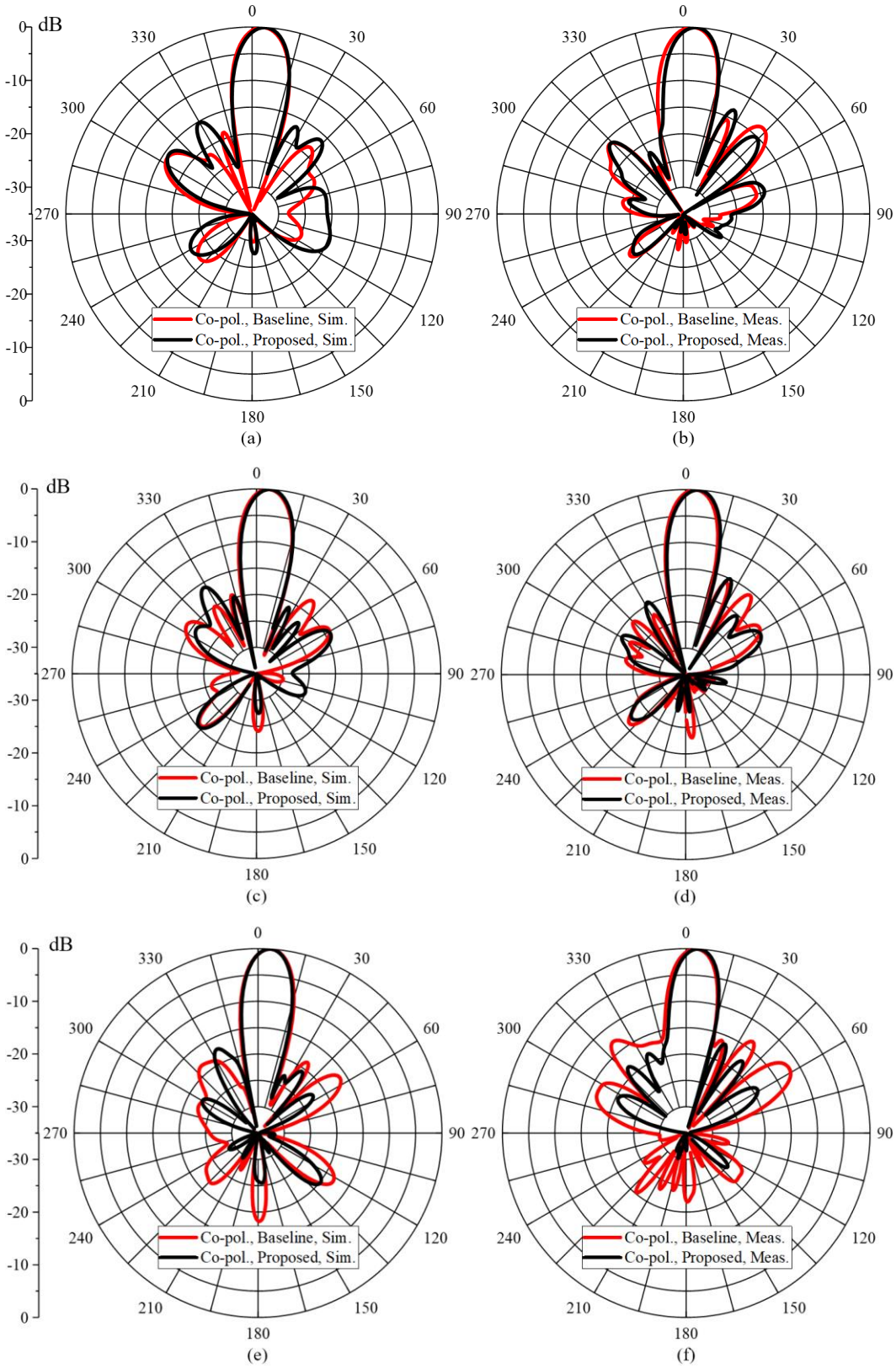
dB
0
-10
-20
-30
-20
-10
0
0
30
60
90
120
150
180
210
240
270
300
330
Co-pol., Baseline, Sim.
Co-pol., Proposed, Sim.
(a)
Co-pol., Baseline, Meas.
Co-pol., Proposed, Meas.
(b)
(c)
(d)
(e)
(f)

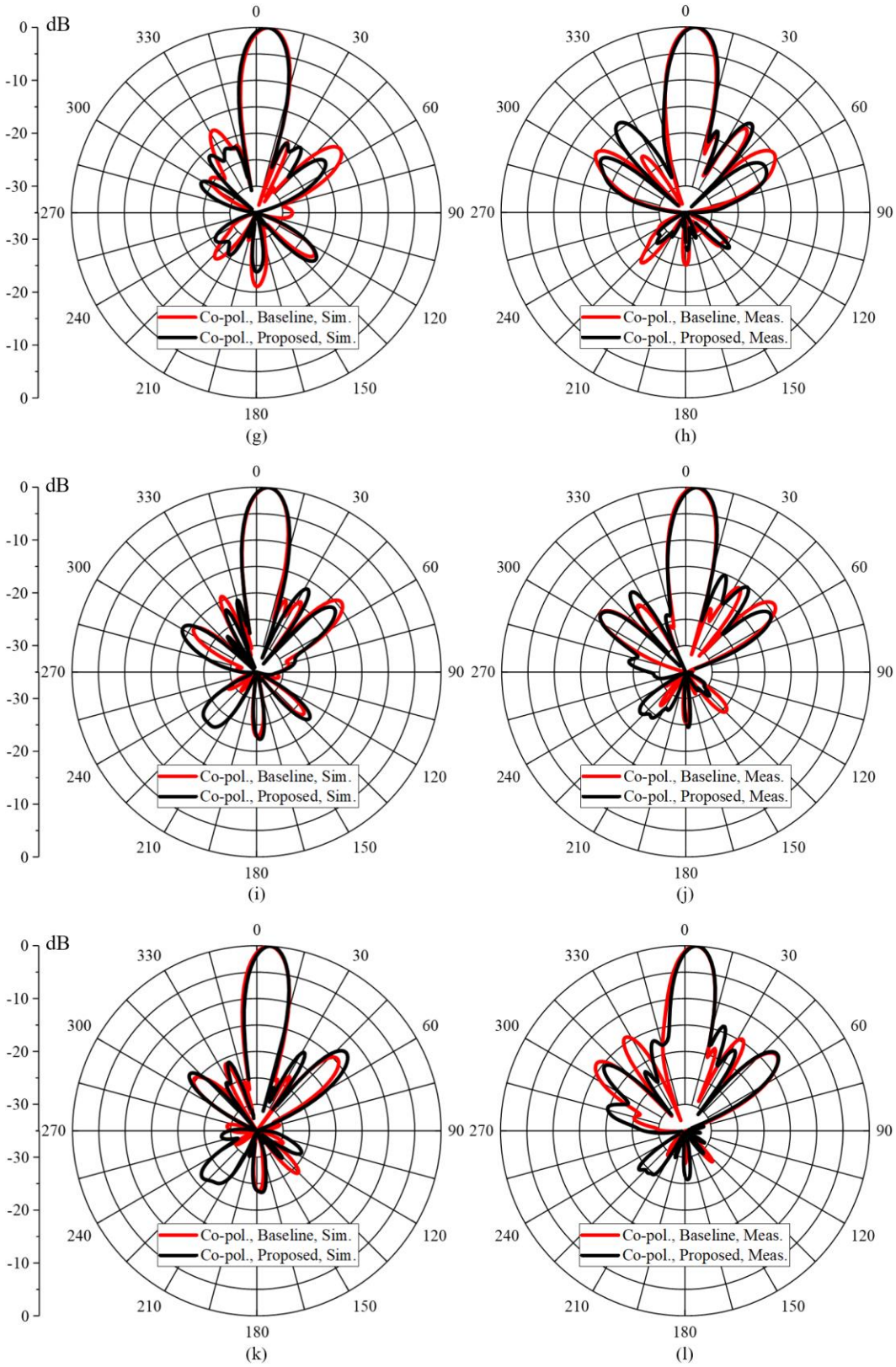

Figure 4-5: Simulated/measured +45° V-plane radiation patterns of the LB array at (a)/(b) 698 MHz, (c)/(d) 740 MHz, (e)/(f) 796 MHz, (g)/(h) 816 MHz, (i)/(j) 858 MHz, and (k)/(l) 894 MHz.

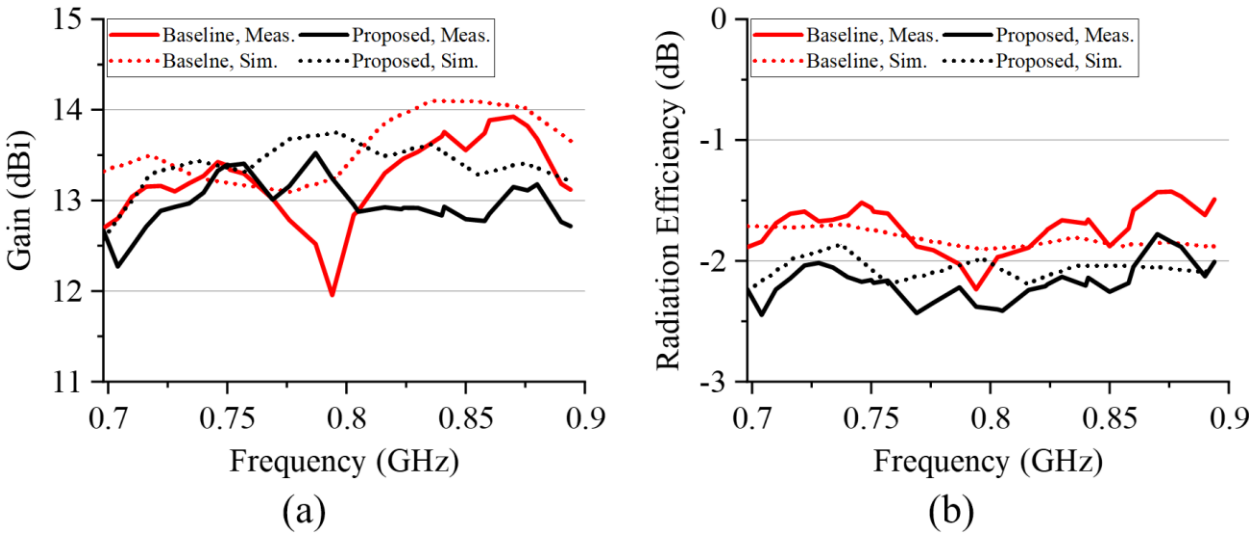

Figure 4-6: Simulated and measured (a) peak system gain and (b) radiation efficiency of the +45° polarization LB array.

The peak gain of the baseline LB array exceeds that of the proposed LB array; however, the proposed design offers more stability in gain across the operating band. The reason that gain stability is important is that it ensures uniform coverage and received signal strength across the entirety of the operating band to all users connected to the BSA array. Both the UC simulations and array simulations predict a reduction in the proposed gain above 810 MHz, albeit less severe than what is observed in measurement.

It is seen from Figure 4-6(b) that the LB radiation efficiency of the proposed design is lower than the baseline radiation efficiency both in simulation and measurement. The difference between the baseline and proposed average radiation efficiencies for the simulated/measured results is 0.26 dB/0.46 dB, where in both cases the average radiation efficiency of the proposed design is worse than the baseline design. Furthermore, the average measured radiation efficiency is 0.1 dB worse than in simulation, for both the baseline and proposed designs. The additional losses present in the proposed measurement beyond those predicted in simulation are likely due to the losses of the

adhesive used to bond the serially loaded capacitive LB dipole arm PCBs exceeding that which is modeled in simulation. If so, a multi-layer PCB using a low-loss prepreg could be used to form the parallel plate capacitors present in the proposed LB dipole arms to improve the losses of the proposed design.

4.2 Evaluation of the MB Performance

Next, the MB S-parameters of the BSAs are measured to ensure that the inclusion of the phase shifters, power dividers, and additional coaxial cables necessary for feeding the array do not significantly degrade the active scan impedance of the dual-polarized MB array. Figure 4-7 shows that the simulated and measured return losses agree well with each other. The measured worst-case MB return loss improves slightly from the baseline to the proposed BSA, increasing from 17.6 dB to 17.8 dB, respectively. Overall, the baseline and proposed measured return losses are very similar and both offer excellent matching across the band for evaluation of the radiation pattern improvements expected from the proposed mutual coupling reduction techniques.

The measured MB intra-array cross-polar isolation improves in the lower half of the band in moving to the proposed design, as shown in Figure 4-8, remaining otherwise similar to the baseline design. This improvement in cross-polar isolation in the lower part of the band is predictable from the results of Section 2.5; however, this confirms that the capacitive MB feed stems, which are not present in Chapter 2, do not adversely affect the MB cross-polar isolation. The measured worst-case MB cross-polar isolation for the baseline/proposed MB array is −21.6 dB/−24.5 dB. The simulated and measured proposed cross-polar isolation curves agree closely with each other, with a noticeable difference being the ripples observed in measurement. The simulated and measured

baseline cross-polar isolation curves have similar shapes; however, they differ in magnitude by approximately 5 dB. Given that this 5 dB difference occurs below 20 dB, the magnitude of this difference is relatively small and is likely due to a combination of simulation accuracy, manufacturing tolerances, and measurement accuracy.

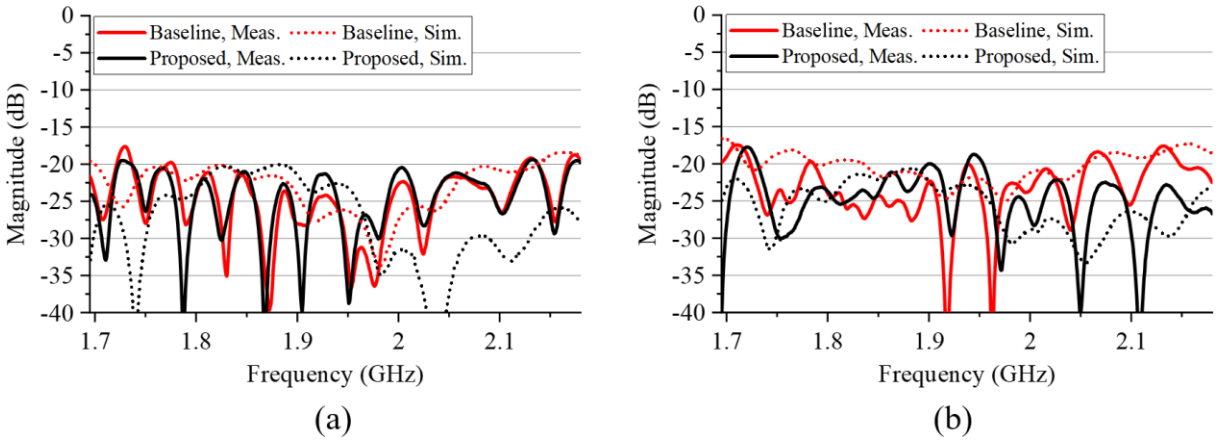

Figure 4-7: Simulated and measured reflection coefficient of the baseline and proposed left MB arrays for the (a) +45° and (b) −45° polarizations.

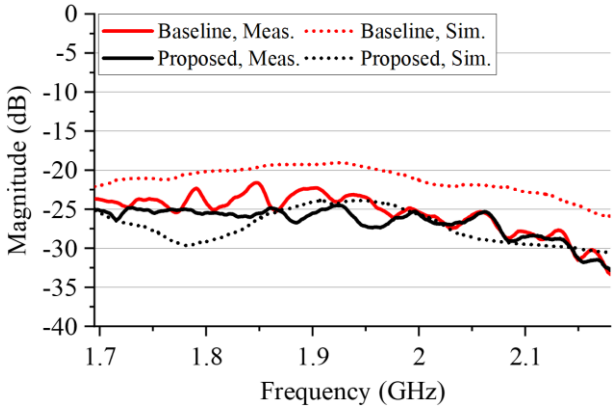

Figure 4-8: Simulated and measured MB intra-array cross-polar isolation of the baseline and proposed BSAs.

The MB H-plane radiation patterns are shown for +45° and −45° polarizations in Figure 4-9 and Figure 4-10, respectively. The simulated and measured results are seen to agree quite well across the operating band. Improvements in the CPR are observed with the proposed BSA over

that of the baseline design for both polarizations in both simulation and measurement. For example, for the +45° polarization the measured CPR at 1.800 GHz, 1.900 GHz, and 2.00 GHz improves from −10.0 dB to −12.7 dB, from −9.0 dB to −11.8 dB, and from −11.9 dB to −13.9 dB, respectively. At 1.695 GHz and 1.800 GHz the measured CPR of the −45° polarization improves from −10.4 dB to −14.0 dB and from −13.3 dB to −16.3 dB, before and after implementation of the proposed techniques, respectively. Co-polar radiation pattern improvements also occur for the −45° polarization at 1.695 GHz and 1.800 GHz, as shown in Figure 4-10(b) and Figure 4-10(d) for which the radiation pattern symmetry improves. The proposed −45° polarization also experiences a reduction in the −10 dB horizontal beamwidth (HBW) in comparison to that of the baseline design. The front-to-back ratio is seen to improve across the band for the −45° polarization. While the −45° polarization improvements are predictable from the UC improvements observed in Section 2.5, the reason for the improvement in the CPR of the +45° polarization is not immediately apparent; however, it is discussed at length in Section 4.3

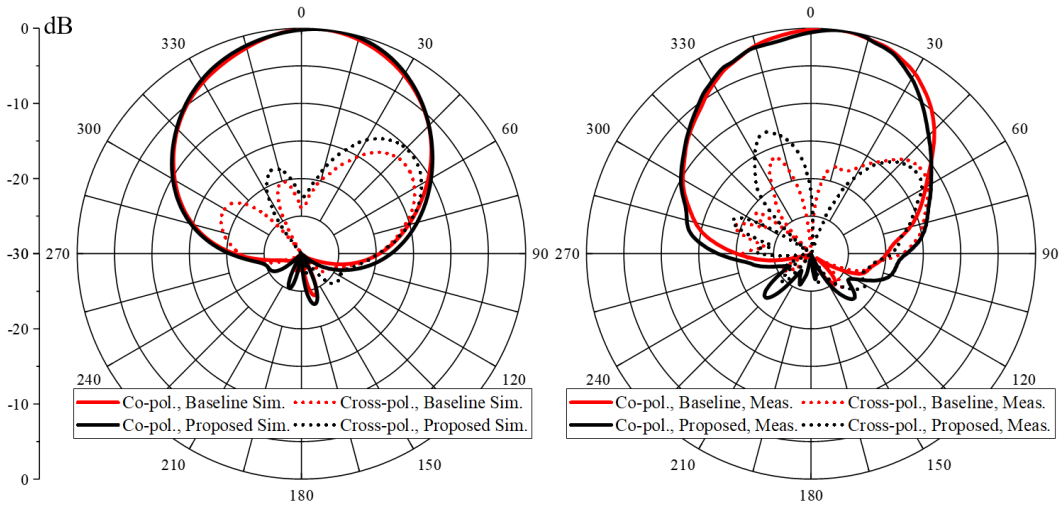
dB
0
-10
-20
-30
-20
-10
0
30
60
90
120
150
180
210
240
270
300
330
Co-pol., Baseline Sim.
Cross-pol., Baseline Sim.
Co-pol., Proposed Sim.
Cross-pol., Proposed Sim.

(a)

0
30
60
90
120
150
180
210
240
270
300
330
Co-pol., Baseline, Meas.
Cross-pol., Baseline, Meas.
Co-pol., Proposed, Meas.
Cross-pol., Proposed, Meas.

(b)

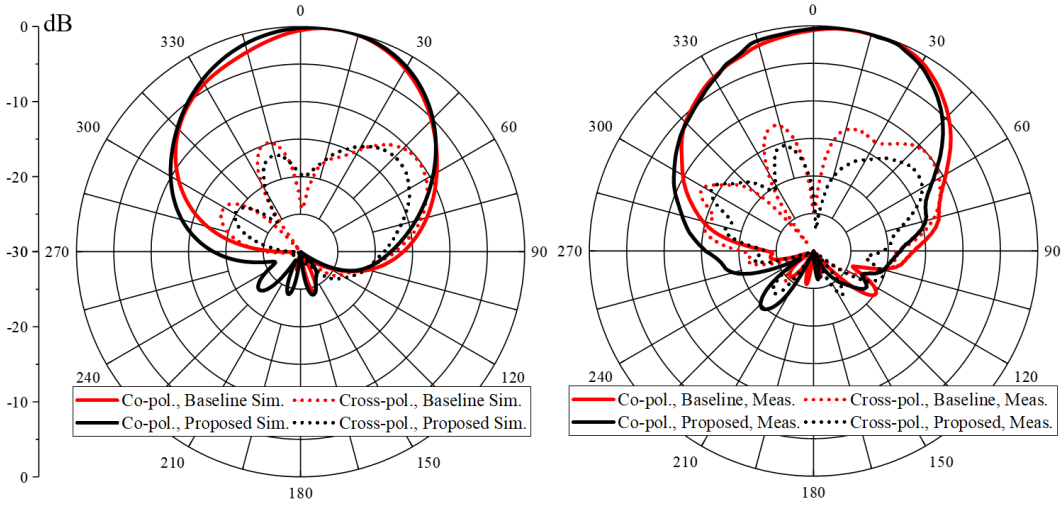
dB
0
-10
-20
-30
-20
-10
0
30
60
90
120
150
180
210
240
270
300
330
Co-pol., Baseline Sim.
Cross-pol., Baseline Sim.
Co-pol., Proposed Sim.
Cross-pol., Proposed Sim.

(c)

0
30
60
90
120
150
180
210
240
270
300
330
Co-pol., Baseline, Meas.
Cross-pol., Baseline, Meas.
Co-pol., Proposed, Meas.
Cross-pol., Proposed, Meas.

(d)

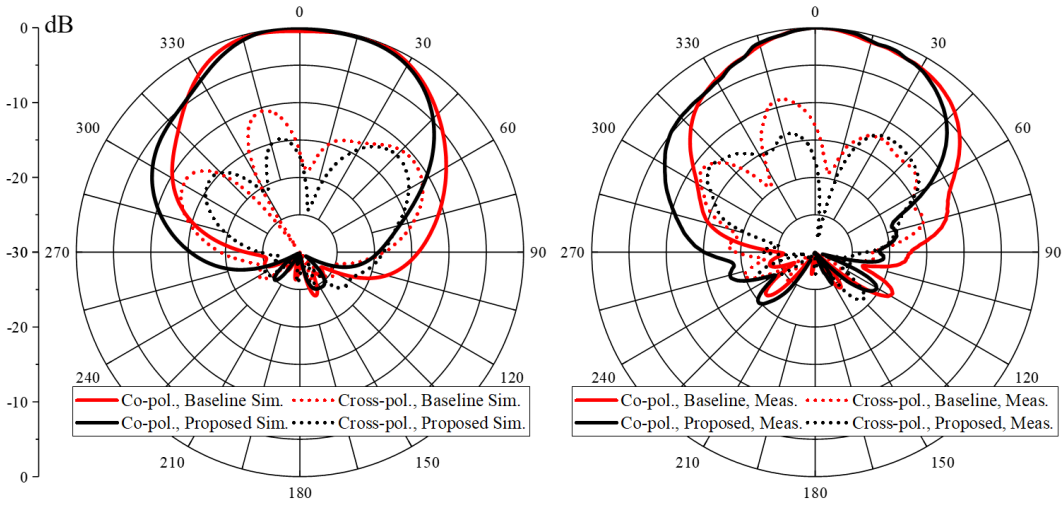
dB
0
-10
-20
-30
-20
-10
0
30
60
90
120
150
180
210
240
270
300
330
Co-pol., Baseline Sim.
Cross-pol., Baseline Sim.
Co-pol., Proposed Sim.
Cross-pol., Proposed Sim.

(e)

0
30
60
90
120
150
180
210
240
270
300
330
Co-pol., Baseline, Meas.
Cross-pol., Baseline, Meas.
Co-pol., Proposed, Meas.
Cross-pol., Proposed, Meas.

(f)

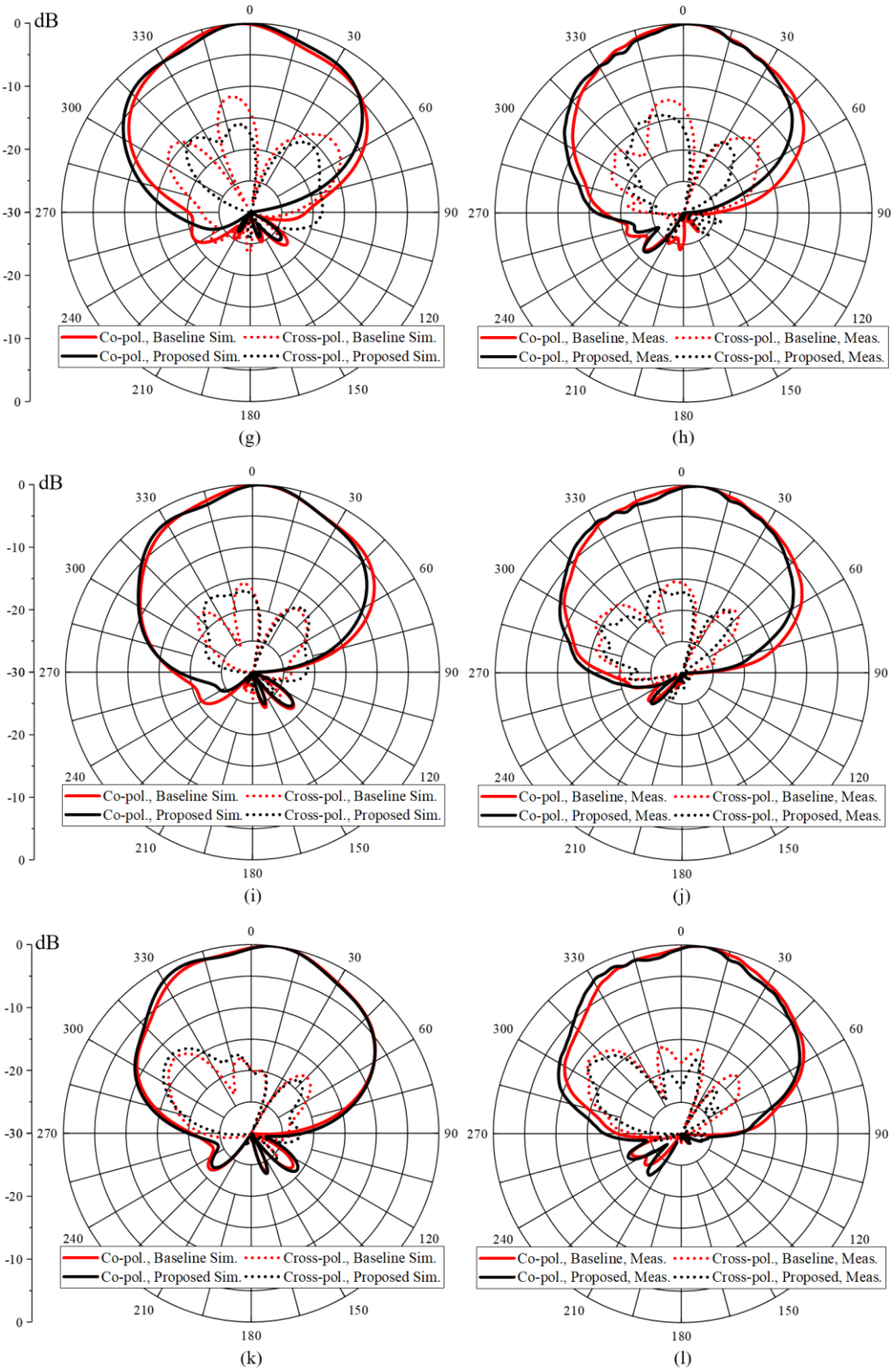

Figure 4-9: Simulated/measured +45° H-plane radiation patterns of the left MB array at (a)/(b) 1.700 GHz, (c)/(d) 1.800 GHz, (e)/(f) 1.900 GHz, (g)/(h) 2.000 GHz, (i)/(j) 2.100 GHz, and (k)/(l) 2.180 GHz.

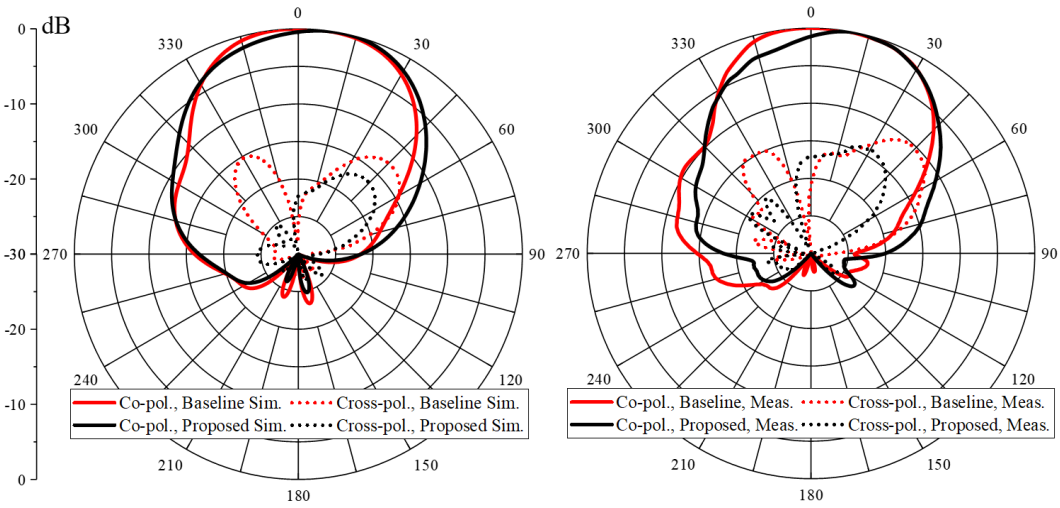
dB
0
-10
-20
-30
-20
-10
0
30
60
90
120
150
180
210
240
270
300
330
Co-pol., Baseline Sim.
Cross-pol., Baseline Sim.
Co-pol., Proposed Sim.
Cross-pol., Proposed Sim.

(a)

0
30
60
90
120
150
180
210
240
270
300
330
Co-pol., Baseline, Meas.
Cross-pol., Baseline, Meas.
Co-pol., Proposed, Meas.
Cross-pol., Proposed, Meas.

(b)

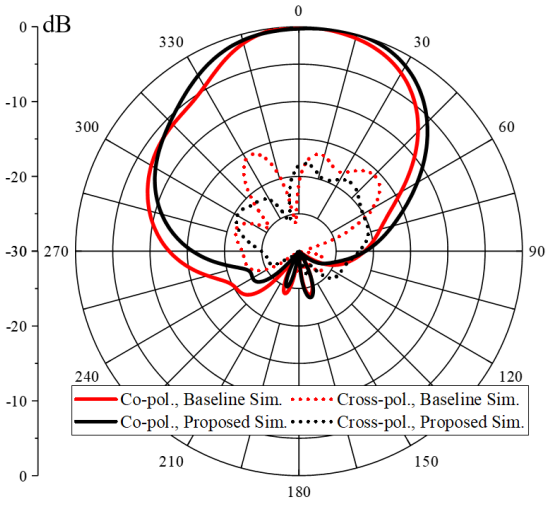
dB
0
-10
-20
-30
-20
-10
0
30
60
90
120
150
180
210
240
270
300
330
Co-pol., Baseline Sim.
Cross-pol., Baseline Sim.
Co-pol., Proposed Sim.
Cross-pol., Proposed Sim.

(c)

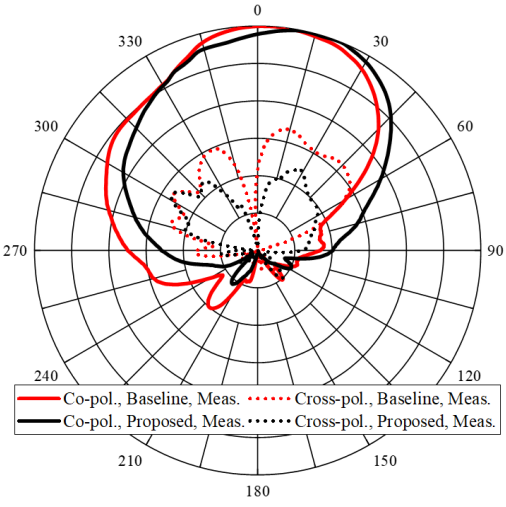
0
30
60
90
120
150
180
210
240
270
300
330
Co-pol., Baseline, Meas.
Cross-pol., Baseline, Meas.
Co-pol., Proposed, Meas.
Cross-pol., Proposed, Meas.

(d)

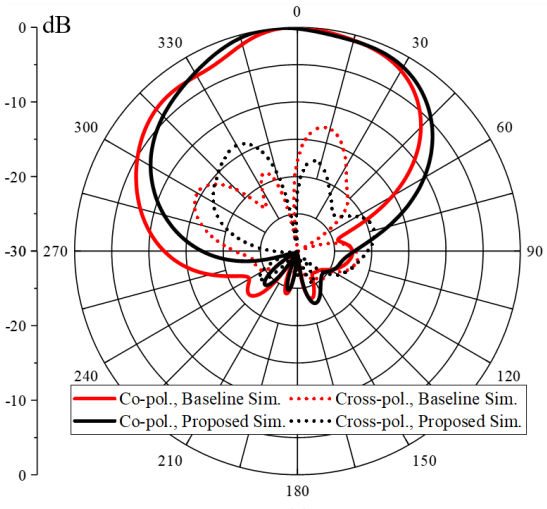
dB
0
-10
-20
-30
-20
-10
0
30
60
90
120
150
180
210
240
270
300
330
Co-pol., Baseline Sim.
Cross-pol., Baseline Sim.
Co-pol., Proposed Sim.
Cross-pol., Proposed Sim.

(e)

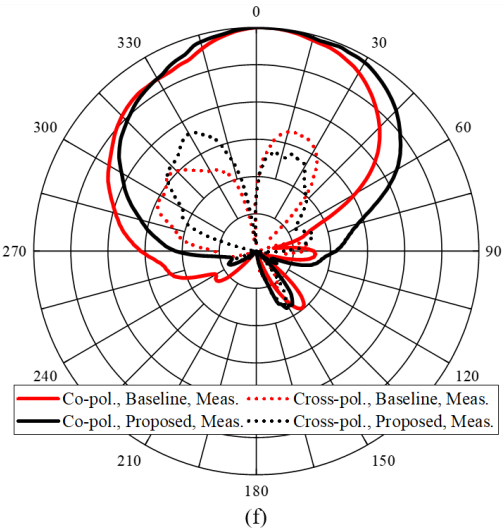
0
30
60
90
120
150
180
210
240
270
300
330
Co-pol., Baseline, Meas.
Cross-pol., Baseline, Meas.
Co-pol., Proposed, Meas.
Cross-pol., Proposed, Meas.

(f)

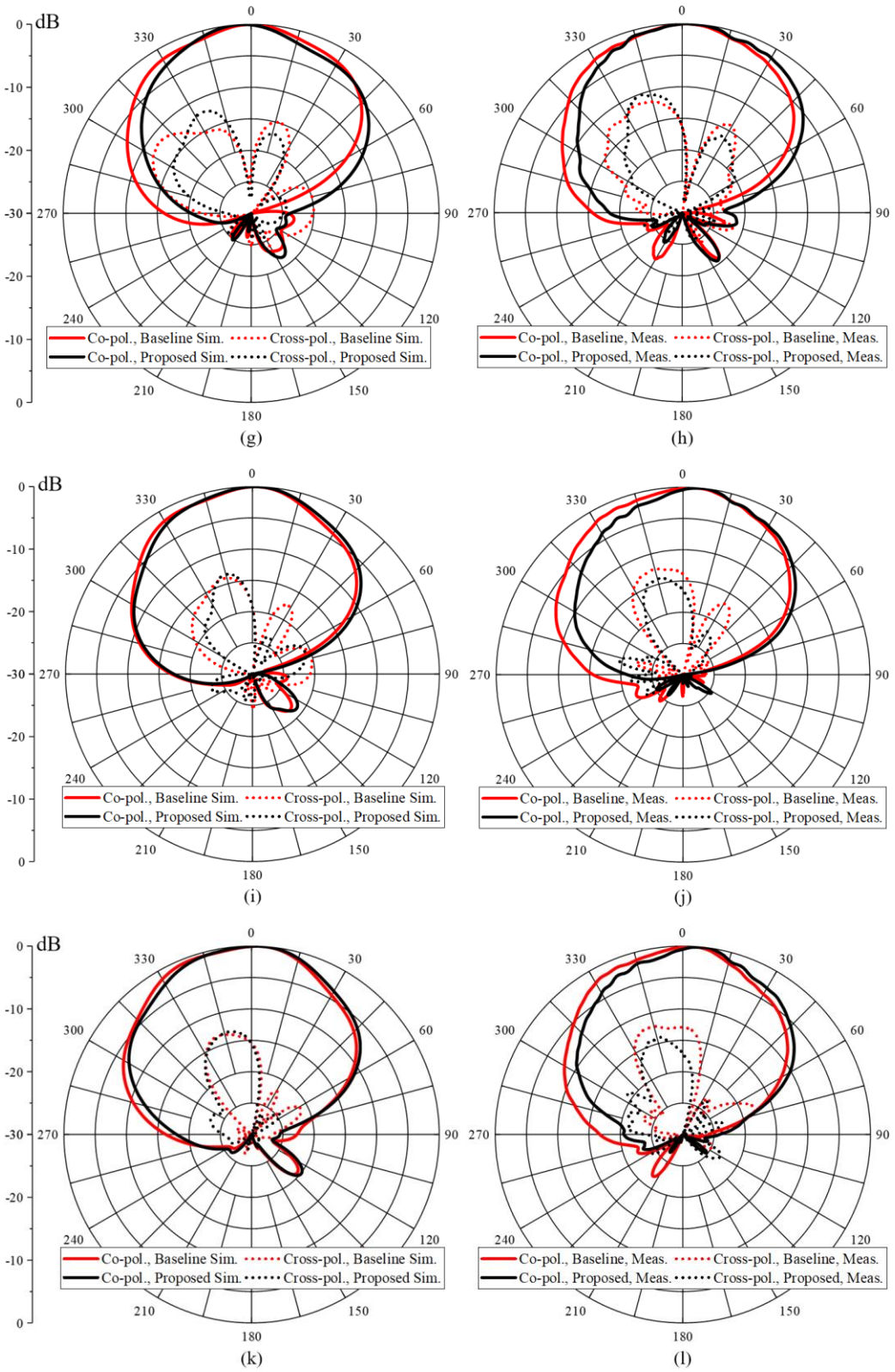

Figure 4-10: Simulated/measured −45° H-plane radiation patterns of the left MB array at (a)/(b) 1.700 GHz, (c)/(d) 1.800 GHz, (e)/(f) 1.900 GHz, (g)/(h) 2.000 GHz, (i)/(j) 2.100 GHz, and (k)/(l) 2.180 GHz.

The MB V-plane radiation patterns are shown for +45° and −45° polarizations in Figure 4-11 and Figure 4-12, respectively. A reduction in the PUSLL is realized across most of the operating band for the proposed design. For example, the PUSLL for the +45° polarization improves for 1.900 GHz from −16.3 dB to −19.0 dB, for 2.000 GHz from −11.5 dB to −16.2 dB, for 2.100 GHz from −11.3 dB to −13.5 dB, and for 2.180 GHz from −11.6 dB to −12.8 dB. Furthermore, the PUSLL for the −45° polarization improves for 1.700 GHz from −17.7 dB to −20.0 dB, for 1.900 GHz from −15.9 dB to −18.9 dB, for 2.100 GHz from −15.5 dB to −18.5 dB, and for 2.180 GHz from −13.1 dB to −15.1 dB. The improvements in the PUSLL and peak CPR are shown in comparing the baseline and proposed measurements in Table 4-2.

The measured gain of the baseline and proposed BSAs are shown in Figure 4-13 for the ±45° polarizations. The simulated gains for the baseline and proposed BSAs agree well with the measurements. Both polarizations show peak and average gain improvements across the band for both simulation and measurement of the proposed BSA. The average gain improvement for both the +45° and −45° polarizations is 0.3 dB. The measured peak system gain of the proposed BSA for the +45° polarization exceeds that of the baseline BSA for all frequencies in the band, excluding 1.695−1.780 GHz. The peak improvement in gain for the +45° polarization occurs at 1.870 GHz for which it increases from 14.9 dBi to 15.7 dBi, a 0.8 dB improvement. The measured peak system gain of the proposed BSA for −45° polarization exceeds that of the baseline BSA for all frequencies in the band, excluding two small bands between 1.850−1.930 GHz. The peak gain improvement for the −45° polarization occurs at 1.730 GHz, for which it increases from 15.9 dBi to 16.7 dBi, a 0.8 dB improvement. Although an average gain improvement of 0.3 dB and a peak gain improvement of 0.8 dB may not sound as significant as the 1.5 dB improvement of UC 1 in Section 2.5, they are quite significant for a 14-element array, as is discussed in Section 4.3.

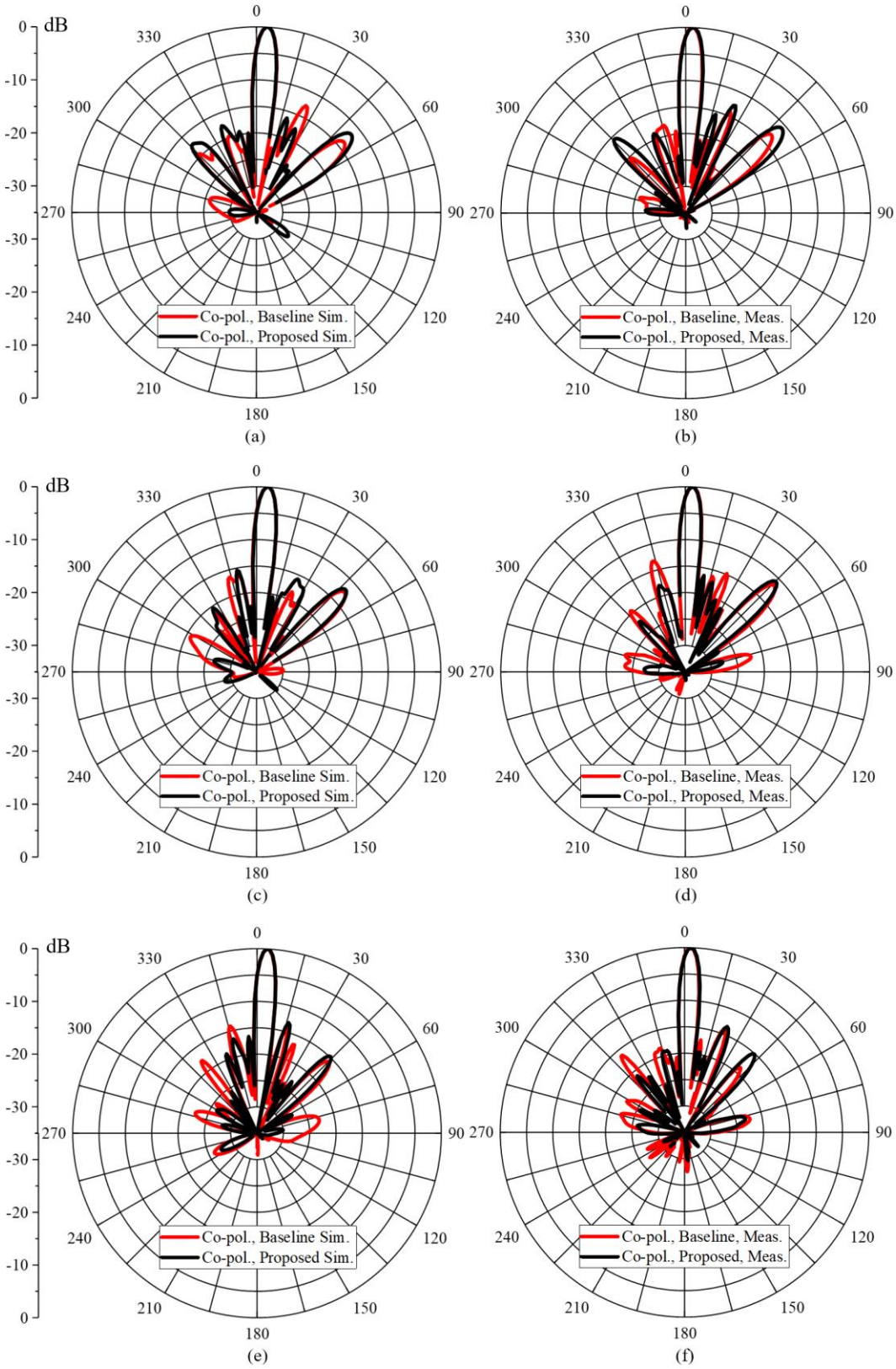
dB
0
-10
-20
-30
-20
-10
0
0
30
60
90
120
150
180
210
240
270
300
330
Co-pol., Baseline Sim.
Co-pol., Proposed Sim.
(a)
Co-pol., Baseline, Meas.
Co-pol., Proposed, Meas.
(b)
(c)
(d)
(e)
(f)

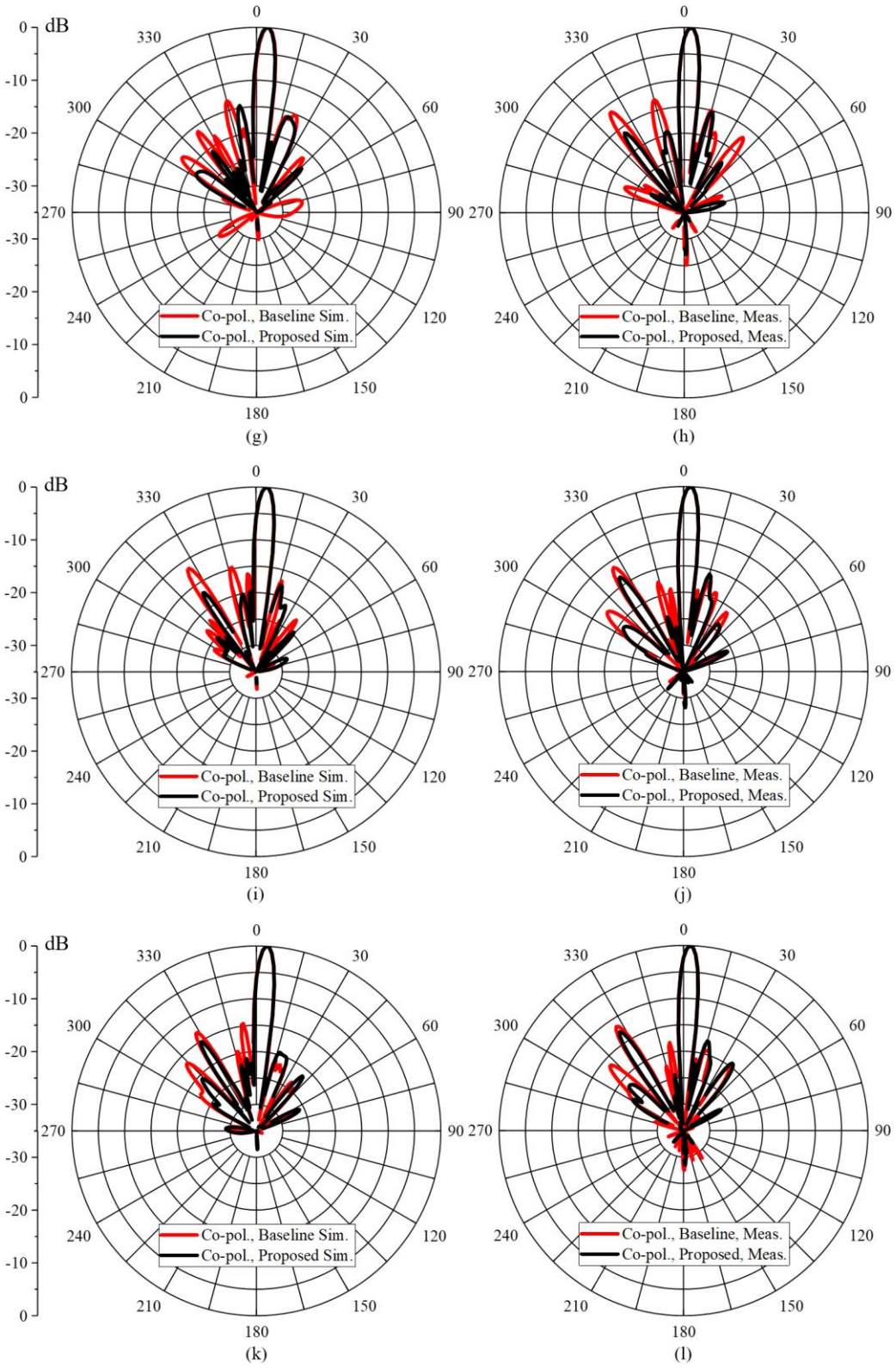

Figure 4-11: Simulated/measured +45° V-plane radiation patterns of the left MB array at (a)/(b) 1.700 GHz, (c)/(d) 1.800 GHz, (e)/(f) 1.900 GHz, (g)/(h) 2.000 GHz, (i)/(j) 2.100 GHz, and (k)/(l) 2.180 GHz.

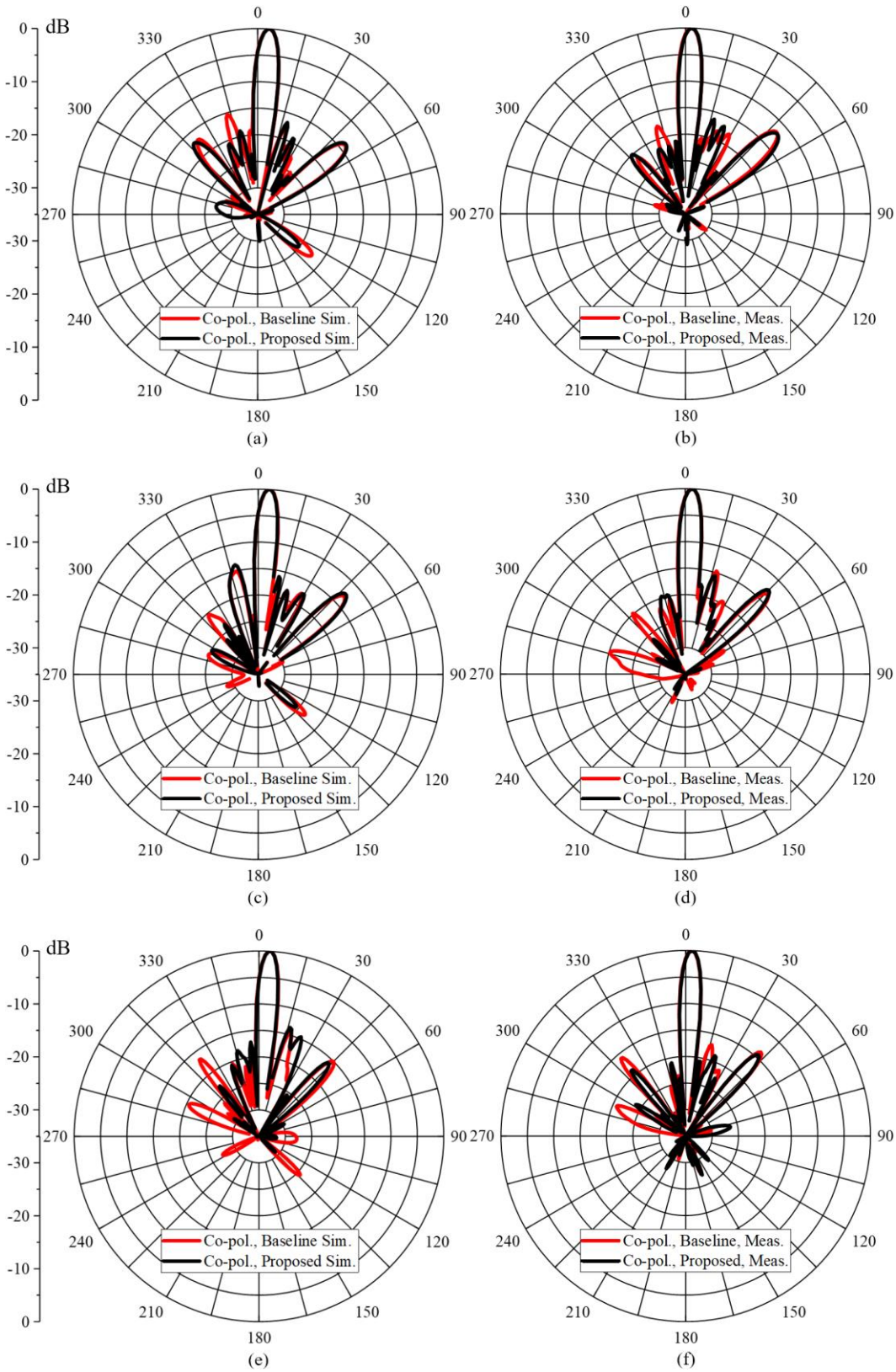
dB
0
-10
-20
-30
-20
-10
0
0
30
60
90
120
150
180
210
240
270
300
330
Co-pol., Baseline Sim.
Co-pol., Proposed Sim.
(a)
Co-pol., Baseline, Meas.
Co-pol., Proposed, Meas.
(b)
(c)
(d)
(e)
(f)

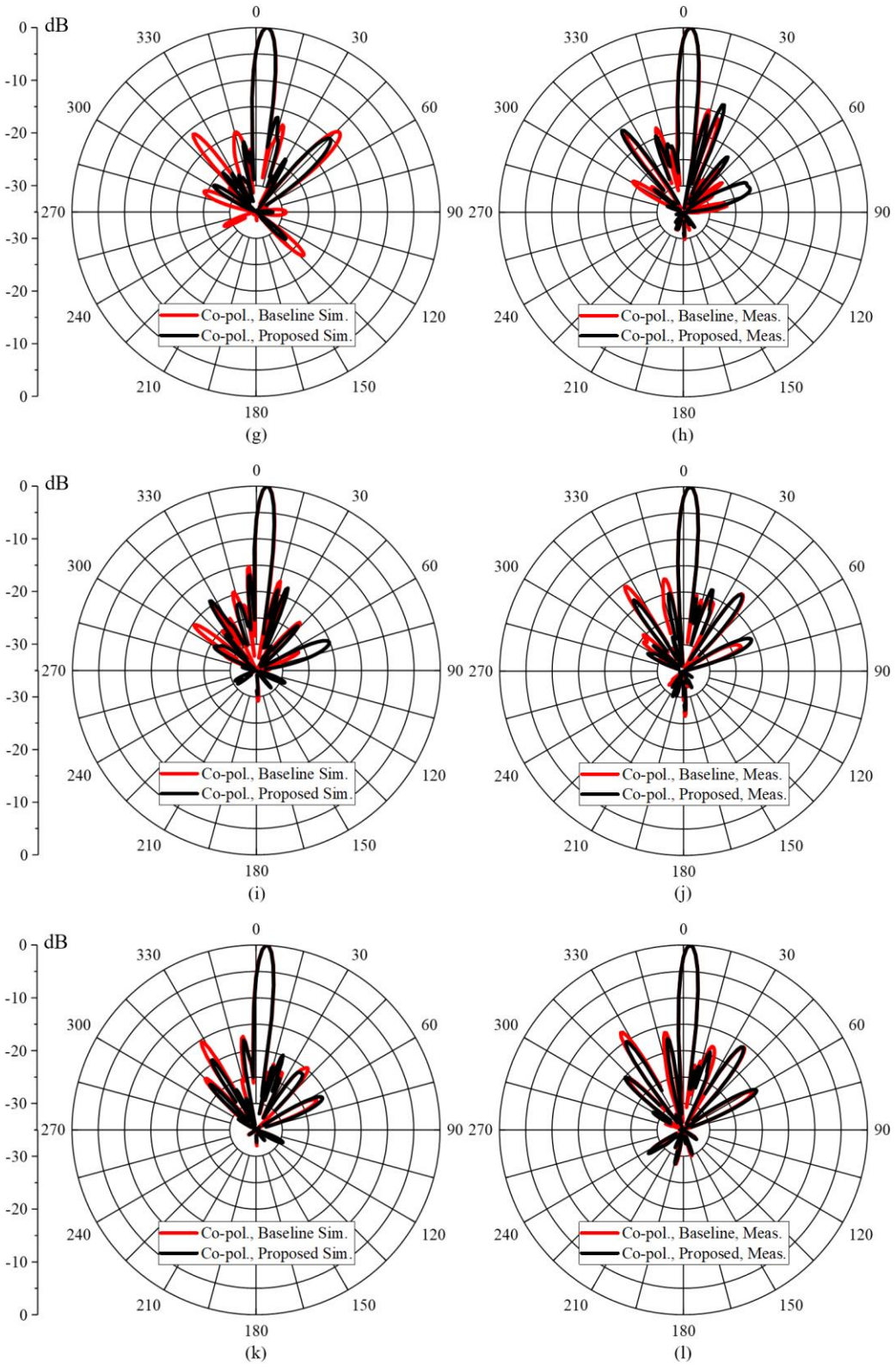

Figure 4-12: Simulated/measured −45° V-plane radiation patterns of the left MB array at (a)/(b) 1.700 GHz, (c)/(d) 1.800 GHz, (e)/(f) 1.900 GHz, (g)/(h) 2.000 GHz, (i)/(j) 2.100 GHz, and (k)/(l) 2.180 GHz.

Table 4-2: Measured baseline and proposed MB peak CPR and PUSLL.

	Peak CPR (dB)		PUSLL (dB)	
Frequency (GHz)	+45° Baseline/Proposed	−45° Baseline/Proposed	+45° Baseline/Proposed	−45° Baseline/Proposed
1.700	−11.5/−12.7	−10.4/−14.0	−18.0/−15.6	−17.7/−20.0
1.800	−10.0/−12.7	−13.3/−16.3	−13.2/−17.9	−19.8/−19.7
1.900	−9.0/−11.8	−13.3/−11.8	−16.3/−19.0	−15.9/−18.9
2.000	−11.9/−13.9	−11.3/−10.1	−11.5/−16.2	−16.7/−15.6
2.100	−13.9/−15.3	−12.4/−14.1	−11.3/−13.5	−15.5/−18.5
2.180	−11.3/−11.8	−12.1/−13.9	−11.6/−12.8	−13.1/−15.1

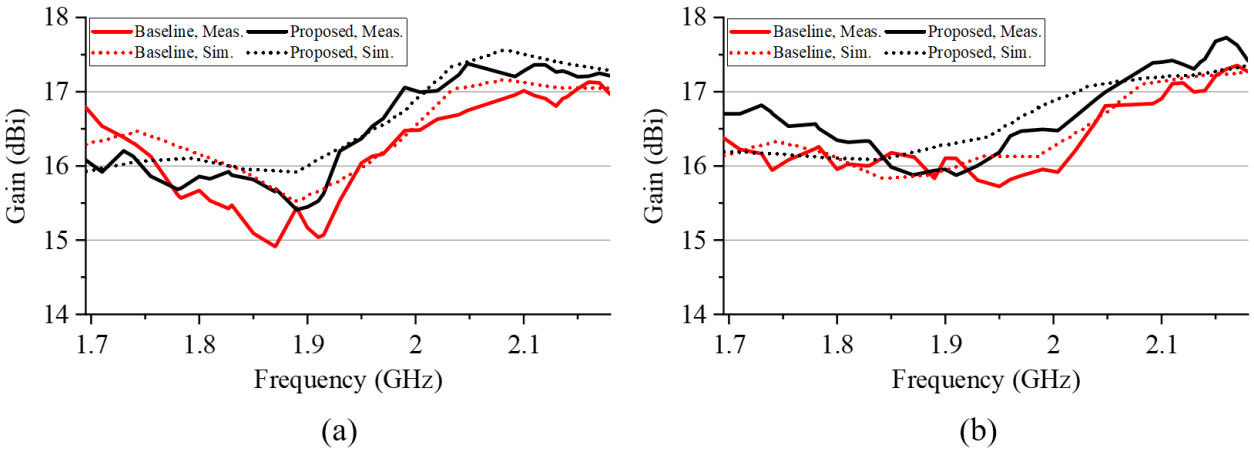

Figure 4-13: Simulated and measured peak system gain of the left MB array for (a) +45° and (b) −45° polarizations.

4.3 Discussion of Results

The radiation pattern degradation observed in the baseline LB BSA simulation/measurement near 796 MHz is in agreement with the results of UC 1 in Chapter 3. Both the baseline UC and baseline BSA exhibit a sharp reduction in gain near this frequency due to the distortion in their radiation patterns from the presence of CM currents induced on the baseline MB dipole feed stems upon excitation of the baseline LB dipoles. In particular, the relatively low front-to-back ratio and

high side lobe levels lead to this sharp reduction in gain in the baseline BSA at 796 MHz. The proposed BSA improves the front-to-back ratio at this frequency, as shown in Figure 4-4(f) and Figure 4-5(f), while also significantly reducing the side lobe levels, as shown in Figure 4-5(f). The increase in the front-to-back ratio in the proposed design would help to reduce interference with neighboring cell sites if the BSA were deployed as part of a cellular network meant to service a 60° sector around boresight, as is the typical coverage angle in many BSA deployments. The reduction in the side lobe levels focuses the energy into the main beam, thereby improving the directivity and gain at this frequency. By improving the radiation pattern and thereby gain near 796 MHz, the received signal strength of a cellular user connected to the proposed BSA will be stable across the frequency band from 698 MHz to 894 MHz.

One unexpected and significant result found in the baseline BSA array, which is not predictable from the LB UC results of Chapter 3, is that of the unacceptable intra-array cross-polar isolation performance. The LB cross-polar isolation of the baseline BSA exhibits a sharp discontinuity near 796 MHz, which is not found in the results of UC 1 shown in Section 3.5.1. Although the baseline UC does not predict a similar sharp discontinuity in the cross-polar isolation around this frequency, this is precisely where the induced CM currents in the baseline MB dipole feed stems are the strongest, as shown in Section 3.4.2. Furthermore, 796 MHz is also where the LB radiation characteristics of the baseline UC exhibit the most degradation, as shown in Section 3.5.1. The severity of the LB cross-polar isolation degradation in the baseline BSA, as opposed to that found in the baseline UC, is likely due to the CM currents induced in the MB dipole feed stems coupling to the nearby LB dipole of the opposite polarization. For example, upon excitation of the +45° polarization LB array, labeled 1a−1g in Figure 4-14, CM currents induced on the MB dipole feed

stems not only radiate but also couple to the −45° polarization LB elements, labeled 2a−2g in Figure 4-14.

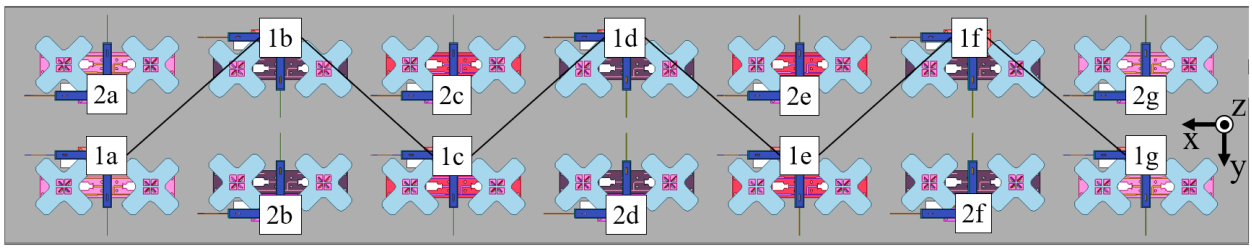

Figure 4-14: Top view of the baseline BSA simulation model.

The baseline −45° polarization H-plane radiation pattern of the left MB array exhibits more severe co-polar radiation degradation than the baseline +45° polarization; however, the baseline +45° polarization exhibits more severe cross-polar radiation (CPR) degradation than the baseline −45° polarization. From the results of the baseline UC in Section 2.5 the degradation in the H-plane co-polar radiation of the −45° polarization is expected; however, the degradation in the CPR of the +45° polarization was not predicted. This difference between the two polarizations is seen in comparing the asymmetry in the H-plane co-polar radiation of the baseline −45° polarization of Figure 4-10(b)/(d) with the more symmetric +45° co-polar radiation pattern of Figure 4-9(b)/(d). Similarly, the difference in CPR degradation between the two polarizations is seen in juxtaposing the more severe CPR degradation present in the baseline +45° polarization of Figure 4-9(d)/(f) with the lower CPR of the −45° polarization of Figure 4-10(d)/(f). This degradation in CPR for the +45° polarization, occurring near 1.870 GHz, is precisely what leads to the severe peak gain degradation in the baseline BSA, as shown in Figure 4-13(a).

One unexpected and significant result found in the BSA array which was not predicted from the baseline MB UC results of Chapter 2 is the CPR degradation observed in the baseline +45°

polarization of the left MB array. Section 2.3.1 shows that upon the excitation of the +45° baseline MB radiators of the left sub-array the currents induced on the +45° baseline LB parasitic are low in magnitude, and their vector sum is cross-polarized. Considering the excitation of the +45° polarization of the left MB array, as shown in Figure 4-15(a), it is seen that of the seven LB dipoles which reside over the top of this MB array, four have cross-polarized induced currents, whereas only three have co-polarized induced currents. It is for this reason that the baseline +45° polarization of the left MB array exhibits more degradation in the CPR than co-polar radiation. Although the magnitude of the baseline cross-polar induced currents are relatively low, their composite effect in the array is substantial.

The degradation of the baseline co-polar radiation patterns of the −45° left MB array are expected from the results of Chapter 2. Section 2.3.1 shows that upon the excitation of the −45° baseline MB radiators of the left sub-array the currents induced on the +45° baseline LB parasitic are high in magnitude, and their vector sum is co-polarized. Considering the excitation of the −45° polarization of the left MB array, as shown in Figure 4-15(b), it is seen that of the seven LB dipoles which reside over the top of this MB array, four have co-polarized induced currents, whereas only three have cross-polarized induced currents. It is for this reason that the baseline −45° polarization of the left MB array exhibits more degradation in the co-polar radiation pattern than the CPR.

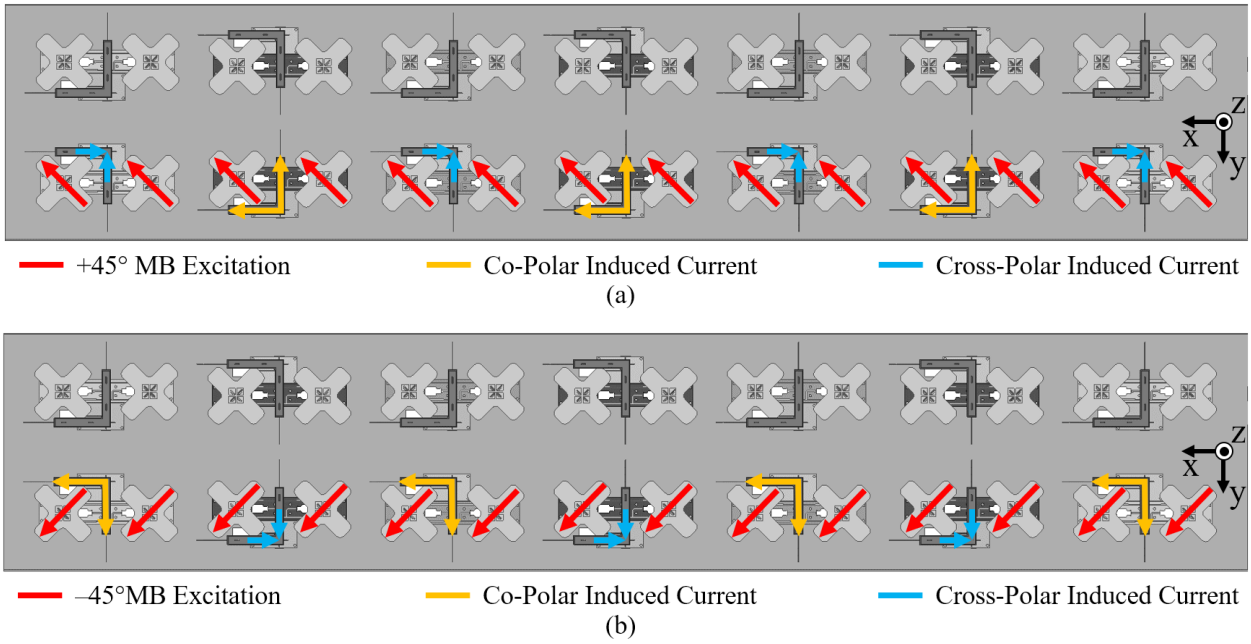

Figure 4-15: Orientation of the currents induced on the baseline LB parasitic upon excitation of the baseline left MB (a) +45° and (b) −45° polarization arrays.

The improvements in the MB ±45° CPR and side lobe level along with the −45° polarization H-plane co-polar radiation pattern improvements increase the MB gain over most of the band for the proposed BSA. The average MB gain improvement of 0.3 dB and peak MB gain improvement of 0.8 dB, realized in moving from the baseline to the proposed 14-element array is very significant. It is known that the directivity of an array approximately doubles, i.e., increases by 3.01 dB, every time the number of antenna elements in the array is doubled [66]. From this, it is expected that as the number of radiating elements increases within an array, realizing a given increase in directivity, in dB, becomes increasingly difficult. For example, moving from two sub-arrays to three sub-arrays theoretically increases the directivity by approximately 1.76 dB. Similarly, moving from three sub-arrays to four sub-arrays theoretically increases the directivity by approximately 1.25 dB. Given that the BSA under consideration has seven MB sub-arrays, if the length of the BSA were theoretically increased by adding an additional sub-array to improve

the gain, the directivity would only theoretically increase by approximately 0.58 dB. Therefore, by designing a BSA with the proposed design techniques the peak gain improvement exceeds that which is theoretically expected were an additional sub-array to be added. Furthermore, the addition of an eighth MB sub-array would require an increase in the BSA length, which is set by the design specifications at a value of six feet.

Another way to quantify the peak MB gain improvement in the system, is to consider how much transmit power is required for the baseline and proposed BSAs at a fixed frequency to yield the same effective isotropic radiated power (EIRP). Considering an input power of 300 W (54.77 dBm) to the baseline BSA and a peak gain improvement of 0.8 dB in moving to the proposed BSA, for a fixed EIRP the transmit power of the proposed BSA could be reduced to 249 W. Given that some BSAs have more than 24 input ports, this reduction in transmit power for each port to realize an equivalent EIRP as the baseline design would greatly improve the power requirements and therefore cost of the system. Furthermore, the lower transmit power would lessen the heating of the antenna which could allow for the use of lower cost components within the BSA which are rated for lower temperatures.

A third way in which to quantify the peak MB gain improvement of the BSA is to consider how much the radius of the service cell increases for a fixed transmit power and receiver sensitivity in moving from the baseline to the proposed design. Assuming free space propagation, it follows from the Friis transmission formula that the relationship between the gain of two transmitting BSAs G_1 and G_2 and the distance at which the power will be received d_1 and d_2, can be expressed as

$$\frac{G_2}{G_1} = \left(\frac{d_2}{d_1}\right)^2 \tag{4-1}$$

From equation (4-1) it follows that

$$|d_2| = |d_1| \sqrt{\frac{G_2}{G_1}} \tag{4-2}$$

Therefore, if the baseline BSA achieves a service cell radius of $d_1 = 3$ miles, and the peak MB gain improvement for the proposed BSA is 0.8 dB it follows that given the same transmit power and receiver, the proposed BSA could service a cell with radius 3.29 miles. This amounts to almost a 10% increase in cell radius and therefore nearly a 20% increase in service area.

In addition to the peak gain improvements for both the LB and MB arrays and the improved gain stability in the LB array, the improvements in the H-plane co-polar patterns in the proposed BSA would lead to a more uniform distribution of power across a given service area, if this BSA were to be deployed in a cellular network meant to cover a 60° sector around boresight, as is commonly desired in cellular networks. The improved CPR observed in the proposed design improves the orthogonality between the ±45° data streams, thereby improving the data throughput of the network through the use of polarization diversity, were the BSA to be used in the deployment of a cellular network. The reduction in the upper side lobe levels exhibited in the proposed BSA increases the directivity/gain of the array, which would result in higher received signal strength at a fixed distance for cellular users being serviced by the proposed BSA.

4.4 Summary

The mutual coupling reduction techniques developed in Chapter 2 and Chapter 3 are utilized to design a dual-polarized six-port BSA operating from 698 MHz to 894 MHz (LB) and 1.695 GHz to 2.180 GHz (MB) with improved performance over that of the baseline design. In particular, a common mode (CM) resonance which occurs in the baseline design at 796 MHz, due to the CM currents induced on the vertical MB dipole feed stems, is suppressed through the introduction of series capacitance integrated into the vertical MB dipole feed stems, as first suggested in Chapter 3. This mutual coupling reduction allows for significant improvements in the LB cross-polar isolation, front-to-back ratio, CPR, and reduction in the side lobe levels at 796 MHz. Furthermore, the suppression of the CM resonance improves the gain at 796 MHz by 1.2 dB, allowing for a more constant gain profile across the LB frequency band while also greatly increasing coverage at this frequency.

The MB currents induced on the electrically long baseline LB parasitics, which are required for broadband tuning of the baseline LB dipoles, are eliminated by matching the LB dipoles using an electrically short LB parasitic after reducing the self-impedance of the dipole by serially loading the dipole arms with capacitance. This reduction in mutual coupling improves the MB co-polar radiation symmetry and reduces the CPR and PUSLLs across the band. These improvements lead to significant peak gain improvements across most of the band, with a maximum improvement occurring at 1.870 GHz for which the gain increases from 14.9 dBi to 15.7 dBi, a 0.8 dB improvement. Similarly, an MB average gain improvement of 0.3 dB is realized in moving to the proposed BSA. It is shown that both the average and peak gain improvements lead to significant system performance improvements in the proposed BSA when used for coverage in a cellular network.

Both the LB and MB BSA simulations and measurements uncovered improvements in the proposed BSA which were not predicted from the UC simulations alone. For example, the baseline LB cross-polar isolation exhibits an abrupt degradation to −16.3 dB near 796 MHz, where the induced CM currents are the strongest. The proposed BSA eliminates the strong CM currents present in the baseline MB feed stems, thereby improving the array level LB cross-polar isolation. The CPR of the baseline +45° polarization left MB array exhibits severe degradation at 1.900 GHz at which it becomes worse than −9.0 dB. The proposed BSA eliminates both the co-polarized and cross-polarized currents that are induced in the baseline LB parasitic, thereby improving the co-polar radiation and CPR characteristics of the ±45° polarizations of the left MB array.

Although the techniques of Chapter 2 and Chapter 3 do not completely remove the mutual coupling present within the array, they lead to significant improvements as compared to the baseline BSA. This chapter presents just one example of an array architecture in which the proposed techniques of Chapter 2 and Chapter 3 can be utilized. Depending on the BSA design specifications, different array architectures, such as the architecture of Figure 1-7 using UC 2 of Chapter 3, may yield even more significant improvements upon the application of the proposed techniques to the design of a BSA.

Chapter 5

Fabry-Perot Cavity Antenna and Frequency Selective Parasitic for Mutual Coupling Reduction

This chapter considers a dual-polarized high-band (HB) array operating adjacent to two dual-polarized low-band (LB) elements and two dual-polarized mid-band (MB) sub-arrays, all of which are located beneath a dielectric radome. The HB, MB, and LB operating bands are 3.4 – 4.2 GHz, 1.695 – 2.180 GHz, and 698 – 894 MHz, respectively. Due to the close proximity of the adjacent arrays, and the radome presence, the baseline tri-band array environment has multiple sources of mutual coupling. The dielectric radome, necessary for protecting the array face from environmental effects such as wind, precipitation, and UV radiation when the base station antenna (BSA) is mounted outside, is identified as a partially reflecting surface (PRS) which adversely affects the HB radiation patterns in the upper part (4.0 – 4.2 GHz) of the HB operating band. The baseline MB parasitics, necessary for broadband matching of the MB sub-arrays, are identified as secondary radiation sources which adversely affect the HB radiation patterns in the lower and middle part (3.4 – 3.8 GHz) of the HB operating band.

Two methods for mutual coupling reduction are proposed to improve the HB performance in the presence of the LB dipoles, MB sub-arrays, and dielectric radome. The first proposed design technique uses a dielectric superstrate between the HB array and the dielectric radome to create a Fabry-Perot cavity antenna (FPCA) to increase the boresight directivity of the HB array from 3.8 GHz to 4.2 GHz. The FPCA is designed to be resonant at 4.2 GHz while accommodating the fixed height of the dielectric radome. The second proposed design technique uses modifications to the geometry of the baseline MB parasitics to suppress the excitation of currents on the parasitics upon the excitation of the HB array, while maintaining broadband matching of the MB sub-arrays. The

currents induced on the baseline MB parasitics become secondary sources of radiation which combine with the primary radiation sources of the HB array. The suppression of these induced currents leads to improvements in the stability of the H-plane (yz-plane) half power beamwidth (HPBW) across the HB operating band. The H-plane HPBW is defined as the angle between the two directions in which the radiation intensity is −3 dB below the maximum value [61]. This densely populated tri-band environment demonstrates the need for the simultaneous use of multiple mutual coupling reduction techniques to suppress the interactions from multiple sources of interference.

This chapter begins by presenting the simulated performance of the baseline HB array and demonstrates the impact of the tri-band array environment on the HB radiation characteristics. Next, the impact of the radome on the HB performance is identified and an FPCA is proposed for improvement in the HB boresight directivity. The FPCA design is confirmed both analytically as well through three-dimensional (3-D) full-wave electromagnetic (EM) analysis using Ansys HFSS [115]. The impact of the baseline MB parasitics on the HB radiation patterns is then identified. The physical phenomenon caused by the baseline MB parasitics, which gives rise to the HB radiation pattern degradation, is investigated using full-wave EM simulation, analytic methods utilizing array theory, and a characteristic mode (CRM) analysis. A design technique is then proposed for modifying the baseline MB parasitics, which greatly reduces the mutual coupling between the HB array and the MB parasitics. The results of the simulated and measured baseline and proposed tri-band array environments are then presented and discussed.

5.1 Design of Tri-Band Array Environment

The baseline array environment considered in this chapter consists of one dual-polarized HB array, two dual-polarized MB sub-arrays, and two dual-polarized LB sub-arrays located beneath a dielectric radome, as shown in Figure 5-1. Just as UCs are considered in previous chapters as portions of a larger BSA, this array environment can also represent a small portion of a larger BSA, in which there are additional MB and LB sub-arrays, and possibly additional HB arrays. The dielectric radome acts as an enclosure to protect the array from precipitation, wind, and other environmental conditions which could damage the components within the array, were the BSA to be used outside for a prolonged period of time. The radome is made of fiberglass which has an approximate relative permittivity of $\varepsilon_{r_1} = 3.2$ and thickness $T_{RA} = 0.080$". All printed circuit boards (PCBs), excluding the HB and MB parasitics, are designed using a 0.030" thick laminate with a relative permittivity of $\varepsilon_r = 2.94$ and dielectric loss-tangent of $\delta_t = 0.0025$. The HB parasitics are designed using 0.030" thick FR-4, whereas the MB parasitics are designed using 0.039" thick FR-4.

The HB array consists of five dual-polarized crossed dipoles separated by a distance, $S_{HB1} = 1.772$", corresponding to approximately $0.57\lambda_{0,f_c,HB}$, where $\lambda_{0,f_c,HB}$ represents the free-space wavelength at the center of the HB operating band. The dual-polarized HB array is fed by two phase shifters, one for each polarization, to achieve the desired amplitude and phase taper for the array. In order to reduce the solve time of the simulation models, the phase shifters were omitted and short 50 Ω microstrip feed lines were included in their place. The input cables, and S-parameter block of the phase shifter was then connected to the HFSS model through the creation of a system circuit model. In this way, the amplitude and phase distributions set by the phase shifter were used

to excite the HB array in the baseline HFSS model. The relative positions of the HB, MB, and LB elements, as well as the radome are labeled in Figure 5-1 and tabulated in Table 5-1.

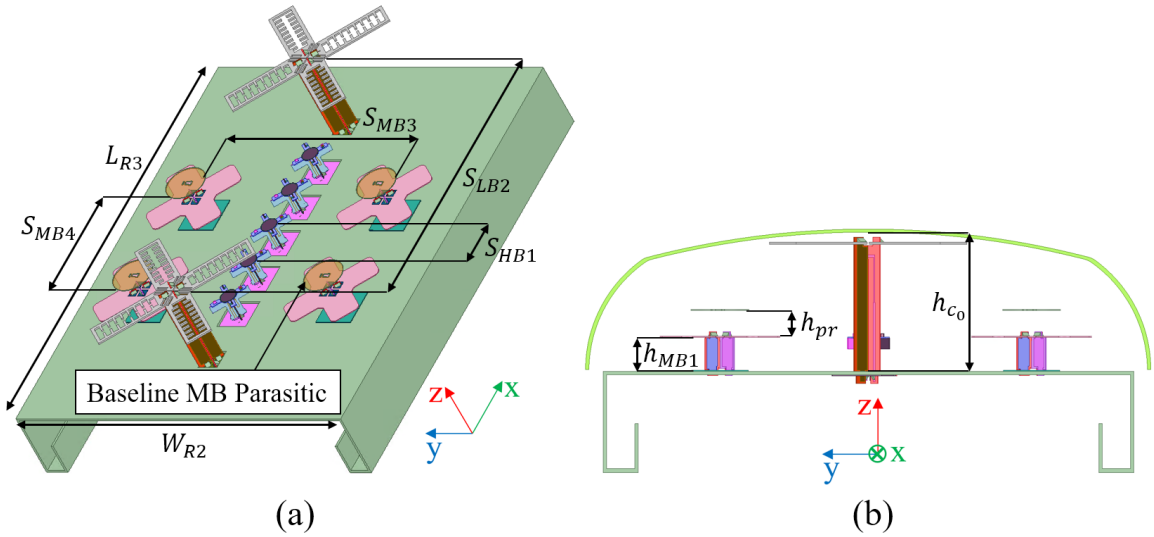

Figure 5-1: Baseline tri-band array face with centered HB array, left and right dual-polarized MB sub-arrays, and top and bottom dual-polarized LB elements (a) without and (b) with radome.

Table 5-1: Dimensions controlling layout of tri-band array environment. All units are in inches.

W_{R2}	L_{R3}	S_{LB2}	S_{MB3}	S_{MB4}	S_{HB1}	h_{c_0}	h_{pr}	h_{MB1}
14.080	17.539	11.614	8.270	4.600	1.772	3.677	0.676	0.898

All of the dipoles used in this array geometry are half-wave dipoles fed using open stub Marchand balun feed stems. The LB dipole arms are made out of 0.059” thick stamped aluminum which are tin plated to allow the dipole arms to be soldered to the LB PCB balun feed stems. The HB dipoles use a conductive parasitic PCB to improve the bandwidth of the radiator. Unlike in the previous chapters, here the MB dipoles use a conductive circular parasitic disk for broadband matching.

The reason that the baseline MB parasitic is necessary is because the dual-polarized MB dipole used in this tri-band array environment has a much shorter feed stem than the MB dipoles discussed

in the previous chapters, making it more challenging to match over a broad bandwidth. In particular, for the free-space wavelength at the center of the MB operating band, denoted by $\lambda_{0,f_c,MB}$, the MB dipole used in this chapter resides 0.898" ($0.167\lambda_{0,f_{c,MB}}$) above the reflector, whereas the MB dipole discussed in Chapters 2 – 4 is 1.300" ($0.242\lambda_{0,f_c,MB}$) above the reflector.

Although it is demonstrated in Chapter 3 and Chapter 4 that series capacitance can be used on the MB dipole feed stems to suppress common mode (CM) resonances which occur at LB frequencies, the additional complexity and cost required for this may not always be desirable. Therefore, instead of using series capacitance integrated into the MB dipole feed stems to suppress the CM resonance, in this tri-band array the MB dipole feed stems are shortened to push the CM resonance of the MB subassembly higher in frequency, out of the LB operating band, thereby reducing the interaction it has with the LB radiators.

The implications of lowering the dipole to the reflector in this manner are that the MB dipole becomes more difficult to match over a broad bandwidth, and that it exhibits a broader HPBW. Introducing an MB parasitic over the shorter MB dipole helps to recover the bandwidth in the same way that the baseline parasitic located above the LB dipole of Section 2.1.1 broadens the bandwidth of the LB radiator. Furthermore, the MB parasitic behaves as a director which reduces the HPBW and increases the MB directivity.

The geometry pertinent to the HB antenna, HB parasitic, and baseline MB parasitic is labeled in Figure 5-2 and tabulated in Table 5-2.

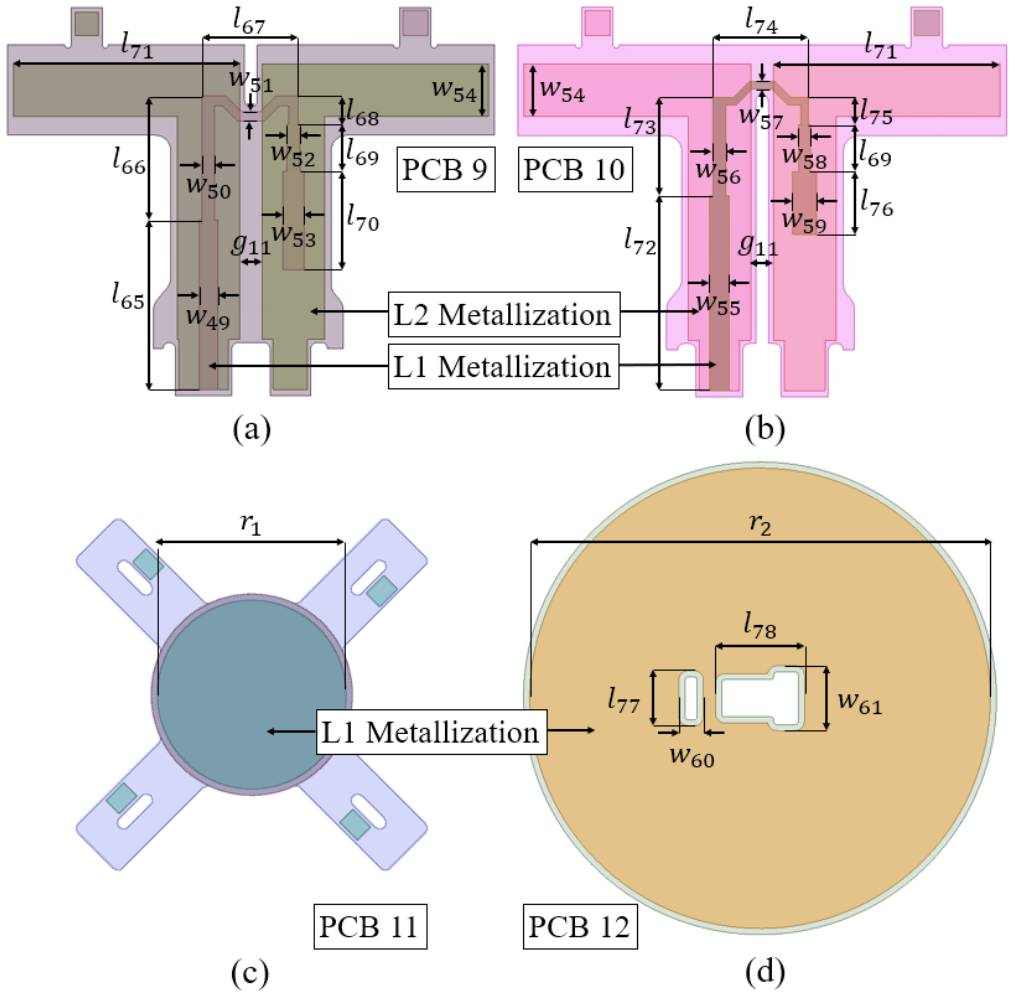

Figure 5-2: PCBs of (a) HB +45° balun, (b) HB −45° balun, (c) HB parasitic, and (d) baseline MB parasitic for use in the tri-band array environment.

Table 5-2: Dimensions of HB PCBs and MB parasitic PCBs. All units are in inches.

w_{49}	w_{50}	w_{51}	w_{52}	w_{53}	w_{54}	w_{55}	w_{56}	w_{57}	w_{58}	w_{59}
0.059	0.040	0.030	0.044	0.069	0.169	0.063	0.042	0.024	0.038	0.077
w_{60}	w_{61}	l_{65}	l_{66}	l_{67}	l_{68}	l_{69}	l_{70}	l_{71}	l_{72}	l_{73}
0.080	0.212	0.542	0.396	0.307	0.090	0.150	0.314	0.723	0.620	0.314
l_{74}	l_{75}	l_{76}	l_{77}	l_{78}	g_{11}	r_1	r_2			
0.305	0.087	0.200	0.180	0.290	0.072	0.600	0.151			

5.2 Impact of Tri-Band Array Environment on HB Performance

The impact which the presence of the LB dipoles, MB dipoles, baseline MB parasitics, and radome have on the HB radiation patterns and performance in the baseline design is investigated in this section. Due to the symmetry of the array face, the performance of the +45° polarization of the HB array alone suffices in characterizing the HB performance.

5.2.1 Simulation of HB with/without Baseline Tri-Band Array Environment

This section presents the H-plane radiation patterns, boresight directivities, and HPBWs of the HB array alone on the reflector, as shown in Figure 5-3(a), and in the tri-band environment with the radome, as shown in Figure 5-3(b).

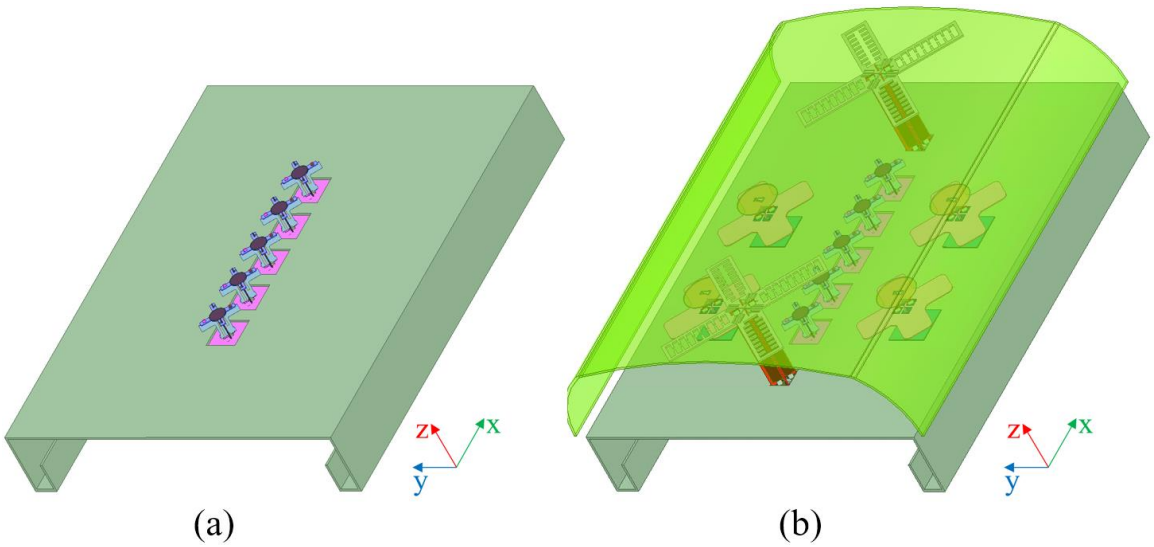

Figure 5-3: Simulation model of HB array (a) alone and (b) with LB dipoles, MB dipoles, baseline MB parasitics, and radome.

The H-plane radiation patterns of the HB array in the absence and presence of the baseline tri-band array environment are shown in Figure 5-4(a) and Figure 5-4(b), respectively. The −3 dB contour is denoted in Figure 5-4 using a dashed red arc. Upon the introduction of the baseline tri-band environment, the shape of the H-plane radiation pattern changes across the band. The −3 dB

half power beamwidth (HPBW) becomes considerably narrower from 3.4 GHz to 3.8 GHz, and the radiation is attenuated at boresight ($\theta = 0°$, in the coordinate system of Figure 5-1) upon placing the HB array in the baseline tri-band array environment. For example, at 4.1 GHz and 4.2 GHz the boresight radiation attenuates by 2.5 dB and 4.4 dB, respectively, relative to the HB array in the absence of the baseline tri-band array environment. Given that the attenuation is at boresight, a similar attenuation is found in the V-plane (xz-plane) radiation pattern.

This attenuation at boresight present upon the introduction of the baseline tri-band array environment degrades the HB boresight directivity from 13.9 dBi to 10.3 dBi at 4.2 GHz, as shown in Figure 5-5. This is a 3.6 dB reduction in boresight directivity at 4.2 GHz. Although the directivity increases between 3.4 GHz and 3.8 GHz, it is due to the unacceptable narrowing in the HPBW which occurs in this frequency range.

Unlike the other frequencies, the magnitude of the H-plane radiation pattern at 4.2 GHz drops below the −3 dB contour at four angles, namely the angles corresponding to the labels A, B, C, and D, in Figure 5-4(b). This introduction of the boresight radiation attenuation at 4.2 GHz renders the HPBW at this frequency somewhat ill-defined. The reason for this is that there are now two angular regions in which the magnitude of the normalized radiation pattern exceeds −3 dB at 4.2 GHz. As shown in Figure 5-4(b), one of these regions extends from angle A = 324° to B = 352° and the other region extends from angle C = 8° to D = 39°. This leads to three different possible definitions for the HPBW at 4.2 GHz. The HPBW could be defined using the angle between A and B, yielding 28°, C and D, yielding 31°, or A and D, yielding 75°.

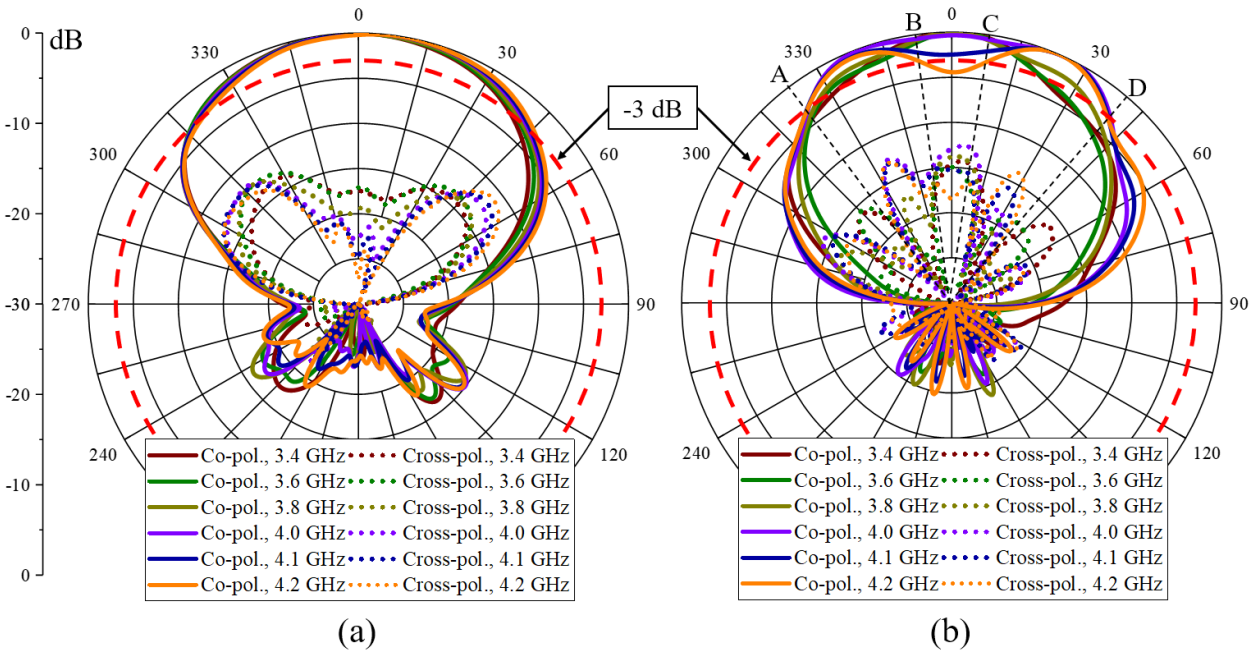

Figure 5-4: Simulated +45° HB H-plane radiation patterns with the HB array (a) alone and (b) with LB dipoles, MB dipoles, baseline MB parasitics, and radome.

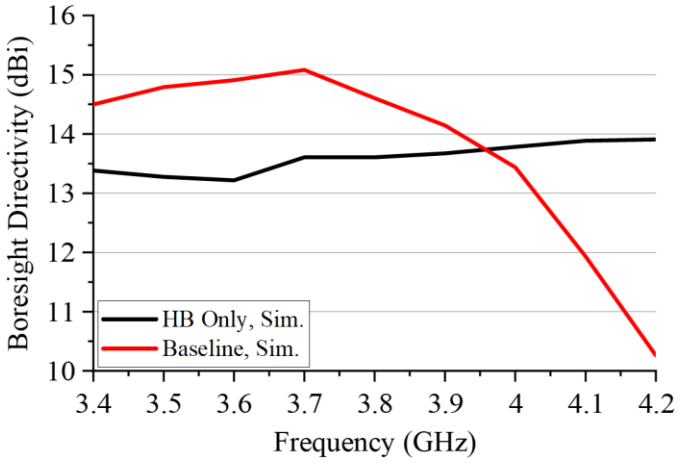

Figure 5-5: Simulated boresight directivity of the +45° HB array for HB only and the baseline tri-band array environments.

The HPBW is plotted as a function of frequency across the HB operating band in Figure 5-6, in which the three different definitions for the HPBW at 4.2 GHz are denote AB, CD, and AD. The targeted HPBW, per the design specification, of 60° is denoted by the black dashed line.

Although it is not possible to maintain a perfectly flat 60° HPBW across the band, the design should achieve this on average across the operating band with as low of variance as possible. The HB array alone on the reflector exhibits a stable HPBW across the band, which varies from 82° to 88°; however, it exceeds the targeted 60° HPBW substantially. Upon the introduction of the baseline tri-band array environment, the HPBW varies from 48° to 77° from 3.4 GHz to 4.1 GHz. Regardless of which definition for the HPBW is selected at 4.2 GHz, this result is unacceptable. Therefore, the simulation shows that the introduction of the baseline tri-band array environment significantly reduces the HPBW from 3.4 GHz to 4.0 GHz, while also exhibiting severe boresight attenuation from 4.1 GHz to 4.2 GHz.

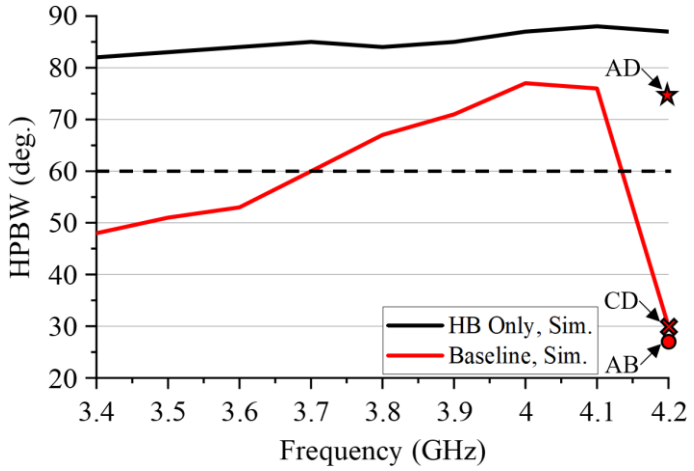

Figure 5-6: Simulated HPBW of the +45° HB array for HB only and the baseline tri-band array environments.

5.2.2 Discussion of Baseline HB Performance

The degree to which the mutual coupling between the baseline HB array and the LB dipoles, MB dipoles, MB parasitics, and radome degrades the HB performance has been demonstrated through full-wave simulation. The implications of the H-plane radiation pattern, boresight directivity, and HPBW instability, if the baseline tri-band array environment were to be used as part of a BSA, are discussed below.

In order to provide uniform cellular coverage across the HB operating band, a BSA should have a radiation pattern which is stable across the operating band. This helps to ensure that no matter what frequency within the operating band the cellular service provider is operating at, the angular coverage and received signal strength within the service sector remains the same. Furthermore, unless a BSA is specifically designed to have an H-plane radiation pattern which is steered off of boresight, typically the maximum radiated power is meant to occur in the boresight direction.

The variation in the H-plane radiation pattern across the band for the HB array alone on the reflector, as shown in Figure 5-4(a), is minimal and the maximum radiated power is directed at boresight. However, this is an oversimplified array environment which is not indicative of the dense array environments commonly found in BSA designs. Furthermore, the HPBW corresponding to the HB array alone on the reflector, although stable, is significantly higher than the target HPBW of 60°.

The HB H-plane radiation patterns corresponding to the baseline tri-band array environment with radome vary drastically across the band. This variation across the band can be captured through visually overlaying the H-plane radiation patterns, as shown in Figure 5-4(b); however, it is also quantifiable through evaluating the boresight directivity and HPBW as functions of frequency, as well as the beam peak location, and beam peak center of each radiation pattern. The beam peak location is the angle at which maximum power is radiated, which is nominally the boresight direction. The beam peak center location is the direction of the angle which bisects the angle between the two half-power, −3 dB, points, which is also nominally the boresight direction.

The simulated beam peak location of the baseline design changes from boresight at 3.4 GHz, to +24° at 4.1 GHz and 4.2 GHz, as shown in Figure 5-7(a) and Figure 5-7(b), respectively. Here

the blue crosses denote the simulated beam peak locations for the baseline design. From Figure 5-7(a) it is seen that at 4.1 GHz the simulation of the baseline design has a beam peak center location which is well centered near the target beam peak center. However, the beam peak itself deviates from the design target beam peak location by +24°.

For a BSA designed to have maximum radiation in the boresight direction, the beam peak center should also be at boresight. However, as is shown in Figure 5-7(b) at 4.2 GHz, this is not the case for the simulated baseline design due to the attenuation at boresight. Ideally, for a BSA the peak of the radiation would occur at boresight and monotonically decrease in magnitude away from this region, with little to no radiation in the 180° sector opposite boresight. However, in the simulated baseline design, not only is the beam peak directed away from boresight at 4.1 GHz and 4.2 GHz, but also due to the attenuation at boresight, the radiation pattern does not monotonically decrease away from this peak point. For example, Figure 5-7(a) and Figure 5-7(b) show that though the radiation intensity decreases to the right side of the beam peak, the radiation intensity reaches nearly another second peak at +335° off of boresight (left of boresight).

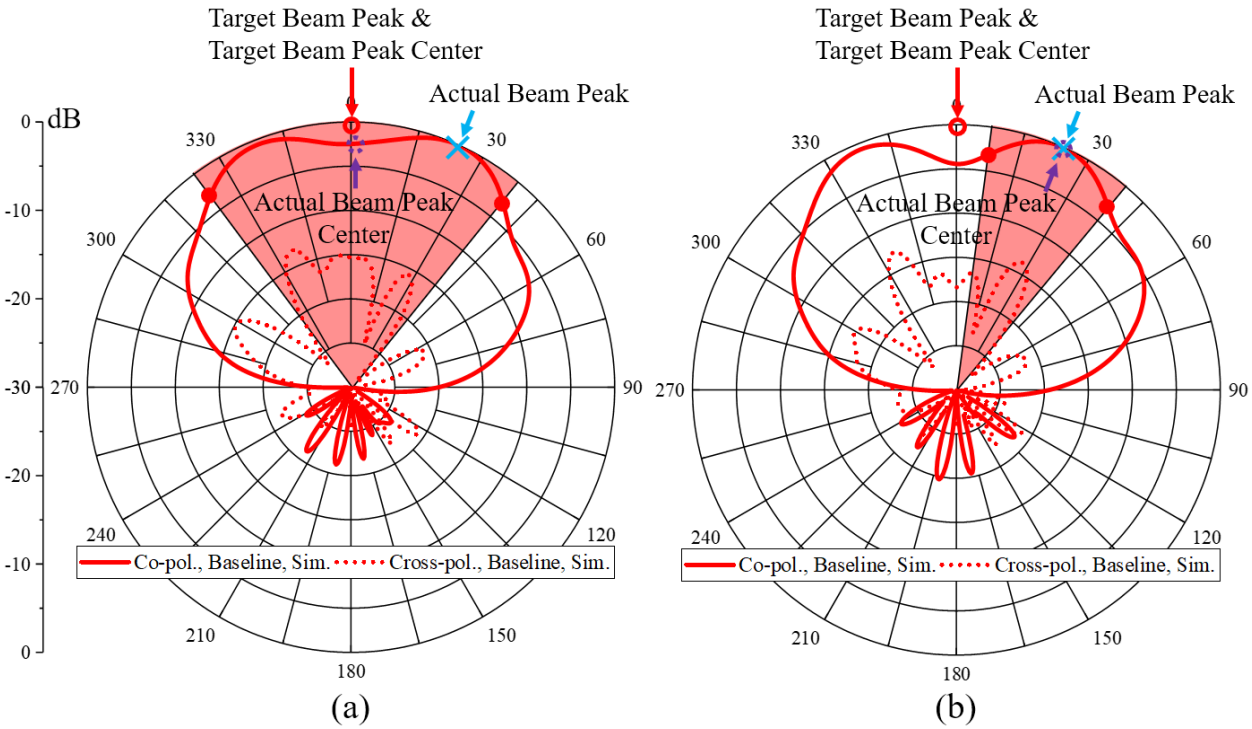

Figure 5-7: Beam peak of simulated H-plane radiation pattern of the HB array in the baseline tri-band array environment at (a) 4.1 GHz and (b) 4.2 GHz.

When the radiation intensity does not monotonically decrease away from the beam peak, the shape of the radiation pattern is difficult to determine from the HPBW alone. For example, the HPBW at 4.2 GHz for the baseline simulation is only 30°. If one assumes that the radiation intensity corresponding to this HPBW is monotonically decreasing, a narrow pencil beam would be expected. However, from Figure 5-7(b) it is seen that the pattern is not that of a narrow pencil beam, but instead more of a fan beam with significant radiation attenuation at boresight.

The change in radiated power at boresight versus frequency is quantified via the boresight directivity shown in Figure 5-5. Due to the fact that the boresight directivity at 3.4 GHz is 14.5 dBi, and at 4.2 GHz is only 10.3 dBi, the difference in signal strength available at these frequencies for a user positioned at boresight would be approximately 4.2 dB. This variation in signal strength would lead to degraded cellular service for users at boresight at 4.2 GHz compared to 3.4 GHz.

The drastic variation in the HPBW observed across the band, as shown in Figure 5-6, would also significantly change the angular region over which a user can be serviced for a given receiver sensitivity, were the baseline tri-band array to be used as part of a BSA system. This variation in the service area as a function of frequency would also lead to issues when planning a cellular network consisting of many BSAs distributed throughout a region. Ultimately, the variation observed in the boresight directivity and HPBW across frequency would lead to non-uniform cellular coverage areas across the HB frequency range if the HB array in the baseline tri-band environment were to be used as part of a BSA. The non-uniform cellular coverage would lead to geographical areas which would have poor cellular reception, and therefore a poor cellular network.

No one single parameter alone, such as HPBW, directivity, cross-polar radiation, etc., should be used in determining whether an antenna array will perform well if used in a BSA system. Only after considering all of the key performance parameters together can a full picture be constructed regarding how the proposed antenna array will perform. The performance of a BSA system depends on the simultaneous optimization of a multitude of electrical parameters.

The next sections will systematically identify and propose solutions to the multiple sources of mutual coupling which degrade the HB array performance in the presence of the baseline tri-band array environment. Due to the complexity of the array face and the multiple sources of mutual coupling, two different proposed design techniques will be implemented in the final proposed tri-band array environment to address the two different sources of interference.

5.3 Fabry-Perot Cavity Antenna (FPCA) for Directivity Enhancement

This section addresses the hypothesis that the radome is a partially reflecting surface (PRS), which results in reflected waves which destructively interfere with the incident wave above 4.0 GHz. The destructive superposition of these EM waves leads to a reduction in the boresight directivity, thereby causing a deviation of the beam peak location, and beam peak center away from boresight in the H-plane. In order to improve the boresight directivity and control the HPBW of the HB array, an FPCA is proposed.

First, the baseline design along with the proposed FPCA model are discussed. Then, equivalent circuit models are presented for the baseline environment and the proposed FPCA design. The resonance condition of the FPCA is shown to be satisfied using both an equivalent circuit analysis, as well as through analytic evaluation based on results of ray tracing. Finally, the proposed FPCA is added to the baseline tri-band array environment and the radiation characteristics are evaluated through full-wave simulation across the HB operating band. The results show that the inclusion of the FPCA in the baseline tri-band array environment greatly improves the boresight directivity of the HB array, while also stabilizing the HPBW around the targeted value of 60° from 4.0 GHz to 4.2 GHz and centering the beam peak near boresight. Finally, this section concludes with a discussion of the findings.

5.3.1 PRSs and using FPCAs for Directivity Enhancement

Trentini's 1956 publication [75] was the first work to propose the idea of using PRSs to form resonant cavities, which would be excited by antennas, for increased directivity. The PRSs discussed throughout his work were realized using multiple methods. For example, perforated conductive sheets, conductive mesh wire screens, and conductive wires were three types of PRSs considered in his work. Others have since used the results of [75] to design FPCAs using multilayer

periodic surfaces [130]–[132], electrically thick dielectric slabs [133], and electrically thin dielectric slabs [134]. Trentini derived the resonance condition for an FPCA using ray tracing theory in [75]. Considering a plane wave defined with zero-phase incident on a PRS, which has a reflection phase (phase of reflection coefficient) φ_{PRS}, located a height h above a conducting ground plane, which has reflection phase φ_{GND}, this resonance condition can be expressed as

$$f_o = \frac{c}{4\pi h}(\varphi_{PRS} - \varphi_{GND} + 2N\pi), \qquad N = 0,1,2,\ldots \tag{5-1}$$

in which c is the speed of light in vacuum. Most often, publications have focused on the first resonance mode, i.e., $N = 0$ since it minimizes the resonant cavity height, h, for a fixed frequency. In order for the resonance condition to be satisfied at two frequencies, f_l and f_h, such that $f_h > f_l$, with h and φ_{GND} held constant it follows that

$$f_l = \frac{c}{4\pi h}\left(\varphi_{PRS,l} - \varphi_{GND} + 2N\pi\right), \qquad N = 0,1,2,\ldots \tag{5-2}$$

$$f_h = \frac{c}{4\pi h}\left(\varphi_{PRS,h} - \varphi_{GND} + 2N\pi\right), \qquad N = 0,1,2,\ldots \tag{5-3}$$

Under these constraints, these two equations are satisfied for all values of N if $\varphi_{PRS,h} > \varphi_{PRS,l}$. This is to say that equations (5-2) and (5-3), along with the stated constraints, imply that for broadband operation of the FPCA, over which the resonance condition is satisfied, the phase of the PRS must increase with frequency, i.e., have a positive phase slope.

Neglecting the curvature of the radome, the baseline design can be modeled as an HB radiation source below a PRS, denoted by PRS_1. This PRS representing the radome has radome thickness T_{RA}, relative permittivity ε_{r_1}, and is positioned a height h_{c_0}, above the reflector. This simplified baseline geometry is shown in Figure 5-8(a).

The proposed FPCA utilizes the same radome and radome height as the baseline design, after all it is a design constraint; however, it introduces a dielectric superstrate, denoted by PRS_2, at a height h_{c_2} above the conducting ground plane. The geometry of the proposed FPCA is shown in Figure 5-8(b), in which T_{SS} and ε_{r_2} represent the thickness and relative permittivity of PRS_2, respectively. In the proposed geometry, PRS_1, PRS_2, and the air gap h_{c_1} between these two PRSs can be thought of as an equivalent PRS, denoted by PRS_{EQ}. Since the height and thickness of the radome remain unchanged from the baseline design it follows that

$$h_{c_0} = h_{c_2} + T_{SS} + h_{c_1} \tag{5-4}$$

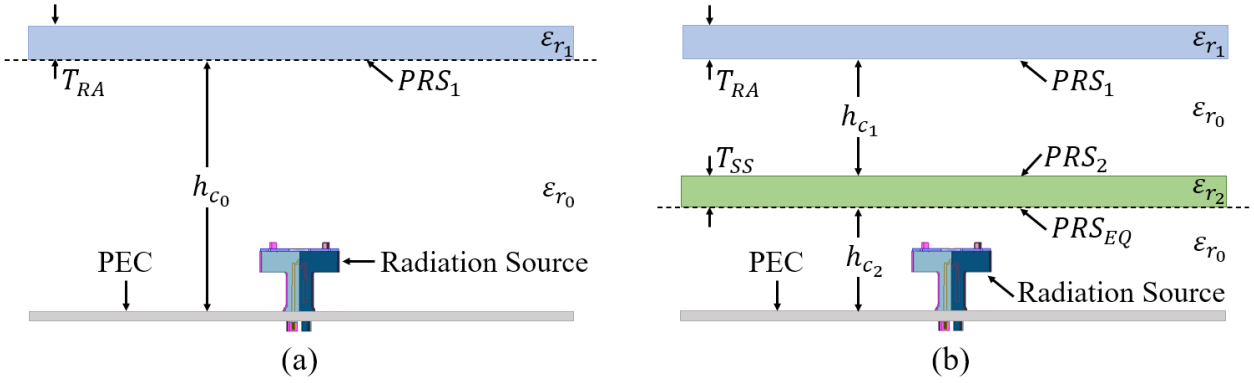

Figure 5-8: Simplified geometry of (a) baseline PRS environment and (b) proposed FPCA environment.

The equivalent circuits of the baseline environment and proposed FPCA can also be constructed using transmission line theory. The equivalent circuit of the baseline design is shown in Figure 5-9(a). Here, the semi-infinite region of free-space above PRS_1 is modeled as a wideband load with corresponding impedance Z_{Air}, in which Z_{Air} is the impedance of free-space. The radome is represented by a transmission line with impedance $Z_{RA} = Z_{Air}/\sqrt{\varepsilon_{r_1}}$. The circuit is excited using a source V_g with source impedance $Z_g = Z_{Air}$. Therefore, Γ_1 corresponds to the reflection

coefficient at the bottom surface of PRS_1, and Γ_0 corresponds to the reflection coefficient at the top surface of PRS_1.

Similarly, the equivalent circuit of the proposed FPCA design can be modeled as three cascaded transmission lines, as shown in Figure 5-9(b). In this circuit the dielectric superstrate, the air between the dielectric superstrate and radome, and the radome itself are modeled having impedances $Z_{SS} = Z_{Air}/\sqrt{\varepsilon_{r_2}}$, Z_{Air}, and $Z_{RA} = Z_{Air}/\sqrt{\varepsilon_{r_1}}$, respectively. There is a reflected wave at the top and bottom surface of each of the dielectric regions. The reflection coefficients at the bottom and top of PRS_2 are denoted by Γ_3 and Γ_2, respectively, whereas the reflection coefficients at the bottom and top of PRS_1 are denoted by Γ_1 and Γ_0, respectively. The length of each transmission line is expressible in terms of the corresponding slab thicknesses. For example, $L_{SS} = 360°(T_{SS}/\lambda_{0,f_c,HB})$, represents the length of the transmission line, in degrees, representing the dielectric superstrate PRS_2, where $\lambda_{0,f_c,HB}$ is the free-space wavelength at the center of the HB operating band, i.e., at 3.8 GHz. Similarly, $L_{Air} = 360°(h_{c_1}/\lambda_{0,f_c,HB})$ and $L_{RA} = 360°(T_{RA}/\lambda_{0,f_c,HB})$ correspond to the length of the transmission lines, in degrees, representing the air region between PRS_1 and PRS_2, and the radome, respectively.

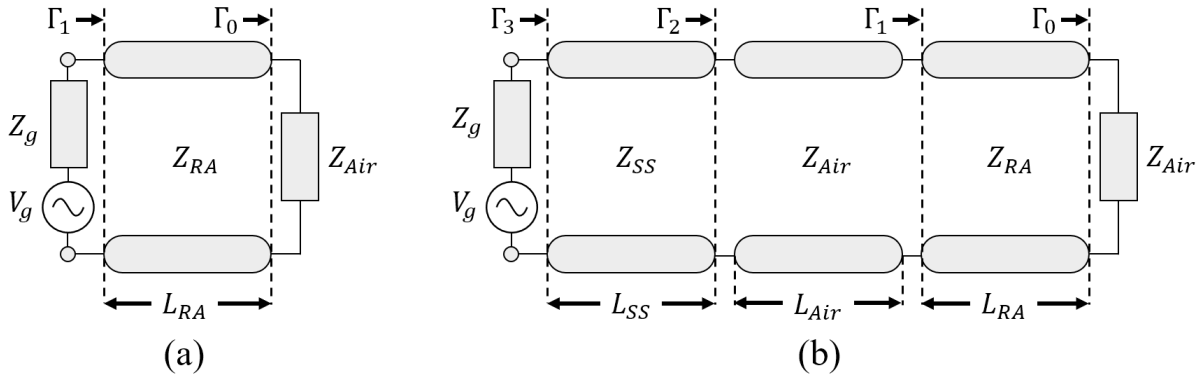

Figure 5-9: Equivalent circuit of (a) baseline PRS environment and (b) proposed FPCA environment.

Since T_{RA}, ε_{r_1}, and h_{c_0} are typically driven by the materials available for forming the radome as well as the design specification governing the overall antenna dimensions, which are outside the control of the designer, the resonance condition for the FPCA becomes a constrained synthesis problem in which T_{SS}, ε_{r_2}, and h_{c_2} are to be optimized. However, a low-cost solution requires a material thickness and relative permittivity which is readily available. It is for this reason that an FR-4 substrate with thickness $T_{SS} = 0.125$" with an approximate dielectric constant of $\varepsilon_{r_2} = 4.4$, is selected for use as the dielectric superstrate PRS_2, in the proposed design.

Given this material selection, the spacing between PRS_1 and PRS_2, namely h_{c_1}, is then selected to satisfy the resonance condition at 4.2 GHz. As is shown in Section 5.2.1, the baseline design has boresight directivity which decreases with frequency from 3.7 GHz to 4.2 GHz, while also having a HPBW which is less than the targeted value of 60° from 3.4 GHz to 3.6 GHz, and greater than the targeted value from 4.0 GHz to 4.2 GHz. Therefore, the FPCA is designed such that it is resonant between 4.0 – 4.2 GHz, thereby increasing the directivity and reducing the HPBW between 4.0 – 4.2 GHz, while not further reducing the HPBW for the lower and middle part of the HB operating band.

Considering the implications of equations (5-2) and (5-3) for $f_l = 4.0$ GHz and $f_h = 4.2$ GHz with h and φ_{GND} held constant, the resonance condition is satisfied for all values of N if $\varphi_{PRS,h} > \varphi_{PRS,l}$, i.e., when the reflection coefficient of the FPCA has a positive phase slope. It is for these reasons that, the value of h_{c_1} is selected such that the equivalent circuit exhibits a positive phase slope beginning at 4.0 GHz. In this way, the HPBW from 3.4 GHz to 3.6 GHz will not be adversely affected, by being made narrower, and yet the HPBW from 4.0 GHz to 4.2 GHz will reduce closer to the targeted value of 60° while increasing the boresight directivity in the upper part of the

operating band as well. For these reasons, a value of $h_{c_1} = 1.884$" is selected for the proposed design.

The equivalent circuit shown in Figure 5-9(b) is evaluated over a broad bandwidth using the proposed parameter values. The magnitude and phase, $\varphi_{PRS_{EQ}}$, of the reflection coefficient Γ_3 is shown in Figure 5-10. In the figure, three regions with positive phase slope and corresponding reflection magnitudes with local minimums are identified. These regions correspond to the first three FPCA resonance modes with $N = 0$, $N = 1$, and $N = 2$; these modes are centered at 1.38 GHz, 4.38 GHz, and 7.35 GHz, respectively. Furthermore, the broadband design criteria outlined above, namely that the positive phase slope begins at 4.0 GHz, has been confirmed for the second resonance mode, i.e., $N = 1$, as shown in Figure 5-10.

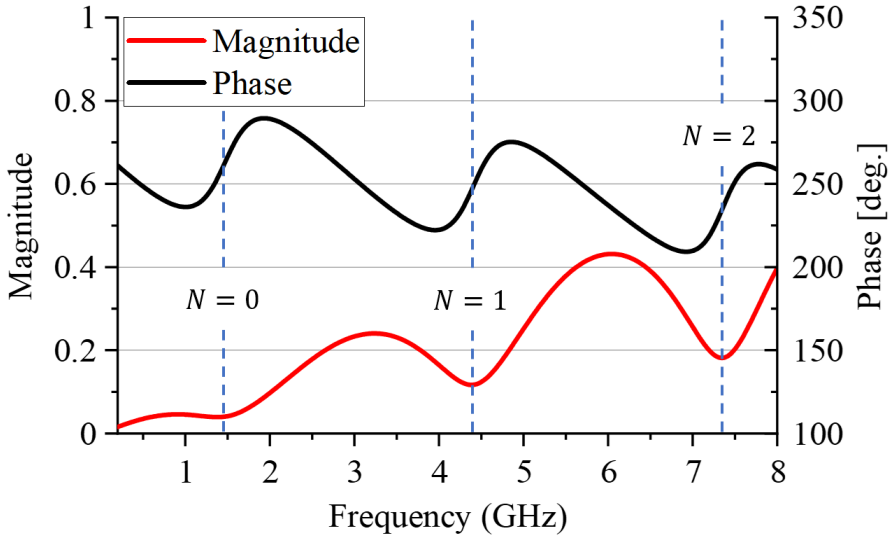

Figure 5-10: Reflection coefficient of proposed FPCA equivalent circuit.

It is seen from (5-1) that for a fixed resonant frequency, the height of the FPCA increases as the mode-order increases. Therefore, while $N = 0$ will theoretically yield the lowest profile FPCA for a fixed resonant frequency, physically it is not possible in this array environment due to the

minimum height of the radome being driven by the overall height of the LB dipole itself. It is for this reason that the second resonance mode ($N = 1$) is selected for the proposed design.

The fact that the proposed design satisfies the FPCA resonance condition described by equation (5-1) can also be shown analytically using the results of the ray tracing analysis first demonstrated in [75]. In order to do this, equation (5-4) is used to calculate h_{c_2}, yielding $h_{c_2} = 1.668" = 0.0424$ m. Assuming the metallic ground plane to be a perfect electric conductor (PEC) with reflection phase $\varphi_{GND} = \pi$, and using $\varphi_{PRS_{EQ}} = +248.7°$ at the center of the positive phase slope region shown for $N = 1$ in Figure 5-10, equation (5-1) yields

$$f_{N=1} = \frac{c}{4\pi(0.0424\ m)}\left(248.7°\frac{\pi}{180°} - \pi + 2\pi\right) = 4.22\ GHz \tag{5-5}$$

Therefore, it has been demonstrated through the use of an equivalent circuit that the proposed design satisfies the resonance condition for an FPCA resonant in mode $N = 1$ beginning at 4.0 GHz through 4.8 GHz. Furthermore, the satisfaction of the resonance condition through the use of the proposed geometry has been verified analytically using equation (5-1). The next section evaluates the proposed technique through simulation of the tri-band array environment in the presence of the proposed FPCA. The resulting radiation characteristics are presented and discussed.

5.3.2 Evaluation of Proposed FPCA in Tri-Band Array Environment

This section presents the results of the simulated radiation patterns of the HB array in the baseline tri-band array environment upon the addition of the FPCA proposed in Section 5.3.1. The geometry of the array environment is shown in Figure 5-11, in which the geometry matches the baseline design with the exception that now the proposed FR-4 dielectric superstrate is introduced at the height h_{c_2}, above the metallic reflector.

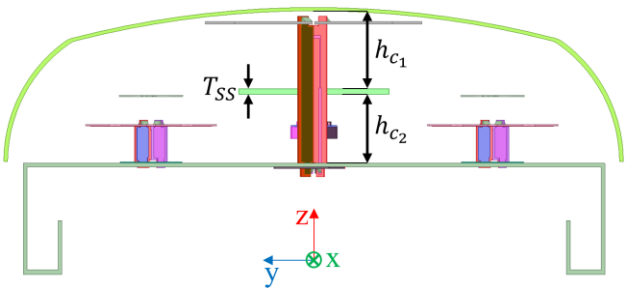

Figure 5-11: Tri-band array environment with the proposed FPCA.

The H-plane radiation patterns of the HB array with the proposed FPCA are shown in Figure 5-12. Upon the introduction of the FPCA, the shapes of the H-plane patterns become more uniform across the band than those of the baseline design, whose patterns are shown in Figure 5-4(b). In particular, the radiation patterns at 4.1 GHz and 4.2 GHz no longer exhibit unacceptable attenuation in the boresight direction. Given that the improvement in radiation occurs at boresight, a similar increase in radiated power is found in the V-plane. The increase in the radiated power at boresight results in an increase in the boresight directivity, while also moving the beam peak location closer to boresight.

Figure 5-13 shows the increase in boresight directivity in the upper part of the of the operating band, upon the implementation of the proposed FPCA into the baseline environment. The boresight directivity at 4.2 GHz improves from 10.3 dBi to 14.0 dBi in moving from the baseline to the proposed FPCA design. Similarly, the boresight directivity at 4.0 GHz increases from 13.4 dBi to 15.2 dBi in moving to the proposed FPCA. Although the boresight directivity increases across the entirety of the HB operating band, the increase in the lower part of the operating band is much less than in the upper part of the operating band. The increase in the middle part of the operating band is primarily due to the reduction in the HPBW.

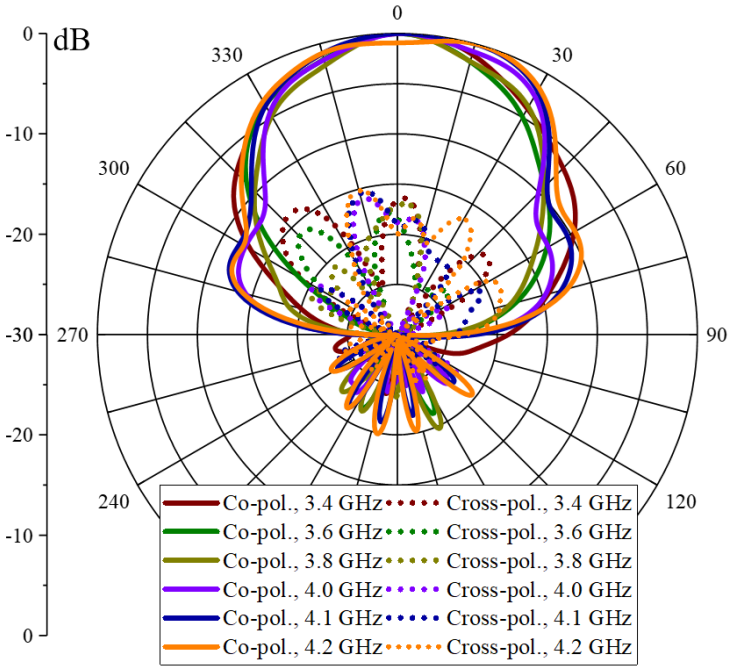

Figure 5-12: Simulated +45° HB H-plane radiation patterns of baseline design with proposed FPCA.

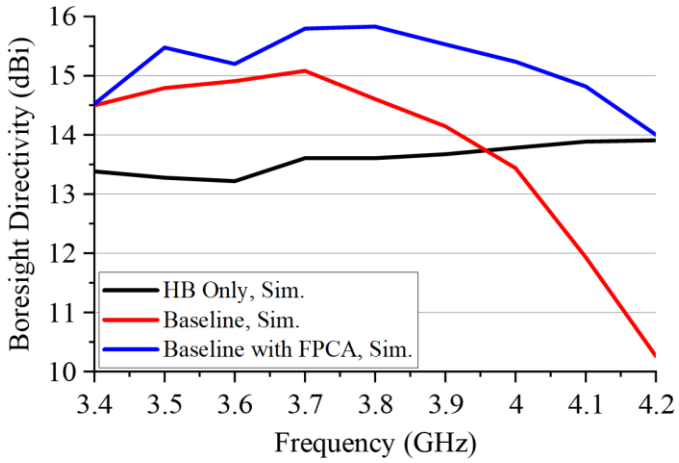

Figure 5-13: Simulated +45° HB boresight directivity for HB only, baseline, and baseline with FPCA array environments.

The HPBW is compared for the HB only, baseline, and baseline with the proposed FPCA simulations in Figure 5-14. The targeted design HPBW of 60° is marked on the figure using a dashed black line across the operating band. In the lower part of the operating band, from 3.4 GHz

to 3.6 GHz, the HPBW does not become significantly narrower upon the introduction of the FPCA. From 3.7 GHz to 4.1 GHz the beamwidth reduces significantly in moving to the design using the FPCA antenna, falling below the targeted HPBW of 60°. At 4.2 GHz the HPBW improved from 30° in the baseline design to 63° in the design using the proposed FPCA.

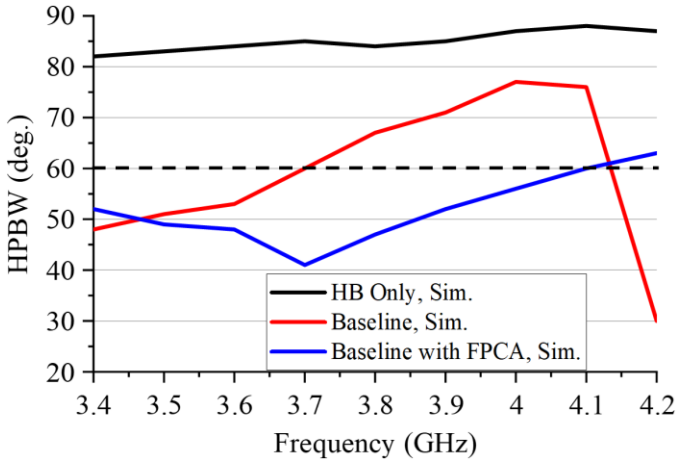

Figure 5-14: Simulated +45° HB HPBW for HB only, baseline, and baseline with FPCA array environments.

5.3.3 Discussion of Results

An FPCA, realized using low-cost widely available electrically thin dielectric materials, is designed for resonance in the $N = 1$ mode. The design is carried out through the use of an equivalent circuit model of the FPCA. The proposed FPCA design is verified both analytically as well as through full-wave simulation of the tri-band array environment. The simulated performance of the baseline array with the proposed FPCA demonstrates a significant increase in the boresight directivity for frequencies above 4.0 GHz, corresponding to the region for which the FPCA is designed to be resonant with positive phase slope. Furthermore, the proposed FPCA left the radiation characteristics from 3.4 GHz to 3.6 GHz largely unchanged, in the region that the FPCA is designed to be non-resonant. Therefore, the proposed FPCA has been shown to minimize

the effect of the radome by increasing the boresight directivity over the upper part of the operating band, from 4.0 GHz to 4.2 GHz.

Although the proposed FPCA greatly improves the HB array performance, the HPBW, ranging from 41° to 63°, still does not meet the design criteria of an average HPBW of 60° with minimal variance. The design should have a stable HPBW of approximately 60° across the band. However, the FPCA is designed to address the poor directivity in the upper part of the operating band, not to change radiation characteristics on the lower and middle part of the operating band for which the baseline HPBW is already too narrow.

In order to further improve the radiation characteristics of the HB array, the HPBW must have an average value of approximately 60° and be stabilized across the operating band. In order to do this, a second source of mutual coupling is identified and discussed in Section 5.4, along with a proposed design technique to significantly reduce the mutual coupling which is identified as the primary source of the narrow HPBW in the lower and middle part of the HB operating band.

5.4 Reducing Modal Significance (MS) of MB Parasitic for Increased HPBW

This section confirms the hypothesis that a radiating resonance mode is excited on the baseline MB parasitics in the lower part of the HB operating band upon the excitation of the HB array in the tri-band array environment. Once excited the MB parasitics become secondary radiation sources which produce radiated fields that superimpose with the primary radiated fields produced by the HB array. The superposition of the primary and secondary radiation sources behaves as a pseudo-three-element array in the H-plane, which thereby leads to a reduction in the H-plane HPBW across the band, but most significantly from 3.4 GHz to 3.7 GHz as shown in both the

baseline results of Section 5.2.1 and the proposed FPCA results of Section 5.3.2. Although currents are also induced on the baseline MB parasitics at higher frequencies, such as at 4.2 GHz, the magnitude of the secondary excitations at these frequencies are much less; therefore, the narrowing of the H-plane HPBW is negligible for these higher frequencies.

First, a discussion regarding the hypothesis that the baseline MB parasitics behave as secondary radiation sources, which narrow the HPBW in the vicinity of 3.4 GHz, is presented. The basis for this hypothesis is first presented through a pair of full-wave EM simulations in which the MB sub-arrays are positioned adjacent to the HB array with and without the baseline MB parasitics. Next, array theory is used to derive an analytic expression approximating the normalized HB H-plane radiation pattern under the assumption that the baseline MB parasitics behave as secondary dipole-like radiation sources with magnitudes which decrease with increasing frequency. The reason that the magnitudes are assumed to decrease with frequency in the analytic expression is that the narrowing of the HPBW caused by the mutual coupling sources, decreases with frequencies; therefore, so too should the magnitude of the sources of the mutual coupling. The analytically derived normalized HB H-plane radiation pattern exhibits a reduction in the HPBW near 3.4 GHz, the effect of which decreases with increasing frequency, which is strikingly similar to that which is observed through full-wave simulation.

Next, a characteristic mode (CRM) analysis is performed on the conducting baseline MB parasitic in order to understand if the baseline MB parasitics can theoretically support radiating dipolar current modes. The modal significance (MS) and current distributions of the first six modes are presented and discussed in the context of the hypothesis. Then, the distribution of current induced on the baseline MB dipoles upon the excitation of the HB array in the tri-band array environment is evaluated to confirm its dipolar nature.

A design technique is then proposed to reduce the mutual coupling between the HB array and the MB parasitics, while preserving the MB performance. In particular, the geometry of the MB parasitic is altered in such a way as to reduce the MS of the proposed MB parasitic, thereby ensuring that *if* a CRM is indirectly excited on the proposed MB parasitic in the tri-band array environment, upon the excitation of the HB array, it will result in less radiation than the baseline MB parasitic. Finally, this section concludes with a discussion of the findings.

5.4.1 Hypothesis of Induced Currents on Baseline MB Parasitics

In order to investigate the impact of the MB dipoles and baseline MB parasitics on the HB radiation performance, two simplified array environments are considered. First, the tri-band array environment is simplified to contain only the HB dipoles, reflector, MB dipoles, and baseline MB parasitics, as shown in Figure 5-15(a). Next, the baseline MB parasitics are removed from the model, leaving the HB dipoles, reflector, and MB dipoles, as shown in Figure 5-15(b). The radiation characteristics are then calculated using HFSS in order to quantify the effect of the baseline MB parasitics' presence on the HB array, as well as to understand what effect, if any, the MB dipole itself plays in the mutual coupling observed in the baseline design.

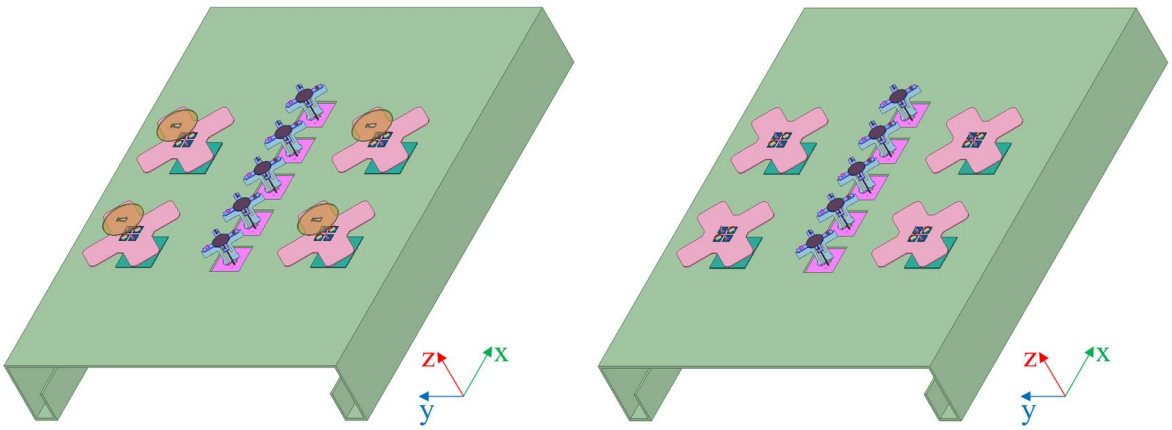

Figure 5-15: HB array with MB dipoles (a) with and (b) without baseline MB parasitics.

The HB H-plane radiation patterns in the presence of the MB dipoles with and without the baseline MB parasitics are shown in Figure 5-16(a) and Figure 5-16(b), respectively. When the baseline MB parasitics are present, the shape of the H-plane radiation pattern changes with frequency. Whereas, when the MB parasitics are removed from the model, leaving the HB in the presence of the MB dipoles alone, the H-plane radiation pattern is nearly constant over the HB operating band. In fact, the HB H-plane radiation patterns in the presence of the MB dipoles alone look very similar to the results shown in Figure 5-4(a), for which the HB array is alone on the reflector. These results demonstrate that it is the presence of the baseline MB parasitics, not the MB dipoles themselves, which cause narrowing of the HPBW in the lower part of the HB operating band.

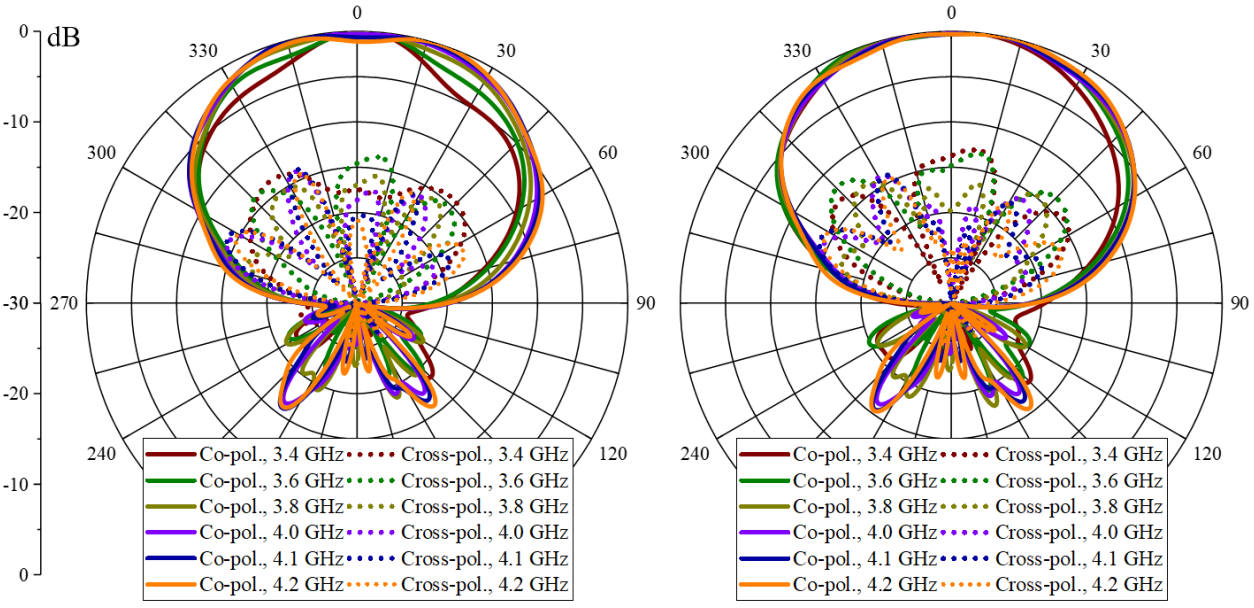

Figure 5-16: Simulated +45° HB H-plane patterns in the presence of the MB dipoles (a) with and (b) without baseline MB parasitics.

The reduction in the HPBW caused by the presence of the baseline MB parasitic can be quantified through observing the HPBW of the two array environments versus frequency, as shown

in Figure 5-17. The reduction in the HPBW is seen to be the most severe at 3.4 GHz for which the HPBW reduces from 72° in the presence of the MB dipoles alone, to 37° (48.6%) in the presence of the MB dipoles and baseline MB parasitics. The effect of the baseline MB parasitics on the HPBW decreases increasing frequency, which further suggests that the magnitude of the sources of mutual coupling, i.e., currents induced on the baseline MB parasitics, decrease with increasing frequency. From 3.7 GHz to 4.2 GHz the reduction in the HB HPBW is minimal, due to the presence of the baseline MB parasitic, remaining approximately constant at 7°.

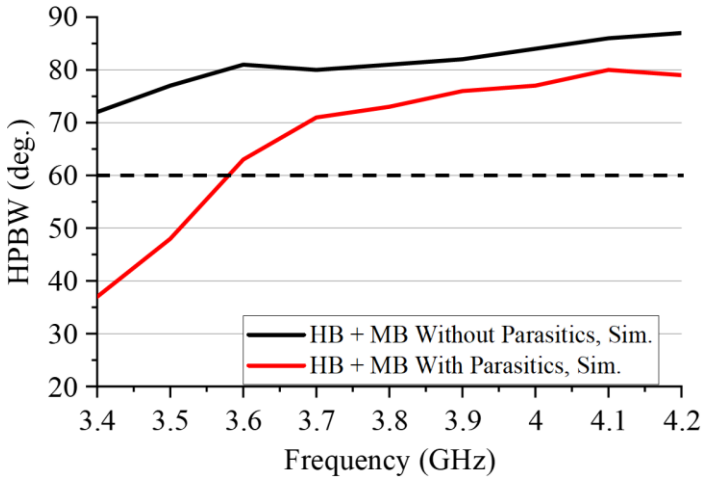

Figure 5-17: Simulated +45° HB HPBW in the presence of the MB dipoles with and without baseline MB parasitics.

The narrowing of the HPBW due to the presence of the MB parasitics has been demonstrated through full-wave simulation of a simplified array environment. The reduction of the H-plane HPBW, which decreases with increasing frequency, is characteristic of an array factor (AF) in the H-plane whose magnitude also decreases with frequency. If currents are induced on the baseline MB parasitics, they can behave as secondary sources of radiation. Since the parasitics reside in the H-plane, these secondary radiation sources would theoretically lead to an AF in the H-plane, and hence a narrower beamwidth. The degree to which the HPBW narrows depends on the magnitude

and phase of the induced current on the baseline MB parasitics as a function of frequency, as well as the spatial distribution of the current on the parasitics. If the magnitude of the induced currents present on the MB parasitics decrease with frequency, as is suspected from the results of this section, it is expected that the reduction in the HPBW will also decrease with frequency.

The hypothesis that a radiating characteristic mode (CRM), whose magnitude decreases with frequency, is excited in the lower part of the HB operating band, for example from 3.4 GHz to 3.7 GHz, on the baseline MB parasitics upon the excitation of the HB array in the tri-band array environment can be confirmed analytically. In order to demonstrate this analytically a two-dimensional (2-D) array configuration, consisting of point sources, is used as an approximate model of the HB array in the presence of the baseline MB parasitics. The geometry of the simplified array is shown for the xy-plane in Figure 5-18(a) and the yz-plane in Figure 5-18(b). In Figure 5-18(a), the orange crosses represent the five HB dipoles spaced linearly along the x-axis with spacing d_{x1} between adjacent HB elements. The blue circles represent the four baseline MB parasitics. The magnitudes of the five HB dipoles are denoted by a_1, a_2,…, a_5, and the four baseline MB parasitics by b_1, b_2,…, b_4. In Figure 5-18(b), the blue lines represent the baseline MB parasitics, and the orange line represents the HB dipoles. The baseline MB parasitics reside at a height d_{z1} above the HB dipoles in the yz-plane. The positions of the point sources representing the HB dipoles and the baseline MB parasitics are tabulated in Table 5-3.

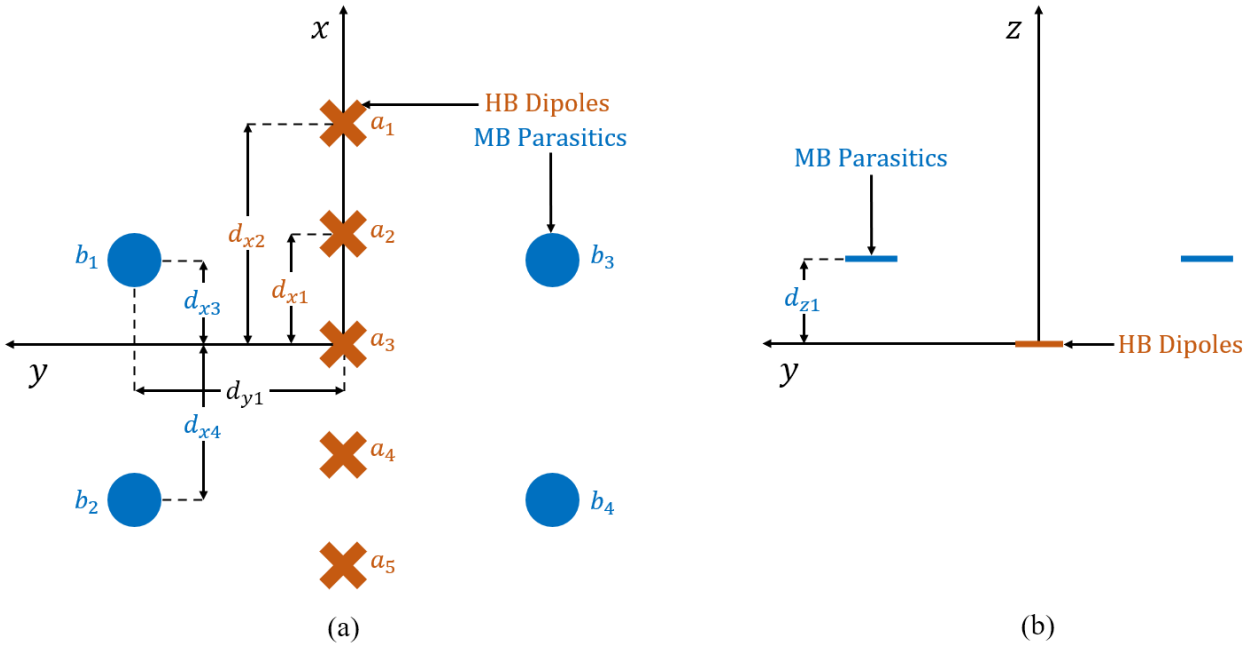

Figure 5-18: Locations of baseline MB parasitics and HB elements in the (a) xy-plane and (b) yz-plane, for use in the analytic 2-D AF model.

Table 5-3: Dimensions used in the analytic 2-D AF model. All units are in inches.

d_{x1}	d_{x2}	d_{x3}	d_{x4}	d_{y1}	d_{z1}
1.772	3.544	1.370	3.230	3.945	0.870

Considering the five HB radiating elements located along the x-axis in the xy-plane, the normalized position vector pointing to the location of the m^{th} radiating element may be written as

$$\hat{\mathbf{r}}'_{HB,m} = x'_{HB,m}\hat{\mathbf{x}} \tag{5-6}$$

Similarly, the four baseline MB parasitics are located with normalized position vectors pointing to the location of the n^{th} radiating baseline MB parasitic by

$$\hat{\mathbf{r}}'_{MB,n} = x'_{MB,n}\hat{\mathbf{x}} + y'_{MB,n}\hat{\mathbf{y}} + d_{z1}\hat{\mathbf{z}} \tag{5-7}$$

The normalized position vector pointing in the direction at which the radiated fields are observed may be written in spherical coordinates as

$$\hat{\mathbf{r}} = \frac{x\hat{\mathbf{x}} + y\hat{\mathbf{y}} + z\hat{\mathbf{z}}}{r} = \sin\theta\cos\phi\,\hat{\mathbf{x}} + \sin\theta\sin\phi\,\hat{\mathbf{y}} + \cos\theta\,\hat{\mathbf{z}} \tag{5-8}$$

Therefore, the AF for the geometry of Figure 5-18, can be expressed as [66]

$$f(\theta,\phi) = \sum_{m=1}^{5} a_i e^{jk\hat{\mathbf{r}}\cdot\hat{\mathbf{r}}'_{HB,m}} + \sum_{n=1}^{4} b_i e^{jk\hat{\mathbf{r}}\cdot\hat{\mathbf{r}}'_{MB,n}} \tag{5-9}$$

where

$k = \dfrac{2\pi f_0}{c}$

$f_0 =$ the frequency of operation

Therefore, the AF can be written as

$$\begin{aligned} f(\theta,\phi) = {} & a_3 + a_2 e^{jkd_{x1}\sin\theta\cos\phi} + a_1 e^{jkd_{x2}\sin\theta\cos\phi} + a_4 e^{-jkd_{x1}\sin\theta\cos\phi} \\ & + a_5 e^{-jkd_{x2}\sin\theta\cos\phi} + b_1 e^{jkd_{y1}\sin\theta\sin\phi + jkd_{x3}\sin\theta\cos\phi + jkd_{z1}\cos\theta} \\ & + b_2 e^{jkd_{y1}\sin\theta\sin\phi - jkd_{x3}\sin\theta\cos\phi + jkd_{z1}\cos\theta} \\ & + b_3 e^{-jkd_{y1}\sin\theta\sin\phi + jkd_{x3}\sin\theta\cos\phi + jkd_{z1}\cos\theta} \\ & + b_4 e^{-jkd_{y1}\sin\theta\sin\phi - jkd_{x3}\sin\theta\cos\phi + jkd_{z1}\cos\theta} \end{aligned} \tag{5-10}$$

Evaluating in the H-plane, i.e., for $\phi = 90°$, gives

$$\begin{aligned} f(\theta,\phi = 90°) &= f(\theta) \\ &= a_3 + a_2 + a_1 + a_4 + a_5 + b_1 e^{jkd_{y1}\sin\theta + jkd_{z1}\cos\theta} \\ &\quad + b_2 e^{jkd_{y1}\sin\theta + jkd_{z1}\cos\theta} + b_3 e^{-jkd_{y1}\sin\theta + jkd_{z1}\cos\theta} \\ &\quad + b_4 e^{-jkd_{y1}\sin\theta + jkd_{z1}\cos\theta} \end{aligned} \tag{5-11}$$

Assuming equal magnitude for all four of the baseline MB parasitics, i.e., $Be^{j\phi_b} \equiv b_1 = b_2 = b_3 = b_4$, where ϕ_b is the phase of parasitic excitation, and B is the magnitude of the MB parasitic

excitation, which is a frequency dependent unknown which is hypothesized to decrease with frequency. This simplifies to

$$f(\theta, \phi = 90°) = f(\theta) = \\ = a_3 + a_2 + a_1 + a_4 + a_5 \\ + Be^{j\phi_b} e^{jkd_{z1}\cos\theta}\left(2e^{jkd_{y1}\sin\theta} + 2e^{-jkd_{y1}\sin\theta}\right) \tag{5-12}$$

Defining $A \equiv a_1 + a_2 + a_3 + a_4 + a_5$, and using the cosine identity from Euler's formula

$$\cos(x) = \frac{e^{jx} + e^{-jx}}{2} \tag{5-13}$$

with $x \equiv kd_{y1}\sin\theta$, the AF can be rewritten as

$$f(\theta, f) = A + 4Be^{j\phi_b} e^{jkd_{z1}\cos\theta}\cos\left(kd_{y1}\sin\theta\right) \tag{5-14}$$

In order to evaluate the resulting normalized array pattern, the H-plane element patterns for the MB parasitic and the HB dipoles must be selected. As is discussed in [6, pp. 51−52] and [135], the radiation patterns of a large class of antennas are commonly approximated with a function of the form $\cos^n\theta$, where n is chosen such that the resulting HPBW of the element pattern matches that of the radiating element which it approximates. As described in [6, p. 902], "although idealistic, these patterns were chosen because (1) closed form solutions can be obtained, and (2) they often are used to represent a major part of the main lobe for many practical antennas." Approximating the element pattern in this way provides an accurate radiation pattern shape in the sector of interest, neglecting the minimal radiation found in the sector opposite boresight.

It is known that the HB dipoles have dipolar current distributions when excited. Figure 5-17 shows that the HPBW of the HB dipoles, in the presence of the MB dipoles without MB parasitics, varies from 72° to 81° for frequencies between 3.4 GHz and 3.8 GHz, with a single main lobe and

minimal radiation in the sector opposite boresight. The analytic model is formulated to investigate the reduction observed in the HPBW upon the introduction of the MB parasitics within this frequency range. It is for this reason that an element pattern of the form $\cos^n \theta$, where $n = 1$, corresponding to a HPBW of 75°, is chosen for the HB dipole element patterns between 3.4 GHz and 3.8 GHz. It can be shown that even for an HB element pattern with $n = 1$ (90° HPBW) or $n = 2$ (65.6° HPBW) the reduction of the HPBW in the resulting normalized array pattern can still be predicted; however, the −10 dB HBW will be wider ($n = 1$) or narrower ($n = 2$) than that observed in Figure 5-16(a).

It is hypothesized that the excitation of the HB dipoles induces dipolar current distributions on the baseline MB parasitics at HB frequencies. Under this assumption and the fact that these secondary radiation sources reside over top of an electrically large reflector, it is expected that the radiation patterns corresponding to the secondary radiation sources will resemble that of a sector antenna with one main lobe which can be approximated with a function of the form $\cos^n \theta$. Given that the currents induced on the MB parasitics are indirectly excited, it is expected that they will have a much lower magnitude than the magnitude of the directly excited HB dipoles ($B \ll A$). It can be shown that under these assumptions the shape of the HB element pattern dominates the shape of the resulting normalized array pattern and that the shape of the MB parasitic element pattern results in very little change in the resulting normalized array pattern. For example, selecting $n = 1$ (90° HPBW) or $n = 2$ (65.6° HPBW) for the MB parasitic element pattern results in almost no change in the resulting normalized array pattern due to the relatively low magnitude of B with respect to A. Although the exact radiation patterns could be further refined, for the purpose of this model a value of $n = 1.5$ is chosen, which corresponds to a HPBW of approximately 75°. Therefore, the element patterns are approximated as

$$g_a(\theta) = \cos^{1.5}\theta \tag{5-15}$$

where $g_a(\theta)$ is the element pattern for each of the HB and MB point sources. Under this assumption, the normalized array pattern in the $\phi = 90°$ plane, can be expressed as

$$F(\theta) = f(\theta)g_a(\theta) = \left(A + 4Be^{j\phi_b}e^{jkd_{z1}\cos\theta}\cos\left(kd_{y1}\sin\theta\right)\right)\cos^{1.5}\theta \tag{5-16}$$

In order to evaluate the resulting normalized array pattern, the magnitudes of the element patterns B corresponding to the baseline MB parasitics and their relative excitation phases ϕ_b must be defined as a function of frequency. Given that the MB parasitics are individual indirectly excited secondary radiation sources, it is expected that their magnitude of excitation is much less than the magnitude of the directly excited HB array comprised of five dipoles, namely A. Furthermore, based on the results of Section 5.4.1 it is expected that the magnitude of the currents, and thereby the magnitude of the MB parasitic element patterns, induced on the baseline MB parasitics decrease with increasing frequency. Subject to these constraints the parameters B and the unknown excitation phase ϕ_b are optimized iteratively using MATLAB [136] such that the resulting normalized array patterns at 3.4 GHz, 3.6 GHz, and 3.8 GHz approximate the simulated patterns at these frequencies shown in Figure 5-16(a).

Assuming that $A = 1$, the resulting magnitudes B, corresponding to the element patterns of the MB parasitics versus frequency, are found to be 0.1, 0.05, and 0.02 for 3.4 GHz, 3.6 GHz, and 3.8 GHz, respectively. Although all MB parasitic excitation phases in the vicinity of 180° result in a noticeable reduction in the HPBW from 3.4 GHz to 3.8 GHz, it is found that for $\phi_b = -150°$, the resulting normalized array pattern, as shown in Figure 5-19, matches closest with that of the HB H-plane patterns in the presence of the baseline MB disks shown in Figure 5-16(a).

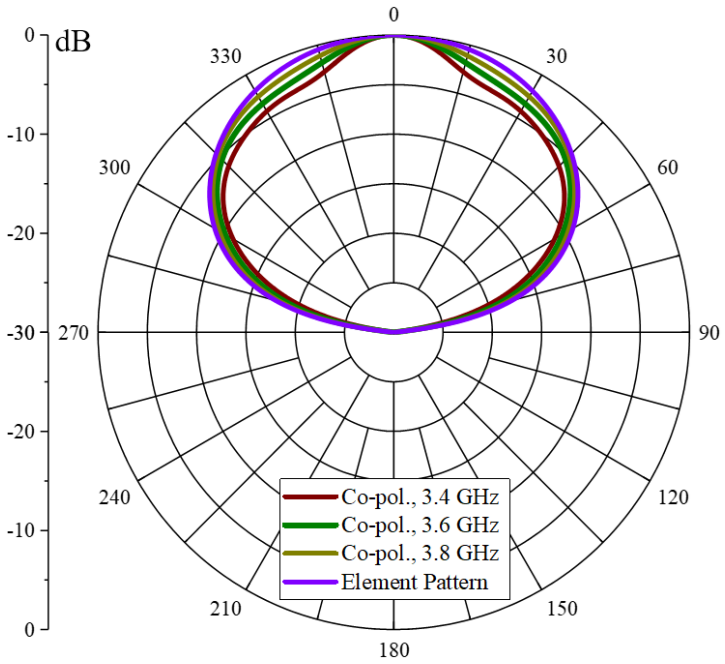

Figure 5-19: The normalized array pattern calculated from the analytic 2-D AF calculation.

The analytic formulation demonstrates that if the baseline MB parasitics behave as parasitic dipole radiators, due to currents induced upon the excitation of the HB array, the resulting HB H-plane radiation patterns can exhibit a narrow HPBW in the lower part of the HB operating band. Furthermore, the results show that if the magnitude of the induced current decreases with increasing frequency, then the reduction in the HPBW also diminishes with increasing frequency. In order for this to occur, the phase of the induced current needs to be approximately $-150°$ out of phase with respect to the HB excitation. It is verified in the following section that these criteria, predicted by the analytic model, are in fact satisfied in the tri-band array environment.

5.4.2 Identification of Induced Currents on Baseline MB Parasitics

In order to verify that this hypothesis is indeed the underlying phenomenon causing the narrowing of the HPBW, the characteristic modes (CRMs) theoretically supported by the geometry of the baseline MB parasitic are identified. Upon identification of the CRMs, the degree to which

each mode contributes to the overall radiated emission is identified and the CRMs are considered as possible modes which *could* be excited in the tri-band array environment. After all, not all CRMs result in radiated emissions and the hypothesis postulates that the CRM excited on the baseline MB parasitic leads to significant radiated emissions. Furthermore, the shape of the resulting radiation pattern should be considered to ensure that the dipole-like element pattern assumed in the analytic model is an accurate approximation to the actual element patterns of the secondary radiation sources.

One method for determining the surface current distributions supported at resonance by an arbitrarily shaped conducting body is through the use of CRM theory. CRM theory was first proposed in 1965 by Garbacz in the context of scattering matrices [137]. Garbacz recognized that an object in resonance behaves "as a parasitically excited antenna," and that the "knowledge of the modes associated with an obstacle would aid the location and design of antennas on its surface to minimize coupling between them" [137]. Although Garbacz first developed CRM theory, it was Harrington and Mautz who generalized the theory for use in antennas [138], [139]. The use of CRM analysis for the design of antennas provides the designer with physical insight into the radiation mechanism of the antenna. A review of CRM theory was published in 2007 and can be found in [140]. More recently, computational electromagnetic (CEM) tools such as Ansys HFSS have introduced CRM solvers for arbitrary geometries.

CRM theory solves an eigenvalue problem of the form

$$X(\vec{J}_n) = \lambda_n R(\vec{J}_n) \tag{5-17}$$

in which X and R are the imaginary and real parts of the symmetric impedance operator, λ_n are the eigenvalues, and $\vec{\boldsymbol{J}}_n$ are the eigenfunctions, i.e., eigencurrents. This eigenvalue problem is typically solved through matrix methods, such as those outlined in [141].

The eigencurrents of a conducting object are real surface currents governed by the object's geometry, independent from any form of excitation. Therefore, although an object may theoretically support a particular resonance mode, a suitable excitation must be applied in order to activate the resonance mode. In the case of a scattering problem in which scattered fields from an obstacle are to be minimized, if possible, it would be desirable to design the source antenna in such a way that it does not excite any CRMs in the obstacle. If the source antenna cannot be changed, altering the obstacles geometry can change the CRMs in such a way as to minimize the interaction.

The eigenvalues of a conducting object describe whether the CRM radiates energy through resonance ($|\lambda_n| = 0$), stores energy in a magnetic field ($|\lambda_n| > 0$), or stores energy in an electric field ($|\lambda_n| < 0$). In practice it is often more insightful to define a term called the modal significance (MS), which is defined in terms of the eigenvalues as,

$$MS = \left| \frac{1}{1 + j\lambda_n} \right| \tag{5-18}$$

The total surface current present on the conducting body is proportional to this term when it is expanded using the CRMs as a basis set, as shown in [138]. It is seen from expression (5-18) that $0 < MS < 1$, and that for maximum radiation ($|\lambda_n| = 0$), MS becomes unity. Therefore, CRMs which have an MS of nearly unity contribute significantly to radiated fields, whereas CRMs which have an MS approaching zero are decaying modes which do not contribute significantly to radiated emissions.

The CRM solver in HFSS is used to calculate the first six CRMs of the baseline MB parasitic satisfying the condition that $MS > 0.002$. For these CRMs, the corresponding MS is shown as a function of frequency in Figure 5-20, with the i^{th} baseline CRM/MS here forward denoted by $CRM_{b,i}/MS_{b,i}$, where the "b" is for "baseline". Of the six baseline CRMs, four of the modes form degenerate pairs. Namely, $CRM_{b,1}$ and $CRM_{b,2}$, taken together, form a degenerate mode pair as do $CRM_{b,4}$ and $CRM_{b,5}$. $CRM_{b,1}$ and $CRM_{b,2}$ have the highest MS, which means that *if* these modes are excited when the HB array is activated then they will contribute significantly to the radiated emissions at HB frequencies. In particular, $MS_{b,1} = MS_{b,2} = 0.81$ at 3.4 GHz, and this value monotonically increases to $MS_{b,1} = MS_{b,2} = 0.97$ at 4.2 GHz. The MS is found to reduce as the CRM order increases, therefore $CRM_{b,3}$ through $CRM_{b,6}$ radiate far less than $CRM_{b,1}$ and $CRM_{b,2}$.

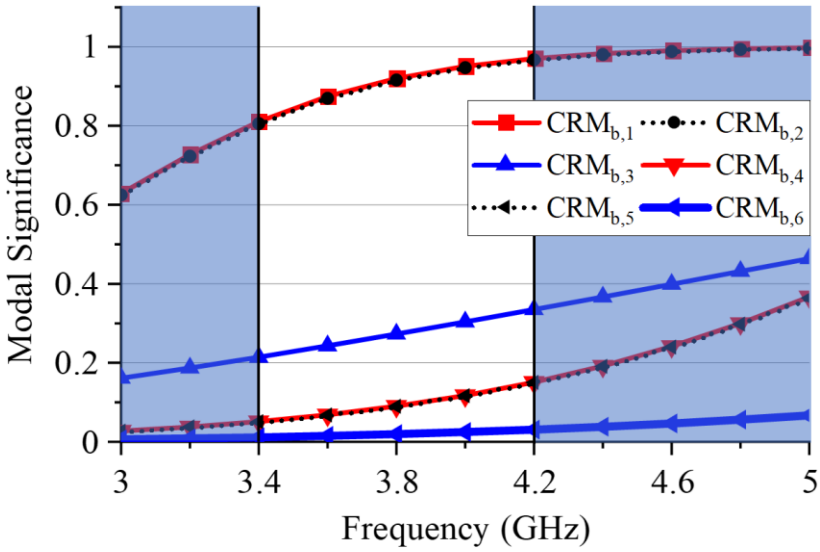

Figure 5-20: The modal significance of the first six CRMs for the baseline metallic MB parasitic.

In order to better understand the CRMs, the vector surface current density is overlaid on the metallic baseline MB parasitic for $CRM_{b,1}$ through $CRM_{b,4}$ at 3.4 GHz, as shown in Figure 5-21(a)-(d). The current distributions of the CRMs are very similar across the operating band to those

shown at 3.4 GHz. $CRM_{b,1}$ and $CRM_{b,2}$ are found to have dipolar distributions where on the two opposing edges of the baseline disk there are currents which form electric dipoles. $CRM_{b,2}$ is a degenerate mode of $CRM_{b,1}$, which is spatially orthogonal to $CRM_{b,1}$. $CRM_{b,3}$ exhibits a current loop along the outside edge of the baseline MB parasitic, forming a magnetic dipole. $CMR_{b,4}$ shows four opposing currents, forming a quadrupole field configuration.

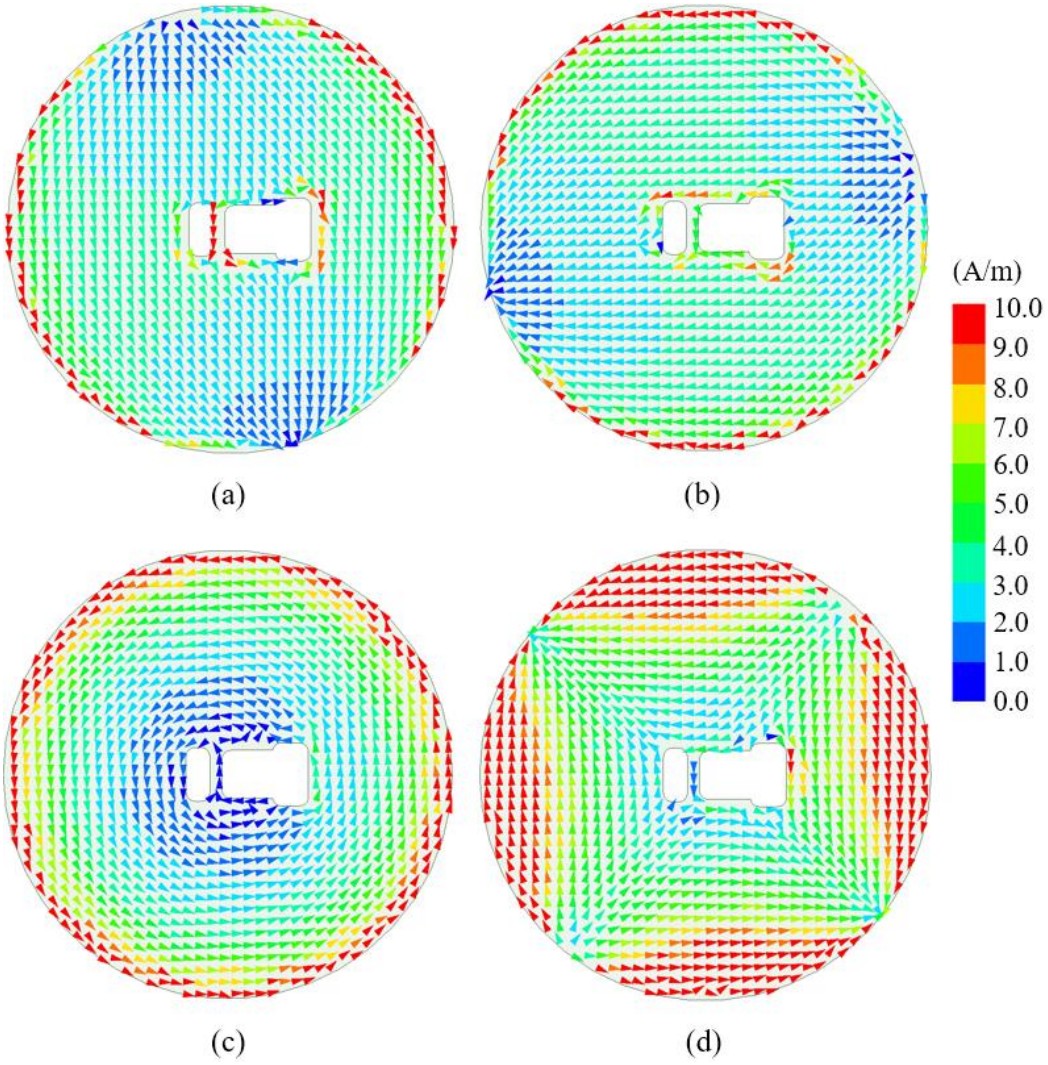

Figure 5-21: Vector surface current density calculated at 3.4 GHz on the conducting baseline MB parasitic using the HFSS CRM solver for (a) $CRM_{b,1}$, (b) $CRM_{b,2}$, (c) $CRM_{b,3}$, and (d) $CRM_{b,4}$.

Although the results of the CRM analysis show that $CRM_{b,1}$ and $CRM_{b,2}$ have the highest MS of the first six CRMs, the MS does not account for the excitation. $CRM_{b,1}$ and $CRM_{b,2}$ will only radiate in the tri-band array environment if they are excited indirectly by the HB dipoles upon the direct excitation of the HB array. In order to determine which CRMs, if any, are excited on the baseline MB parasitics upon the excitation of the HB array environment shown in Figure 5-11, the vector surface current density induced on the parasitics are overlaid on the parasitic geometry. The induced vector surface current densities are shown for 3.4 GHz and 4.2 GHz in Figure 5-22(a) and Figure 5-22(b), respectively.

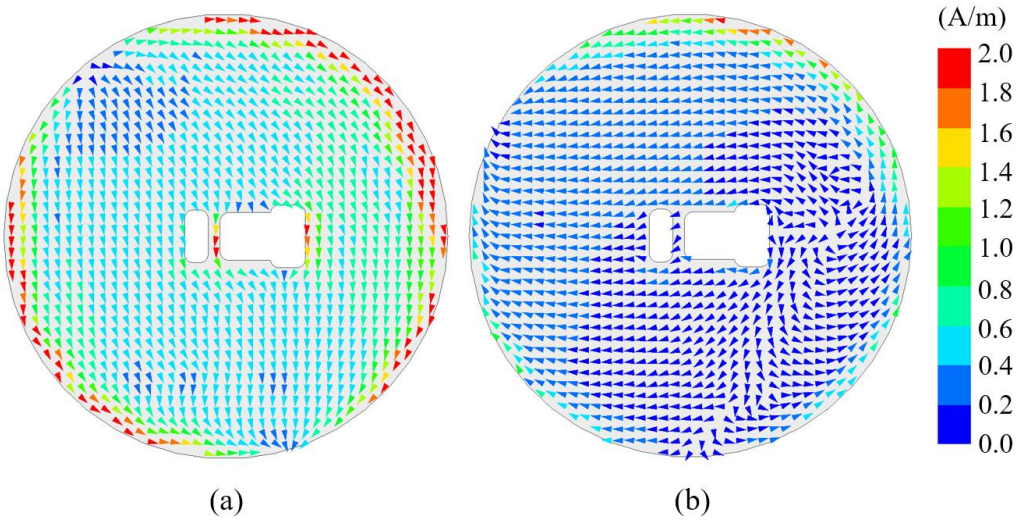

Figure 5-22: Vector surface current density induced on the baseline MB parasitics in the tri-band array environment with the proposed FPCA at (a) 3.4 GHz and (b) 4.2 GHz upon the excitation of the +45° HB array.

The surface current density distribution, which is induced on the conducting surface of the baseline MB parasitics upon the excitation of the +45° polarization of the HB array, matches that of the surface current distribution of $CRM_{b,1}$. The compelling similarity between the two surface current distributions is seen in comparing Figure 5-21(a), calculated using CRM analysis of the baseline MB parasitic alone, with Figure 5-22(a), calculated from using full-wave EM analysis of

the tri-band array environment. It is also found that the excitation of the −45° HB array induces currents corresponding to the spatially orthogonal mode, $CRM_{b,2}$. Due to the high MS of $CRM_{b,1}$ and $CRM_{b,2}$, it is expected that these parasitic excitations do result in radiated fields similar to those assumed in the AF calculation of Section 5.4.1. From Figure 5-22, the magnitude of the surface current density induced on the baseline MB parasitics at 4.2 GHz is far less than that induced at 3.4 GHz. Therefore, although the MS of $CRM_{b,1}$ and $CRM_{b,2}$ increases with frequency, the magnitude of the parasitic excitation decreases with frequency, as is hypothesized in Section 5.4.1. Therefore, it follows that the magnitude of the radiated fields caused by the baseline MB parasitics at 3.4 GHz will exceed those at 4.2 GHz. This finding is consistent with the hypothesis made in Section 5.4.1 in the analysis of the 2-D AF calculation. Furthermore, it validates the assumption that the HB element pattern of the radiating baseline MB parasitic is that of a dipole over a conducting ground plane.

Further insight regarding the current induced on the baseline MB parasitics is found through overlaying the vector surface current density on both the baseline MB parasitic as well as the HB dipole, as shown in Figure 5-23. It is seen from Figure 5-23(a) that the current induced on the baseline MB parasitic at 3.4 GHz is approximately 180° out of phase with respect to the current present on the directly excited HB dipole. This phase difference is also present at 4.2 GHz although the magnitude of the induced current is far less than what is induced at 3.4 GHz, as shown in Figure 5-23(b). This finding is consistent with the hypothesis made in Section 5.4.1 in the analysis of the AF calculation. A discussion regarding the investigation of the hypothesis that currents are induced on the baseline MB parasitics upon the excitation of the HB array, which then become secondary sources of radiation, follows in Section 5.4.3.

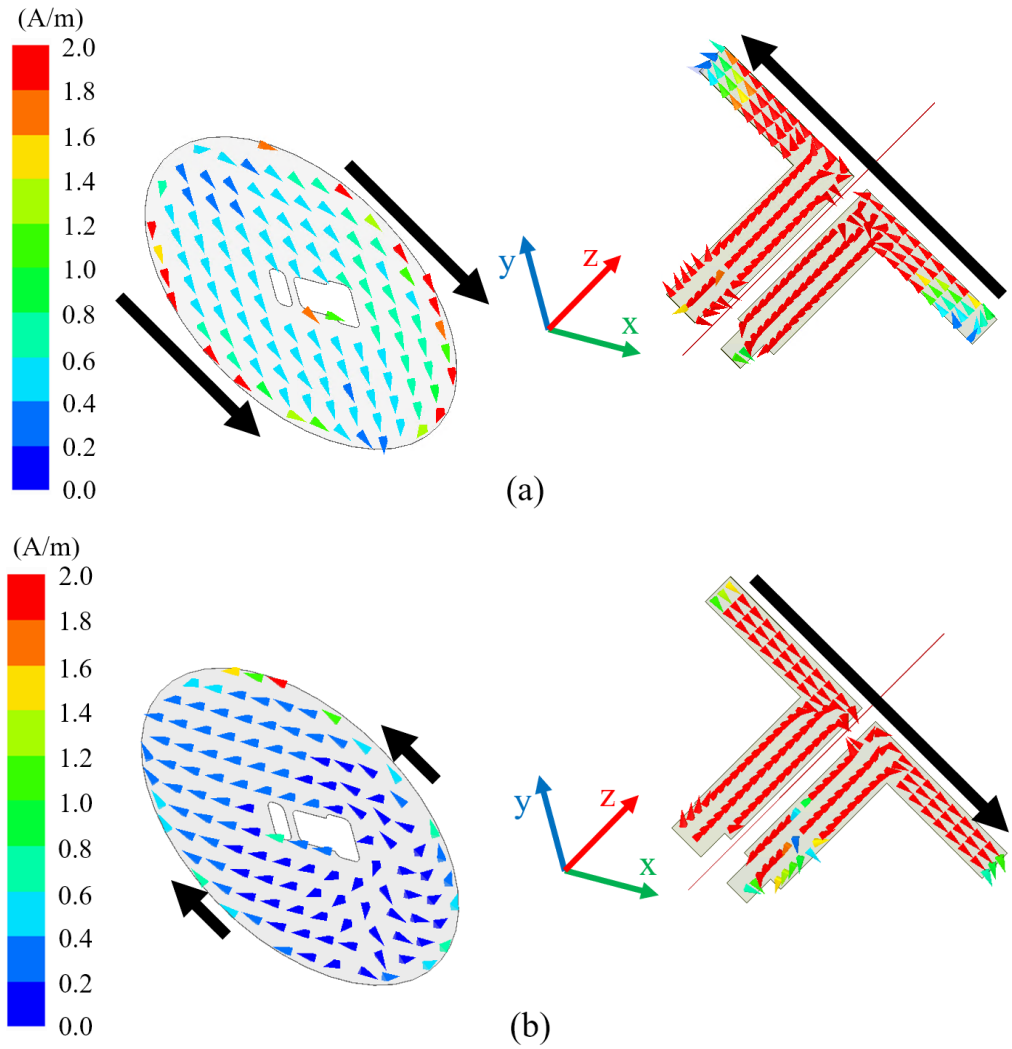

Figure 5-23: Induced vector surface current density on the HB dipole and baseline MB parasitic at (a) 3.4 GHz and (b) 4.2 GHz, upon the excitation of the HB array.

5.4.3 Discussion of Induced Currents on Baseline MB Parasitics

The results of the investigation into the hypothesis that currents are induced on the baseline MB parasitics upon the excitation of the HB array, which then become secondary sources of radiation, has been confirmed. The finding that the magnitude of the current induced on the baseline MB parasitics decreases with increasing frequency agrees well with the results of Section 5.4.1. Furthermore, the 180° phase difference observed between the induced current on the baseline MB parasitics and the HB dipoles agrees well with the finding of Section 5.4.1. In

particular, the phase of the parasitic excitation ϕ_b, used in the HB H-plane AF calculation is $\phi_b = -150°$.

The 30° difference between the phase of the parasitic excitation used in the analytic calculation, to that found through full-wave simulation of the tri-band array environment with the FPCA is suspected to be due to simplifying assumptions made in the analytic calculation. For example, the analytic calculation assumes each baseline MB parasitic to be a single radiation source centered at the location of the middle of the baseline MB parasitic. However, the induced current on the baseline MB parasitic forms two sources along the two opposing edges of the disk, as shown in Figure 5-22. Another source of phase approximation which is made in the analytic calculation is the distance between the HB dipole sources and the baseline MB parasitics along the z-axis, d_{z1}. The conductors comprising the HB dipole arms have a finite width to them, however the center point along this width is selected for the location of the HB dipole sources along the z-axis in the analytic calculation.

Although the analytic calculation could be further refined, it serves as a simplified model to bring to light the underlying phenomenon causing the reduction in the HPBW in the lower part of the HB operating band first observed in Section 5.2.1. The following section proposes a design technique for which the reduction in the HPBW, due to the baseline MB parasitic presence, can be eliminated through modifications in the baseline MB parasitic to lower the MS and change the CRMs, and hence radiated fields, current distributions, and excitation mechanism across the band.

5.4.4 Proposed Technique for Reducing MS of MB Parasitic

The mutual coupling due to the presence of the baseline MB parasitics can in theory be eliminated if the MB parasitics themselves are eliminated. However, upon removing the MB parasitic, the matching of the MB dipole becomes very difficult across the broad MB operating

band. Therefore, a technique is proposed in which the geometry of the MB parasitic is modified in such a way as to maintain broadband matching of the MB dipole while also reducing the mutual coupling between the HB array and the MB parasitic, and therefore the additional radiated fields due to the MB parasitic presence.

The matching of the MB dipole is primarily a function of the macroscopic features of the MB parasitic, such as the parasitic radius and the height of the parasitic above the MB dipole. Whereas the CRMs of the MB parasitic in the HB operating band can be changed through modifications in the electrically small details of the MB parasitic, such as through adding radial slots in the MB parasitic. It is for this reason that a series of radial slots are proposed in the baseline MB parasitic; however, it can be shown that using variations to the proposed technique, other parasitic geometries exist which also simultaneously satisfy the design criteria of low HB MS with broadband MB matching. The length of each slot is optimized to minimize the MS of the MB parasitic across the MB operating band. By reducing the peak MS of the CRMs across the MB bandwidth, the radiation caused by each CRM is minimized. Furthermore, when the geometry is changed, the CRMs themselves can change and the new CRMs may not be excited upon the excitation of the MB dipoles. The optimization of the proposed MB parasitic must satisfy the reduction in the MS at HB frequencies while also maintaining broadband matching at MB frequencies. Together, these two criteria form a multi-objective optimization problem which was solved iteratively to ensure the proposed solution satisfies both criteria.

The geometry of the proposed MB parasitic is shown in Figure 5-24 below, after optimizing the slot lengths to minimize the MS of each CRM in the HB operating band. The dimensions of the proposed MB parasitic are tabulated in Table 5-4.

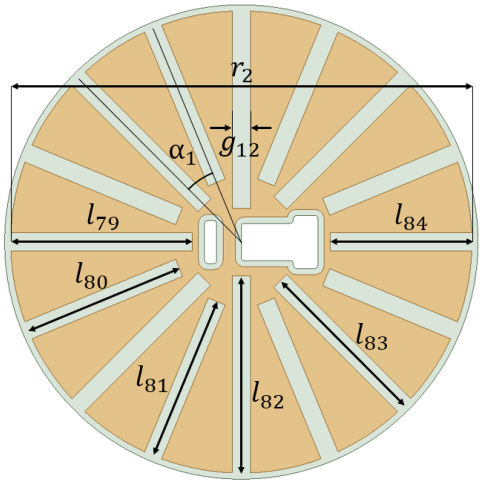

Figure 5-24: Geometry of the proposed MB parasitic.

Table 5-4: Dimensions corresponding to the geometry of the proposed MB parasitic.

l_{79}	l_{80}	l_{81}	l_{82}	l_{83}	l_{84}	g_{12}	r_2	α_1
0.592”	0.532”	0.542”	0.642”	0.572”	0.462”	0.060”	0.151”	22.5°

5.4.5 Evaluation of Proposed Technique

The CRM solver within HFSS was utilized to calculate the MS of the proposed MB parasitic for the first ten CRMs satisfying the criteria $MS > 0.02$. The significance of the criteria $MS > 0.02$ is that for MS below this threshold the CRMs are very weakly radiating and therefore not of interest for the purposes of this research. The first six CRMs are shown in Figure 5-25, with the i^{th} CRM/MS supported by the proposed MB parasitic here forward denoted by $CRM_{p,i}/MS_{p,i}$, where the “p” is for “proposed”. In comparing Figure 5-20 and Figure 5-25 from 3.4 GHz to 4.2 GHz, it is seen that the peak MS has been reduced in moving from the baseline to the proposed MB parasitic. Furthermore, the proposed MB parasitic supports only three CRMs with $MS > 0.02$ across the entirety of the HB operating band, as opposed to five which the baseline MB parasitic supports. For example, $CRM_{p,4}$ only satisfies the $MS_{p,4} > 0.02$ criteria from 4.0 GHz to 5.0 GHz, for all other frequencies $MS_{p,4} < 0.02$, it is for this reason that there are no data points for the MS

of $CRM_{p,4}$ for frequencies below 4.0 GHz. Similarly, $CRM_{p,5}$ and $CRM_{p,6}$ only satisfy the criteria of $MS > 0.02$, from 4.2 GHz to 5.0 GHz, and only at 5.0 GHz, respectively. Unlike the baseline MB parasitic, the proposed MB parasitic does not appear to support degenerate modes, owing to the fact that none of the MSs are identical.

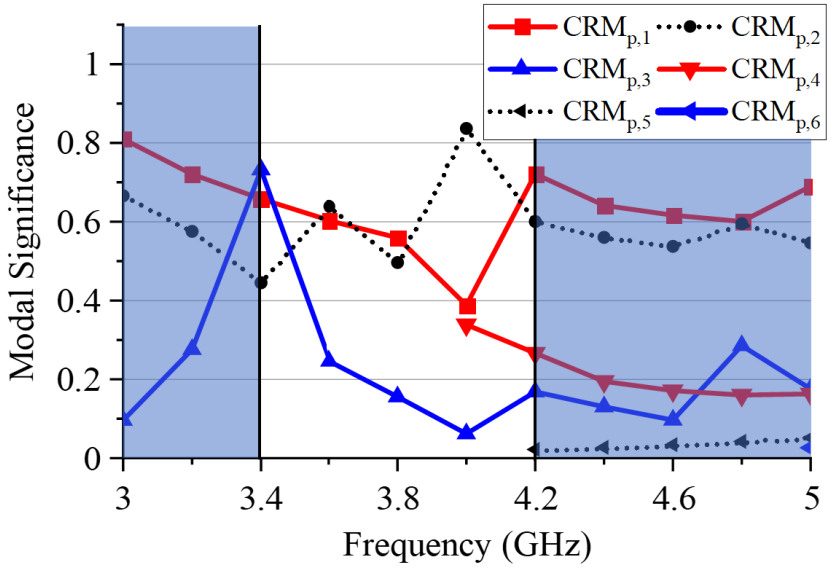

Figure 5-25: Modal significance of the first six CRMs for the proposed MB parasitic.

The vector surface current density of the first three CRMs supported by the proposed MB parasitic are overlaid with the geometry of the proposed MB parasitic, as shown in Figure 5-26. The current distributions of the three CRMs confirm that no spatially orthogonal degenerate radiating modes are present at 3.4 GHz. The distributions of the eigencurrents have changed significantly from the baseline design, confirming that the new design not only has lower MS across the band but also that entirely new CRMs are supported by the modified geometry. The proposed MB parasitic does not support the degenerate dipolar modes present in the baseline MB parasitic, namely $CRM_{b,1}$ and $CRM_{b,2}$, which were identified as secondary sources of radiation; instead, different CRMs are supported by the proposed MB parasitic, for example $CRM_{p,1}$ –

$CRM_{p,3}$, which do not exhibit dipolar eigencurrent distributions. The supported CRMs have a lower MS than $CRM_{b,1}$ and $CRM_{b,2}$ and hence will result in less radiated emissions if excited. The baseline MB parasitic disk exhibits two electric dipole CRMs, one magnetic dipole CRM, and an electric quadrupole CRM, none of which the proposed MB parasitic supports, based on the eigencurrents. Furthermore, many of the currents on opposing sides of a given slot have similar magnitudes with opposite directions. The effects of these equal and opposite currents in the far field will cancel since they are electrically close together. This is expected from the intrinsically lower MS which is observed in the proposed parasitic as compared to the baseline parasitic.

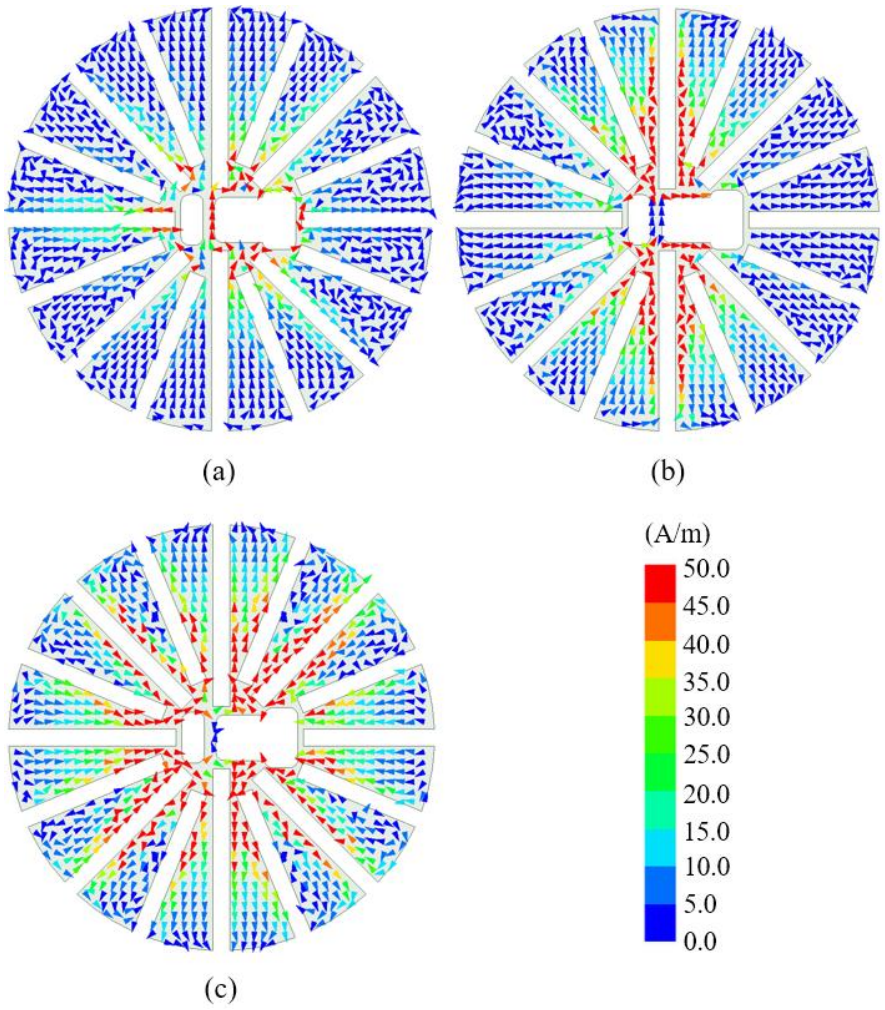

Figure 5-26: Vector surface current density calculated at 3.4 GHz on the proposed conducting MB parasitic using the HFSS CRM solver for (a) $CRM_{p,1}$, (b) $CRM_{p,2}$, and (c) $CRM_{p,3}$.

5.4.6 Discussion of Results

The baseline MB parasitics are identified as the sources of the mutual coupling which lead to the narrowing of the HPBW in the baseline design in the lower part of the HB operating band. The confirmation of this hypothesis is demonstrated in Section 5.4.1 and Section 5.4.2 using three different techniques. First, the basis for the hypothesis is demonstrated through a pair of full-wave simulations in which the reduction in the HB HPBW is only observed in the presence of the MB dipoles with baseline MB parasitics, not in the presence of the MB dipoles themselves. These results turned the focus towards the baseline MB parasitics acting as secondary radiation sources in the HB frequency range. Next, a simplified 2-D array factor (AF) calculation subject to the condition that the baseline MB parasitics are behaving as secondary dipole sources is formulated analytically. The resulting normalized radiation pattern exhibits a similar reduction in the HB HPBW at frequencies near the lower part of the HB operating band. Finally, the current distribution supported by the baseline MB parasitic is calculated using CRM analysis, and two electric dipole modes are identified as likely causes of the radiation due to their high MS as well as the relative ease for which their dipolar eigencurrents could be excited by the neighboring HB dipole array. The excitation of these two CRMs is confirmed through evaluation of the current distributions on the baseline MB parasitics upon the excitation of the HB array. Furthermore, the phase and magnitude relationship between the HB array and the currents induced on the baseline MB parasitics closely matches that which is hypothesized from the analytic AF calculation.

A technique, in which only the electrically small details of the baseline MB parasitics are modified, is presented in order to maintain a well-matched MB dipole while also lowering the MS and altering the eigencurrents of the supported CRMs across the HB operating band. The low MS of the proposed MB parasitic implies that *if* the CRMs are excited, the amount of radiation due to

the excited CRMs will be less than that of the baseline CRMs. Furthermore, the proposed technique yields eigencurrents whose distributions are non-dipolar in nature. Therefore, it is expected that the close proximity of the proposed MB parasitics to the HB dipole array will not excite the CRMs supported in the HB operating band.

In order to evaluate the proposed mutual coupling reduction technique in the tri-band array environment the proposed MB parasitic is utilized in place of the baseline MB parasitic in the geometry of Figure 5-11. That is, the proposed MB parasitic is used in conjunction with the proposed FPCA, of Section 5.3, to address the mutual coupling caused by the baseline MB parasitics and the radome, respectively. The next section presents the simulated and measured results of the baseline and proposed tri-band array environment in which both design techniques are utilized simultaneously to increase the HPBW in the lower part of the HB operating band, resulting in a stable HPBW with an average value of approximately 60° across the HB frequency range, while also improving the boresight directivity, beam peak location, and beam peak center.

5.5 Evaluation of Proposed Mutual Coupling Reduction Techniques in Tri-Band Array Environment

The purpose of this section is to present the simulated and measured results of the HB array in the presence of the proposed tri-band array environment. The proposed tri-band array environment differs from the baseline tri-band array environment in that it utilizes the FPCA proposed in Section 5.3.1 and the modified MB parasitic proposed in Section 5.4.4 to increase the boresight directivity in the upper part of the HB operating band, and increase the HPBW in the lower part of the HB operating band, respectively. Furthermore, the simulated and measured reflection coefficient and isolation of the LB and MB arrays are presented for the baseline and proposed

configuration to demonstrate that the proposed design techniques do not significantly degrade the performance of these bands.

The dipole feed stems, dipole tops, and feed PCBs are assembled in a manner similar to that described in Section 2.1. The LB dipole arms are supported through a custom plastic support. The LB dipole arms are secured to the LB dipole support through the use of plastic rivets. The MB parasitics are supported through a custom plastic support. The MB parasitics are secured to the MB parasitic support through a snap-fit feature in which the plastic component snaps into the cutout in the MB parasitic. Plastic radome supports are used at the top and bottom of the array to position the radome at the proper height throughout the measurements. The FR-4 superstrate, which makes up part of the FPCA in the proposed design, is supported using plastic standoffs. The baseline and proposed tri-band array prototypes are shown in Figure 5-27(a) and Figure 5-27(b), respectively.

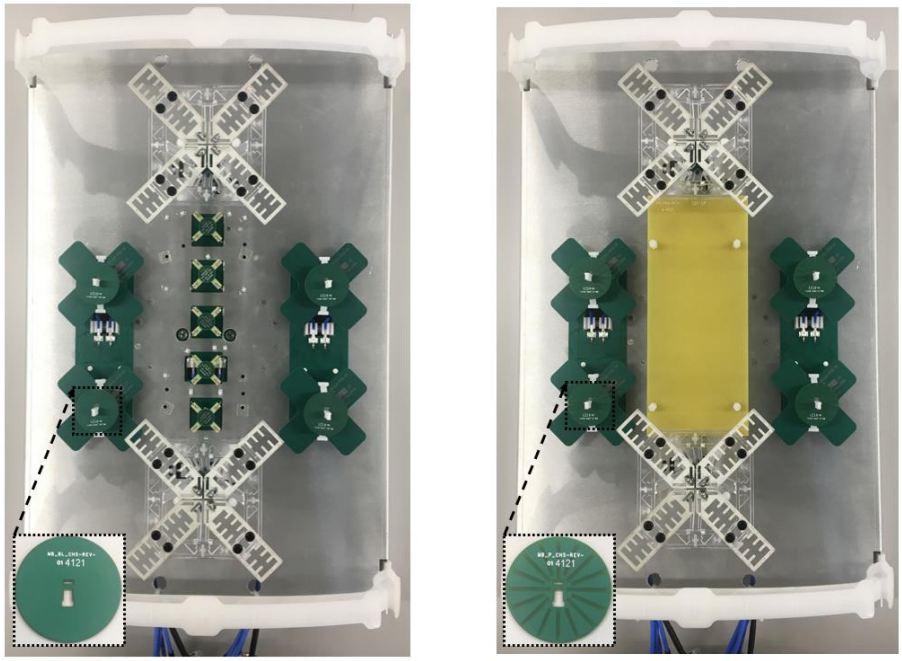

(a) (b)

Figure 5-27: Prototype of (a) baseline and (b) proposed tri-band array environment shown without radome.

5.5.1 Proposed Tri-Band Array Environment Results

The simulated and measured S-parameters for the LB and MB arrays are summarized in order to better understand what implications the proposed design has on their performance. The simulated and measured LB reflection coefficients agree closely with each other and are shown in Figure 5-28 for the bottom LB dipole. The top LB dipole exhibit similar S-parameters as the bottom LB dipole, as expected from symmetry, and therefore the results of the top LB dipole are not included. The targeted 10 dB return loss is exceeded in both simulation and measurement. The difference between simulation and measurement is within that which is expected based on manufacturing tolerances and simulation/measurement accuracy. For example, the radome supports, cables and LB dipole supports were omitted from the simulation to simplify the model. The worst-case measured LB return loss is 12.3 dB for both the baseline and proposed design.

The measured intra-array cross-polar isolation is better than the simulated result; however, as shown in Figure 5-29, both the simulated and measured worst-case intra-array cross-polar isolation are better than −24.5 dB across the band. Although the difference between the simulated and measured intra-array cross-polar isolation appears large when expressed in dB, when it is converted to magnitude this difference is quite small. Overall, the differences observed in the simulated and measured S-parameters are within those expected from manufacturing processes and simulation/measurement accuracy.

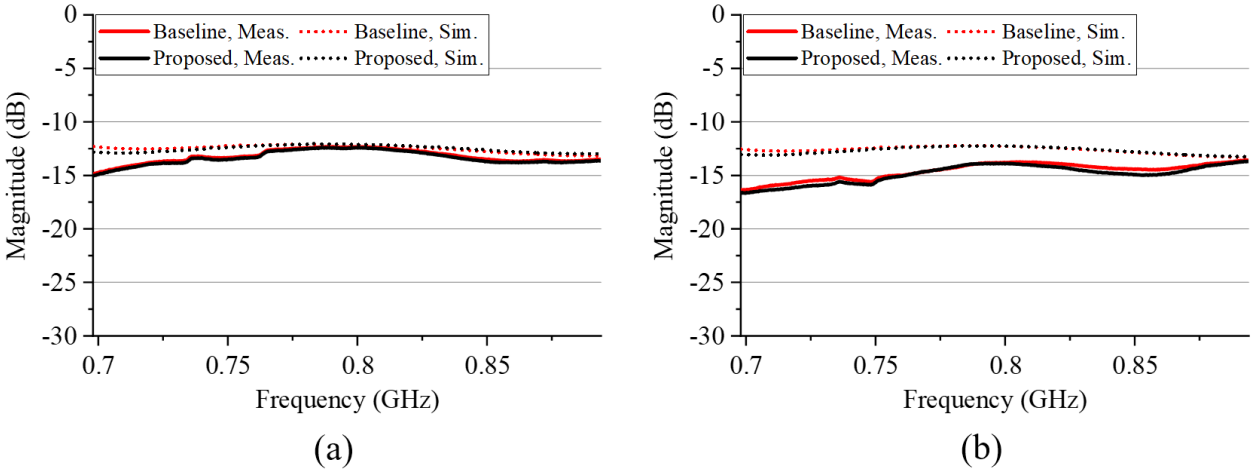

Figure 5-28: Simulated and measured reflection coefficients of the bottom LB sub-array in the baseline and proposed tri-band array environment for the (a) +45° and (b) −45° polarizations.

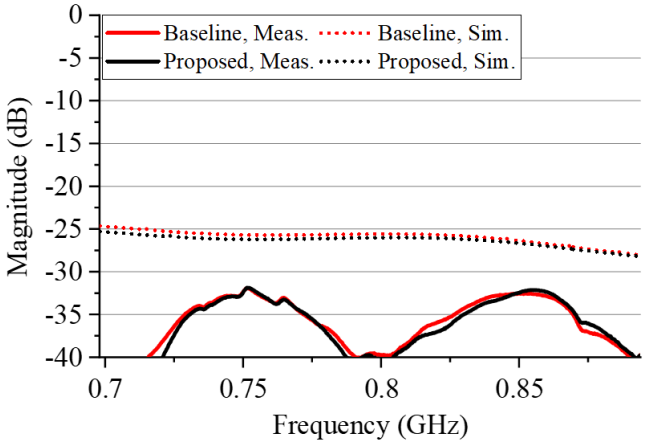

Figure 5-29: Simulated and measured intra-array cross-polar isolation of the bottom LB sub-array in the baseline and proposed tri-band array environment.

The simulated and measured MB reflection coefficients agree closely with each other and are shown in Figure 5-30 for the left MB sub-array. The right MB sub-array exhibits similar S-parameters as the left MB sub-array, as expected from symmetry, and therefore the results of the right MB sub-array are omitted. The targeted 10 dB return loss is exceeded in both simulation and measurement. The MB shows slightly larger differences between simulation and measurement due to the higher frequency of operation. As the frequency increases, the performance of each of the

components in the system becomes more sensitive to a given manufacturing tolerance. The differences observed are within those expected from manufacturing tolerances, and simulation/measurement accuracy. The worst-case measured MB return loss is 11.3 dB and 10.1 dB for the baseline and proposed designs, respectively. The measured intra-array cross-polar isolation agrees with the simulated results, as shown in Figure 5-31. These results validate that the iterative multi-objective optimization used in developing the proposed MB parasitic maintained similar S-parameters, with a slight degradation in intra-array cross-polar isolation in the upper part of the MB operating band.

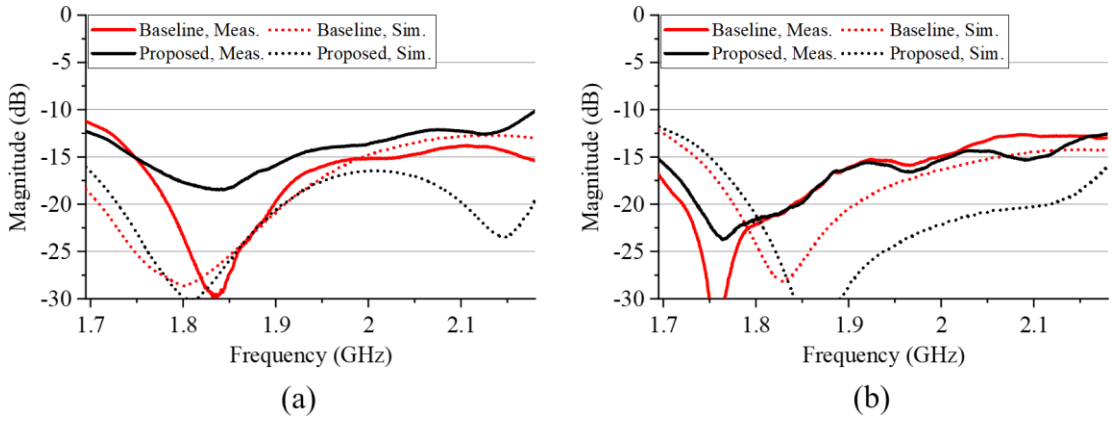

Figure 5-30: Simulated and measured reflection coefficient of the left MB sub-array in the baseline and proposed tri-band array environment for the (a) +45° and (b) −45° polarizations.

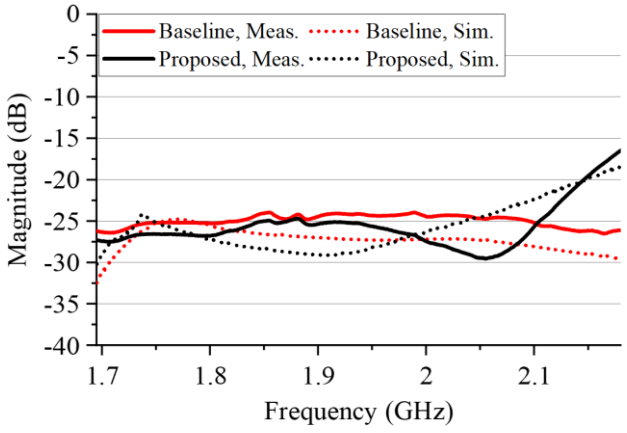

Figure 5-31: Simulated and measured intra-array cross-polar isolation of the left MB sub-array in the baseline and proposed tri-band array environment.

Figure 5-32 shows the simulated and measured HB reflection coefficient of the baseline and proposed designs, both of which agree well. The targeted 10 dB return loss is exceeded in both simulation and measurement. The worst-case simulated/measured return loss is 13.2/12.6 dB and 12.5/12.4 dB for the baseline and proposed design, respectively. The worst-case measured intra-array cross-polar isolation is −21.8 dB and −22.1 dB for the baseline and proposed designs, respectively, as shown in Figure 5-33. The differences observed between simulation and measurement are well within those expected at HB frequencies. The HB frequency typically exhibits the largest difference in moving from simulation to measurement amongst the three bands. This is due to the fact that for a given manufacturing tolerance, for example PCB thickness, circuit etching, or solder volume, the tolerance is electrically larger at HB frequencies, and therefore more significant. It is for these reasons that designers typically strive to tune simulations to exceed the targeted performance.

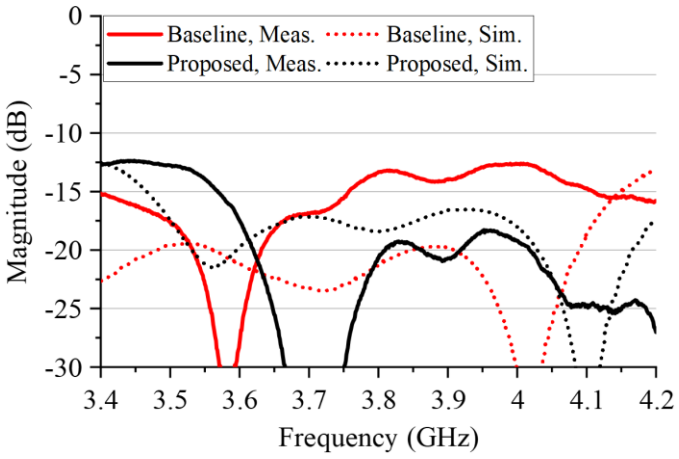

Figure 5-32: Simulated and measured reflection coefficient for the +45° polarization of the baseline and proposed HB array in tri-band array environment.

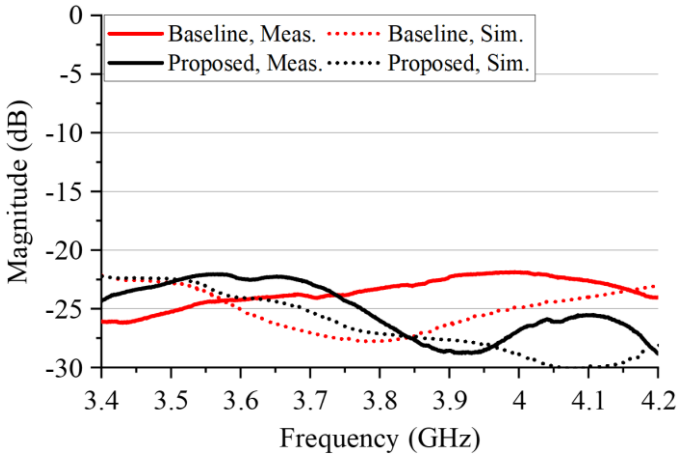

Figure 5-33: Simulated and measured intra-array cross-polar isolation of the baseline and proposed HB array in tri-band array environment.

Although the radiation patterns were measured at eighteen equally spaced frequency points spanning from 3.4 GHz to 4.2 GHz, for the sake of brevity the radiation pattern characteristics at 3.4 GHz, 3.6 GHz, 3.8 GHz, 4.0 GHz, 4.1 GHz, and 4.2 GHz are presented in this work. The measured radiation patterns of the baseline and proposed designs observed from 3.4 GHz to 4.2 GHz are representative of these six frequency points.

The simulated and measured HB H-plane radiation patterns are shown in Figure 5-34 for the +45° polarization. The simulated and measured HB H-plane patterns agree well with each other. The radiation attenuation in the boresight direction, present in the upper part of the HB operating band in both the simulated and measured baseline designs, is successfully eliminated through the use of the proposed design technique of Section 5.3.1, namely, the FPCA operating in the $N = 1$ resonance mode. Furthermore, the narrow HPBW in the lower part of the HB operating band is successfully eliminated through the use of the proposed design technique of Section 5.4.4, namely, the proposed slotted MB parasitic. The peak and average cross-polar radiation (CPR) exhibit improvements across the band for the proposed design, as shown in Figure 5-34. The measurement comparisons are shown in Table 5-5 for the baseline and proposed tri-band array environments.

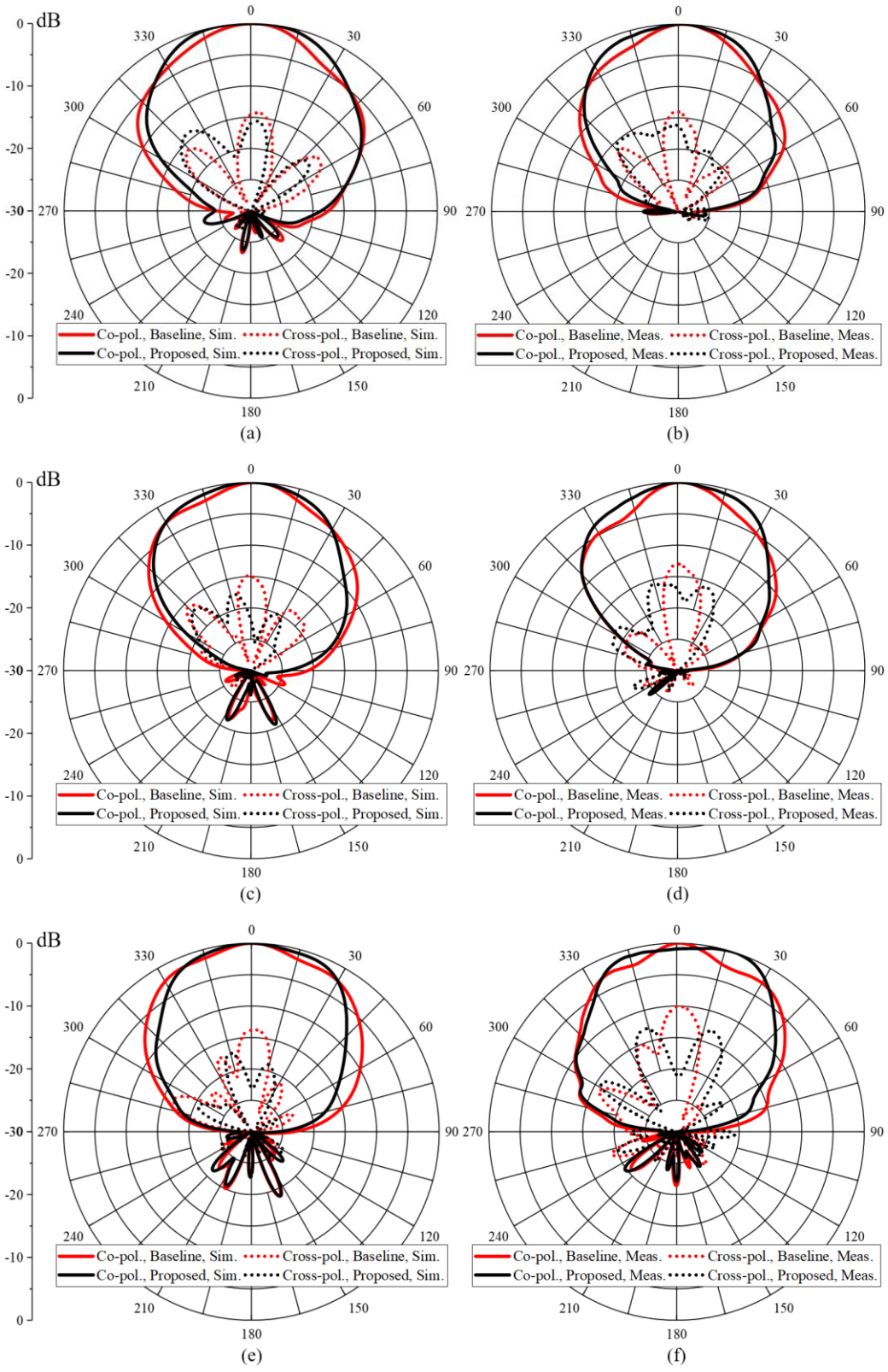
dB
0
-10
-20
-30
-20
-10
0
30
60
90
120
150
180
210
240
270
300
330
Co-pol., Baseline, Sim.
Cross-pol., Baseline, Sim.
Co-pol., Proposed, Sim.
Cross-pol., Proposed, Sim.
Co-pol., Baseline, Meas.
Cross-pol., Baseline, Meas.
Co-pol., Proposed, Meas.
Cross-pol., Proposed, Meas.
(a)
(b)
(c)
(d)
(e)
(f)

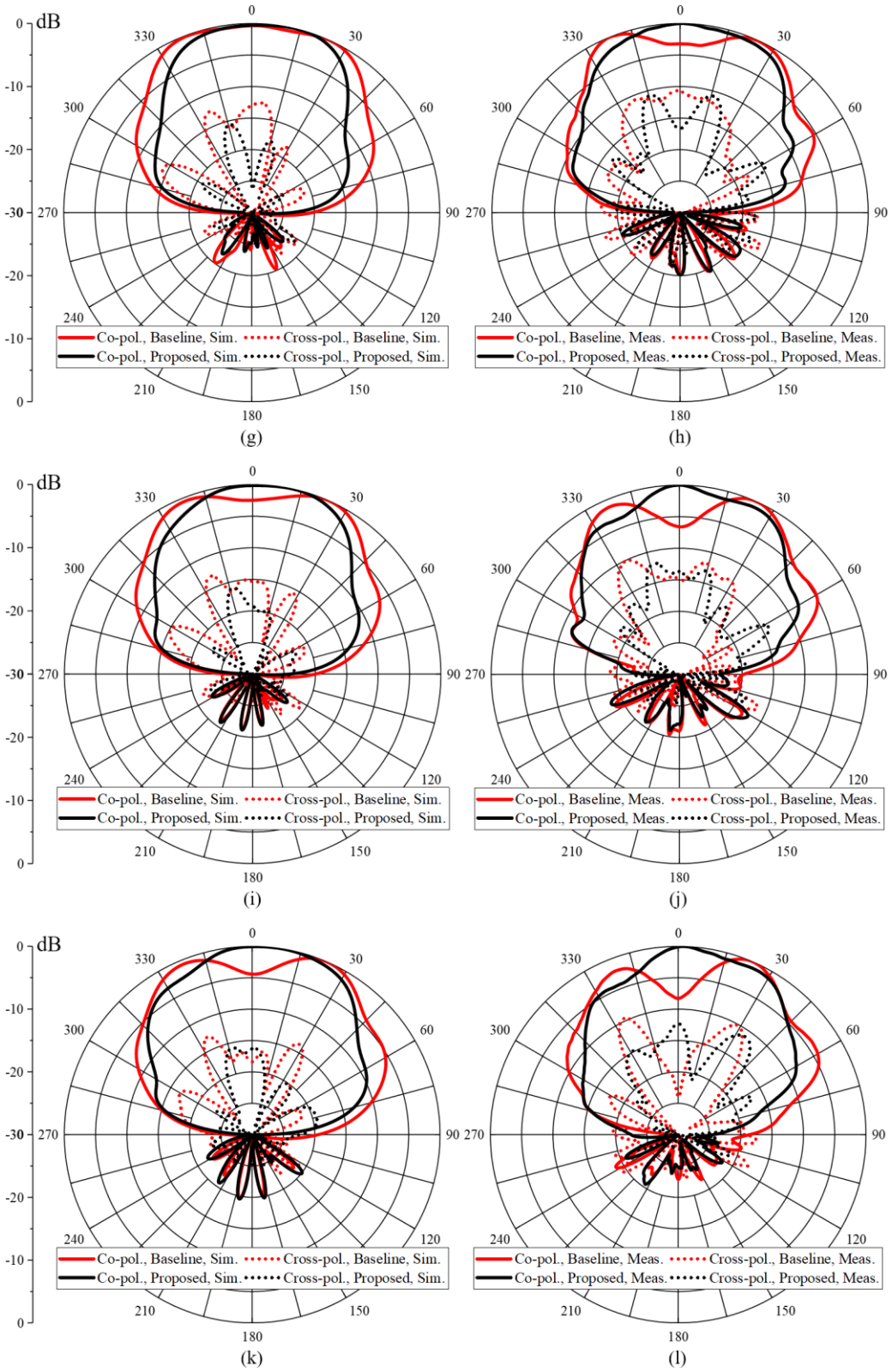

Figure 5-34: Simulated/measured H-plane radiation patterns of the +45° HB array at (a)/(b) 3.4 GHz, (c)/(d) 3.6 GHz, (e)/(f) 3.8 GHz, (g)/(h) 4.0 GHz, (i)/(j) 4.1 GHz, and (k)/(l) 4.2 GHz in the tri-band array environment.

Table 5-5: Comparison of measured key performance parameters for the baseline and proposed tri-band array environment.

Frequency (GHz)	Peak CPR (dB) Baseline/Proposed	Beam Peak (deg.) Baseline/Proposed	Beam Peak Center (deg.) Baseline/Proposed	Boresight Directivity (dBi) Baseline/Proposed	HPBW (deg.) Baseline/Proposed
3.4	–14.0/–15.2	+2/+1	+1/-2	15.5/15.1	40/56
3.6	–13.0/–15.7	+1/+1	+3/+1	15.3/14.9	33/56
3.8	–10.0/–12.8	+1/+18	+4/+3	14.5/13.5	61/60
4.0	–10.6/–10.7	–22/+1	–20/+5	10.4/13.8	27/65
4.1	–10.0/–12.0	+25/0	+26/+11	8.0/14.1	27/53
4.2	–9.6/–11.1	+23/+2	+25/+13	6.7/14.3	26/50

The simulated baseline array exhibits boresight attenuation from 4.1 GHz to 4.2 GHz, with the amount of attenuation increasing with frequency, as shown in Figure 5-34(i) and Figure 5-34(k). The measured baseline array exhibits boresight attenuation from 4.0 GHz to 4.2 GHz, with the amount of attenuation increasing with frequency, as shown in Figure 5-34(h), Figure 5-34(j), and Figure 5-34(l). The measured boresight attenuation in the baseline design exceeds what is found through simulation and is shifted down in frequency relative to the simulation. For example, at 4.2 GHz the magnitude of the radiation pattern at boresight for the baseline simulation is −4.4 dB, whereas in measurement it is −8.3 dB, as shown in Figure 5-34(k) and Figure 5-34(l), respectively. Furthermore, the boresight attenuation is calculated to be negligible at 4.0 GHz in simulation, but is measured to have significant attenuation, as shown in Figure 5-34(g) and Figure 5-34(h), respectively. In both simulation and measurement, the proposed design eliminates the boresight attenuation which is present in the baseline design.

This improvement in boresight radiation in the upper part of the HB operating band is captured through examination of the boresight directivity, which is shown in Figure 5-35. Both the simulated and measured baseline designs exhibit a reduction in boresight directivity towards the

upper part of the HB operating band. The proposed design exhibits stable boresight directivity across the entire HB operating band. The peak improvement in HB boresight directivity, in moving from the baseline to the proposed design, occurs at 4.2 GHz for which it increases a staggering 7.7 dB, from 6.7 dBi to 14.4 dBi.

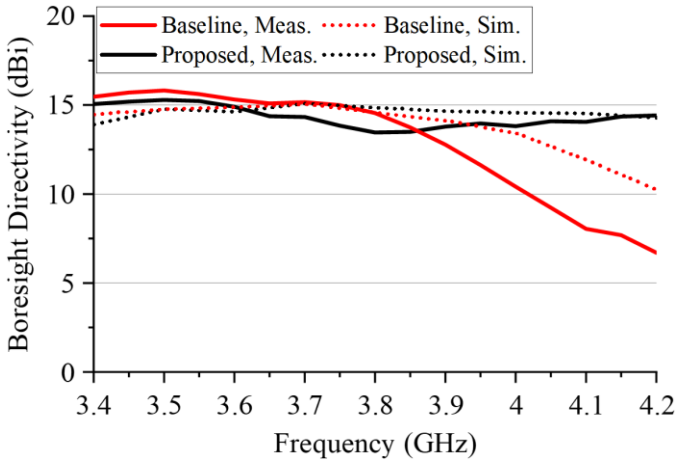

Figure 5-35: Simulated and measured boresight directivity for the +45° HB array in tri-band array environment.

The simulated and measured baseline arrays exhibit narrowing of the H-plane radiation patterns around boresight from 3.4 GHz to 3.8 GHz, as shown in Figure 5-34(a)-(f). The narrowing of the beam is more severe in the measured results than the simulated results. This is observed visually at 3.6 GHz and 3.8 GHz through comparing the baseline simulated/measured results shown in Figure 5-34(c)/(d) and Figure 5-34(e)/(f), respectively. In both simulation and measurement, the proposed design eliminates the narrow HPBW.

In order to quantify the improvement that the proposed design offers over that of the baseline design, the HPBW is plotted as a function of frequency in Figure 5-36. The dashed line in Figure 5-36 represents the target design HPBW of 60°. Figure 5-36 shows that the HPBW of the measured baseline design is narrower than that of the simulated baseline design from 3.4 GHz to 3.8 GHz.

Furthermore, it demonstrates that the proposed design exhibits a stable HPBW through the entirety of the band from 3.4 GHz to 4.2 GHz, as opposed to the baseline design which varies greatly with frequency. For example, the range of the measured HPBW spans from 50° to 65° for the proposed design, whereas the range of the measured baseline design varies from 25° to 76° across the band. It is seen that the proposed design has an average HPBW of 57.4°, while maintaining a standard deviation of 4.6°. This HPBW satisfies the criteria for having an approximate average HPBW of 60° with low variance across the HB operating band.

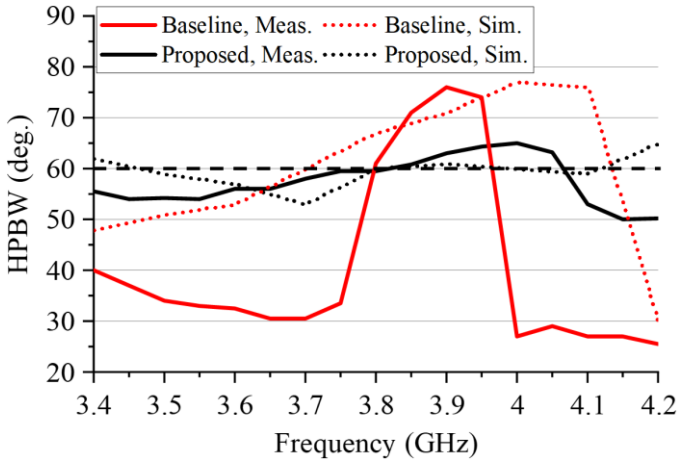

Figure 5-36: Simulated and measured HPBW for +45° HB array in the tri-band array environment.

5.5.2 Discussion of Proposed Tri-Band Array Environment Performance

The HB array demonstrates significant improvements in the radiation characteristics upon the implementation of the two proposed mutual coupling reduction techniques proposed in this chapter. In particular, the proposed FPCA used in conjunction with the proposed slotted MB parasitics work together to reduce two simultaneous sources of mutual coupling in the tri-band array environment. The peak improvement in the boresight directivity is designed to occur at 4.2 GHz in Section 5.3, which is precisely where the proposed design demonstrates the most significant boresight directivity improvement. The peak improvement in the HPBW is designed in

Section 5.4 to occur from 3.4 GHz to 3.8 GHz, which is precisely the region over which the proposed design demonstrates the most significant improvements in the HPBW.

The boresight directivity improvements realized in the proposed H-plane radiation pattern would greatly increase the received power of a cellular user near boresight over that of the baseline design if the proposed design were to be used as part of a base station antenna (BSA) system. This would provide more uniform coverage to the users operating within the BSAs service sector. BSAs are designed to provide uniform cellular coverage over the angular sector which they service. In this way, a user can expect uniform cellular reception as they move within the cellular sector at a fixed distance from the BSA. Therefore, when planning the location of adjacent BSAs the network planner can calculate the maximum radial distance from the BSA the user can operate at for a given receiver sensitivity. The 8.3 dB of attenuation at boresight which was measured at 4.2 GHz for the baseline design would lead to non-uniform spatial coverage within the BSAs service cell, were the baseline design to be used as part of a BSA. For example, if two users whose cellular devices were operating at 4.2 GHz were located at a fixed radial distance from the BSA with one user located at boresight and the other user located 30° from of boresight, their received signal strengths would differ by more than 8 dB for the baseline design. This means that if the user located 30° from boresight is receiving the minimum signal strength required to maintain cellular service, then the user at boresight would have no service despite being the same distance from the BSA and residing within the BSA's intended service sector. The network planner would then have to determine how to provide coverage to the user at boresight, for example through servicing with an adjacent BSA, while also not creating inter-cell interference with users located at 30° from boresight. The proposed design overcomes this problem, providing uniform signal strength angularly within the BSAs service sector as well as from frequency-to-frequency.

Another way in which BSAs are designed to provide uniform angular/spatial coverage across the frequency band is to achieve an HPBW which is stable with frequency. It is observed in Figure 5-36 that the HPBW of the baseline design varies significantly across frequency, whereas the proposed design has a stable HPBW centered around the targeted value of 60°.

The proposed design closely aligns the beam peak location and the beam peak center towards boresight, as is shown for the measured results in Figure 5-37(a) and Figure 5-37(b) for 4.1 GHz and 4.2 GHz, respectively. The deviation of the baseline beam peak location and beam peak center from boresight, which is shown for the simulated baseline design in Figure 5-7, is also present in the baseline measurements. In fact, the depth of the attenuation at boresight is even more severe in the baseline measurement than in the simulation. The proposed design overcomes this problem, by closely aligning the beam peak center and beam peak location to boresight.

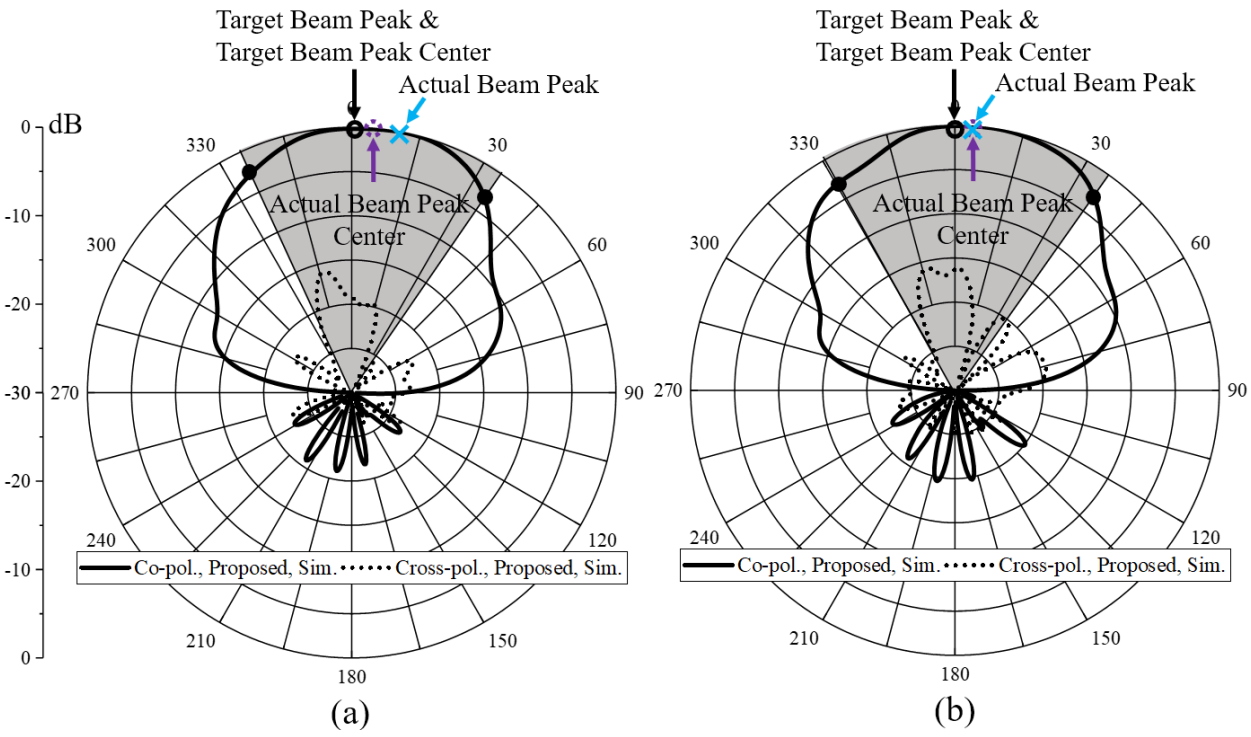

Figure 5-37: Beam peak of measured H-plane radiation pattern of HB array in the proposed tri-band array environment at (a) 4.1 GHz and (b) 4.2 GHz.

5.6 Summary

In this chapter two design techniques are proposed for reducing the mutual coupling between the HB array and the adjacent LB and MB arrays and dielectric radome in a tri-band array environment. One of the significant sources of mutual coupling is identified as the dielectric radome, whose presence is necessary in BSAs to protect the array face from environmental factors such as wind, precipitation, and UV radiation. The radome behaves as a partially reflecting surface (PRS) which introduces reflections of the incident EM waves generated by the HB array. The phase and amplitude of these reflected waves are such that the reflected wave superimposes destructively at boresight with the incident waves generated by the excitation of the HB array.

It is shown that by introducing an electrically thin dielectric superstrate between the HB array and the dielectric radome, a resonant FPCA can be formed. The resulting FPCA, operating in the second resonance mode ($N = 1$), greatly increases the boresight directivity at the resonant design frequency of 4.2 GHz. Furthermore, the positive phase slope of the FPCA allows for improved boresight directivity starting at 4.0 GHz. The resonant frequency of the FPCA is selected such that the increase in directivity for frequencies from 3.4 GHz to 3.8 GHz is minimized, since the baseline HPBWs in this frequency range are already narrower than the target design HPBW of 60° due to the mutual coupling between the HB array and the baseline MB parasitics. The proposed FPCA demonstrates a 3.7 dB increase in boresight directivity at 4.2 GHz, for which the boresight directivity improves from 10.3 dBi to 14.0 dBi upon implementation of the proposed FPCA.

A second significant source of mutual coupling is identified to be the baseline MB parasitics, whose presence is necessary for broadband matching of the MB dipole. It is shown through CRM analysis and full-wave simulation that the baseline MB parasitics support two dipolar degenerate CRMs with high modal significance (MS) which are excited upon the excitation of the adjacent

dual-polarized HB dipole array. The high MS, coupled with the fact that the CRMs are excited in the tri-band array environment by the adjacent HB dipole array, means that the baseline MB parasitics become secondary dipole radiation sources. Due to the spacing of the baseline MB parasitics to both sides of the HB array in the H-plane, the secondary radiation sources combine with the primary radiation sources resulting in a narrow H-plane HPBW from 3.4 GH to 3.6 GHz.

It is shown that by modifying the electrically small details of the baseline MB parasitic geometry, the radiation caused by currents induced on the proposed MB parasitics upon the excitation of the HB array can be minimized. The proposed technique leaves the macroscopic geometry, such as the radius of the parasitic and its height above the MB dipole, unchanged in order to maintain broadband matching of the MB sub-arrays, while changing the electrically small details of the MB parasitic to minimize the modal significance (MS) of the CRMs present within the HB operating band. The electrically small geometry modifications which are selected for use in the proposed MB parasitic are radial slots of varying lengths. Not only did the proposed MB parasitic have lower MS across the HB operating band, but unlike the baseline MB parasitic, the eigencurrents associated with the CRMs within the band for the proposed parasitic are not dipolar in nature. In this way, the CRMs supported by the proposed MB parasitic not only have less radiation than the baseline MB parasitic *if* excited, but they are also less likely to be excited upon the excitation of the adjacent dual-polarized HB dipole array.

The dense tri-band array environment considered in this chapter had multiple sources of mutual coupling which required multiple innovative design techniques to be utilized simultaneously, in order to optimize the performance of the HB array. The techniques proposed in this chapter are versatile techniques which antenna designers can add to their toolboxes for use in designing dense multi-band dual-polarized broadband arrays for BSA applications.

Chapter 6

Conclusions

6.1 Conclusion

In this dissertation, innovative design techniques for the reduction of mutual coupling in dense wide-band multi-band dual-polarized array environments for use in next-generation base station antenna (BSA) systems are proposed. The techniques are demonstrated through extensive full-wave electromagnetic (EM) analysis, as well as through prototype measurements of the baseline and proposed designs. The design techniques are demonstrated in several different array environments. The design techniques provide a means of increasing the number of antenna arrays within a fixed volume, without which the increase in mutual coupling present in the densified array would lead to degradation in the radiation characteristics of the individual arrays.

A review of existing state of the art mutual coupling reduction techniques and broadband antenna design techniques used for BSA design are presented. A dual-polarized dual-band BSA array architecture is proposed which minimizes the BSA width for a given low-band (LB) horizontal-plane (H-plane), i.e., yz-plane, spacing. A unit cell (UC), from the proposed BSA array architecture is used throughout the dissertation to demonstrate two different innovative mutual coupling reduction techniques for improved radiation pattern performance.

First, a mutual coupling reduction technique is proposed and demonstrated to improve the mid-band (MB) performance (1.695 – 2.180 GHz, 25.0% bandwidth) in the presence of the LB dipoles (698 – 894 MHz, 24.6% bandwidth) in a UC environment. This UC, UC 1, is one of the UCs from the BSA architecture proposed to minimize the BSA width for a given LB H-plane spacing. It is shown through full-wave simulation that the *electrically long* LB parasitic, which is required for

broadband matching of the baseline LB dipole, is a source of strong mutual coupling to the MB sub-arrays. Upon the excitation of the MB sub-arrays, currents are induced on the baseline LB parasitic. The induced currents generate secondary MB radiated fields which superimpose with the primary radiated fields generated by the direct excitation of the MB sub-arrays. This superposition of radiation sources degrades the MB radiation characteristics, such as the half power beamwidth (HPBW), peak upper sidelobe level (PUSLL), and cross-polar radiation (CPR).

The proposed design technique replaces the two conductors comprising the baseline LB dipole arms with multiple disconnected, but tightly coupled, conducting segments. These baseline and proposed metallization layers are etched on printed circuit boards (PCBs). Metallization layers of secondary PCBs are etched and bonded to the segmented primary metallization layer such that the centers of the conducting segments on the secondary PCB align with the gaps between neighboring segments on the primary PCB. The two PCBs are bonded together using a thin dielectric pressure sensitive adhesive to form tightly coupled parallel plate capacitors between the primary and secondary metallization layers.

The series capacitance integrated into the arms of the proposed LB dipole lowers the self-resistance of the LB dipole, while also canceling its inductive reactance in the center of LB operating band. The resulting LB dipole self-impedance is then able to be matched across the band through use of an *electrically short* LB parasitic. This electrically short LB parasitic also introduces a second resonance in the self-impedance of the LB dipole, thereby broadening the LB dipole bandwidth. The electrically short parasitic shows significantly less mutual coupling effects as compared to the baseline electrically long LB parasitic in both simulation and measurement.

In moving to the proposed design, the measured peak gain improvement occurs at 1.900 GHz for which the gain improves by 1.5 dB, increasing from 9.0 dBi to 10.5 dBi. The measured peak

CPR improvement occurs at 2.100 GHz for which it reduces from −9.8 dB to −14.7 dB. The measured PUSLL improvements occur at 1.800 GHz and 2.100 GHz for which they reduce from −9.0 dB to −13.8 dB and from −6.7 dB to −11.4 dB, respectively. The symmetry of the H-plane radiation patterns are improved across the band.

Secondly, a versatile mutual coupling reduction design technique is proposed and demonstrated to improve the LB performance in the presence of the MB sub-arrays in two UC environments. The proposed technique is demonstrated through simulations and measurements of UC 1 using the proposed capacitively loaded LB dipoles and a second distinct UC, referred to as UC 2, supporting broader bandwidths for both the LB (698 – 960 MHz, 31.6% bandwidth) and MB (1.695 – 2.700 GHz, 45.7% bandwidth) operating bands. It is shown that the baseline vertical MB dipole balun feed stems are the primary sources of mutual coupling corrupting the LB radiation characteristics. Upon the excitation of the LB dipoles, common mode (CM) currents are induced on the vertical MB dipole feed stems at LB frequencies. These induced CM currents radiate as electrically short monopoles over a conducting ground plane. These secondary LB radiation sources superimpose with the primary radiation sources generated by the direct excitation of the LB sub-arrays. This superposition of primary and secondary radiation sources results in degradation of the LB radiation characteristics such as an increased HPBW, reduction in front-to-back ratio, increased CPR, and gain reduction.

The proposed design technique replaces the two conductors comprising the balanced ports of the baseline vertical MB dipole balun feed stems with multiple disconnected, but tightly coupled, conducting segments. The conducting segments on the primary metallization layer of the primary balun PCBs are then bonded to secondary PCBs with segmented secondary metallization layers which overlap the gap formed between neighboring primary metallization layer segments, in a

manner similar to the method proposed for the serially loaded LB dipole. This forms a series of tightly coupled parallel plate capacitors which comprise the balanced ports of the proposed MB balun feed stems.

The series capacitance integrated into the proposed vertical MB dipole balun feed stems suppresses the unwanted excitation of CM currents upon excitation of the LB dipoles. The series capacitance behaves as a high-pass filter which suppresses LB CM currents and passes MB frequencies, thereby greatly improving the LB radiation characteristics without deteriorating the MB performance.

Although significant LB radiation patten improvements are observed in both the proposed UC 1 and UC 2, the most drastic improvements are observed in the proposed UC 2. For UC 2, the measured peak gain improvement occurs at 805 MHz for which it improves by 2.6 dB, increasing from 4.3 dBi to 6.9 dBi in moving to the proposed design. The measured peak CPR improvements occur at 805 MHz and 829 MHz for which it reduces from −7.7 dB to −13.9 dB and from −6.7 dB to −15.9 dB, respectively. The peak improvement in HPBW occurs at 798 MHz for which it reduces from 146° to 74° (49.3%). The peak improvements in the measured −10 dB H-plane beamwidth (HBW) occur at 805 MHz and 829 MHz for which it reduces from 217° to 155° (28.6%) and from 225° to 164° (27.1%), respectively. Similar improvements are observed in the V-plane.

The two distinct mutual coupling reduction design techniques, namely the capacitively loaded LB dipole with electrically short LB parasitic and the MB dipole using capacitively loaded MB dipole feed stems, are then implemented together in a BSA to simultaneously improve the MB and LB radiation characteristics of the BSA array, respectively. The array architecture chosen for the design corresponds to the proposed architecture containing UC 1 which minimizes the reflector

width for a given LB H-plane spacing. The improvements are demonstrated through full-wave EM simulation and prototype measurements of the baseline and proposed BSA. These results validate that the improvements demonstrated in the UCs are significant enough to improve the system performance of the array when used in a BSA, while also demonstrating the simultaneous use of the two different proposed mutual coupling reduction techniques.

The measured peak gain improvement for the LB array occurs at 796 MHz for which it increases 1.2 dB, from 12.0 dBi to 13.2 dBi. The average measured LB gain increase is 0.5 dB. The peak LB CPR improvement is at 894 MHz, for which it decreases from −12.7 dB to –18.0 dB. The measured LB PUSLL improvement occurs at 796 MHz, for which it decreases from −12.8 dB to −18.3 dB. The measured peak gain improvements for the MB arrays occur at 1.730 GHz and 1.870 GHz, for which they increase 0.8 dB, from 14.9 dBi to 15.7 dBi and from 15.9 dBi to 16.7 dBi, respectively. The average measured MB gain increase is 0.3 dB. The peak MB CPR improvement is at 1.695 GHz, for which it decreases from −10.4 dB to –14.0 dB. The measured MB PUSLL improvement occurs at 2.00 GHz, for which it decreases from −11.5 dB to −16.2 dB.

Thirdly, two distinct mutual coupling reduction design techniques are proposed and demonstrated in a tri-band array environment to improve the high-band (HB) (3.4 – 4.2 GHz, 21.0% bandwidth) radiation characteristics in the presence of the LB dipoles, MB dipoles, and dielectric radome. The necessity for two mutual coupling techniques, as opposed to one, to obtain the targeted HB radiation characteristics is due to the high array density and complexity of the tri-band array environment considered in the presence of the radome. It is shown that the dielectric radome, which is required to protect BSAs from environmental factors, and the baseline MB parasitics, which are necessary for broadband matching of the baseline MB sub-arrays, are the two

primary sources of mutual coupling which cause degradation of the HB radiation characteristics in the tri-band array environment.

The radome is identified as a partially reflecting surface (PRS) which introduces reflected waves that superimpose with the incident waves generated by the excitation of the HB array. These reflected waves destructively interfere with the incident waves at boresight, leading to significant boresight attenuation in the upper part of the HB operating band. A low-cost Fabry-Perot cavity antenna (FPCA), operating in the second resonance mode ($N = 1$), is proposed to improve the HB boresight directivity for frequencies above 4.0 GHz.

An FPCA is proposed for the reduction of mutual coupling between the HB array and the dielectric radome. The proposed FPCA is realized using a secondary electrically thin dielectric superstrate positioned between the HB array and the dielectric radome. The FPCA dimensions are synthesized using transmission line theory and an equivalent circuit model to satisfy the $N = 1$ resonance condition. The proposed FPCA technique drastically improves the HB radiation characteristics by increasing the boresight directivity, increasing the HPBW, centering the beam peak location, and beam peak center from 4.0 GHz to 4.2 GHz. For example, the peak measured boresight directivity improvement achieved upon implementing the FPCA occurs at 4.2 GHz, for which it increases by 3.7 dB, from 10.3 dBi to 14.0 dBi. Similarly, the peak measured improvement in the H-plane HPBW occurs at 4.2 GHz, for which it increases from 30° to 60° (100%), with a targeted value of 60°.

Characteristic mode (CRM) analysis and full-wave simulation are used to show that the baseline MB parasitics present in the tri-band array environment support the excitation of two degenerate dipolar CRMs with high modal significance (MS). The excitation of these CRMs, upon the excitation of the HB array, generates secondary sources of HB radiation at the location of the

baseline MB parasitics. The fields from these secondary sources superimpose with the primary radiation generated by the direct excitation of the HB array. It is shown analytically that this superposition results in a reduction in the H-plane HPBW in the lower and middle part of the HB operating band.

The proposed design technique, to suppress the mutual coupling between the HB array and the baseline MB parasitics, introduces electrically thin radially oriented slots in the conducting metallization layer of the circular baseline MB parasitic PCB. The radius and height of the parasitic above the MB dipoles remain fixed in both the baseline and proposed design. A multi-objective optimization of the electrically thin slot lengths and widths is carried out to ensure that the proposed MB parasitic increases the HPBW in the lower part of the HB operating band without degrading the broadband matching of the MB dipole. In this way, the proposed MB parasitic results in stabilization of the H-plane HPBW from 3.4 GHz to 3.8 GHz.

Upon combining the proposed FPCA with the proposed slotted MB parasitics, the HB radiation characteristics are significantly improved across the operating band. For example, the peak improvement in boresight directivity occurs at 4.2 GHz for which it improves a staggering 7.7 dB, from 6.7 dBi to 14.4 dBi. Furthermore, the HPBW is stabilized and centered around the targeted value of 60°. The proposed HPBW varies from 50° to 65°, a significant improvement over the baseline design which varies from 25° to 75° across the HB operating band. Lastly, the peak measured CPR improvements occur at 3.6 GHz and 3.8 GHz for which they decrease from −13.0 dB to −15.7 dB and from −10.0 to −12.8 dB, respectively.

6.2 Future Work

The design techniques and methods which are proposed and carried out throughout this dissertation give rise to additional questions and challenges which warrant future research.

The proposed serially loaded LB dipole could be further improved through reducing the need for multi-layer printed circuit board (PCB) technology, or pressure sensitive adhesives, in realizing the capacitors integrated into the LB dipole arms. Other methods of realizing the capacitance can be investigated, such as interdigital capacitors. Furthermore, methods for minimizing the currents induced on the vertical LB stems can be investigated for further MB improvements. For example, redesigning the LB dipole to be fed by a Marchand balun instead of a direct feed may help to minimize radiated emissions due to the feed line. Lastly, a physically insightful method for future research is to use array theory to derive approximate expressions for the normalized MB radiation pattern in the presence of the secondary MB radiation sources caused by the currents induced onto the baseline LB parasitic and vertical feed stems. This could be done in a manner similar to the analytic approach used in this dissertation for demonstrating the effect of the MB parasitics on the HB radiation patterns in the tri-band array environment.

Similarly, the proposed design technique in which series capacitance is used to suppress CM LB currents on the vertical MB dipole feed stems, could potentially be implemented using a low-cost single layer approach to simplify the manufacturability of the proposed technique. For example, the feasibility of using single layer microstrip interdigital capacitors in place of the proposed parallel plate capacitors, could be investigated. Array theory could also be used to derive an analytic expression describing the approximate LB radiation pattern in the presence of the secondary LB radiation sources, namely the electrically short monopoles created by the baseline vertical MB dipole feed stems. Furthermore, an investigation into why the proposed design

technique degrades the LB intra-band isolation when used in UC 2 could be carried out for improved LB S-parameter performance.

The results of the proposed FPCA could be extended to design a *multi-band* FPCA for BSAs, for example an FPCA which simultaneously uses the $N = 0$ resonance mode to increase the MB directivity and the $N = 1$ resonance mode to increase the HB directivity. Furthermore, CRM analysis could be used to propose additional MB parasitic geometries which have less MS than the proposed MB parasitic. Lastly, the radiation degradation caused at boresight by the radome presence, along with the FPCA solution, could be formulated analytically by considering a radiation source embedded in a stratified medium which has a perfect electric conductor (PEC) boundary condition beneath the source. While most texts derive the FPCA resonance condition through use of ray tracing techniques, this is not the only method available. The problem regarding a source embedded in a semi-infinite stratified medium is formulated in Chew's work [142] and Kong's work [143]. Their formulation could be used, along with the application of a PEC boundary condition at the location of the reflector, for a unique analytic formulation to the problem caused by PRSs and the proposed FPCA solution.

References

[1] M. Bertolotti, *The History of the Laser*. IOP Publishing Ltd., 2005.

[2] Z. N. Chen and K.-M. Luk, *Antennas for Base Stations in Wireless Communications*. New York: McGraw-Hill, 2009. Accessed: Nov. 12, 2018. [Online]. Available: http://accessengineeringlibrary.com/browse/antennas-for-base-stations-in-wireless-communications

[3] W. Webb, *Wireless Communications: The Future*. Chichester, England ; Hoboken, NJ: John Wiley & Sons, Ltd, 2007.

[4] "NGMN 5G white paper 2," NGMN Alliance, White Paper Version 1.0, Jul. 2020.

[5] "NGMN 5G white paper," NGMN Alliance, White Paper Version 1.0, Feb. 2015.

[6] C. Balanis, *Antenna Theory: Analysis and Design*, 4th Edition. Hoboken, NJ: John Wiley & Sons, Inc., 2016, pp. 51−52, p. 106, pp. 474−476, p. 902.

[7] J. L. Allen and B. L. Diamond, "Mutual coupling in array antennas," Lincoln Lab. MIT, Lexington, MA, Technical Report ESD-TR-66-443, Oct. 1966. Accessed: Mar. 13, 2022. [Online]. Available: https://apps.dtic.mil/sti/pdfs/AD0648153.pdf

[8] M. Lazarus, "The great spectrum famine," *IEEE Spectr.*, vol. 47, no. 10, pp. 26–31, 2010, doi: 10.1109/MSPEC.2010.5583459.

[9] "The FCC's 5G FAST plan," *Federal Communications Commission*, Sep. 28, 2018. https://www.fcc.gov/document/fccs-5g-fast-plan (accessed Dec. 07, 2020).

[10] “T-Mobile’s spectrum haul is a game changer for wireless consumers,” *T-Mobile Newsroom*. https://www.t-mobile.com/news/press/tmobile-spectrum-auction-win (accessed Dec. 07, 2020).

[11] “FCC concludes first 5G mid-band spectrum auction,” *Federal Communications Commission*, Aug. 25, 2020. https://www.fcc.gov/document/fcc-concludes-first-5g-mid-band-spectrum-auction (accessed Dec. 07, 2020).

[12] “FCC announces winning bidders in C-band auction,” *Federal Communications Commission*, Feb. 24, 2021. https://www.fcc.gov/document/fcc-announces-winning-bidders-c-band-auction (accessed Dec. 29, 2021).

[13] “FCC concludes first high-band 5G airwaves auctions,” *Federal Communications Commission*, May 28, 2019. https://www.fcc.gov/document/fcc-concludes-first-high-band-5g-airwaves-auctions (accessed Dec. 07, 2020).

[14] “Auction 103 winning bidders and incentive payments,” *Federal Communications Commission*, Mar. 12, 2020. https://www.fcc.gov/document/auction-103-winning-bidders-and-incentive-payments (accessed Dec. 07, 2020).

[15] “Auctions summary,” *Federal Communications Commission*, Dec. 11, 2017. https://www.fcc.gov/auctions-summary (accessed Dec. 29, 2021).

[16] P. H. Rao, S. Sujitha, and K. T. Selvan, “A multiband, mutipolarization shared-aperture antenna: design and evaluation,” *IEEE Antennas and Propag. Mag.*, vol. 59, no. 4, pp. 26–37, Aug. 2017, doi: 10.1109/MAP.2017.2706654.

[17] C. Beckman and B. Lindmark, “The evolution of base station antennas for mobile communications,” in *2007 Int. Conf. on Electromagn. in Adv. Appl.*, Sep. 2007, pp. 85–92. doi: 10.1109/ICEAA.2007.4387244.

[18] Q. Zhang and Y. Gao, “A compact broadband dual-polarized antenna array for base stations,” *IEEE Antennas and Wirel. Propag. Lett.*, vol. 17, no. 6, pp. 1073–1076, Jun. 2018, doi: 10.1109/LAWP.2018.2832293.

[19] R. Wu and Q. Chu, “Broadband multimode antenna and its array for wireless communication base stations,” *Electron. Telecommun. Res. Inst.*, vol. 41, no. 2, pp. 167–175, Apr. 2019, doi: 10.4218/etrij.2018-0187.

[20] S. X. Ta, I. Park, and R. W. Ziolkowski, “Crossed dipole antennas: a review,” *IEEE Antennas Propag. Mag.*, vol. 57, no. 5, pp. 107–122, Oct. 2015, doi: 10.1109/MAP.2015.2470680.

[21] C. Ding, H.-H. Sun, R. W. Ziolkowski, and Y. J. Guo, “Simplified tightly-coupled cross-dipole arrangement for base station applications,” *IEEE Access*, vol. 5, pp. 27491–27503, 2017, doi: 10.1109/ACCESS.2017.2778229.

[22] Y. Cui, R. Li, and P. Wang, “A novel broadband planar antenna for 2G/3G/LTE base stations,” *IEEE Trans. Antennas Propag.*, vol. 61, no. 5, pp. 2767–2774, 2013.

[23] H. Huang, X. Li, and Y. Liu, “A novel vector synthetic dipole antenna and its common aperture array,” *IEEE Trans. Antennas Propag.*, vol. 66, no. 6, pp. 3183–3188, Jun. 2018, doi: 10.1109/TAP.2018.2819894.

[24] L.-H. Wen, S. Gao, Q. Luo, C.-X. Mao, W. Hu, Y. Yin, Y. Zhou, and Q. Wang, "Compact dual-polarized shared-dipole antennas for base station applications," *IEEE Trans. Antennas Propag.*, vol. 66, no. 12, pp. 6826–6834, Dec. 2018, doi: 10.1109/TAP.2018.2871717.

[25] S.-G. Zhou, P.-K. Tan, and T.-H. Chio, "Low-profile, wideband dual-polarized antenna with high isolation and low cross polarization," *Antennas Wirel. Propag. Lett.*, vol. 11, pp. 1032–1035, 2012, doi: 10.1109/LAWP.2012.2215299.

[26] L.-H. Wen, S. Gao, Q. Luo, W. Hu, Q. Yang, Y. Yin, X. Ren, and J Wu, "A wideband differentially driven dual-polarized antenna by using integrated six-port power divider," *IEEE Trans. Antennas Propag.*, vol. 67, no. 12, pp. 7252–7260, Dec. 2019, doi: 10.1109/TAP.2019.2930205.

[27] C. Ding, H.-H. Sun, R. W. Ziolkowski, and Y. Jay Guo, "A dual layered loop array antenna for base stations with enhanced cross-polarization discrimination," *IEEE Trans. Antennas Propag.*, vol. 66, no. 12, pp. 6975–6985, Dec. 2018, doi: 10.1109/TAP.2018.2869216.

[28] C. Ding, H.-H. Sun, H. Zhu, and Y. Jay Guo, "Achieving wider bandwidth with full-wavelength dipoles for 5G base stations," *IEEE Trans. Antennas Propag.*, vol. 68, no. 2, pp. 1119–1127, Feb. 2020, doi: 10.1109/TAP.2019.2950108.

[29] C. Ding, B. Jones, Y. J. Guo, and P. Qin, "Wideband matching of full-wavelength dipole with reflector for base station," *IEEE Trans. Antennas Propag.*, vol. 65, no. 10, pp. 5571–5576, Oct. 2017, doi: 10.1109/TAP.2017.2738068.

[30] P. J. Bisiules and A. Shooshtari, “Full wave dipole array having improved squint performance,” U.S. Patent Appl. 20160248170A1, Aug. 25, 2016 Accessed: Dec. 04, 2020. [Online]. Available: https://patents.google.com/patent/US20160248170A1/en

[31] H. Huang, X. Li, and Y. Liu, “A dual-broadband base station antenna with ikebana-like arrangement scheme,” *Microw. Opt. Technol. Lett.*, vol. 62, no. 2, pp. 708–713, Feb. 2020, doi: 10.1002/mop.32050.

[32] M. Rezvani and P. Mohammadi, “Dual-polarised broad-band array antenna with suspended plates for base stations,” *IET Microw. Antennas Propag.*, vol. 13, no. 4, pp. 425–430, 2019, doi: 10.1049/iet-map.2018.5093.

[33] A. A. Serra, P. Nepa, G. Manara, S. Cioci, and G. Tribellini, “Wideband dual-polarized stacked-patch antenna array for base stations,” *Microw. Opt. Technol. Lett.*, vol. 52, no. 5, pp. 1048–1052, 2010, doi: 10.1002/mop.25131.

[34] M. Ciydem and E. A. Miran, “Dual-polarization wideband sub-6 GHz suspended patch antenna for 5G base station,” *IEEE Antennas Wirel. Propag. Lett.*, vol. 19, no. 7, pp. 1142–1146, Jul. 2020, doi: 10.1109/LAWP.2020.2991967.

[35] X. Cui, F. Yang, and M. Gao, “Wideband CP magnetoelectric dipole antenna with microstrip line aperture-coupled excitation,” *Electron. Lett.*, vol. 54, no. 14, pp. 863–864, Jul. 2018, doi: 10.1049/el.2018.1046.

[36] M. Li and K.-M. Luk, “Wideband magnetoelectric dipole antennas with dual polarization and circular polarization,” *IEEE Antennas Propag. Mag.*, vol. 57, no. 1, pp. 110–119, Feb. 2015, doi: 10.1109/MAP.2015.2397091.

[37] P. Fernandez-Martinez, S. Martin-Anton, and D. Segovia-Vargas, “Design of a wideband Vivaldi antenna for 5G base stations,” in *2019 IEEE Int. Symp. Antennas Propag. USNC-URSI Radio Sci. Meet.*, Jul. 2019, pp. 149–150. doi: 10.1109/APUSNCURSINRSM.2019.8888989.

[38] M. Sonkki, S. Myllymäki, J. Putaala, E. Heikkinen, T. Haapala, H. Posti, and H. Jantunen, “Dual polarized dual fed Vivaldi antenna for cellular base station operating at 1.7–2.7 GHz,” *Int. J. of Antennas and Propag.*, vol. 2017, pp. 1–8, 2017, doi: 10.1155/2017/1304359.

[39] J. R. Sanford, “High gain dual polarized omni antenna for four channel MIMO applications,” in *2019 IEEE Int. Symp. Antennas Propag. USNC-URSI Radio Sci. Meet.*, Atlanta, GA, USA, Jul. 2019, pp. 1423–1424. doi: 10.1109/APUSNCURSINRSM.2019.8888769.

[40] L. Wu, R. Li, Y. Qin, and Y. Cui, “Bandwidth-enhanced broadband dual-polarized antennas for 2G/3G/4G and IMT services,” *Antennas Wirel. Propag. Lett.*, vol. 17, no. 9, pp. 1702–1706, Sep. 2018, doi: 10.1109/LAWP.2018.2864185.

[41] A. Adams and D. Warren, “Dipole plus parasitic element,” *IEEE Trans. Antennas Propag.*, vol. 19, no. 4, pp. 536–537, Jul. 1971, doi: 10.1109/TAP.1971.1139962.

[42] J. Wu, Z. Zhao, Z. Nie, and Q. H. Liu, “A broadband unidirectional antenna based on closely spaced loading method,” *IEEE Trans. Antennas Propag.*, vol. 61, no. 1, pp. 109–116, Jan. 2013, doi: 10.1109/TAP.2012.2216492.

[43] Y. Cui, L. Wu, and R. Li, “Bandwidth enhancement of a broadband dual-polarized antenna for 2G/3G/4G and IMT base stations,” *IEEE Trans. Antennas Propag.*, vol. 66, no. 12, pp. 7368–7373, Dec. 2018, doi: 10.1109/TAP.2018.2867046.

[44] L. H. Ye, X. Y. Zhang, Y. Gao, and Q. Xue, “Wideband dual-polarized four-folded-dipole antenna array with stable radiation pattern for base-station applications,” *IEEE Trans. Antennas Propag.*, vol. 68, no. 6, pp. 4428–4436, Jun. 2020, doi: 10.1109/TAP.2020.2969749.

[45] H. Huang, X. Li, and Y. Liu, “A low-profile, dual-polarized patch antenna for 5G MIMO application,” *IEEE Trans. Antennas Propag.*, vol. 67, no. 2, pp. 1275–1279, Feb. 2019, doi: 10.1109/TAP.2018.2880098.

[46] H. Huang, “An effective way regarding to coupling reduction and pattern correction in base station design,” *Microw. Opt. Technol. Lett.*, vol. 60, no. 11, pp. 2707–2712, Nov. 2018, doi: 10.1002/mop.31430.

[47] B. Wang, C. Zhu, C. Liao, W. Luo, B. Yin, and P. Wang, “Broadband dual-polarized dipole antenna for LTE/5G base station applications,” *Electromagnetics*, vol. 40, no. 1, pp. 13–22, Jan. 2020, doi: 10.1080/02726343.2019.1695087.

[48] M. Rezvani and P. Mohammadi, “Enhancing characteristics of dual-polarized BTS element antenna using metal director,” *Int. J. RF Microw. Comput.-Aided Eng.*, vol. 30, no. 1, Jan. 2020, doi: 10.1002/mmce.21972.

[49] Z. Tang, Y. Li, Z. Zhao, and Y.-Z. Yin, "Design of compact, wideband dual-polarized multi-dipole antenna for 2G/3G/LTE base station applications," *Prog. Electromagn. Res. C*, vol. 90, pp. 41–49, 2019, doi: 10.2528/PIERC18121902.

[50] C. Liao, B. Wang, C. Zhu, H. Hao, and B. Yin, "Broadband dual-polarized loop cross-dipole antenna for 5G base station applications," *Electronics*, vol. 9, no. 10, p. 1574, Sep. 2020, doi: 10.3390/electronics9101574.

[51] John D. Kraus, *Antennas for All Applications*, 3rd Edition. McGraw-Hill, 1988.

[52] J. Park, Y. Ryu, and J. Lee, "Mu-zero resonance antenna," *IEEE Trans. Antennas Propag.*, vol. 58, no. 6, pp. 1865–1875, Jun. 2010, doi: 10.1109/TAP.2010.2046832.

[53] K. Wei, Z. Zhang, and Z. Feng, "Design of a wideband horizontally polarized omnidirectional printed loop antenna," *IEEE Antennas Wirel. Propag. Lett.*, vol. 11, pp. 49–52, 2012, doi: 10.1109/LAWP.2012.2182670.

[54] H. Xiong, J.-S. Hong, and D.-L. Jin, "Wideband dipole antenna with inter-digital capacitor," *Chin. Phys. B*, vol. 22, no. 4, p. 048401-1−048401-4, Apr. 2013, doi: 10.1088/1674-1056/22/4/048401.

[55] H. Li and Y. Li, "Mode compression method for wideband dipole antenna by dual-point capacitive loadings," *IEEE Trans. Antennas Propag.*, vol. 68, no. 8, pp. 6424–6428, Aug. 2020, doi: 10.1109/TAP.2020.2972642.

[56] N. Marchand, "Transmission line conversion transformers," *Electronics*, vol. 17, pp. 142–145, Dec. 1944.

[57] W. Roberts, “A new wide-band balun,” *Proc. IRE*, vol. 45, no. 12, pp. 1628–1631, 1957, doi: 10.1109/JRPROC.1957.278293.

[58] M. R. Naeini, M. Mirmozafari, and D. van der Weide, “Monolithic 3-D printing of an integrated Marchand balun with a dipole antenna,” *IEEE Trans. Compon. Packag. Manuf. Technol.*, vol. 10, no. 4, pp. 654–658, Apr. 2020, doi: 10.1109/TCPMT.2020.2966535.

[59] Z. N. Chen and M. Y. W. Chia, *Broadband Planar Antennas: Design and Applications*. Chichester, UK: John Wiley & Sons, Ltd, 2005. doi: 10.1002/0470871768.

[60] “Recommendation on base station antenna standards,” NGMN Alliance, White Paper Version 11.1, Mar. 2019. Accessed: Dec. 05, 2020. [Online]. Available: https://www.ngmn.org/publications/recommendation-on-base-station-antenna-standards-v11-1.html

[61] B. Bruno, “Recommendation on base station active antenna system standards,” NGMN Alliance, White Paper Version 1.0, Jan. 2020. Accessed: Dec. 05, 2020. [Online]. Available: https://www.ngmn.org/publications/basta-active-antenna-systems-v1-0.html

[62] R. J. Mailloux, *Phased Array Antenna Handbook*, 3rd ed. Norwood, MA: Artech House, 2018.

[63] R. C. Hansen, *Phased Array Antennas*. NY: John Wiley and Sons, 2001.

[64] B. Munk, *Finite Antenna Arrays and FSS*. Hoboken, N.J: IEEE Press ; Wiley-Interscience, 2003.

[65] "IEEE standard for definitions of terms for antennas," *IEEE Std 145-2013 (Revision of IEEE Std 145-1993)*, pp. 1–50, Mar. 2014, doi: 10.1109/IEEESTD.2014.6758443.

[66] W. Stutzman and G. Thiele, *Antenna Theory and Design*, 3rd ed. John Wiley and Sons, 2013.

[67] A. W. Rudge, K. Milne, A. D. Olver, and P. Knight, *The Handbook of Antenna Design*. IET, 1982.

[68] Z. Liang, C. Lu, Y. Li, J. Liu, and Y. Long, "A broadband dual-polarized antenna with front-to-back ratio enhancement using semicylindrical sidewalls," *IEEE Trans. Antennas Propag.*, vol. 66, no. 7, pp. 3735–3740, Jul. 2018, doi: 10.1109/TAP.2018.2835500.

[69] Y. He, J. Li, S. W. Wong, X. Pan, L. Zhang, and Z. N. Chen, "A miniaturized base station antenna with novel phase shifter for 3G/LTE applications," *IEEE Access*, vol. 6, pp. 52877–52888, 2018, doi: 10.1109/ACCESS.2018.2866482.

[70] C. Biancotto, E. Ebrahimi, and C. D. Hills, "Circumferential frame for antenna back-lobe and side-lobe attenuation," U.S. Patent Appl. 20170338568A1, Nov. 2017.

[71] C. Ding, H.-H. Sun, Y. J. Guo, P. Qin, and Y. Yang, "Beamwidth control of base station antennas employing reflectors and directors," in *2015 Int. Symp. Antennas and Propag.*, Nov. 2015, pp. 1–3.

[72] L. Zhang, S. Gao, Q. Luo, P. R. Young, Q. Li, Y. Geng, and R. A. Adb-Alhameed, "Single-feed ultra-wideband circularly polarized antenna with enhanced front-to-back ratio," *IEEE*

Trans. Antennas Propag., vol. 64, no. 1, pp. 355–360, Jan. 2016, doi: 10.1109/TAP.2015.2501844.

[73] L. Y. Nie, X. Q. Lin, Y. J. Chen, J. Zhang, B. Wang, Z. Q. Yang, and Y. Fan, "A low-profile coplanar dual-polarized and dual-band base station antenna array," *IEEE Trans. Antennas Propag.*, vol. 66, no. 12, pp. 6921–6929, Dec. 2018, doi: 10.1109/TAP.2018.2869222.

[74] M. Li, Q. L. Li, B. Wang, C. F. Zhou, and S. W. Cheung, "A low-profile dual-polarized dipole antenna using wideband AMC reflector," *IEEE Trans. Antennas Propag.*, vol. 66, no. 5, pp. 2610–2615, 2018.

[75] G. V. Trentini, "Partially reflecting sheet arrays," *IRE Trans. Antennas Propag.*, vol. 4, no. 4, pp. 666–671, Oct. 1956, doi: 10.1109/TAP.1956.1144455.

[76] D. Jackson and N. Alexopoulos, "Gain enhancement methods for printed circuit antennas," *IEEE Trans. Antennas Propag.*, vol. 33, no. 9, pp. 976–987, Sep. 1985, doi: 10.1109/TAP.1985.1143709.

[77] R. Mittra, Y. Li, and K. Yoo, "A comparative study of directivity enhancement of microstrip patch antennas with using three different superstrates," *Microw. Opt. Technol. Lett.*, vol. 52, no. 2, pp. 327–331, Feb. 2010, doi: 10.1002/mop.24898.

[78] H. Liu, S. Lei, X. Shi, and L. Li, "Study of antenna superstrates using metamaterials for directivity enhancement based on Fabry-Perot resonant cavity," *Int. J. Antennas Propag.*, vol. 2013, pp. 1–10, 2013, doi: 10.1155/2013/209741.

[79] Z. Li, Y. Mu, J. Han, X. Gao, and L. Li, “Dual-polarized antenna design integrated with metasurface and partially reflective surface for 5G communication,” *EPJ Appl. Metamaterials*, vol. 7, no. 3, pp. 1–7, 2020, doi: 10.1051/epjam/2020004.

[80] N. Nguyen-Trong, H. H. Tran, T. K. Nguyen, and A. M. Abbosh, “Wideband Fabry–Perot antennas employing multilayer of closely spaced thin dielectric slabs,” *IEEE Antennas Wirel. Propag. Lett.*, vol. 17, no. 7, pp. 1354–1358, Jul. 2018, doi: 10.1109/LAWP.2018.2846240.

[81] F. Li, Y. Cui, and R. Li, “A novel broadband AMC surface for lowering the height of planar antennas,” in *2015 Int. Symp. Antennas and Propag. & USNC/URSI Nat. Radio Sci. Meeting*, Vancouver, BC, Canada, Jul. 2015, pp. 1110–1111. doi: 10.1109/APS.2015.7304943.

[82] Y. Cui, X. Gao, H. Fu, Q.-X. Chu, and R. Li, “Broadband dual-polarized dual-dipole planar antennas: analysis, design, and application for base stations,” *IEEE Antennas Propag. Mag.*, vol. 59, no. 6, pp. 77–87, Dec. 2017, doi: 10.1109/MAP.2017.2753038.

[83] S. X. Ta, M. D. Nguyen, T. H.-Y. Nguyen, T. K. Nguyen, K. K. Nguyen, and C. Dao-Ngoc, “A low-profile ±45^{o} dual-polarized antenna based on metasurface and its arrays for base station applications,” *J. Electromagn. Waves Appl.*, vol. 32, no. 14, pp. 1748–1767, Sep. 2018, doi: 10.1080/09205071.2018.1468284.

[84] B. Feng, X. He, J.-C. Cheng, Q. Zeng, and C.-Y.-D. Sim, “A low-profile differentially fed dual-polarized antenna with high gain and isolation for 5G microcell communications,”

IEEE Trans. Antennas Propag., vol. 68, no. 1, pp. 90–99, Jan. 2020, doi: 10.1109/TAP.2019.2935091.

[85] G. Li, H. Zhai, L. Li, and C. Liang, "AMC-loaded wideband base station antenna for indoor access point in MIMO system," *IEEE Trans. Antennas Propag.*, vol. 63, no. 2, pp. 525–533, 2015.

[86] S. X. Ta and I. Park, "Dual-band low-profile crossed asymmetric dipole antenna on dual-band AMC surface," *IEEE Antennas Wirel. Propag. Lett.*, vol. 13, pp. 587–590, 2014, doi: 10.1109/LAWP.2014.2312950.

[87] Z. Fneish, F. Mazeh, H. Ayad, A. A. Khalil, G. Faour, M. Fadlallah, and J. Jomaah, "Design of a miniaturized dual wide band and tri band artificial magnetic conductor in LTE regions," in *2017 Sensors Netw. Smart Emerging Technol. (SENSET)*, Beirut, Sep. 2017, pp. 1–4. doi: 10.1109/SENSET.2017.8125023.

[88] G. K. Pandey, H. S. Singh, and M. K. Meshram, "Investigations of triple band artificial magnetic conductor back plane with UWB antenna," *Microw. Opt. Technol. Lett.*, vol. 58, no. 8, pp. 1900–1906, 2016, doi: 10.1002/mop.29943.

[89] Y. Zhu, Y. Chen, and S. Yang, "Decoupling and low-profile design of dual-band dual-polarized base station antennas using frequency-selective surface," *IEEE Trans. Antennas Propag.*, vol. 67, no. 8, pp. 5272–5281, Aug. 2019, doi: 10.1109/TAP.2019.2916730.

[90] Y. Chen, J. Zhao, and S. Yang, "A novel stacked antenna configuration and its applications in dual-band shared-aperture base station antenna array designs," *IEEE Trans. Antennas Propag.*, vol. 67, no. 12, pp. 7234–7241, Dec. 2019, doi: 10.1109/TAP.2019.2930136.

[91] N. Sundararajan, C. Buondelmonte, A. Litteer, and W. Chen, “Low cost high performance multiband cellular antenna with cloaked monolithic metal dipole,” U.S. Patent Appl. 20200328533A1, Oct. 15, 2020.

[92] F. Hyjazie, P. Watson, and H. Boutayeb, “Dual band interleaved base station phased array antenna with optimized cross-dipole and EBG/AMC structure,” in *2014 IEEE Antennas and Propag. Soc. Int. Symp. (APSURSI)*, Jul. 2014, pp. 1558–1559. doi: 10.1109/APS.2014.6905105.

[93] L. Wu, B. Wu, and J. Sun, “Ultra wide band radiators and related antennas arrays,” U.S. Patent Appl. 20170294715A1, Oct. 12, 2017.

[94] H.-H. Sun, C. Ding, H. Zhu, B. Jones, and Y. J. Guo, “Suppression of cross-band scattering in multiband antenna arrays,” *IEEE Trans. Antennas Propag.*, vol. 67, no. 4, pp. 2379–2389, Apr. 2019, doi: 10.1109/TAP.2019.2891707.

[95] X. Zhang, D. Xue, L. Ye, Y. Pan, and Y. Zhang, “Compact dual-band dual-polarized interleaved two-beam array with stable radiation pattern based on filtering elements,” *IEEE Trans. Antennas Propag.*, vol. 65, no. 9, pp. 4566–4575, Sep. 2017, doi: 10.1109/TAP.2017.2723914.

[96] Y. He, Z. Pan, X. Cheng, Y. He, J. Qiao, and M. M. Tentzeris, “A novel dual-band, dual-polarized, miniaturized and low-profile base station antenna,” *IEEE Trans. Antennas Propag.*, vol. 63, no. 12, pp. 5399–5408, Dec. 2015, doi: 10.1109/TAP.2015.2481488.

[97] Y.-B. Jung and S.-Y. Eom, “A compact multiband and dual-polarized mobile base-station antenna using optimal array structure,” *Int. J. Antennas Propag.*, vol. 2015, pp. 1–11, 2015, doi: 10.1155/2015/178245.

[98] R. Wu and Q.-X. Chu, “A compact, dual-polarized multiband array for 2G/3G/4G base stations,” *IEEE Trans. Antennas Propag.*, vol. 67, no. 4, pp. 2298–2304, Apr. 2019, doi: 10.1109/TAP.2019.2902652.

[99] Y. He, W. Tian, and L. Zhang, “A novel dual-broadband dual-polarized electrical downtilt base station antenna for 2G/3G applications,” *IEEE Access*, vol. 5, pp. 15241–15249, 2017, doi: 10.1109/ACCESS.2017.2720591.

[100] N. Sundararajan, C. Kozak, A. Teillet, and K. Le, “Dual band, multi column antenna array for wireless network,” U.S. Patent Appl. 20170062952A1, Mar. 02, 2017 Accessed: Dec. 04, 2020. [Online]. Available: https://patents.google.com/patent/US20170062952A1/en

[101] J.-H. Lan, B.-H. Sun, Q.-Y. Liang, and J.-F. Li, “Suppression of cross-band scattering by using sleeve loads,” *IEEE Antennas Wirel. Propag. Lett.*, vol. 20, no. 12, pp. 2230–2234, Dec. 2021, doi: 10.1109/LAWP.2021.3103943.

[102] H. Sheng and Z. N. Chen, “Radiation pattern improvement of cross-band dipoles using inductive-loading mode-suppression method,” *IEEE Trans. Antennas Propag.*, vol. 67, no. 5, pp. 3467–3471, May 2019, doi: 10.1109/TAP.2019.2902649.

[103] Q. Wu, W. Su, Z. Li, and D. Su, “Reduction in out-of-band antenna coupling using characteristic mode analysis,” *IEEE Trans. Antennas Propag.*, vol. 64, no. 7, pp. 2732–2742, Jul. 2016, doi: 10.1109/TAP.2016.2522459.

[104] M. L. Zimmerman and P. J. Bisiules, “Method of eliminating resonances in multiband radiating arrays,” U.S. Patent Appl. 20150295313A1, Oct. 15, 2018.

[105] J. C. Soric, A. Monti, A. Toscano, F. Bilotti, and A. Alu, “Dual-polarized reduction of dipole antenna blockage using mantle cloaks,” *IEEE Trans. Antennas Propag.*, vol. 63, no. 11, pp. 4827–4834, Nov. 2015, doi: 10.1109/TAP.2015.2476468.

[106] J. C. Soric, A. Monti, A. Toscano, F. Bilotti, and A. Alù, “Multiband and wideband bilayer mantle cloaks,” *IEEE Trans. Antennas Propag.*, vol. 63, no. 7, pp. 3235–3240, Jul. 2015, doi: 10.1109/TAP.2015.2421951.

[107] M. Li, R. Wang, J. M. Yasir, and L. Jiang, “A miniaturized dual-band dual-polarized band-notched slot antenna array with high isolation for base station applications,” *IEEE Trans. Antennas Propag.*, vol. 68, no. 2, pp. 795–804, Feb. 2020, doi: 10.1109/TAP.2019.2940471.

[108] C. R. Paul, *Introduction to Electromagnetic Compatibility*, 2nd ed. Hoboken, NJ, USA: John Wiley & Sons, Inc., 2006.

[109] H. Ott, *Electromagnetic Compatibility Engineering*. John Wiley & Sons, 2009.

[110] D. Cavallo, A. Neto, and G. Gerini, “PCB slot based transformers to avoid common-mode resonances in connected arrays of dipoles,” *IEEE Trans. Antennas Propag.*, vol. 58, no. 8, pp. 2767–2771, Aug. 2010, doi: 10.1109/TAP.2010.2050430.

[111] Y. Zhu, Y. Chen, and S. Yang, “Helical torsion coaxial cable for dual-band shared-aperture antenna array decoupling,” *IEEE Trans. Antennas Propag.*, vol. 68, no. 8, pp. 6128–6135, Aug. 2020, doi: 10.1109/TAP.2020.2986725.

[112] B. B. Jones, “High-band radiators with extended-length feed stalks suitable for basestation antennas,” U.S. Patent 9711871B2, Jul. 18, 2017 Accessed: Dec. 06, 2020. [Online]. Available: https://patents.google.com/patent/US9711871/en

[113] J. Gilmore and D. B. Davidson, “Suppressing undesired common-mode resonances in connected antenna arrays,” *IEEE Trans. Antennas Propag.*, vol. 63, no. 11, pp. 5245–5250, Nov. 2015, doi: 10.1109/TAP.2015.2478141.

[114] A. Shooshtari, M. L. Zimmerman, and P. J. Bisiules, “Low common mode resonance multiband radiating array,” U.S. Patent Appl. 20160285169A1, Sep. 29, 2016 Accessed: Dec. 06, 2020. [Online]. Available: https://patents.google.com/patent/US20160285169A1/en

[115] *HFSS - High Frequency Structures Simulator*. Ansys. [Online]. Available: https://www.ansys.com/products/electronics/ansys-hfss

[116] *NSI 2000 Antenna Measurement Software*. Nearfield Systems, Inc., 2016. [Online]. Available: https://www.nsi-mi.com/products/software-products/nsi2000-professional-edition-upgrade

[117] T. Jang, L. Bamford, K. Le, E. Wayton, C. Anderson, J. Ragos, and N. Sundararajan, “Low profile telecommunications antenna,” U.S. Patent 11043752B2, Jun. 22, 2021.

[118] T. Jang, L. Bamford, K. Le, E. Wayton, C. Anderson, J. Ragos, and N. Sundararajan, “Low profile telecommunications antenna,” U.S. Patent 10680347B2, Jun. 09, 2020.

[119] T. Jang, N. Sundararajan, L. Bamford, and E. Wayton, “Cloaking arrangement for low profile telecommunications antenna,” U.S. Patent 10854959B2, Dec. 01, 2020.

[120] K. Le, L. Bamford, T. Jang, E. Wayton, C. Anderson, J. Ragos, and N. Sundararajan, “Modular unit cell construction for a high performance, low profile (HPLP) telecommunications antenna,” U.S. Patent 10320092B2, Jun. 11, 2019.

[121] A. Waldauer, C. Buondelmonte, T. Jang, N. Sundararajan, E. Wayton, and L. Bamford, “Multi-band fast roll off antenna having multi-layer PCB-formed cloaked dipoles,” U.S. Patent 11018438B2, May 25, 2021.

[122] A. D’Aquino, “Recommendation on base station antenna standards,” NGMN Alliance, White Paper Version 10.0, 2017. Accessed: Nov. 09, 2018. [Online]. Available: https://www.ngmn.org/fileadmin/user_upload/170217_NGMN-N-P-BASTA_White _Paper_V10.0.pdf

[123] T. S. M. Maclean, “Impedance properties of capacitively loaded dipoles,” *Proc. Inst. Elect. Eng.*, vol. 115, no. 10, pp. 1411–1418, 1968, doi: 10.1049/piee.1968.0251.

[124] C. R. Paul, “A comparison of the contributions of common-mode and differential-mode currents in radiated emissions,” *IEEE Trans. Electromagn. Compat.*, vol. 31, no. 2, pp. 189–193, May 1989, doi: 10.1109/15.18789.

[125] C. R. Paul and D. R. Bush, “Radiated emissions from common-mode currents,” in *1987 IEEE Int. Symp. on Electromagn. Compat.*, Aug. 1987, pp. 1–7. doi: 10.1109/ISEMC.1987. 7570770.

[126] D. S. Prinsloo, R. Maaskant, M. V. Ivashina, and P. Meyer, “Mixed-mode sensitivity analysis of a combined differential and common mode active receiving antenna providing near-hemispherical field-of-view coverage,” *IEEE Trans. Antennas Propag.*, vol. 62, no. 8, pp. 3951–3961, Aug. 2014, doi: 10.1109/TAP.2014.2322896.

[127] H. Xu, S. S. Gao, H. Zhou, H. Wang, and Y. Cheng, “A highly integrated MIMO antenna unit: Differential/common mode design,” *IEEE Trans. Antennas Propag.*, vol. 67, no. 11, pp. 6724–6734, Nov. 2019, doi: 10.1109/TAP.2019.2922763.

[128] A. Andújar, J. Anguera, C. Puente, and A. Pérez, “On the radiation pattern of the L-shaped wire antenna,” *Prog. Electromagn. Res. M*, vol. 6, pp. 91–105, 2009, doi: 10.2528 /PIERM09012204.

[129] H. R. Stuart, “Eigenmode analysis of a two element segmented capped monopole antenna,” *IEEE Trans. Antennas Propag.*, vol. 57, no. 10, pp. 2980–2988, Oct. 2009, doi: 10.1109 /TAP.2009.2028604.

[130] C. Mateo-Segura, A. P. Feresidis, and G. Goussetis, “Bandwidth enhancement of 2-D leaky-wave antennas with double-layer periodic surfaces,” *IEEE Trans. Antennas Propag.*, vol. 62, no. 2, pp. 586–593, Feb. 2014, doi: 10.1109/TAP.2013.2292076.

[131] N. Wang, Q. Liu, C. Wu, L. Talbi, Q. Zeng, and J. Xu, “Wideband Fabry-Perot resonator antenna with two complementary FSS layers,” *IEEE Trans. Antennas Propag.*, vol. 62, no. 5, pp. 2463–2471, May 2014, doi: 10.1109/TAP.2014.2308533.

[132] K. Konstantinidis, A. P. Feresidis, and P. S. Hall, “Multilayer partially reflective surfaces for broadband Fabry-Perot cavity antennas,” *IEEE Trans. Antennas Propag.*, vol. 62, no. 7, pp. 3474–3481, Jul. 2014, doi: 10.1109/TAP.2014.2320755.

[133] N. Wang, C. Zhang, Q. Zeng, N. Wang, and J. Xu, “New dielectric 1-D EBG structure for the design of wideband resonator antennas,” *Prog. Electromagn. Res.*, vol. 141, pp. 233–248, Oct. 2013, doi: 10.2528/pier13061207.

[134] N. Wang, L. Talbi, Q. Zeng, and J. Xu, “Wideband Fabry-Perot resonator antenna with electrically thin dielectric superstrates,” *IEEE Access*, vol. 6, pp. 14966–14973, 2018, doi: 10.1109/ACCESS.2018.2810085.

[135] S. Silver, Ed. *Microwave Antenna Theory and Design*. New York: McGraw-Hill, 1949, p. 425.

[136] *MATLAB*. MathWorks, 2021. [Online]. Available: https://www.mathworks.com/products/matlab.html

[137] R. J. Garbacz, “Modal expansions for resonance scattering phenomena,” *Proc. IEEE*, vol. 53, no. 8, pp. 856–864, Aug. 1965, doi: 10.1109/PROC.1965.4064.

[138] R. Harrington and J. Mautz, “Theory of characteristic modes for conducting bodies,” *IEEE Trans. Antennas Propag.*, vol. 19, no. 5, pp. 622–628, Sep. 1971, doi: 10.1109/TAP.1971.1139999.

[139] R. Harrington and J. Mautz, “Computation of characteristic modes for conducting bodies,” *IEEE Trans. Antennas Propag.*, vol. 19, no. 5, pp. 629–639, Sep. 1971, doi: 10.1109/TAP.1971.1139990.

[140] M. Cabedo-Fabres, E. Antonino-Daviu, A. Valero-Nogueira, and M. F. Bataller, “The theory of characteristic modes revisited: a contribution to the design of antennas for modern applications,” *IEEE Antennas Propag. Mag.*, vol. 49, no. 5, pp. 52–68, Oct. 2007, doi: 10.1109/MAP.2007.4395295.

[141] Z. Bai, J. Demmel, J. Dongarra, A. Ruhe, and H. A. van der Vorst, Eds., *Templates for the Solution of Algebraic Eigenvalue Problems*. Society for Industrial and Applied Mathematics, 2000. doi: 10.1137/1.9780898719581.

[142] W. C. Chew, *Waves and Fields in Inhomogeneous Media*. New York: Van Nostrand Reinhold, 1990, pp. 76–79.

[143] J. A. Kong, *Electromagnetic Wave Theory*. Cambridge, MA: EMW Publishing, 2008, pp. 572–581.

Vita

Evan C. Wayton

Born: December 17th, 1987, in Toledo, Ohio
Current Residence: Otisco, NY

Education

Master of Science Syracuse University Electrical Engineering	May 2013 Syracuse, New York
Bachelor of Science The University of Toledo Electrical Engineering (Physics Minor)	May 2011 Toledo, Ohio

Awards & Honors

The Anaren Gerst-Hair Graduate Studies Fellowship Syracuse University	2011-2013 Syracuse, New York
Summa Cum Laude The University of Toledo	May 2011 Toledo, Ohio
Pride Scholarship The University of Toledo	2007-2011 Toledo, Ohio

Publications

Journal Papers

J1. E. C. Wayton, T. Jang, J. K. Lee, "A serially loaded capacitive dipole for mutual coupling reduction in dual-band environments", *IEEE Trans. Antennas Propag*., (Under review).

Conference Presentations

C1. E. C. Wayton and J. K. Lee, "Fabry-Perot cavity antenna for tri-band array environment with radome", in *2022 IEEE Int. Symp. Antennas Propag. USNC-URSI Radio Sci. Meet.*, July 2022, Denver, Colorado, *accepted.*

C2. E. C. Wayton, W. Chen, N. Sundararajan, and J. K. Lee, "Common mode suppression technique for dual-band array environment", in *2021 IEEE Int. Symp. Antennas Propag. USNC-URSI Radio Sci. Meet.*, December 2021, Marina Bay Sands, Singapore.

C3. E. Wayton, T. Jang, N. Sundararajan, L. Bamford, and J. Lee, "Capacitive Cloaking Technique for Antenna Elements in Multi-Band Array Environment", in *2020 IEEE Int. Symp. Antennas Propag. USNC-URSI Radio Sci. Meet.*, July 2020, Montréal, Quebec, Canada.

Patents

Patents Granted

P1. *Low profile telecommunications antenna*
Co-Inventor, (Patent Number: US 11,043,752 B2), June 2021.

P2. *Multi-band fast roll off antenna having multi-layer PCB-formed cloaked dipoles*
Co-Inventor, (Patent Number: US 11,018,438 B2), May 2021.

P3. *Cloaking arrangement for low profile telecommunications antenna*
Co-Inventor, (Patent Number: US 10,854,959 B2), December 2020.

P4. *Low profile telecommunications antenna*
Co-Inventor, (Patent Number: US 10,680,347 B2), June 2020.

P5. *Modular unit cell construction for a high performance, low profile (HPLP) telecommunications antenna*
Co-Inventor (Patent Number: US 10,320,092 B2), June 2019.

Patents Pending

P6. *Frequency selective parasitic director for improved midband performance and reduced C-band/CBRS interference*
Lead-Inventor (Application Number: 63/254235), October 2021.

P7. *Miniaturized wideband 3-way splitters for ultra-dense quasi-omni base station antennas*
Co-Inventor (Application Number: 63/239684), September 2021.

P8. *8T8R Quasi-Omnidirectional Antenna*
Co-Inventor (Application Number: 63/218631), July 2021.

P9. *Low-cost miniaturized vertical coaxial cable to PCB transition for use in ultra-dense base station antennas*
Co-Inventor (Application Number: 63/191016), May 2021.

P10. *Antenna having an internal cable tower and guides for precise cable placement and method for constructing the same*
Co-Inventor (Publication Number: WO 2021081042 A1), April 2021.

P11. *Toroidal gradient index lens for omni and sector antennas*
Lead-Inventor (Publication Number: WO 2020256760 A1), December 2020.

P12. *Luneburg lens formed of assembled molded components*
Co-Inventor (Publication Number: WO 2020209889 A1), October 2020.

Academic Appointment

Syracuse University	Syracuse, New York
Graduate Teaching Assistant	May 2012 to August 2012

Professional Employment

JMA Wireless, Inc.	Liverpool, New York
Senior Principal RF Antenna Engineer	April 2022 to Present
Senior RF Antenna Engineer	May 2019 to April 2022
Antenna Engineer	April 2016 to April 2019
Anaren, Inc.	East Syracuse, New York
RF Engineer II, Space & Defense Group	November 2015 to April 2016
RF Engineer I, Space & Defense Group	May 2013 to October 2015
RF/Ferrite Engineering Cooperative *Space & Defense Group, Wireless Group*	May 2008 to August 2012

Volunteer Work

IEEE MTT-13 Technical Committee on Control Materials and Devices

Webmaster	2015 to 2021

Professional Memberships

IEEE Member	2007 to Present
IEEE MTT-S Member	2011 to Present
IEEE AP-S Member	2012 to Present
IEEE Magnetics Society Member	2011 to 2020
IEEE MTT-13 Board Member	2015 to 2022